

DISS. ETH No. 20994

**Active deformation and landscape evolution of the
Makran Accretionary Wedge (SE-Iran)
New constraints from surface exposure dating of fluvial terraces**

A dissertation submitted to
ETH Zurich

For the degree of
Doctor of Sciences

Presented by

Negar HAGHIPOUR

M.Sc. in Geology. Azad University, Tehran-North branch (Iran)

born 17.05.1977

citizen of

Iran

Accepted on the recommendation of

Prof. Dr. Jean-Pierre Burg
PD Dr. Susan Ivy-Ochs
Dr. Florian Kober
Prof. Dr. Mark T. Brandon

ETH Zurich
ETH Zurich
ETH Zurich
Yale University

Examiner
Co-examiner
Co-examiner
Co-examiner

2013

*I have not failed.
I've just found 10,000 ways that won't work.*

Thomas A. Edison

Table of contents

Abstract	i - ii
Zusammenfassung	iii - iv
Chapter I: Introduction	
1- Study area	6
1-1 Geological setting	6
1-2 Geodynamic and seismicity	8
1-3 Overviews of previous work	11
Inland Makran	11
Coastal Makran	12
1-4 Remaining problems and aims	12
2 Morphometric analysis and methods	13
2-1 Fluvial systems	14
2-2 Morphometric tools	15
3 Terrestrial Cosmogenic Nuclides (TCNs)	16
3-1 Principles	16
3-2 Terrestrial Cosmogenic Nuclide (TCN) application to active tectonics research	18
3-3 Depth profile (surface erosion and inheritance)	19
4 Outline of the thesis	20
Chapter II: Geomorphological analysis	
1-Introduction	26
2-Setting	27
2-1- Tectonic and geological setting	27
2-2- Regional climate	29
2-3- Drainage system on the Makran Accretionary Wedge	29
3- Analytical methods	30
3-1- Local relief and swath profiles	31
3-2- Longitudinal stream profile	31
3-3- Channel steepness index	32
3-4 Steady-state river profile reconstruction	32
4- Results	31
4-1- General topographic features	34
4-2- Stream profiles characteristics	36
4-3- Synthesis of results	51

5- Discussion and interpretation	51
5-1- Knickpoints and causes of transient incision	51
5-2- Quaternary uplift	52
5-3- Regional variation in topographic growth and tectonic activity	52
5-4- Comparison with other accretionary wedges	53
5-5- Possible drivers of morphometric variations along the Makran Accretionary Wedge	54
5-6- Coupled erosion and deformation model	55
6-Conclusion	56
Acknowledgements	57

Chapter III: Cosmogenic nuclide dating

Abstract	61
1. Introduction	62
2. Setting	62
2.1. Geological setting	62
2.2. Seismicity – Active tectonics	65
2.3. Climate setting	65
3. Methods	66
3.1. Field observation and surveying	66
3.2. Channel steepness indices	67
3.3. Cosmogenic nuclide dating and sampling (^{10}Be and ^{26}Al)	69
3.4. Radiocarbon dating	74
3.5. Calculating incision and uplift rate	74
4. Site description of dated fluvial terraces	77
4.1. Sedij catchment	77
4.2. Fanuj catchment	78
4.3. Nikshahr catchment	80
4.4. Pishin catchment	82
5. Results	85
5.1. ^{10}Be abandonment ages and rates of fluvial incision	85
5.2. ^{14}C dating result and coastal uplift	86
5.3. Comparison between incision rate and river gradient	88
6. Discussion	89
6.1. Age uncertainties and resolution	89
6.2. Age distribution and modeled ages	93
6.3. Correlation with Marine Isotopic Stages	94
6.4. Uplift rates	95

Conclusion	92
Acknowledgements	96

Chapter IV Crustal shortening

Introduction	100
1- Setting	100
1-1 Tectonic setting	100
1-2 Seismicity and geodesy background	101
1-3 Structural background of onshore, Central Makran	102
2- Methods	104
2-1 Mapping and surveying	104
2-2 Sampling - Terrace description	106
2-3 ¹⁰ Be terrestrial cosmogenic nuclide surface exposure dating	108
2-4 Uplift and shortening estimation	111
3- Results	112
3-1 Sites A and B: Sedij River	112
3-2 Sites C and D: Nikshahr River	113
3-3 Sites E and F: Sarbaz River – Pishin catchment	114
4- Discussion	117
4-1 ¹⁰ Be age uncertainties	117
4-2 Quaternary folding: Insight from fluvial terraces	118
4-3 Bulk horizontal shortening and shortening rate deduced from mass conservation	119
4-4 Seismotectonic Implications	121
5- Conclusion	121
Acknowledgements	122

Chapter V Conclusion

5-1 Along strike variation of tectonic activity inferred from the river morphology	125
5-2 Surface exposure dating	126
Climatic influence	126
Tectonic implication	126
5-3 Rate of crustal shortening	127
5-4 Outlook	127

Bibliography

Abstract

The topographic evolution of mountain belts results from complex coupling between tectonics, climate and surface processes. However, our ability to infer tectonic information from surface observations is hampered by a lack of quantification of the causal links between tectonic activity and topography. Therefore, a set of methodological tools quantifying landscape evolution has been recently developed to constrain forcing processes over temporal (10^3 - 10^6 a) and spatial (1-100 km) scales characteristic of orogenic systems. For this thesis the first systematic assessment of the landscape response to deformation of the onshore Makran Accretionary Wedge (MAW), in SE Iran, was carried out.

First, we give a general introduction to the scientific problem, to the tectonic setting of the field area, and to the methodology employed in the thesis.

Then, we present the quantitative assessment of the river pattern and link the characteristics of drainage basins and channel length profiles with fluvial incision as a marker of surface uplift. Surface uplift is essentially caused by recent crustal deformation of the wedge. The variations in channel steepness and concavity allow determining a background, regional picture and identifying focused incision where active folds and thrusts are growing. It also indicates a difference in behavior between western and eastern Makran.

The first absolute ages of fluvial terraces over a large part of onshore MAW were obtained using ^{10}Be exposure dating. The 13-379 ka spread of ages offers the chance to clarify whether the formation and abandonments of the studied terraces are associated with climatic cycles or/and tectonic forces. The most widespread levels (at ca 20 and 100 ka) are linked to Marine Isotopes Stages MIS 2-5. The new ages further permit calculating rates of both the regional background and the localized incisions. The regional 'background' incision rate, used as a proxy of surface uplift, is relatively moderate and homogeneous (0.3 mm/a). It fits previous estimates from uplifted marine terraces. This general uplift rate is confirmed by ages we obtained with ^{14}C (radiocarbon) and ^{10}Be methods on newly dated marine terraces. Local incision/uplift rates reach up to 0.8-1 mm/a.

The regional, uniformly distributed incision rate is attributed to the steady growth of the MAW. The locally high incision rates indicate that, however, perfect steady-state is unlikely on short-length scales, local instabilities depict localized deformation.

Folded fluvial terraces taken as passive markers on growing folds and fold trains help constraining the dynamics of both distributed and localized deformation due to shortening/convergence across the onshore MAW. The results are compared to interseismic deformation documented by published GPS data. The calculated average shortening rate due to folding on the millennial time scale accounts for 10-15% of the shortening rate given by kinematic GPS measurements across the Iranian part of the MAW. Active folding depicted in this work shows that the generally accepted concept of 'Coulomb' accretionary wedges is

an excellent, long-term approximation that requires refinements in terms of bulk rheology to account for shortening mechanisms additional to discrete fault movements. The noticeable spatial variation in recent deformation, denoting increasingly stronger impact of Quaternary deformation towards the east, is attributed to eastward increasing convergence, hence subduction rates.

Our results emphasize the link between surficial and deeper crustal processes in active orogenic systems.

Zusammenfassung

Die topographische Entwicklung eines Gebirges erfolgt aus dem komplexen Zusammenspiel zwischen Tektonik, Klima und Oberflächenprozessen. Die Möglichkeit aus Beobachtungen der Erdoberfläche, Informationen über tektonische Prozesse zu erhalten, wird aufgrund fehlender Quantifizierung der Zusammenhänge zwischen tektonischer Aktivität und Topographie geschmälert. Daher wurde kürzlich eine Anzahl methodologischer Werkzeuge, die die Landschaftsentwicklung quantifizieren, entwickelt, um die, für ein Gebirgssystem zeitlich (10^3 - 10^6 a) und räumlich (1-100 km) charakteristischen, treibenden Kräfte einzugrenzen. Im Zuge dieser Arbeit wurde die erste systematische Erfassung der Landschaftsentwicklung aufgrund der Verformung des landwärtigen Makran Akkretionskeils (MAK), im Südosten des Irans, durchgeführt.

Zuerst wird eine allgemeine Einleitung zur wissenschaftlichen Fragestellung, zur tektonischen Situation des Feldgebiets und zur, in der Arbeit angewandten, Methodik präsentiert.

Daraufhin wird die quantitative Bewertung des Flussmusters vorgestellt und die Eigenschaften von Einzugsgebieten und Profilen der Kanallängen werden mit dem Einschneiden von Flüssen, das als Marker für Oberflächenhebung dient, in Zusammenhang gebracht. Oberflächenhebung wird hauptsächlich durch rezente krustale Verformung des Keils verursacht. Die Unterschiede in der Steilheit und Wölbung der Kanäle erlauben es, ein regionales Hintergrundbild zu beschreiben und fokussiertes Einschneiden zu ermitteln, wo Falten und Aufschiebungen entstehen. Dies zeigt auch einen Unterschied im Verhalten zwischen West- und Ost-Makran auf.

Die ersten absoluten Alter der Flussterrassen eines grossen Teils des landwärtigen MAK wurden mit Hilfe der Bestimmung des ^{10}Be Bestrahlungsalters gewonnen. Die Verteilung der Alterswerte zwischen 13-379 ka bietet die Möglichkeit, besser zu verstehen, ob die Bildung und die Stilllegung der untersuchten Terrassen in Zusammenhang mit klimatischen Zyklen und/oder tektonischen Kräften stehen. Die am weitesten verbreiteten Niveaus (um ca. 20 und 100 ka) stehen in Verbindung mit den marinen Isotopen Stadien MIS 2-5. Die neuen Alter erlauben ausserdem, sowohl regionale, Hintergrund- als auch lokale Einschnittraten zu berechnen. Die regionale, Hintergrund-Einschnittrate, die stellvertretend für die Oberflächenhebung steht, ist relativ gemässigt und homogen (0.3 mm/a). Diese stimmt mit früheren Schätzungen von erhobenen marinen Terrassen überein. Diese allgemeine Hebungsrates wird durch ^{14}C und ^{10}Be Alter von neu datierten marinen Terrassen bestätigt. Lokale Hebungs- und Einschnittraten erreichen Werte bis zu 0.8-1 mm/a.

Die regionale, gleichmässig verteilte Einschnittrate wird dem ständig wachsenden MAK zugeordnet. Die lokal hohen Einschnittraten deuten an, dass, obwohl ein perfekter

stationärer Zustand unwahrscheinlich ist auf einer kleinen Skala, lokale Instabilitäten lokalisierte Verformung anzeigen.

Gefaltete Flussterrassen, die man als passive Marker auf wachsenden Falten und Faltenzügen benutzt, helfen, die Dynamik sowohl von verteilter als auch lokalisierter Verformung einzugrenzen, die ausgelöst wird durch Verkürzung/Konvergenz im landwärtigen MAK. Die Resultate werden mit veröffentlichten GPS Daten verglichen, die interseismische Verformung dokumentieren. Die, aufgrund von Verfaltung, in einem Zeitraum von Millionen Jahren, berechnete Verkürzungsrate, erklärt 10-15% der auf kinematischen GPS Messungen, verteilt über den iranischen Teil des MAK, basierenden Verkürzungsrate. Die aktive Verfaltung, die in dieser Arbeit vorgestellt wird, zeigt, dass das allgemein akzeptierte Konzept des „Coulomb“-Akkretionskeils eine hervorragende, langfristige Annäherung ist, die Verfeinerungen in Bezug auf die Gesamtrheologie benötigt, um auch zusätzliche Verkürzungsmechanismen, nebst der diskreten Bewegung auf Störungen, miteinzubeziehen. Die erkennbare räumliche Variation in der neuzeitlichen Verformung, zeigt einen zunehmend grösseren Einfluss von Quartärer Verformung Richtung Osten, und wird der ostwärts zunehmenden Konvergenz, d.h. Subduktionsrate, zugeschrieben.

Unsere Resultate betonen den Zusammenhang zwischen Prozessen an der Oberfläche und in der tieferen Kruste in einem aktiven Gebirgssystem.

Chapter I

Introduction

General Introduction

This thesis deals with the Makran Accretionary Wedge exposed in the Baluchistan of S-E Iran (Fig. 1). The region is sparsely populated, with a traditional nomadic population, although cities on the coast of the Oman Sea tend to grow rapidly. Few inland roads allow usually distant approach to geological sites. The province is notorious for cross-border smuggling, which justifies carefulness and advanced permission from Iranian and provincial authorities for traveling and residing in some places. The area is known for its ancient *ichthyophagi* population, the “fish-eaters” reported by Nearchus, Alexander the Great’s admiral who led the Macedonian fleet from the Indus to the Persian Gulf in 325-324 BC.

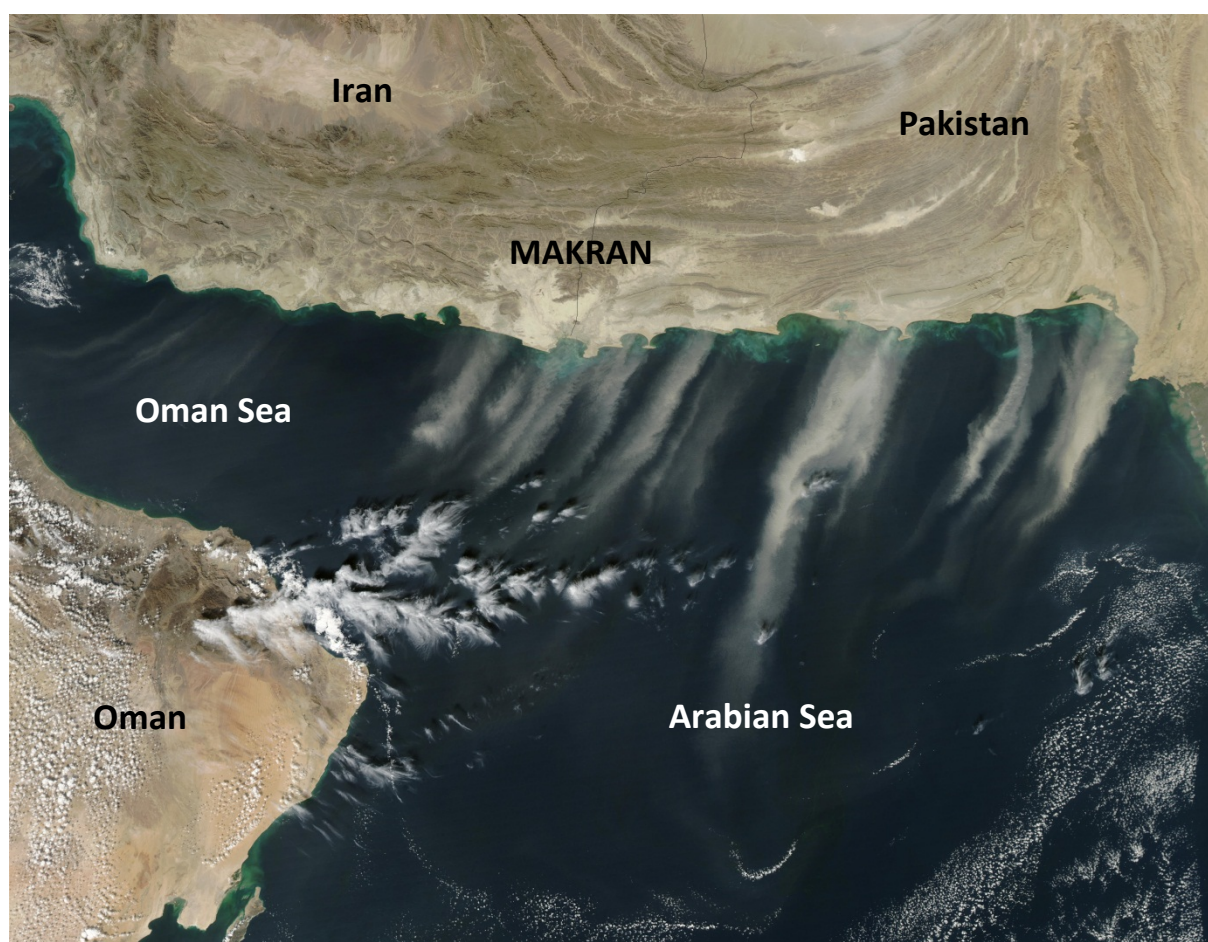


Fig. 1: Satellite picture showing dust transported from inland Makran into the Arabian Sea. Image Pakistan_AMO2002338 from NASA-Earth Observatory:

<http://earthobservatory.nasa.gov/NaturalHazards/view.php?id=10564>

Accretionary wedges have been the focus of much investigation because they provide strategic information on deformation in convergence zones and, by analogy, on the evolution of all accretionary orogenic systems. As part of subduction margin settings, Quaternary marine and fluvial terraces can provide quantitative estimates of deformation in the overriding plate and, where the record allows it, paleoseismic statistics. The morphology of natural and experimental accretionary wedges is classically explained with the critical

wedge model, which considers that the mechanics of orogenic wedges is analogous to pushing loose sand or snow uphill in front of a moving bulldozer (Davis et al. 1983, Dahlen et al. 1984, Dahlen 1990). More precisely, the critical wedge theory predicts that an orogenic wedge will attain a critical surface slope (critical taper) sustained by continued accretion. An important conclusion for this thesis project is that the shape of the taper is maintained during the wedge growth. This general shape is defined by the taper, an acute angle which is the sum of the upper surface slope α and the dip of the basal décollement β (Fig. 2). This implies that the surface uplift is everywhere the same on the wedge while the surface keeps the same slope throughout the accretionary history. The morphology of the wedge, and in particular its upper slope surface, is a function of both the assumed rheology of the wedge material and the strength of the basal décollement. Therefore there is a continuous interplay between wedge deformation at subcritical taper conditions and periods of sliding at critical taper conditions so that constant re-equilibration of the wedge slope should be recorded by surfaces processes.

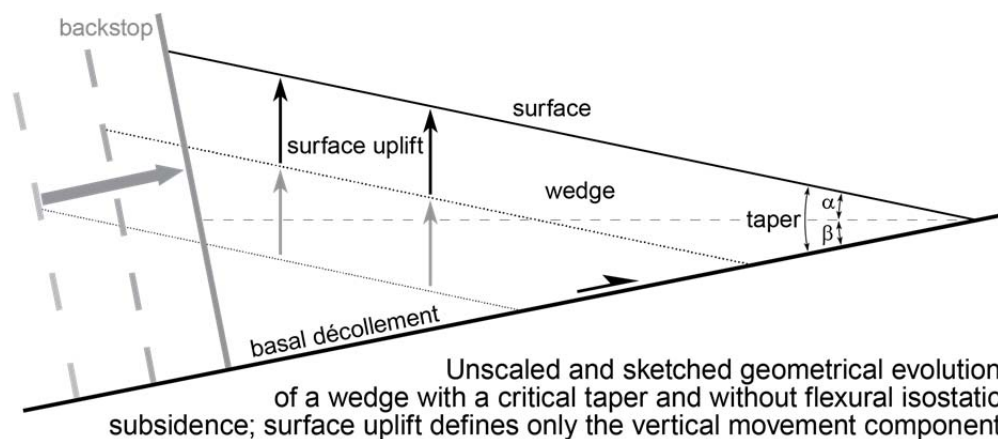


Fig. 2: Geometrical evolution and surface behavior of a self-similarly growing accretionary wedge. Note that vertical surface uplift is equal everywhere. Drawn from concepts developed in Davis et al. (1983), Dahlen et al. (1984) and Dahlen (1990).

The critical wedge theory has been supported by many analogue experiments (e.g. Davis et al. 1983, Malavieille 1984, Graveleau et al. 2012, and references therein) and numerical studies (e.g. Willett 1992, Buiter et al. 2006, Simpson 2010, Ruh et al. 2012) and has had an impressive success in explaining geological observations at active margins (e.g. Dahlen et al. 1984, Platt 1986, Dahlen 1990, Sengor 1991, Willett et al. 1993). However, the models of critical taper only simulate the large scale geometry of the wedge while paying less attention to the nature of the internal deformation, which is simply assumed to follow a “Coulomb”, elasto-plastic rheology (e.g. Stockmal 1983, Borja & Dreiss 1989, Willett et al. 1993). Now, if we want to refine our understanding of tectonic accretion, the assumptions on the internal dynamics of wedges need to be confronted with actual observation of spatial and time variations. A major cause of this data deficiency derives from the fact that most of the information comes from submarine wedges (e.g. Barbados, Biju-Duval et al. 1982; Costa Rica, Ye et al. 1996; Nankai, Ashi & Taira 1992; and Eastern Mediterranean, Chaumillon &

Masle 1997), which are explored with seismic profiles and drill cores. Those provide only linear and two-dimensional data that are not always easy to combine to get a more complete, three-dimensional picture of the wedge behavior. The well-exposed Makran Accretionary Wedge (MAW), the case study of the research reported in this thesis, offers direct observations and access to excellent outcrops.

This thesis seeks to better understand the contribution and feedback of surface processes to the growth of the MAW and to investigate the state of the landscape over the wedge in Quaternary times. In inland Makran two external agents are involved in producing erosional and depositional landforms: water, by far the most efficient (Fig. 3), and wind (Fig. 1).



Fig. 3: Fluvial landforms (terraces in meander partly covered by colluvion) and alluvial channel of the Fanuj River, seen from $N26^{\circ}28'08.2''$; $E059^{\circ}38'19.7''$. Rather regular spacing of stream channels in the background landscape reflects uniform erodibility of the underlying Eocene, shale-dominated turbidites.

Therefore detailed quantitative information on the recent surface uplift, incision, erosion as recorded in the present-day morphology, fluvial terraces and drainage network had to be documented. One of the main goals of this work is the determination of the rates and spatial variability of bedrock incision. These are essential components for apprehending how surface and tectonic processes are linked to the evolution of mountain topography and for evaluating whether mountain landscapes are transient or may achieve steady state. Understanding the temporal and spatial distribution of strain in mountain belts is one of the most important topics in active tectonics. Furthermore, determining the constancy of strain accumulation and release on major structures is fundamental to appreciate how deformation is accommodated in the lithosphere. This thesis is concerned with geomorphic surfaces (marine and fluvial terraces) which are documenting the vertical and, in a lower extent, horizontal crustal movements. By age constraints on this datum we aimed to determine the rate of recent deformations and the spatial distribution of active deformation across the exposed MAW. In this introduction, we provide the basic geological information explaining the general background and justification of the work. Then we explicate the essential, technical knowledge employed for the quantitative geomorphology and dating of the quaternary landforms.

1- Study area

1-1 Geological setting

The Makran Accretionary Wedge is a consequence of the subduction of the oceanic part of the Arabian plate beneath Eurasia (Lut and Afghan blocks). The MAW extends about 1000 km from southern Iran to the Baluchistan of Pakistan. It is separated from the Zagros Mountain Belt, to the west, by the dextral Minab-Zendan Transform Fault and to the east it is restricted by the sinistral Chaman Transform Fault System (Fig. 4).

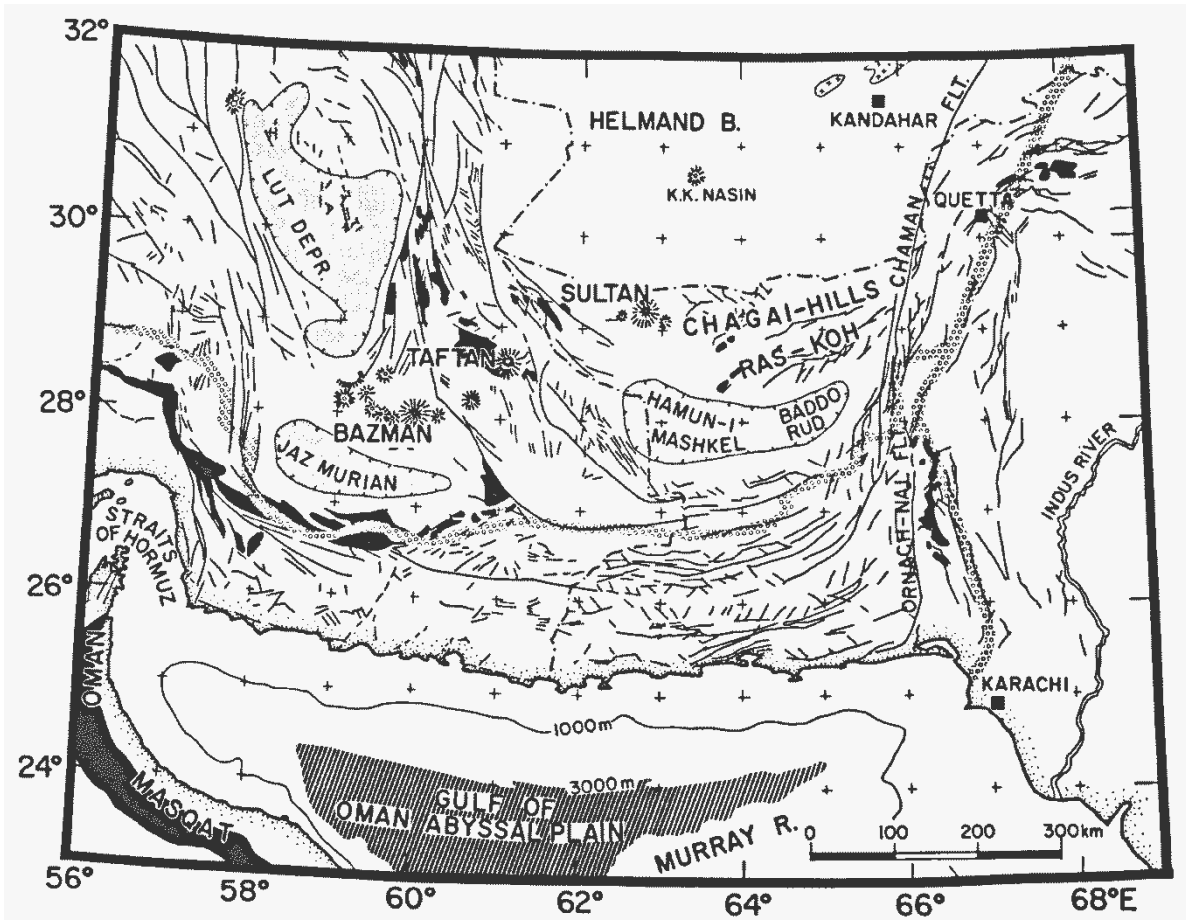


Fig. 4: Geological setting and tectonic sketch map of the Makran region synthesized by Jacob & Quittmeyer (1979)

Tectonic reconstructions consider that subduction initiated in the Late Cretaceous (e.g. Berberian et al. 1982, McCall & Kidd 1982, McCall 2002). Subduction is responsible for the andesitic volcanic arc traced 300-500 km to the north of the coast so that the Jaz-Murian and Mashkel depressions (Fig. 4) are proposed to be fore-arc basins (Farhoudi & Karig 1977, Jacob & Quittmeyer 1979, McCall 1997). Seismic tomography reveals a shallow-dipping but ill-defined slab below Eurasia (Bijwaard et al. 1998, Hafkenscheid et al. 2006). Makran is one the largest accretionary wedges on Earth, and is characterized by a reportedly high sediment thickness of about 7km (Kopp et al. 2000). The sedimentary hanging wall of the main décollement is folded and imbricated in the modern accretionary prism (e.g. White & Loudon 1982, Ellouz-Zimmermann et al. 2007b, Grando & McClay 2007). The modern

accretionary wedge developed offshore since the Early- Middle Miocene. It has formed a typical thrust-and-fold belt with forward propagation of thrusting, sediment underplating at the front and subsequent thickening and uplift of the accretionary complex (Kopp et al. 2000, Schlüter et al. 2002, Ellouz-Zimmermann et al. 2007a, Ellouz-Zimmermann et al. 2007b). This submarine wedge is documented by industrial seismic profiles (Ellouz-Zimmermann et al. 2007b, Grando & McClay 2007), which are rather less than enough published.

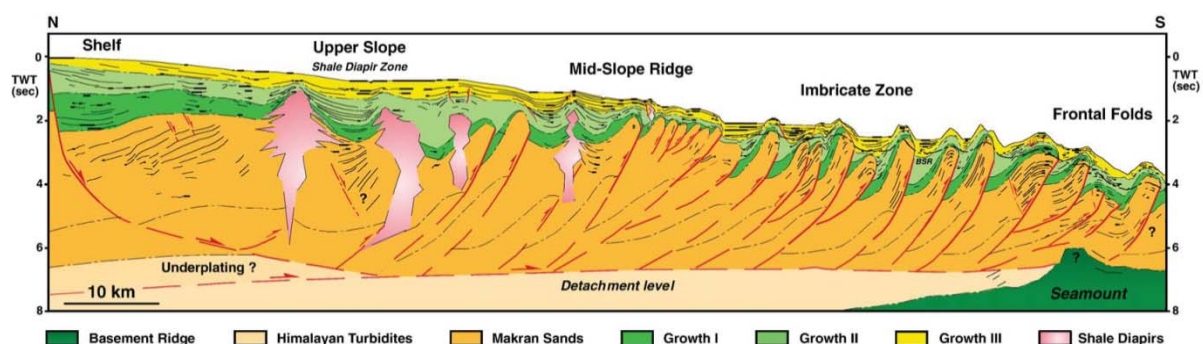


Fig. 5: Interpretation in terms of thrust-and-fold belt of a N-S seismic profile offshore western Makran: Fig. 6b of Grando & McClay 2007.

Seismic profiles document large normal fault systems near the coast (Figs. 5 and 6), which are also found onland in the Coastal plain only (Dolati 2010). The fact that normal faulting occurs along the coast only suggests a trench-parallel structural discontinuity, which is not well understood. This also raises the question as to whether the offshore and onshore fold-and-thrust belts belong to the same active wedge and whether inland Makran is currently deforming. We will answer this question with evidence for active deformation.

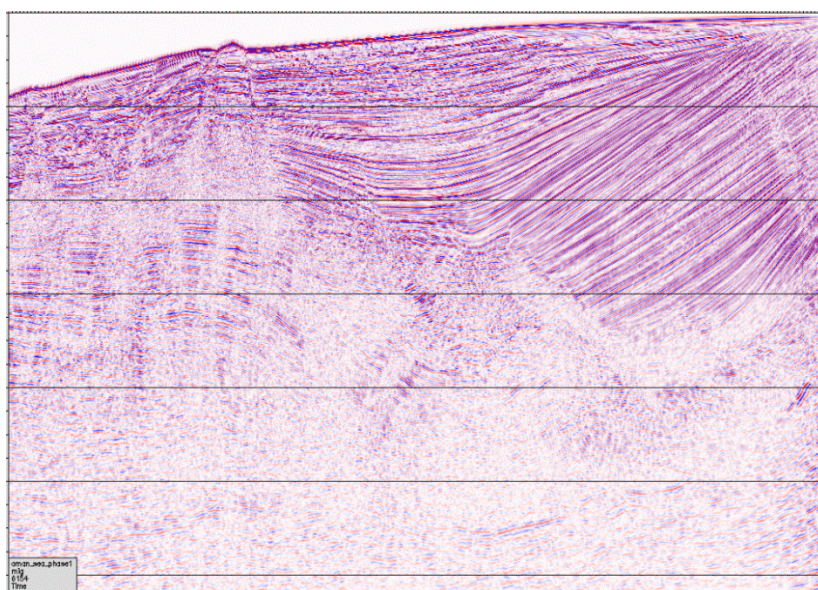


Fig. 6: Unpublished seismic profile offshore the Iranian Makran. ENI, personal communication.

The Makran Accretionary Wedge exposed in Iran was a progressively filled turbidite basin between the Middle Eocene and Middle Miocene times (Burg et al. 2012). Four main thrust

sheets are separated by major thrusts. From North to south they are: North, Inner, Outer and coastal Makran (Figs. 7 and 8).

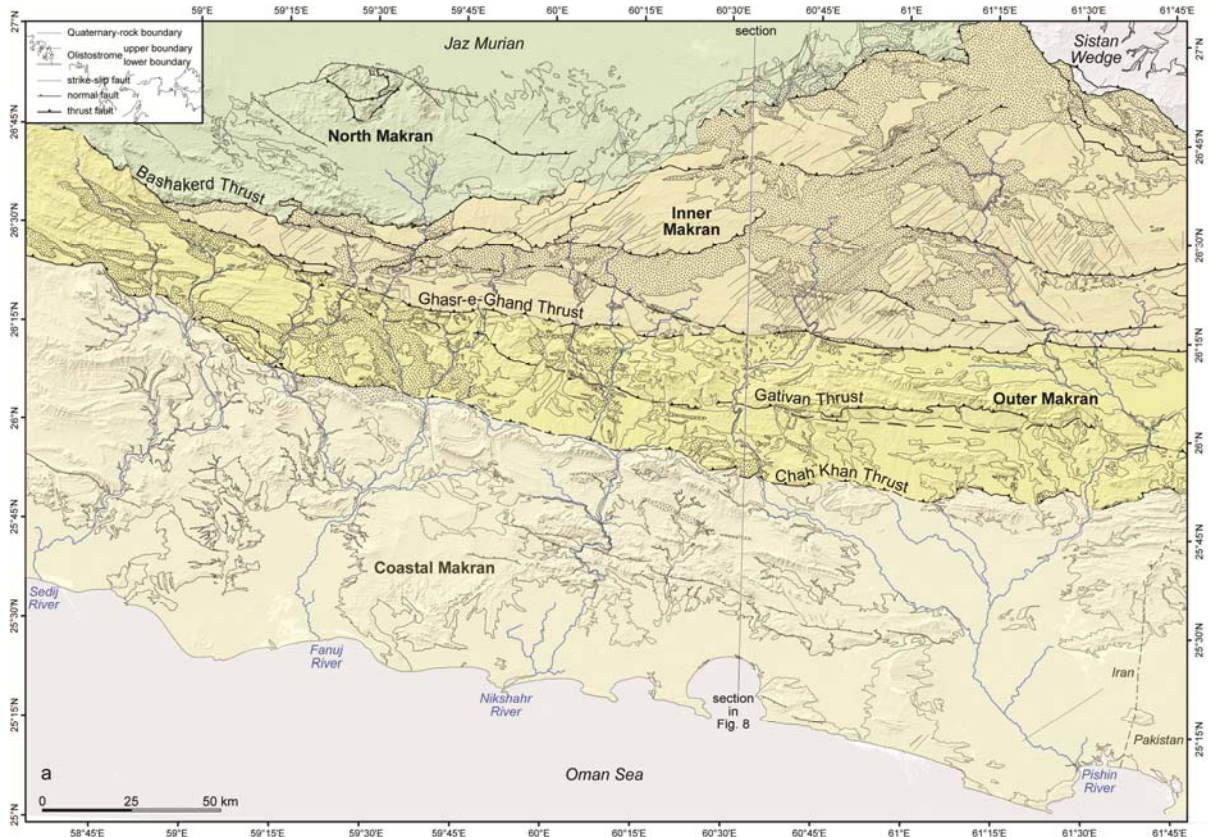


Fig. 7: Simplified geological map of the study area with main thrusts separating the four principal litho-tectonic units; Burg and his group; in progress.

The general south-vergence suggests that folds and major thrusts form an imbricate structure due to bulk N-S shortening. Deformation shifted the active, submarine wedge southward after emplacement of the olistostrome, and coastal Makran evolved into a wedge-top basin with shallower water and continental sedimentation (Burg et al. 2012).

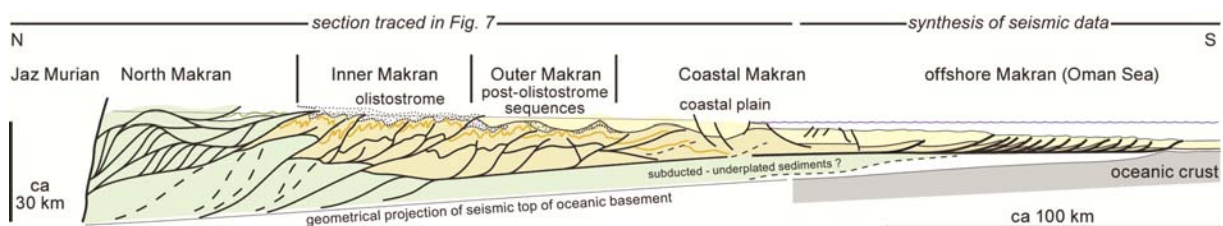


Fig. 8: Cross section of the onshore fold-and-thrust and offshore Makran Accretionary Wedge after Burg et al. (2012).

1-2 Geodynamic and seismicity

Current motions recalculated from seafloor spreading rates and fault azimuths for all major plates account for an increasing amount of plate convergence from 35.5-36.5 mm/a in the west to 40-42 mm/ in the east (DeMets et al. 2010). This is apparently corroborated by a small anticlockwise rotation of the rigid Arabian plate with respect to Eurasia. Such a

rotation corroborates GPS measurements disclosing a general anticlockwise rotation of Arabia with respect to Eurasia, around a vertical axis located somewhere in Kurdistan (Hatzfeld & Molnar 2010).

The seismicity of the Makran subduction zone demonstrates that large and shallow earthquakes regarded as tsunami generation potentials are common in this region (e.g. Ambraseys et al. 2002). The bulk shape of the north-dipping subduction of Tethys oceanic lithosphere below western Makran is interpreted from location of the 1960-1975 hypocenters (Fig. 9). Although inconclusive, because of rather scarce information, the accepted shape displays northward deepening of the slab with flexure beneath the trench slope break at the surface. The seismic zone is 80 km deep beneath the Bazman—Taftan--Koh-i-Sultan volcanic arc (Fig. 9, Jacob & Quittmeyer 1979).

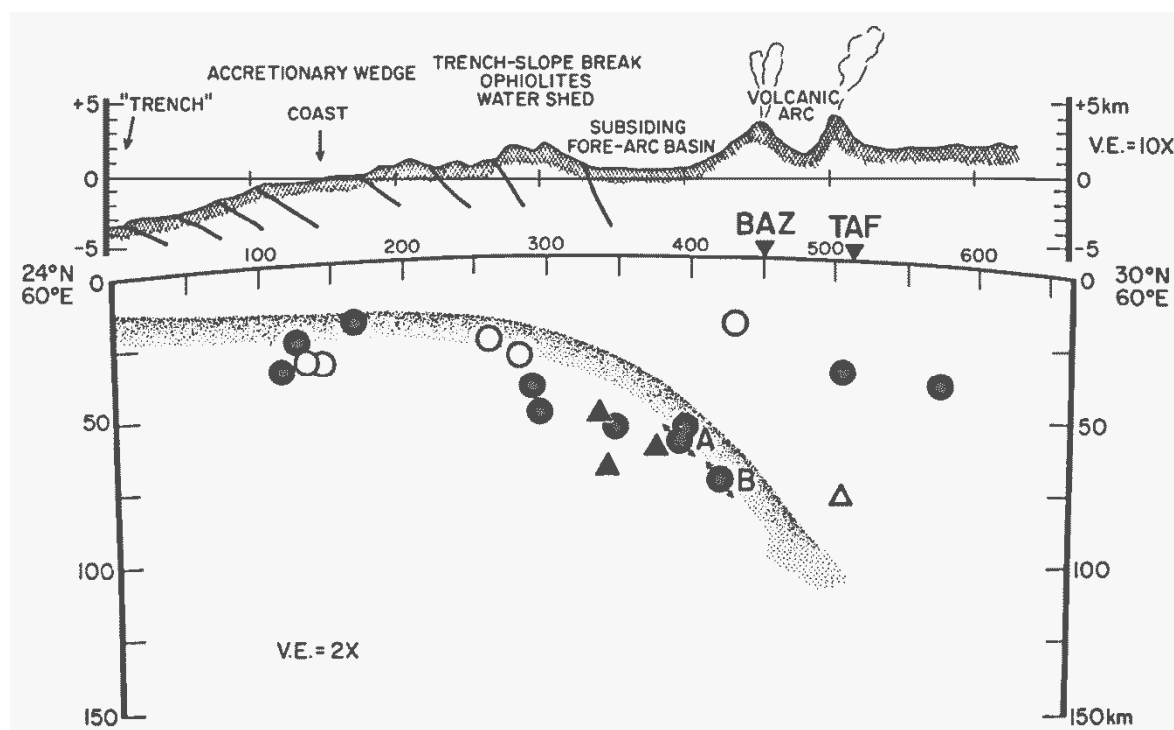


Fig. 9: Figure 6 of Jacob & Quittmeyer (1979). N-S cross section through the western Makran showing the 1960-1975 earthquake hypocenters and the inferred shape of the oceanic slab (shaded). Circles = events up to 200km to the east of the section line; triangles = up to 200 km to the west. Filled symbols represent events for which the depth is constrained by at least one reported depth phase; open symbols represent events for which the depth is determined by minimizing the residual of first P arrivals only.

All studies agree that both historical and instrumental records indicate that eastern Makran is seismically more active than western Makran (Fig. 10). This geographical variability in seismicity is attributed to possible segmentation of the subduction zone (Dykstra & Birnie 1979), or to a locked plate boundary that experiences great earthquakes with long repeat times in the west (Jacob & Quittmeyer 1979, Byrne et al. 1992). The average return period of magnitude > 8 earthquakes in eastern Makran is estimated at 100-250 years (Byrne et al. 1992). The magnitude 8.1, November 28, 1945 event is the first instrumentally recorded,

tsunami-generating earthquake in the Makran region and possibly the second deadliest in the Indian Ocean region (Heck 1947). This event and associated aftershocks (Fig. 10) were due to thrust faulting that ruptured about one-fifth of the subduction zone (Byrne et al. 1992). Jackson & McKenzie (1984) suggested that the big Makran earthquakes for which it has been possible to estimate the epicentral depth have occurred at shallow average depths between 25-35km.

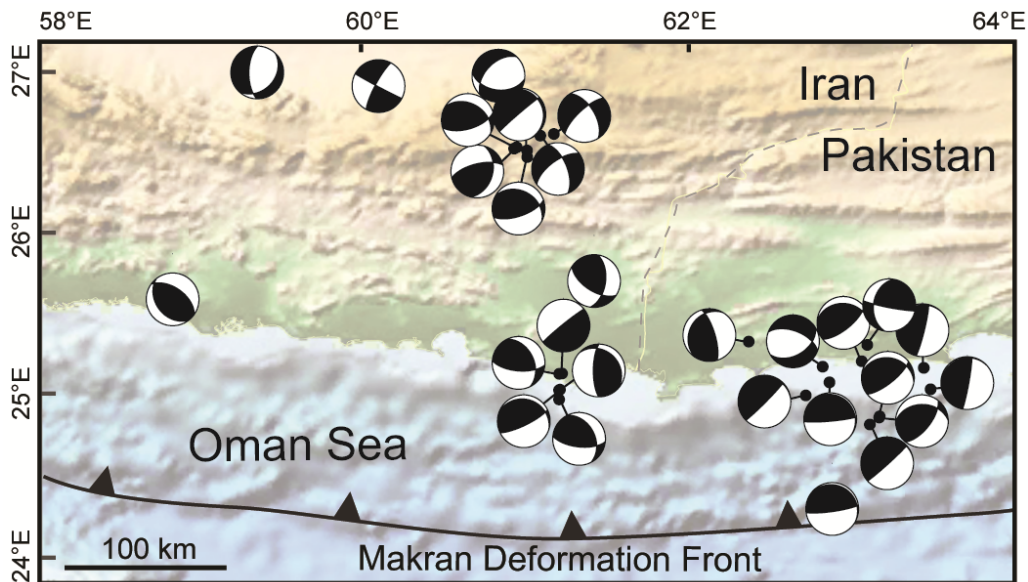


Fig. 10: Focal mechanisms in Makran, synthesized by Dolati (2010; list of catalogues herein). Filled quadrants are compressional. The eastern cluster includes the 28 November 1945, tsunami-generating event.

However, slow-slip or silent earthquakes may relieve a significant amount of stress in Makran like at other subduction plate boundaries where instrumentation is sufficiently dense to provide a reliable record of silent and/or tremor related slow slip (e.g. Kanamori & Kikuchi 1993, Hirose et al. 1999, Dragert et al. 2001, Rogers & Dragert 2003).

Geodetic data are scarce over the Makran itself. Measurements directly concerning our field area document a nearly N-S convergence rate of about 2 cm/a between the Arabian and Eurasian plates at the longitude of the Gulf of Oman (Vigny et al. 2006, Masson et al. 2007). A large part of this convergence rate is demonstrably absorbed in the Makran subduction, between Muscat and Chabahar. However, a convergence rate of 5-6 mm/a is measured between Chabahar, on the Makran coast and Bazman in Central Iran (Fig. 11, Vernant et al. 2004, Masson et al. 2005). This information, albeit slim, suggests that there is current crustal shortening within the onshore Makran wedge. Better constraining the distribution of the related strain and/or fault movements would require GPS stations in the study area.

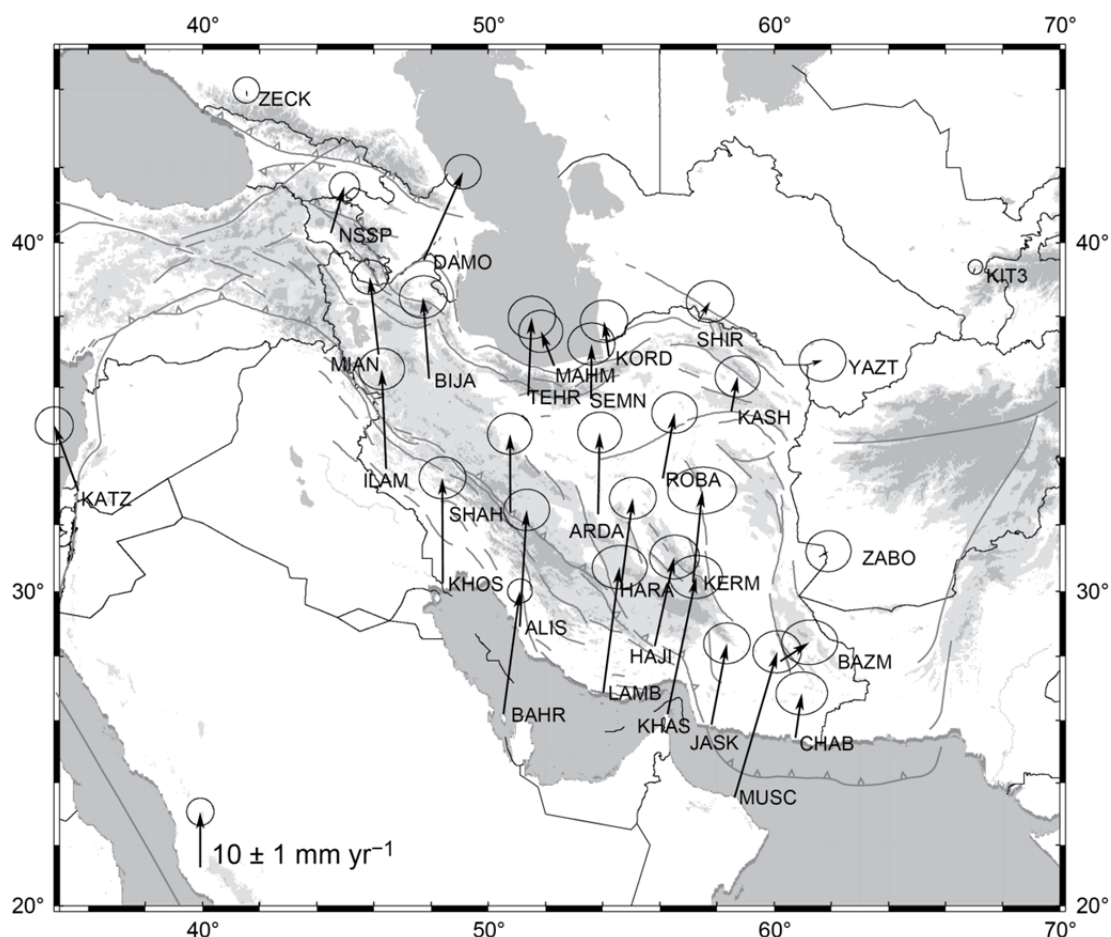


Fig. 11: Figure 4 of Vernant *et al.* (2004). GPS horizontal velocities in Iran and northern Oman in Eurasia-fixed reference frame.

1-3 Overviews of previous work

Inland Makran

The Makran Ranges, in Iran, have been much less studied than the neighbouring Zagros and Oman mountain ranges, and even the Pakistani Makran (e.g. Harms *et al.* 1982), because they are barren of fossil energy and economically valuable raw geomaterials. The pioneering, significant geological work in the Zagros-Makran region is due to the Iranian oil company (Harrison & Falcon 1936). A program of photogeological mapping was initiated in the early 1950ies, covering only the western and southern coastal area of the Iranian Makran (Huber 1952, Stöcklin 1952). The Iranian Makran Range was mapped in the 1970ies in a programme carried out on contract for the Geological and Mineral Survey of Iran by Paragon-Contech (see details in McCall & Kidd 1982). This program resulted in a set of 1/250 000 scale geological maps and associated reports that are a bit disparate and wrong in places, owing to the abundance of clastic fossils in the widespread, Late-Cretaceous to Mid-Miocene turbiditic sequences. In this thesis, we mostly refer to the recently reassessed geological map and structural analysis of central Makran (Dolati 2010, Burg *et al.* 2012). East-west trending folds of the lithologically rather homogeneous turbidites started to amplify in Mid Miocene times. This deformation event is related to a marked change in depositional environment, from turbiditic sequence in the Early Miocene to slope-shelf-shoreline facies

from the Late-Miocene to the Mid-Pleistocene, when uplift and normal faulting occurred in the Coastal region. One of the questions raised for this research work was to know whether deformation, and which deformation style continues in the fold-and-thrust belt of inland Makran.

Coastal Makran

The flat-lying, shallow shelf and continental sediments in Coastal Makran indicate that a major surface uplift event occurred in Plio-Pleistocene times. The correspondingly uplifted Holocene marine terraces all along the coast of Makran (e.g. Vita-Finzi 1975, Page et al. 1979, Snead 1992) are often taken as evidence for large magnitude, sometimes tsunami-generating earthquakes (e.g. Byrne et al. 1992). These well-exposed terraces (Fig. 12) are discussed in terms of number, sequence and numeric ages. Since such information is critical in deriving uplift rates, clarification was one of the side goals of this work.



Fig. 12: Shell-bearing, marine terrace (top brown, hard layer) nearly 60 m above sea level, to the east of Chabahar. GPS: N25°16'35.8"; E060°42'30.4".

1-4 Remaining problems and aims

No quantitative morphotectonic study integrating interpretation of satellite images and field reconnaissance and check had been carried out on the inland landscape of the MAW, despite evidence for coastal uplift and the paleoseismic information such work could bring. The well-preserved alluvial and fluvial deposits were only mapped in a reconnaissance fashion (Falcon 1975; McCall et al. 1982a). Systematic mapping and direct dating on these surfaces were needed and excellent exposure conditions detectable from satellite images were encouraging. Semi-arid climatic conditions with disseminated, poor vegetation and minimal soil cover make the inland Makran an excellent application where remotely sensed data may be used effectively to decipher rocks, structures and landforms (Fig. 13). The first

aim of this study was to provide a detailed morphological analysis of the river networks installed on the exposed MAW to postulate regional, potential correlations and examine how the channel profiles may reflect the recent and active growth of the wedge.

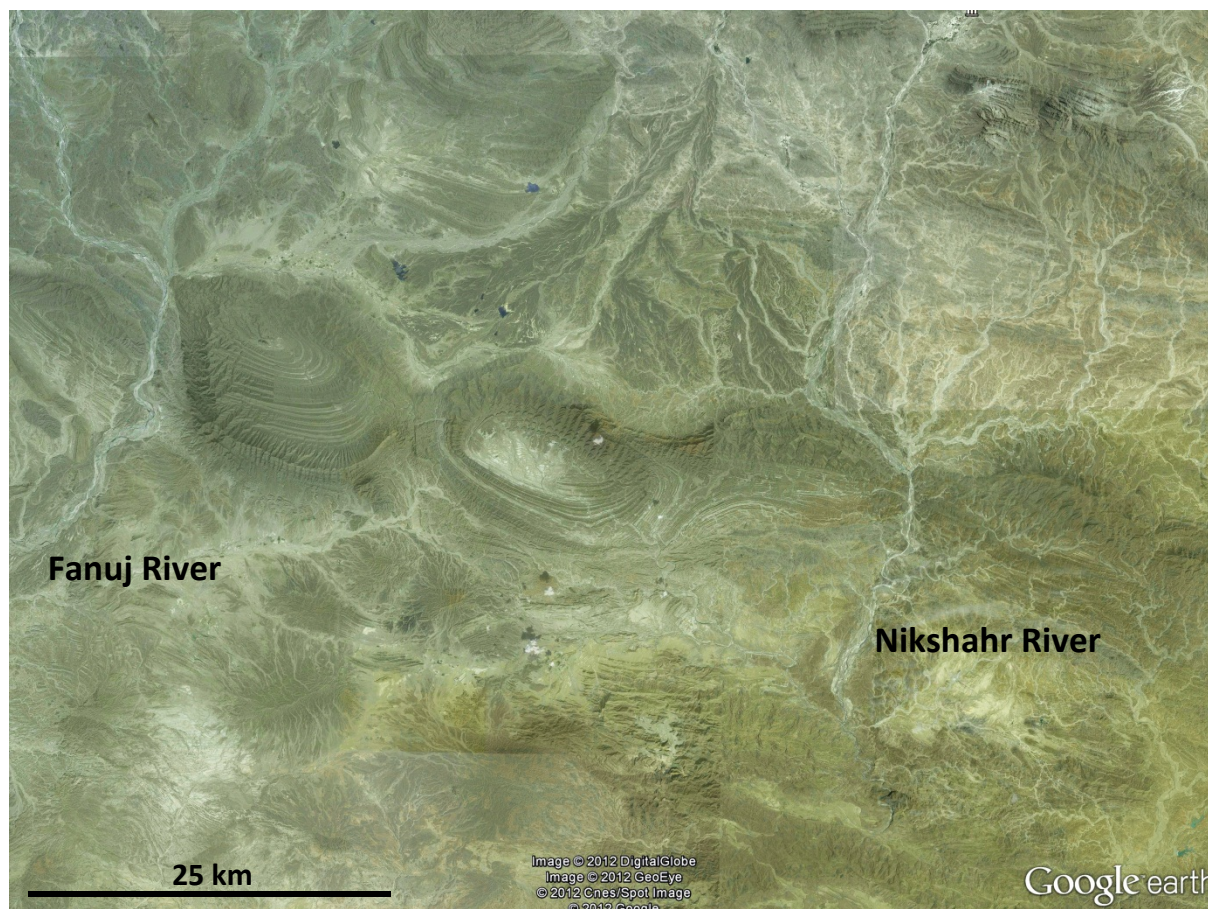


Fig. 13: Satellite image of part of the studied area. The prominent synclines are Upper Miocene (Tortonian-Messinian) sandstone-dominated sequences. Picture centred at $N25^{\circ}56'37.74''$; $E059^{\circ}58'58.34''$.

The morphotectonic study would not have been completed without surface exposure ages to document spatio-temporal variations of incision rates as proxy of surface uplift. Finally, an ultimate goal was to reconstruct the deformed passive strain markers like thin strath terraces to have a measure of recent horizontal crustal shortening.

2 Morphometric analysis and methods

The geomorphology of an area is the first indicator of on-going tectonic activity. In order to measure the amount of deformation due to tectonic processes, the initial geometry of the geomorphic markers has to be reconstructed accurately.

Landforms of tectonically active regions reflect interactions between tectonic, climatic, and surficial processes (Burbank & Anderson 2001, Bull 2007, 2009). Many models that explore feedbacks between these competing processes, given enough time to develop, predict a state of erosional equilibrium if the rates of river incision and hillslope erosion balance rock uplift. In short, orogenic systems tend toward steady state (e.g. Willett & Brandon 2002).

This proposition has deeply influenced research into the dynamics of fluvial incision and into the interpretation of exhumation/denudation rates (e.g. Koons 1989, Stüwe et al. 1994, Ehlers 2005). The concept is so well anchored that most authors now consider that rates of river incision and rock uplift are equal albeit modulated temporally by climatic fluctuations and spatially by the variability or rock resistance to erosion (Whipple 2004, and references therein). Some studies, however, have argued that landscapes will not approach steady-state if the response timescale of hillslopes and fluvial channels is longer than Quaternary climatic fluctuations (e.g. Whipple 2001, Zhang et al. 2001). With this point of caution in mind, we accept with many authors that landscapes in tectonically active regions such as the MAW may approach a long-term topographic and erosional steady-state because relief is permanently refreshed by rock uplift. In these cases, steady river incision is indicative of steady tectonic forcing and morphometric analyses can be used to test or constrain landscape evolution models (e.g. Sklar & Dietrich 1998, Snyder et al. 2000). This dissertation addresses this problem directly by employing existing morphometric methods for identifying steady-state and quantitatively testing relationships between uplift rates, erosion rates, and landscape form from the main rivers flowing on the MAW.

2-1 Fluvial systems

The importance and the morphology of fluvial systems are extensively published topics that are treated in a rich selection of classical textbooks (e.g. Schumm 1977, Frisch 1999, Burbank & Anderson 2001, Bull 2007, 2009, Anderson & Anderson 2010). We refer to this literature for the descriptive terminology and understanding of how river systems function.

Stream terraces are important to understand the climatic, tectonic and erosional histories of drainage basins. A river reaches a “graded” (i.e. equilibrium) state when these forces are balanced such that the river neither aggrades (stores sediments) nor incises (erodes) (e.g. Bridge & Demicco 2008). At that stage, it takes a characteristic, typically concave-up longitudinal profile (Hack 1957, Fig. 14) and maintains it unless one of the balanced forces changes.

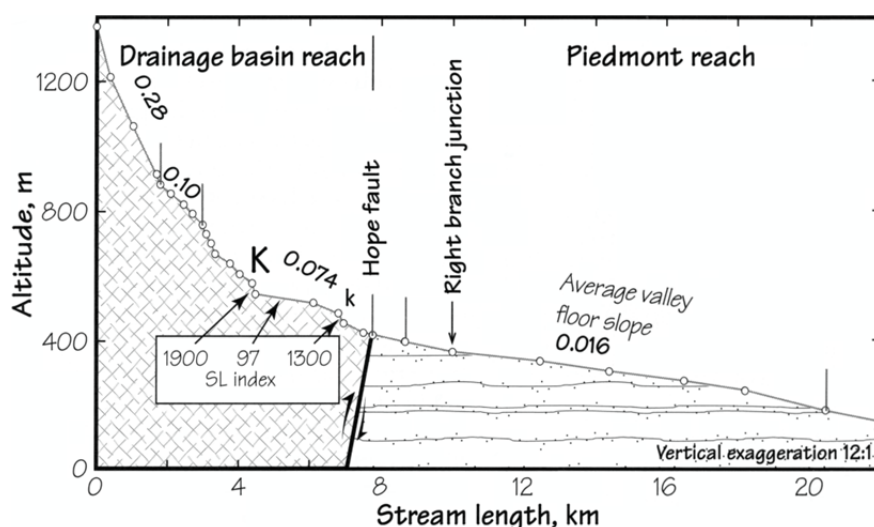


Fig. 14: Typical, concave upward longitudinal profile of a river with knickpoints (K) and morphotectonic indexes (SL : stream gradient); Figure 2.24 in Bull (2007).

Stratigraphic markers of past equilibrium shapes allow calculating incision rates. These past, transient equilibria are recorded in stream terraces by their treads, abandoned after the stream crosses the equilibrium threshold and begins incising, and by their basal straths, buried as a river crosses the threshold between erosion and aggradation (e.g. Bull 1979, Pazzaglia et al. 1998).

The focus of this work is on strath (erosional) terraces. Fill (depositional) terraces have been shown to be more problematic for calculating consistent incision rates because of the cyclic nature of their formation through both incision and alluviation (e.g. Burbank & Anderson 2001, Bridge & Demicco 2008).

2-2 Morphometric tools

Accepting steady state implies that the landscape morphology is adjusted so that river incision and hillslope erosion rates balance rock uplift rates (e.g. Burbank & Anderson 2001). It is thus possible to use measurements of erosion or incision rates to quantify rock uplift rates. Rather than considering absolute results as robust information on the erosion rate the regional scale, we take the concept as more meaningful for inferring relative differences in erosion rates across a landscape. In this study, we take fluvial incision as a proxy for uplift rate and compare bedrock channel gradients to decipher tectonic variations of the MAW surface.

The drainage network was routinely analysed using topographic features extracted from Digital Elevation Models (DEM) of the study area (Fig. 15, for example). Field control and observations were recorded with geographic information system techniques.

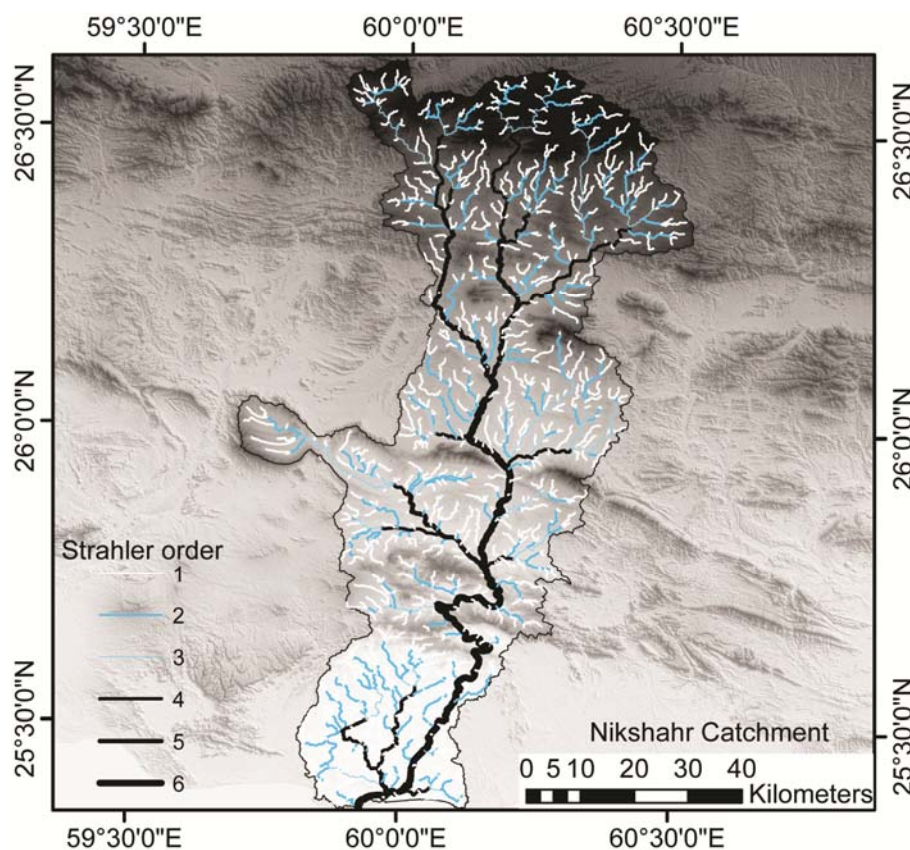


Fig. 15: Extracted river network and drainage area from DEM applying the Strahler order.

Longitudinal channel profiles can be quantified by normalizing the elevation and the distance along rivers. Several parameters such as profile shape (concavity), gradient fluctuations, river grade and valley incision can be derived from the measured longitudinal profiles. The gradient index (Fig. 14) is used to define relative differences in uplift and erosion rates. These quantified parameters and their interrelations allow comparing different drainage basins and identify where the drainage network is affected by tectonic disturbance, whether it is migration and/or rejuvenation of rivers or local evidences for accelerated uplift.

3 Terrestrial Cosmogenic Nuclides (TCNs)

Fluvial terraces are important to understand the climatic/tectonic/erosional history of drainage basins. This history can be constrained if these terraces can be numerically dated. Several geodetic and morphotectonic techniques are available to estimate crustal deformation over periods ranging from the coseismic time scale to hundreds of thousands of years. The development and sophistication of the terrestrial cosmogenic nuclides (TCN) analysis have afforded a modern tool to Earth surface sciences.

3-1 Principles

Cosmogenic nuclides are isotopes produced mostly through spallation of target nuclei hit by secondary cosmic ray particles (Lal & Peters 1967, Lal 1991).

The concentration of cosmogenic nuclides in a mineral subjected to cosmic rays is proportional to the production rate, the decay rate of that isotope, the exposure time of the surface and erosion rate. Thus, one can calculate how long a rock sample has been exposed to the cosmic radiations by measuring the concentration of cosmogenic nuclides and accounting for the flux of the cosmic rays and the half-life of the nuclides. The concentration of cosmogenic nuclides (atoms g^{-1}) is governed by the general equation:

$$C(t) = \frac{P(0)}{\lambda + \frac{\rho\varepsilon}{\Lambda}} \left(1 - e^{-\left(\lambda + \frac{\rho\varepsilon}{\Lambda}\right)t} \right) + C_{in}e^{-\lambda t} \quad (1)$$

where $P(0)$ (atoms $g^{-1} a^{-1}$) is the production rate scaled essentially to the altitude, latitude and shielding of the sampling site at the Earth's surface, t (a) is the exposure time of the surface, λ (a^{-1}) is the decay constant, ρ ($g\ cm^{-3}$) is the density of the irradiated material, ε ($cm\ a^{-1}$) is the average erosion rate, Λ ($g\ cm^{-2}$) is the attenuation length of the cosmic ray particles in the considered material, and C_{in} (atoms g^{-1}) is the inherited nuclide concentration (Lal 1991, Gosse & Phillips 2001). The produced concentration $C(t)$ is a composite of spallation, muon-induced and low energy neutron production.

To calculate an exposure age, one assumes negligible inheritance and zero erosion. Then equation 2 reduces to:

$$C(t) = \frac{P(0)}{\lambda} (1 - e^{-\lambda t}) \quad (2)$$

The nuclide concentration builds up with time until about three to four half-lives (Fig. 16a). After then, the production of radionuclides equals the loss due to decay.

Nuclide concentration diminishes exponentially with depth because most of the cosmic rays are absorbed within few meters of rock. When the rock surface is eroding, the uppermost layer of highest nuclide concentration is lost so that nuclide saturation is reached after a shorter exposure period (lower lines in Fig. 16b for several erosion rates). In regions where bedrock erosion rates are slow (for example in arid and hyper-arid deserts) exposure ages up to several million years could be determined.

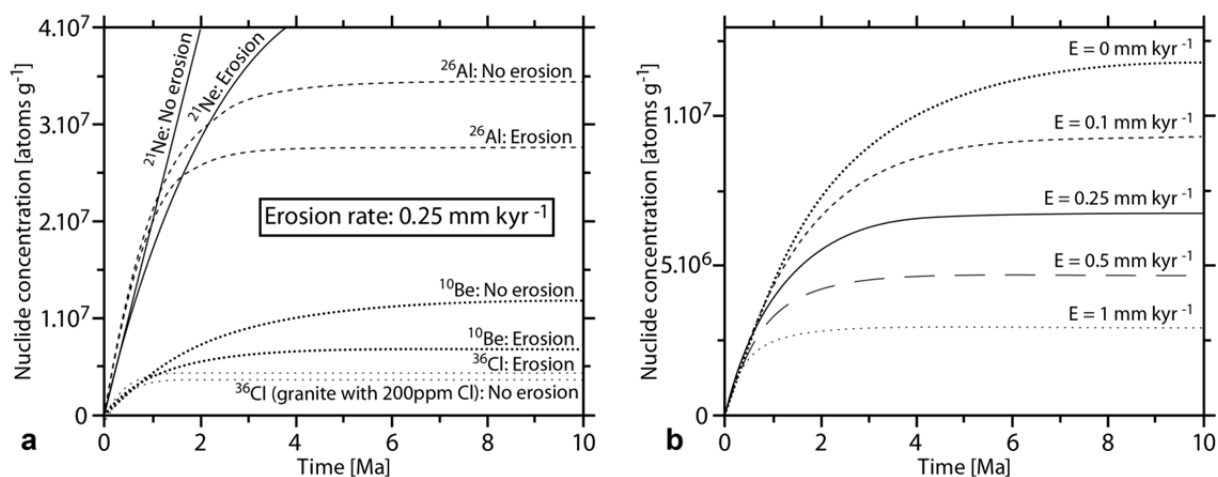


Fig. 16: **a)** Effect of erosion on growth of different nuclide concentrations. For all the nuclides, except ³⁶Cl, concentrations in eroding surfaces are lower than for non-eroding surfaces after the same amount of time. The ³⁶Cl concentration reaches higher concentrations when the rock surface is eroding. **b)** Increase in ¹⁰Be concentration with time taking according to different steady-state erosion rates of exposed surface. Secular equilibrium, where radionuclide gain due to production equals loss due to radioactive decay and erosion, is approached earlier for more rapid steady-state erosion rates (both, a and b from Ivy-Ochs & Schaller 2010).

In contrast, in regions where rocks are eroding more rapidly (a good estimate of crystalline bedrock erosion rate is about 5 mm/kyr or less, Cockburn & Summerfield 2004) the oldest exposure age one can measure is imposed by the erosion rate and may be only a few hundred thousand years.

Production rates have been determined empirically, using natural and artificial targets (e.g. Niedermann et al. 1994, Stone et al. 1996, Kubik et al. 1998, Brown et al. 2000, Nishiizumi et al. 2007), and theoretically (e.g. Masarik 2002). Due to the influence of the Earth's magnetic field and atmosphere on the flux of cosmic rays, the production rates depend on altitude, latitude, and the amount of sky that can be seen from a specific sampling point (= topographic shielding). Production rates increase with altitude because the magnetic field reduces the amount of cosmic rays that reach the Earth's surface (see review article of Gosse & Phillips 2001).

Penetration of cosmic rays into rocks decreases with depth; consequently, the production rate of cosmic nuclides by spallation and muon-induced reactions also decreases exponentially with depth. However, muons penetrate deeper than other particles because they are less apt to react. Therefore, muonic capture becomes more important than production by spallation below depths of about 2 m in rock of density 2.7 g cm^{-3} (Fig. 17).

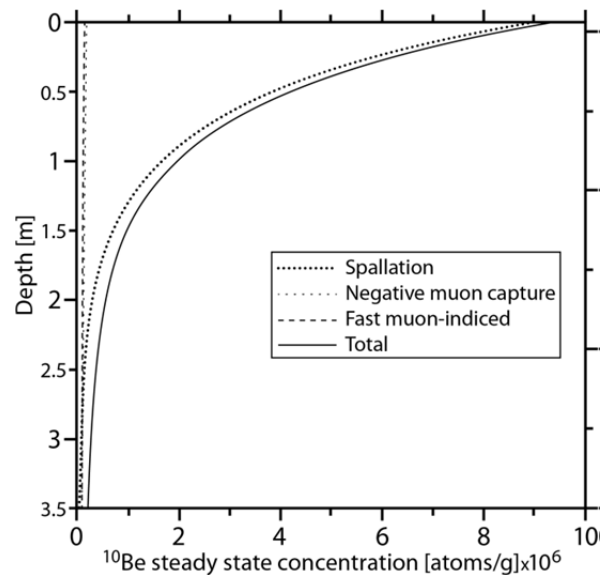


Fig. 17: Production rate of ^{10}Be in quartz as a function of depth. Total production is a composite of the production by neutron spallation, stopped muons and fast muons (after Ivy-Ochs et al. 2012).

3-2 Terrestrial Cosmogenic Nuclide (TCN) application to active tectonics research

Much of TCN dating is applied to measure neotectonics strain rates (e.g. Bierman & Nichols 2004, Owen et al. 2007). The strategy is to constrain the exposure date of a strain marker such as terraces or fans in order to bracket the age of a deformation event. With an effective range of decades to 10^7 years, the TCN method bridges the gap between short geodetic time scales and chronology of longer time scale (e.g., (U-TH-Sm)/He low temperature thermochronology, fission track) processes (Gosse 2012).

^{10}Be and ^{26}Al are the most commonly measured cosmogenic nuclides for geological applications because they are produced within rocks (*in-situ*) when quartz grains, in particular, are hit by cosmic spallation products and they are relatively easy to measure. ^{10}Be (half-life = 1.51 Ma) can also withstand the rigorous cleaning procedures required to remove the meteoric ^{10}Be contamination. ^{26}Al (half-life = 0.716 Ma) can be measured in the aliquots of the quartz dissolved for ^{10}Be measurements. Despite different decay constants and production rates, these two nuclides have the same production profiles. Paired ^{10}Be and ^{26}Al data yield lower limits on the exposure and burial durations (Lal 1991, Bierman et al. 1999). An $^{26}\text{Al}/^{10}\text{Be}$ ratio of ca 6.75, in the same sample, signs a no-burial, simple exposure history (Balco 2009, Balco & Shuster 2009). A particular difficulty and source of measurement/interpretation uncertainty is the amount of nuclide inheritance and surface

erosion. Therefore, these unknowns have to be defined if rates of surface processes must be known with some accuracy. One answer to the caveat is to measure TCN depth-profiles.

3-3 Depth profile (surface erosion and inheritance)

^{10}Be being produced primarily within 1-1.5 meter from the ground surface (Fig. 17), its concentration is proportional to the residence time of analysed material near the Earth's surface. Samples buried below the penetration depth are shielded from cosmic radiations and their cosmogenic nuclide concentrations thus correspond to nuclides accumulated before deposition; this is the inherited component. For deposits that have not been vertically mixed, a depth profile can be utilized to account for a change in TCN production rate (Fig. 18).

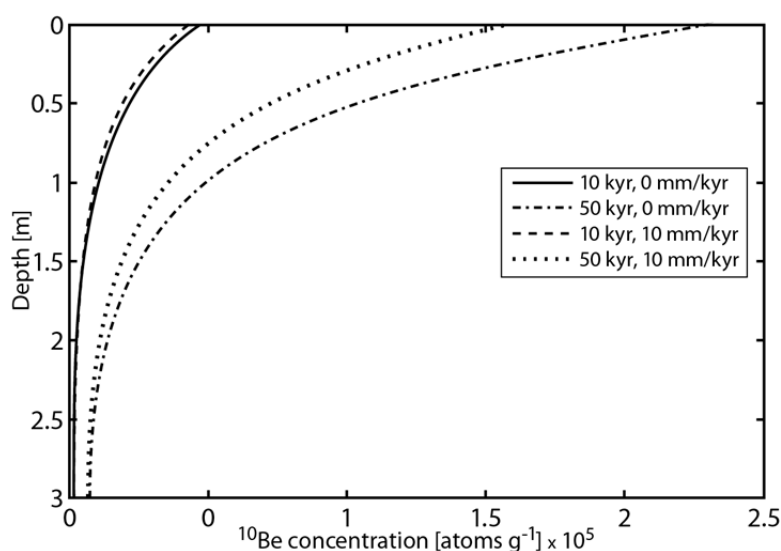


Fig. 18: The evolution of the shape of the depth profile curve with time. ^{10}Be concentration produced at depth in sediment after continuous exposure (10, 50ka) with no erosion and with erosion for the same amount of time (after Ivy-Ochs et al. 2012).

The secondary cosmic ray flux attenuates through the material for nuclides that are produced only from high energy nuclear and muogenic reaction (e.g., ^{10}Be , ^{26}Al and ^{21}Ne). The number of atoms C (cm^{-3}) of the specific nuclide m as a function of depth z (cm), exposure time t (a), and erosion rate ε (cm a^{-1}) is given by:

$$C_m(z, \varepsilon, t) = \sum_i \frac{P_{(0)m,i}}{\left(\frac{\varepsilon \rho_z}{\Lambda_i} + \lambda_m\right)} \exp\left(-\frac{z \rho_z}{\Lambda_i}\right) \left[1 - \exp\left(-t \left\{ \frac{\varepsilon \rho_z}{\Lambda_i} + \lambda_m \right\}\right) \right] + C_{\text{inh},m} \exp(-\lambda_m t) \quad (3)$$

where i represents the various production pathways and negative muon capture, $P_{(0)m,i}$ is the site specific surface production rate for nuclide m via production pathway i ($\text{atoms g}^{-1} \text{a}^{-1}$), λ_m is the decay constant for radionuclide m (a^{-1}), ρ_z is the cumulative bulk density at depth z (g cm^{-3}), Λ_i (g cm^{-2}) is the attenuation length of production pathway i , and $C_{\text{inh},m}$ is the inherited concentration of nuclide m ($\text{atoms g}^{-1} \text{a}^{-1}$) (Hidy et al. 2010). Although theoretical

production from muons does not behave as a simple exponential function with depth as described by equation (3), it has been shown that acceptable approximations to muon production can be made with multiple exponential terms (e.g. Granger & Smith 2000, Schaller et al. 2002).

All parameters defined, a constrained Monte Carlo approach (Hidy et al. 2010) generates solutions to equation (3). The reduced chi-square statistic, which expresses the model misfit, is then generated from each simulated profile solution as:

$$\chi^2 = \frac{1}{d} \sum_{y=1}^x \frac{\left(\int_{T_y} C_m(z_y, \epsilon, t) dz - N_{m,y} \right)^2}{(\sigma_{m,y} N_{m,y})^2} \quad (4)$$

where x is the number of samples in the profile, T_y is the thickness of indexed sample y (cm), $N_{m,y}$ is the measured concentration of nuclide m for sample y (atoms g^{-1}), $\sigma_{m,y}$ is the fractional standard error for $N_{m,y}$ (including all measurement errors), and d is the degree of freedom in the data set, a value equal to the number of samples in the profile less the number of calculated parameters. To obtain statistically robust results, it is imperative that the number of samples analyzed in a depth profile be greater than the number of calculated parameters. Therefore, a minimum of four samples is recommended to resolve solutions for age, erosion rate, and inheritance). Most pertinent to our purpose, analysing buried samples gives access to the amount of inheritance.

4 Outline of the thesis

It has been argued that steady-state is difficult to achieve, since landscape response time may be long compared to unsteady tectonics or Quaternary climatic fluctuations. In the absence of glacial erosion, the rate of channel incision sets the lower boundary condition for hillslopes and thus fundamentally influences denudation rates across the landscape. Determining the rates and spatial variability of long-term incision (as a proxy of surface uplift) in regional scale using strath terraces and morphometric indices is a key to evaluate whether a landscape is transient or achieved its steady state. Morphometric data are used to quantitatively test relationships between uplift rates and erosion rates. A steady-state landscape predicts that incision, erosion, and uplift rates are uniform in space and stable through time. However, over what spatial and temporal scales steady-state can be achieved and maintained remains an open question, and the functional relationships between incision, erosion, and uplift predicted by conceptual and analytical models of steady-state landscapes remain relatively untested. This work brings new information to the dataset of world examples.

This thesis is comprised of three main chapters, each representing a manuscript that has been published (Chapter IV) or will be submitted for publication (Chapters II and III).

Chapter II provides a detailed geomorphologic analysis of the drainage system. The aim is to test whether the shape of channel profiles of the river network reflects potential variations of the surface behaviour in response to active tectonics in the studied part of the Makran Accretionary Wedge. DEM analysis and data processing using GIS and Matlab were combined with field investigations and geological mapping. Measured channel profiles are compared to numerically modelled channel to distinguish tectonics from other factors (for instance, lithology, dam) able to influence river gradients. The results provide clear evidence for a difference between the studied western and eastern catchments. The landscape of the western MAW, where river profiles fit the theoretical dynamic equilibrium, apparently approaches steady state whereas the landscape is still in a transient state in eastern Makran. In the eastern catchments, most of the knickpoints, knickzones and other non-equilibrium features can be correlated with faults and folds previously mapped in the substrate rocks. We conclude that tectonic forcing increases eastward, parallel to the subduction trench, and tentatively attribute this lateral variation to faster plate convergence in the east than in the west of the subduction system.

Chapter III focuses on the geochronology of fluvial and marine terraces using ^{10}Be surface exposure and ^{14}C radiocarbon dating methods. Ages range from ca 15 to ca 350 ka. We used the elevation difference between the dated strath terraces and the modern channel to calculate fluvial incision rates. The resulting spatio-temporal pattern of incision rates let better interpret the landscape adjustment in response to regional uplift and local tectonic deformation. The comparison of incision rates in four adjacent catchments enables distinguishing between a relatively moderate, regional and homogeneous “background” incision rate (0.4mm/a) and higher local incision/uplift (up to 0.8-1 mm/a) rates. The inferred “background” incision rate is close to that calculated from uplifted marine terraces, to within errors. All results are consistent with fluvial incision being in dynamic steady state with rock uplift in the western catchments. Locally high incision rates in the eastern catchments reflect localized tectonic activity. Clusters of ^{10}Be ages suggest that deposition and abandonment of some of the studied strath terraces correlate with Marine Isotopes Stages 3, 5 and 7, thus demonstrating climatic influence on the terrace development. Incision/uplift rates and morphometric data presented here confirm that (1) steady-state has been achieved and maintained in the tectonically active landscapes of western and eastern Makran for about 0.5 Ma, (2) incision rates changed regionally but did not noticeably change during these ca 0.5 Ma and (3) both tectonic and climate are driving forces that controlled the formation of fluvial terraces on the MAW.

Chapter IV makes use of the geochronological age of folded and tilted terraces to further constrain recent to active crustal shortening of the Iranian on-shore Makran. We discovered that the investigated terraces acted as passive markers on growing folds and fold trains in some of the tectonically active areas. Successive treads recorded successive stages of fold amplification as basement shortening progressed. Terraces increasingly tilted with age usually document limb rotation in these Quaternary fault-propagation and detachment

folds. Two fold wavelengths were measured and are linked to two within-wedge décollement levels. Folding absorbed a bulk shortening rate of about 1 mm/a. Folds indicate that, even if shortening strain is homogeneously distributed, vertical uplift rates vary, decreasing from hinge to limb; the corollary is that locally high rock uplift rate is not symptomatic of fault activity. The question remains as to whether long-term shortening rates averaged over thousands to millions of years are compatible with short-term geodetic rates. Our results point out the importance of understanding strain distribution along and between fault structures associated with the active subduction zone. Active folding depicted in this work shows that the generally accepted classical interpretation of “Coulomb” accretionary wedges is an excellent, long-term approximation that now requires refinements in terms of bulk rheology to account for shortening mechanisms additional to discrete fault movements.

Chapter V presents a synthesis of the work, summarizes conclusions reached in each chapter and ends with a short outlook.



Fig. 19: *Uncited fluvial fill-terraces along the Sarbaz River; GPS: N26°06'43.8"; E061°36'08.9.*

Chapter II

Geomorphological analysis of the drainage system on the growing Makran Accretionary Wedge

Negar Haghipour, Jean-Pierre Burg

This chapter will be submitted to *Geomorphology*

Abstract :

We studied the morphology of the five major catchments draining the onshore Makran Accretionary Wedge in southeast Iran and southwest Pakistan to examine how the channel pattern and the length profiles may reflect the recent and active growth of the wedge. We combined qualitative field surveys with the quantitative analysis of channel steepness and concavity measured from digital elevation models. We compare these profiles with modelled profiles using a stream power approach assuming homogeneously uplifting, uniform rock substratum. Results show a neat difference between the studied western and eastern catchments. The western rivers are in morphological equilibrium. The eastern rivers exhibit profiles, with prominent convexities and knickpoints, thus notably diverging from equilibrium concave up shapes. All the studied catchments share the same base level, flow on similar lithologies and developed under uniform climate conditions. Therefore, we interpret the morphometric differences in terms of differential rock uplift rate as a response to local tectonic activity. This interpretation is consistent with both uplift rates of marine terraces along the coast of Makran and the recorded seismicity. Our geomorphological work extends coastal information to wide inland areas and documents longer term tectonic behaviour than seismo-tectonic record. In particular, the studied catchments demonstrate a steeper surface slope and faster surface uplift rates in eastern than in western Makran. We attribute this regional difference to Quaternary variations in tectonic regimes that forced differential uplift rates of the wedge surface. We conjecture that the different tectonic regimes are related to different subduction rates.

1-Introduction

Relief results from the interaction between internal, geological and external, environmental factors. In the absence of glacial erosion, the fluvial system is the main external force that dictates the landscape evolution and sculpts the topographic relief of mountain ranges (e.g. Whipple and Tucker, 1999). Many studies have documented the complex relationships between rock uplift and climatically-modulated erosion efficiency and discussed the respective influence of these driving factors on channel incision (e.g. Burbank and Anderson, 2001; Kirby et al., 2003; Kirby and Whipple, 2012). Therefore, the river sensitivity to climate and/or tectonic variations makes the quantitative analysis of channel morphology a valued archive of active deformation (e.g. Schumm et al., 2000). Leading models relate channel gradients of tectonically active regions to competition between local rates of bedrock uplift with respect to a far-distant, fixed base level and channel erosion/deposition (Howard, 1994; Howard et al., 1994). Even if the details of the dynamic response of rivers to tectonic forcing remain indeterminate (Whipple and Tucker, 1999), the key role of incision channels and their connection to structures and crustal processes are widely accepted (e.g. Bull, 2009). Quantitative geomorphologic tools are particularly appropriate for regions where deformation rates are low to moderate (e.g. Holbrook and Schumm, 1999; Azor et al., 2002; Ponza et al., 2010). Therefore, we decided to analyse the river system installed on the onshore Makran accretionary wedge to investigate the tectonic and geomorphic behaviour of its surface. Relatively weak bedrock (interlayered sandstone, shale and mudstone), homogeneous climate throughout the area and nearly no anthropogenic disturbance make Makran an advantageous geological system to extract the tectonic evolution from topographic variations of the wedge. In support for this endeavour, all catchments share the same base level (Oman Sea) and have been ice free. Therefore the fluvial system counts as the main external force responsible for topography relief of the study area. Concentration of cosmogenic ^{10}Be in quartz pebbles from fluvial terraces in the Iranian Makran established a steady incision rate of about 0.3 mm/a over the last 270 ka (Haghipour et al., 2012). Such information has importance because, according to the critical taper theory, the slope and the elevation of a wedge surface are integral parts of the structural evolution of the wedge (e.g. Davis et al., 1983; Dahlen, 1990). In this line of thoughts, we were most interested in knowing whether longitudinal river profiles would document steady-state equilibrium of the wedge surface, on a large scale, or transient states of landscape adjusting changes in tectonic forcing. First, the quantitative description of topographic and longitudinal river profiles, measured from digital elevation models, helps defining the spatial distribution of major drainage networks and their controlling factors with reference to erosion and deformation, variations of the base level and climate changes. The analysis of classical indices is extended by comparing measured profiles with modelled profiles using a stream power approach applied to homogeneously uplifting, uniform rock substratum. This calculation helps characterizing the landscape of the Makran accretionary wedge and assessing the relative level of tectonic activity. We found noticeable spatial variations over the studied area, revealing an increasingly stronger impact of Quaternary deformation

towards the eastern wedge. We tentatively attribute these variations to variable subduction processes, thus emphasising the link between surficial and deeper crustal processes in active orogenic systems.

2-Setting

2-1- Tectonic and geological setting

The Makran accretionary wedge (MAW) is 300-350 km wide from the submarine deformation front to the Hamun-i-Jaz Murian (Iran) and Hamun-i-Mashkel (Pakistan) depressions (Fig. 1). It stretches for about 1000 km from the Strait of Hormuz in the west (Iran) to near Karachi (Pakistan) in the east. The MAW is separated from the Zagros Mountain Belt, to the west, by the dextral Minab-Zendan Transform Fault and it abuts, to the east, against the Ornach-Nal Fault (Fig. 1), a splay of the sinistral Chaman Transform Fault. The MAW was installed above the on-going, northward subduction of the oceanic part of the Arabian plate beneath Eurasia (Lut and Afghan blocks). This subduction is believed to have started in the Late Cretaceous (e.g. Berberian et al., 1982; McCall, 2002). GPS measurements yielded a current subduction rate of about 2 cm/a in a roughly N-S direction (Vigny et al., 2006; Masson et al., 2007).

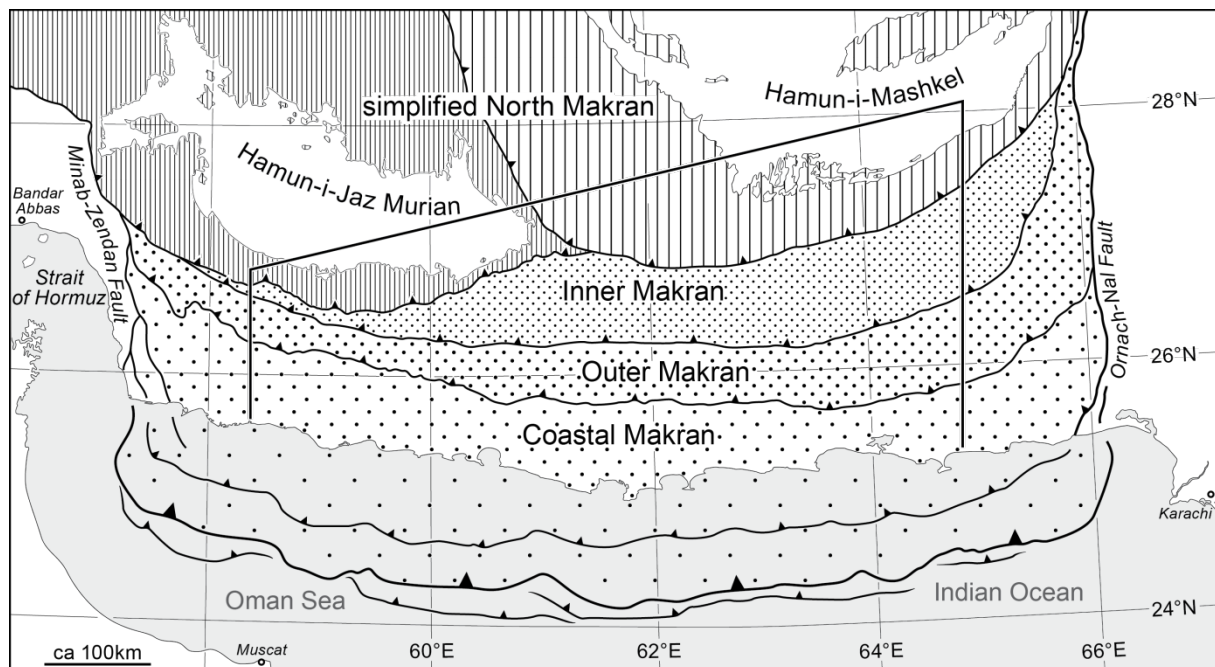


Fig. 1: General setting and simplified structural map of the Makran accretionary wedge. Offshore structures from (Ellouz-Zimmermann et al., 2007; Grando and McClay, 2007) and National Iranian Oil Company, unpublished. Framed: study area.

Seismic tomography portrays a shallow-dipping but ill-defined slab below Eurasia (Bijwaard et al., 1998; Hafkenscheid et al., 2006). Although the Makran appears seismically quiet compared to the surrounding regions and other active margins, the recorded seismicity is more energetic in the Pakistani eastern part than in the Iranian western part of the subduction zone (Byrne et al., 1992). This difference in seismic activity might be reflected in

the gross architecture of the wedge. Its average slope increases from west (ca. 1°) to east (ca. 2°) whereas the size, length and spacing between thrust faults decrease in the same direction (Ellouz-Zimmermann et al., 2007). A <2 Ma sinistral, transform fault possibly separates west and east Makran (Kukowski et al., 2000).

Four tectono-stratigraphic units separated by major, E-W striking thrust faults have been identified after detailed mapping in Central Makran (Dolati, 2010; Burg et al., 2012). Field survey, often slim literature descriptions (e.g. Hunting Survey Corporation, 1960; Ahmed, 1969; Arthurton et al., 1982; McCall and Kidd, 1982; Harms et al., 1984; Bender and Raza, 1995) and satellite imagery permitted following and tracing westward and eastward the continuations of these units and their boundaries (Fig. 1). They characterize the geological basement of the studied watersheds. From north to south, i.e. from the structural top to bottom, these units are: North Makran, Inner Makran, Outer Makran and Coastal Makran. North Makran lumps here two distinct domains (Fig. 1). In Iran, to the west, this unit mainly consists in tectonically imbricated Upper Cretaceous to Eocene igneous rocks, ophiolites and associated deep marine sediments ("coloured mélange" of McCall, 1983). These rocks, bounded to the south by a major southward thrust (so-called Bashakerd Thrust), disappear to the north below the unconformable alluvium and playa deposits of the subsiding Jaz Murian Depression (Fig. 1). In Pakistan, to the east, the Quaternary deposits of the subsiding Mashkel Depression unconformably cover a sequence of Upper Eocene-Lower Miocene turbidites (Harms et al., 1984, work in progress). These turbidites are in continuity with those of the N-S Birjand-Zahedan Belt, a marginal basin closed with the Sistan Suture in mid-Eocene times (Tirrul et al., 1983). The arcuate trace of the corresponding basal thrust interrupts and relays the Bashakerd Thrust, turning from its N-S strike in Iran to run east-northeastward, along the southern flank of the Siah Range, the topographic crest of Makran in Pakistan. Despite lithological differences, we assemble the two domains into one unit because they occupy the same "backstop" position and contain the water divide between landward (into the Jaz Murian and Mashkel endhoreic basins) and oceanward flowing rivers. In addition, and directly relevant to this work, headwaters of the studied rivers incised steep and narrow valleys without leaving meaningful deposits on the dual North Makran. Our simplified classification is therefore adequate for this geomorphological study, and associates the two North Makran subunits with various terranes further north, in Iran and Afghanistan (e.g. Stoecklin, 1968; McCall and Kidd, 1982; Ricou, 1994). Large wavelength, low amplitude folds trending nearly E-W affect Inner, Outer Makran and Coastal Makran. The fold shapes and the presence/absence of axial plane cleavage depict a bulk strain gradient decreasing in intensity from north to south (Hunting Survey Corporation, 1960; Platt et al., 1985; Burg et al., 2012). Inner Makran exposes a thick and laterally continuous sequence of Upper Eocene to Lower Miocene turbidites. The sequence shows a general thickening- and coarsening-upward trend (Hunting Survey Corporation, 1960; Dolati, 2010). The bottom thrust displays evidence for recent tectonic activity (Ghasr-e-Ghand Thrust of Dolati, 2010; Haghypour et al., 2012). Outer Makran mostly comprises Lower to Middle Miocene siltstones and marls with calcareous sandstones that grade up-section into shallower facies, with evidence for a shelf dominated by waves and tidal currents. Most river

terraces, which have been faulted, tilted and folded during the last 150 ka (Haghipour et al., 2012), straddle Outer Makran. An extensive Tortonian (7-11 Ma) olistostrome (Burg et al., 2008) covered, principally in Central Makran, the three previous units and has been partly eroded since then. The basal unconformity indicates that most of the onshore Makran was deforming under bulk N-S shortening during the Early to Middle Miocene. Coastal Makran exposes mostly Late Miocene slope marls grading into Pleistocene coastal to continental deposits. Normal faults, which are not seen in other units, cut lithologies younger than Late Miocene (Dolati, 2010).

Faulted Pliocene-Pleistocene to Holocene marine terraces raised up to 200 m a.s.l. document Quaternary uplift of the coast; inferred uplift rates (e.g. Page et al., 1979; Reyss et al., 1999) vary from western (0-0.2 mm/a) to eastern Makran (0.5-2 mm/a). Longer term, average uplift/erosion rates could not be derived from apatite and zircon fission track thermochronology because zircons retained their detrital age and apatites were partially annealed in the 40 analysed rocks (Dolati, 2010).

2-2- Regional climate

There is no evidence for glaciation events in Makran (Kehl, 2009). The modern climate around the Arabian Sea is dominated by two main sources of monsoon winds. The summer monsoons bring warm and humid conditions from the southwest; the weaker and dry winter monsoons blow from north-northeast and lead to arid to semi-arid conditions (e.g. Sirocko et al., 1991; Lückge et al., 2001; Clemens and Prell, 2003). Makran is beyond the Indian monsoon domain, too far to receive summer rain; it is mostly influenced by the northern summer limit of the Intertropical Convergence Zone (Gasse, 2000; Fleitmann et al., 2007). The present-day regional climate is arid to semi-arid with a mean annual rainfall of 130 mm, nearly all rain falling from November to March with a peak in January – February (Kehl, 2009). Most of these winter precipitations are due to cyclonic low pressure coming from the Eastern Mediterranean (Lückge et al., 2001; Weyhenmeyer et al., 2002). The strong seasonality causes flash flooding of the drainage system which leads to high sediment transfer rate and erosion of the Makran deposits. This applies for the whole MAW, so that climate cannot explain significant lateral variations of erosion patterns.

2-3- Drainage system on the Makran Accretionary Wedge

We investigated five major drainage basins. From west to east they are named after the main cities they surround, namely Sedij, Fanuj, Nikshahr, Pishin and Torbat (Fig. 2). The Oman Sea is the base level common to all these catchments. All display dendritic to parallel, accordant drainage patterns, consistent with the similar subsurface lithologies on which they flow. Headwaters drain the subunits of North Makran, middle streams incise Eocene to Miocene turbidites of Inner and Outer Makran and downstream parts flow over and flood, in rainy seasons, late Miocene-Pliocene shelf deposits of Coastal Makran. The main trunk channels of Sedij, Fanuj and Nikshahr have a bulk N-S trend nearly orthogonal to the structural grain of the MAW. These transverse catchments have smaller stream lengths and drainage areas than the eastern Pishin and Torbat catchments. The rather short, western

pattern can be viewed as rivers flowing N-S, down-slope of a steadily growing wedge reaching its highest elevation at the water divide (trench slope break?), quasi at the boundaries with the Jaz Murian and Mashkel Depressions (Fig. 1). Beyond the Pishin catchment, the river channels are recurrently deflected from the N-S flow direction into E-W streams parallel to the regional faults and folds (Fig. 2). This readily suggests that tectonic folds and faults imprint the eastern part of the Makran fluvial system whereas a regional slope controls its western part.

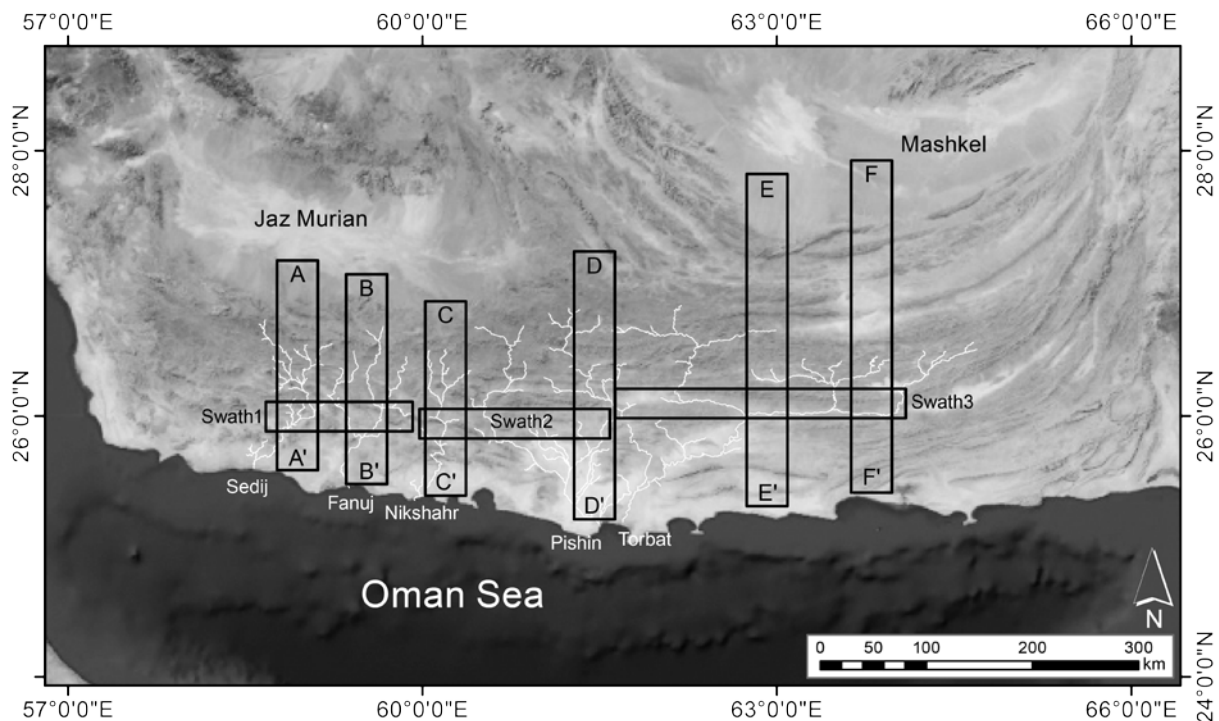


Fig. 2: Studied catchments and rivers (white lines and names) on satellite image of the Makran accretionary wedge (Google Earth). Boxes: swath profiles of Figs. 3 and 4.

3- Analytical methods

We applied the tools commonly used in tectonic geomorphology studies, following the principle that drainage network and river profile anomalies may be related to recent surface, mostly tectonic movements. We do not dispute assumptions inherent to this approach. These can be found and are discussed in several textbooks (e.g. Burbank and Anderson, 2001; Bridge and Demicco, 2008; Bull, 2009). They involve a set of constants that should actually be variables (for instance, area of drainage area, uplift rate all along the channel, etc) influencing the assumed steady-state shape of river long profiles. Yet, accepting the widely-applied stream power analysis allows comparing the different catchment we studied and our results with other studies in other regions. Therefore, we only summarize the analytical method and refer to the given literature for deeper information.

3-1- Local relief and swath profiles

Relief refers to the difference in elevation between highest peaks and valley or depression bottoms of the local landscape. As such, the local relief expresses river and/or glacier incision (Deffontaines et al., 1994; Kühni and Pfiffner, 2001), a proxy for rock uplift (e.g. Ponza et al., 2010).

Six N-S transverse and three E-W longitudinal swath profiles were constructed to characterize the general topography of the studied Makran (Fig. 2). Swath profiles were extracted from the 90m SRTM data. The width of these swath profiles is narrow enough (20km) to avoid averaging along strike variations of geological structures, which typically are linear and cylindrical for long distances. We used ARCGIS Tool Box to obtain the maximum, minimum and mean elevation along each swath profile (Figs. 3 and 4). These mean values were projected on a vertical plane along the midline of the swath rectangles. The difference between the maximum and minimum elevation curves is a measure of the local relief along each transect (Figs. 3 and 4), at length scales equivalent to the swath width (e.g. Masek et al., 1994).

3-2- Longitudinal stream profile

Plots of elevation versus distance along the streamline were extracted from a filled G-ASTER (30m) digital elevation model (DEM). After examination of satellite images, stereo aerial photos and field data, we selected and mapped rivers with mainly bedrock or mixed bedrock-alluvial stream beds with thin alluvial cover and > 70% exposed bedrock. Extracted data were analysed using New Tools for Quantitative Geomorphology (Kirby et al., 2007). The alluvial parts of channels, where river sediment protects channel beds from erosion, were excluded from morphometric analysis.

The Hack's law is one of the oldest scaling functions (Hack, 1957). It relates the outlet to divide river length L to its drainage area A :

$$A = k_a L^h \quad (1)$$

where k_a and h are empirical constants (e.g. Rigon et al., 1996). To know the river profile, the slope of the channel must be defined at each points of its length. This is described by the classical, empirical power-law function (termed Flint's law):

$$S = k_s A^{-\theta} \quad (2)$$

where S is the slope of the channel, k_s is the steepness index, A the upstream drainage area and θ the concavity index (e.g. Flint, 1974; Whipple and Tucker, 1999; Snyder et al., 2000; Kirby et al., 2003). Logarithmic, concave upward longitudinal profiles represent long-term, dynamic equilibrium between uplift and erosion; concave-convex profiles with erosion steps in the middle reaches reflect long-term predominance of erosional processes; where surface uplift is dominant, river display convex-up profiles (e.g. Hovius, 2000; Kirby and Whipple, 2001). The idea is that rivers seek for a stream gradient until their transport capacity finds equilibrium with the erodibility, i.e. sediment production of the geological bedrock. Mapping the variations of the k_s index along the channel flow path visualises places where channel incision is disturbed by either a change in strength of underlying rocks

or by sediment fluxes or by local, tectonically-driven rock uplift (e.g. Kirby et al., 2003). We applied to the channel profiles a smoothing window of 250 m to reduce noise and artefacts of the DEM data while preserving as much original information as possible. We will present smoothed profiles because they were generally superimposed on raw profiles, except at few isolated and incoherent points. We calculated channel slope and upstream drainage area at every 15m elevation interval. Steepness (k_S) and concavity (θ) indexes were obtained from linear regression of the logarithms of channel slope and upstream area given by equation 2 (Wobus et al., 2006). Regression was restricted to data segments exhibiting reliable channel slope - drainage area scaling, while we excluded segments down and up-stream end segments where the channels are dominated by debris flow and alluvial processes.

Several empirical studies showed a positive correlation between k_S and the bedrock erosion rate (or rock uplift rate) E in steady-state detachment-limited fluvial systems.

$$k_S = (E / K)^{1/n} \quad (3)$$

where K is erosion efficiency, which depends on climate and lithology, and n is a positive exponent related to dominant erosion processes (e.g. Whipple and Tucker, 1999; Kirby et al., 2003; Safran et al., 2005; Wobus et al., 2006). This quantitative relationship is an advantageous indicator of rates and patterns of differential rock uplift in steady state river profiles where vertical incision balances rock uplift (e.g. Kirby and Ouimet, 2011).

3-3- Channel steepness index

Because of the strong correlation between channel concavity θ and the steepness index k_S (equation 1), any variation or uncertainty in determined θ can lead to large k_S variations. To dampen this caveat and obtain more representative comparisons between channel profiles of different watersheds, the steepness index was normalised to a reference concavity θ_{ref} (Kirby and Whipple, 2001). We obtained from the slope-area regression of all studied rivers an average, regional convexity $\theta_{ref} = 0.47$. This estimate is very close to the $\theta_{ref} = 0.45$ regularly taken as equilibrium value in similar geomorphological studies (e.g. Snyder et al., 2000; Wobus et al., 2003; DiBiase et al., 2010; Molin et al., 2012). To be consistent and quantitatively comparable to other studies, and assuming that the very small difference of 0.02 does not significantly affect our results, we also used $\theta_{ref} = 0.45$ to calculate the normalized K_{Sn} . We estimated K_{Sn} in a 0.5km moving window along the stream trunks and their tributaries. Resulting, colour-coded maps of normalised channel steepness index detect transient stream incision locally and regionally. This exercise facilitates quantitative spatial comparison.

3-4 Steady-state river profile reconstruction

The state of equilibrium of detachment-limited river channels is defined by comparing actual profiles with calculated steady-state profiles. Combining Hack's law (equation 1) and erosion law (equation 3) yields the equilibrium (time-independent steady-state) profile, assuming that rock uplift and erosion rates are equal at every point of the channel (Willett, 2010) and

imposing a constant ratio $\theta = 0.5$. Under such conditions, θ is the intrinsic concavity that embodies the ratio of area and slope exponents of the stream power law (Snyder et al., 2000; Tucker and Whipple, 2002; Kirby et al., 2003). Calculation further assumes homogeneous erodibility of lithologies underneath all along the channel. Departures between measured and modelled profiles allow estimating a general, constant uplift rate along each river and point out where the channel is affected by tectonic or lithological disturbances. For comparison, we adopted the regionally uniform, average steady incision rate of 0.3 mm/a determined from ^{10}Be dating of strath terraces (Haghipour et al., 2012).

4- Results

A regionally uniform, average steady incision rate, relatively weak bedrock (friable sandstone, shale and mudstone) and homogeneous climatic conditions over Makran make it a favourable field application to extract tectonic uplift from the steady-state variation in topography. Since all studied catchments share the same base level (Oman Sea) and no evidence of glaciation has been reported or observed in the area, we are confident that the fluvial system is one of the main external forces responsible for the topographic relief.

Catchment Name	Area (km ²)	Diameter(km)	Mean Slope°	θ	ksn
Sedij catchment	4627	133	4.6		
Hoor River				0.31	48.1
Sedij River I				0.35	30.3
Sedij River II				1.8	48.9
Bidak River I				0.98	30
Bidak River II				0.63	52.2
Fanuj catchment	8386	150	4.9	–	–
Guredak River I				0.57	58
Guredak River II				0.65	48
Fanuj River I				0.26	19.8
Fanuj River II				0.59	76
Tik Genah River				0.46	50.1
Nikshahr catchment	5399	144	6.6	–	–
Nikshahr River				0.28	94.6
Pishin catchment	20776	208	3.2	0.66	238
Peer sohrab River I				0.48	29.8
Peer sohrab River II				-0.31	57.6
Peer sohrab River III				1.2	117
Sarbaz River I				0.22	49.4
Sarbaz River II				0.93	118
Torbat catchment	29498	349	3.3	–	–
Kash River I				0.42	38.9
Kash River II				-0.11	93
Kash River III				1.2	12.9
Kaur River I				0.5	13.7
Kaur River II				-0.97	39.4
Nihing River I				-0.34	49.7
Nihing River II				-8	112
Nihing River III				0.44	13.6
Sarai River I				0.46	14.6
Sarai River II				-0.22	54.3

Table 1: Synthesis of morphological parameters of the studied catchments. Latin numbers indicate different segments of the rivers.

4-1- General topographic features

Altogether, the river and swath profiles indicate that inland Makran experienced significant vertical movements during the Holocene, in consistency with surface uplift previously recognised along the coast of the Oman Sea (Snead, 1967; Page et al., 1979; Vita-Finzi, 1987; Reyss et al., 1999). The topographic characteristics of the studied catchments are given in Table 1. The mean elevation increases gently from west (445 m a.s.l.) to east (813 m a.s.l., Fig. 3).

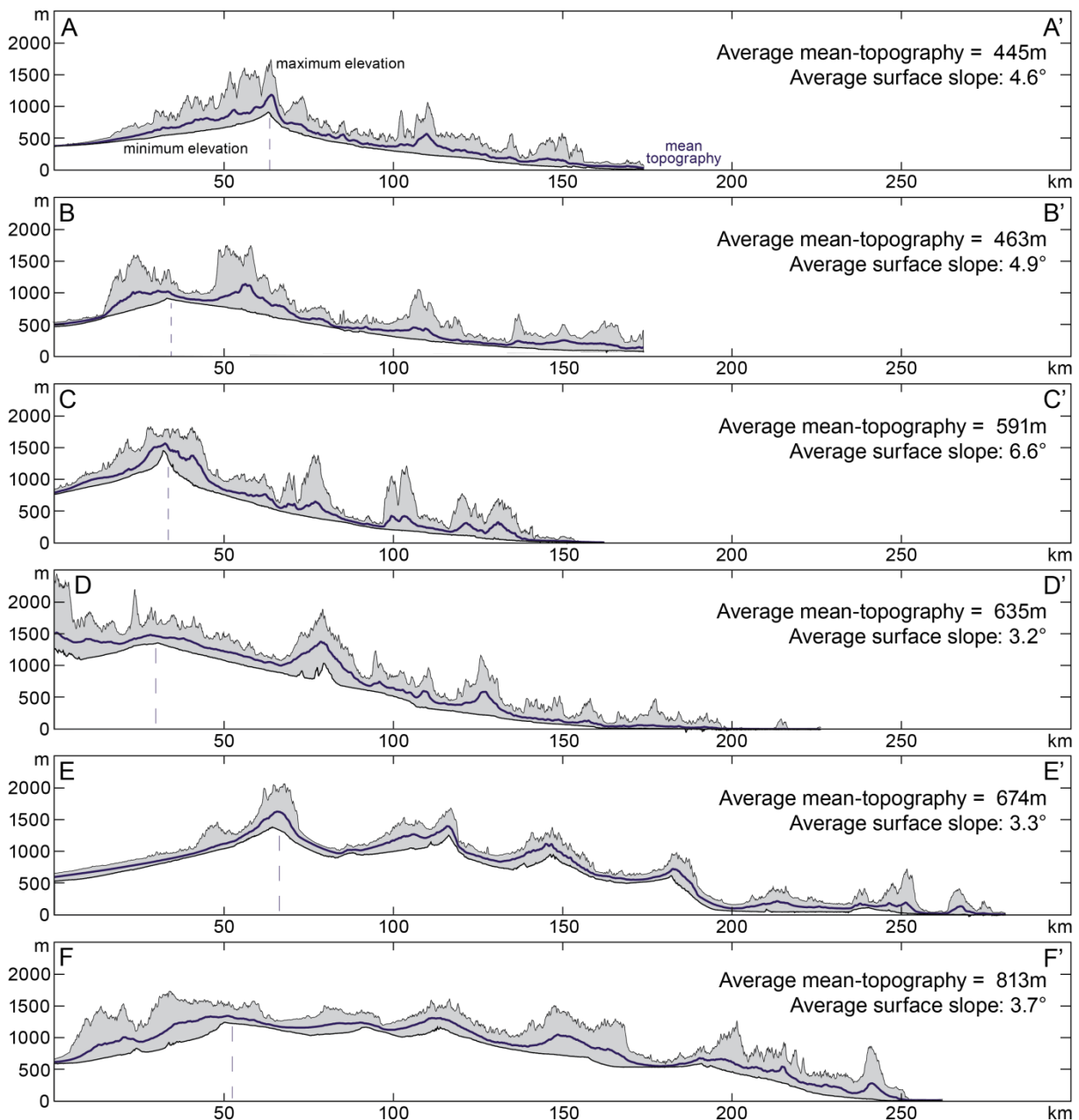


Fig. 3: Topographic swath profiles across Makran (width of swath is 20km). Maximum, mean and minimum elevation profile curves projected onto median axis of swath profiles located in Fig. 2. Dashed vertical line: Water divide. Average surface slope from water divide to coastal plain.

The mean surface slope measured on N-S profiles decreases from west to east with a significant change from Nikshahr to Pishin catchments (Table 1). This may be correlated with the larger width (Fig. 1), hence smaller general taper of eastern MAW. Note that the given slopes (Fig. 3) reflect inland topography and relief, not the wedge taper, which is in average very small (ca 2°) if it is measured from trench to divide. The E-W swath profiles (Fig. 4) show that relief and river spacing increases eastward. The landscape is more dissected in western Makran, which exhibits mature landscapes, whereas landscapes of eastern Makran are less mature, characterized by river patterns mainly controlled by folds and faults (Fig. 2). Relatively reduced topographic dissection suggests recent growth of basement structures.

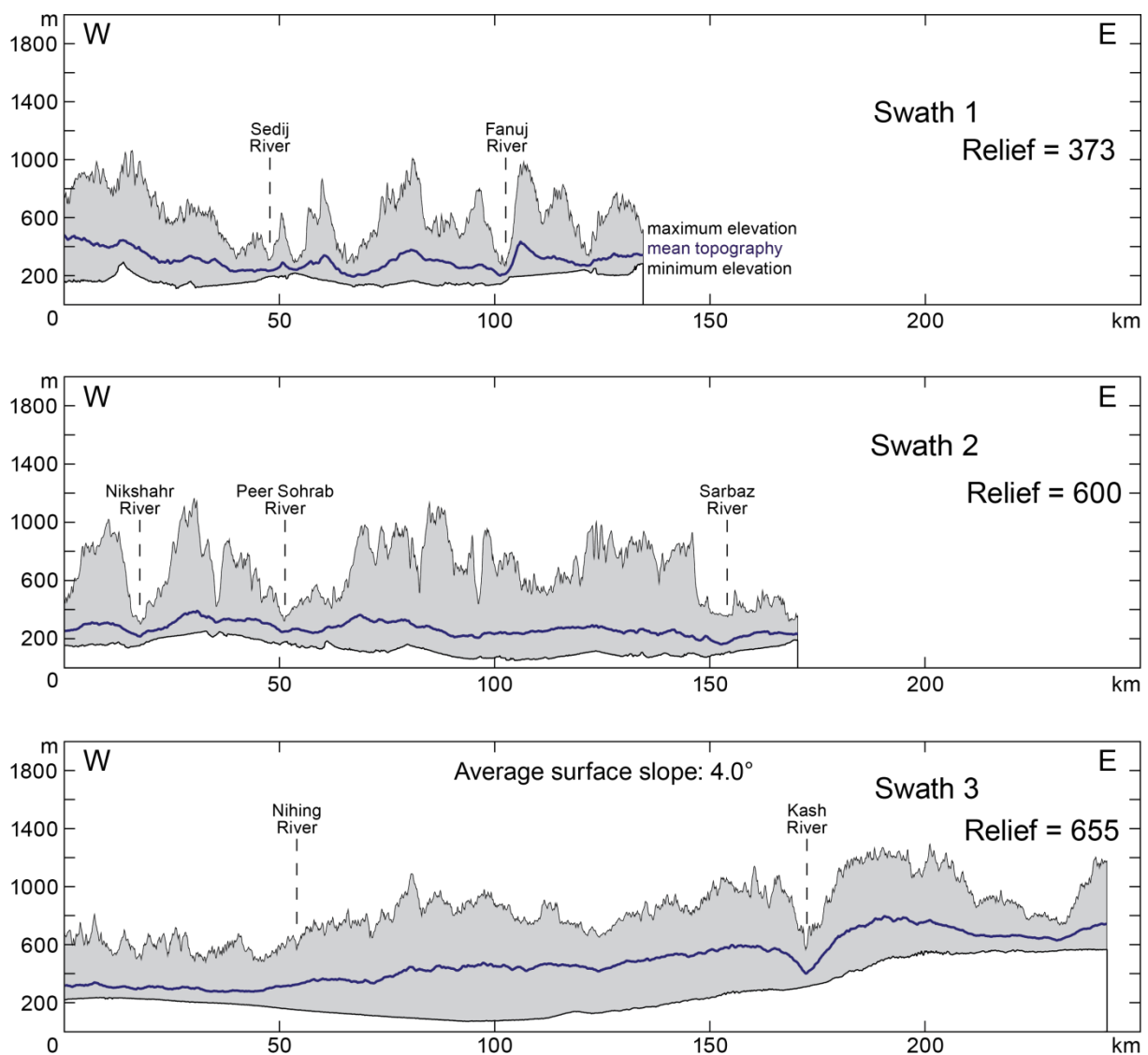


Fig. 4: Topographic swath profiles parallel to structural trends in Makran. Width of swath: 18km, location in Fig. 2. Same legend as Fig. 3.

4-2- Stream profiles characteristics

Sedij Catchment

Sedij Catchment has the smallest catchment area (4627km²) and diameter (133km, Table 1). The three important streams (from west to east, Hoor, Sedij and Bidak, Fig. 5) measured in this catchment have relatively low gradients and smooth, concave up profiles (Fig. 6). The upper reaches of Hoor and Sedij Rivers have concavity index ($> \sim 0.3$; Fig. 6) in the 0.3-0.6 theoretical range expected for steady-state profiles (e.g. Whipple and Tucker, 1999; Kirby and Whipple, 2001).

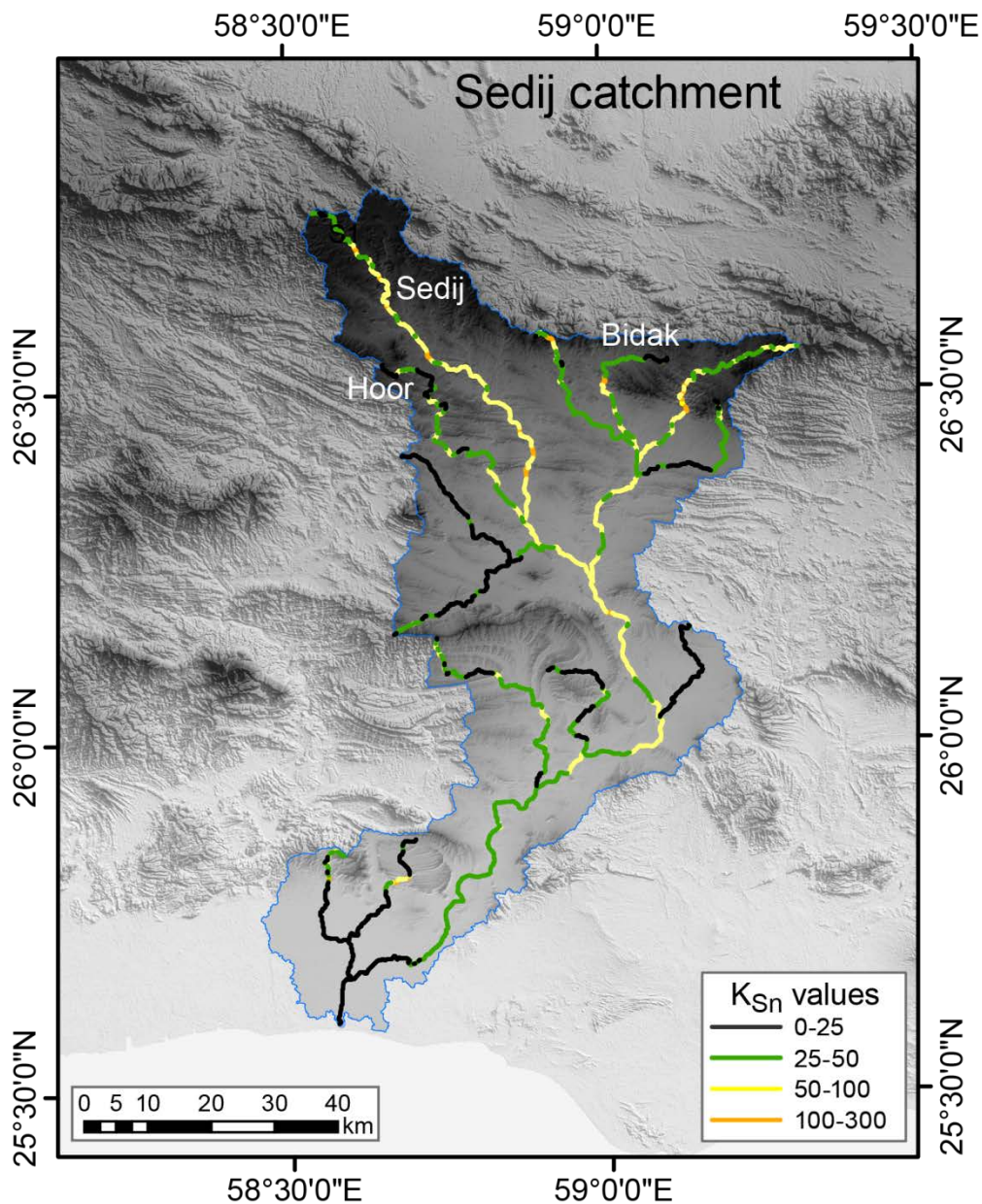


Fig. 5: Map of colour-coded steepness indices determined for main channels of Sedij Catchment (methodological details in text). Background: shaded relief map derived from ASTER GDEM version 1, NASA.

The downstream, lower course of Sedij River displays a higher concavity value ($\theta \approx 1.8$, Fig. 6), which we attribute, after field confirmation, to a change in channel bed type from mixed bedrock-alluvial (Fig. 7a) to alluvial, with no bedrock exposure. Therefore, we excluded this river segment from further analysis.

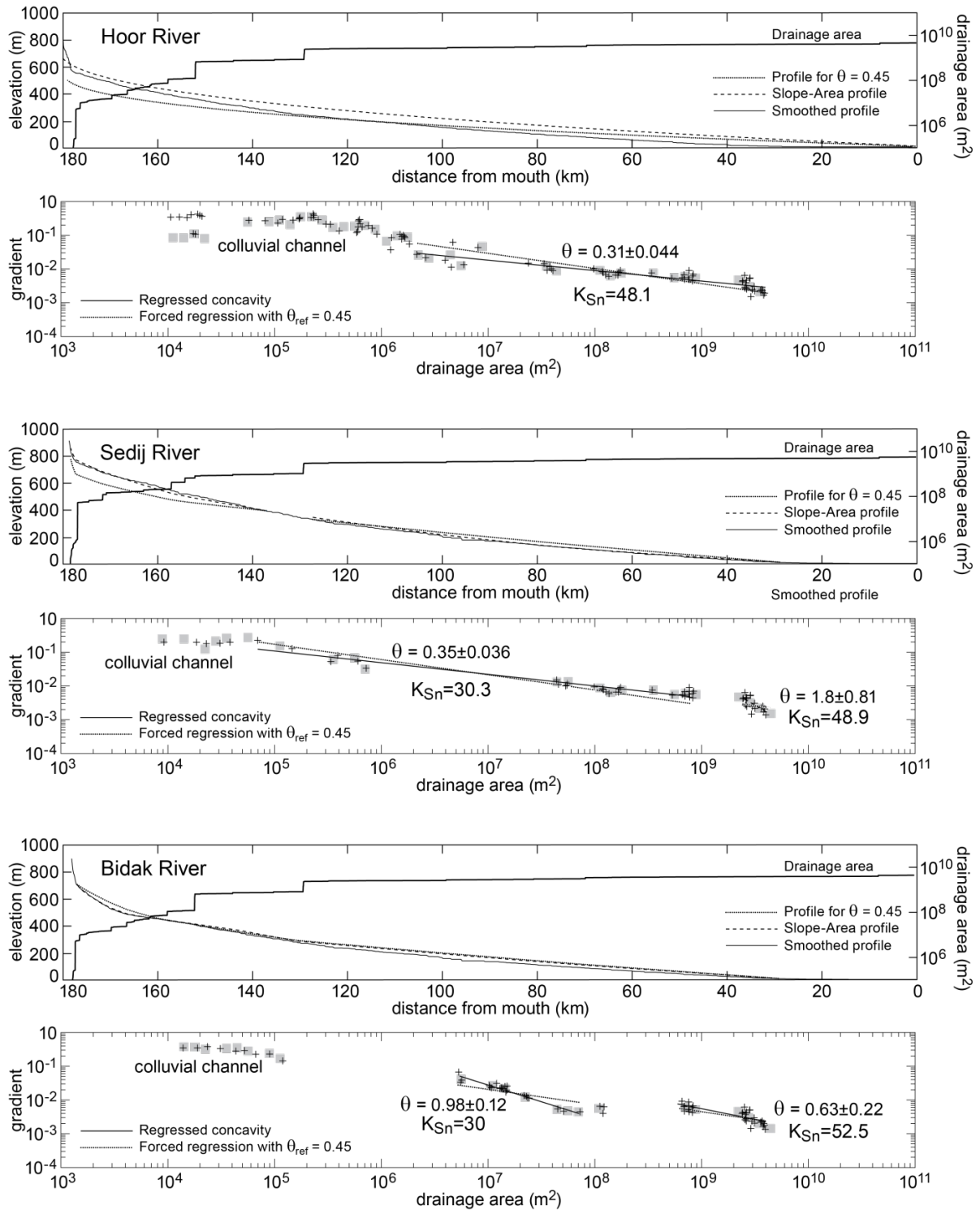


Fig. 6: Longitudinal channel profiles and associated slope–area log–log plots with best-fit regression lines defining concavity and gradient values for the studied channels of Sedij catchment. Present-day channel profiles extracted from the ASTER GDEM version 1, NASA. Curves explained in figure and text. Lines in log–log plot are regressed and forced regressed. Grey-filled squares are log-bin average of gradient/area data (crosses).

Bidak River displays a generally smooth profile (Fig. 6) with a concavity value of ~ 0.6 in its lower reach, consistent with near steady-state. Its upper reach has a high concavity index (almost 1; Fig. 6). Field control revealed that this local disequilibrium is due to a downstream decrease of bedrock erodibility, the upper part of the river flowing on sandstone-dominated turbidites whereas the lower segment flows on shale-dominated turbidite.

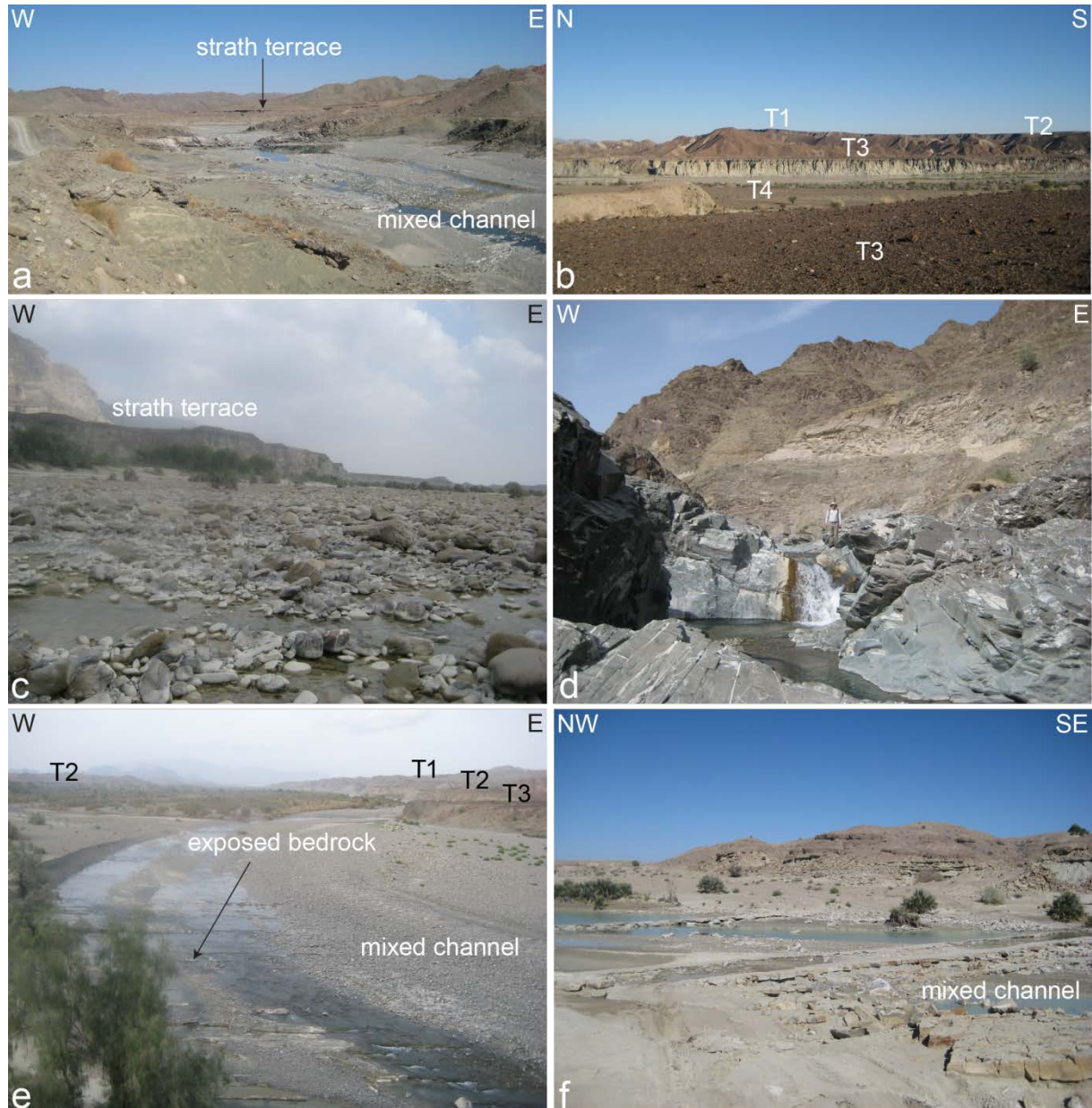


Fig. 7: Photographs of channel bed morphology and fluvial terraces. (a) exposed bedrock and mixed alluvial-bedrock channel of Sedij River; GPS: N26°04'57.059", E059°02'58.63"; (b) Four levels of strath terraces on Nikshahr River; GPS: N25°50'11.20", E060°09'07.86"; (c) Nikshahr river bed mantled by cobbles and boulders indicating high discharge at GPS: N25°47'26.88", E060°08'49.93"; (d) Bedrock incision at knickpoint upstream Nikshahr River; GPS: N26°28'02.63", E060°00'44.60"; (e) View towards upstream the middle reach of Peer Sohrab River; note exposed bedrock (arrowed) and T–T3 strath terraces; GPS: N26°02'34.41", E060°31'36.37"; (f) mixed bedrock-alluvial channel of Sarbaz River; GPS: N26°06'53.66", E061°35'44.32".

The average K_{Sn} values obtained from slope-area regression of the three rivers range between 30 and 50 (Fig. 6) without any distinct change. The derived K_{Sn} map of Sedij catchment (Fig. 5) shows a general down-basin decrease in incision rate without any prominent gradient change. Locally higher gradients (very short segments in Fig. 5) were verified to occur on prominent sandstone layers, visible from the background DEM of figure 5. However, these layers are unusual and rock resistance to erosion does not exert a major control on the catchment averaged erosion rate. The modelled steady state and actual channel profiles largely coincide for a constant uplift rate of 0.3mm/a (Fig. 8), which indicates general steady state for that graded river.

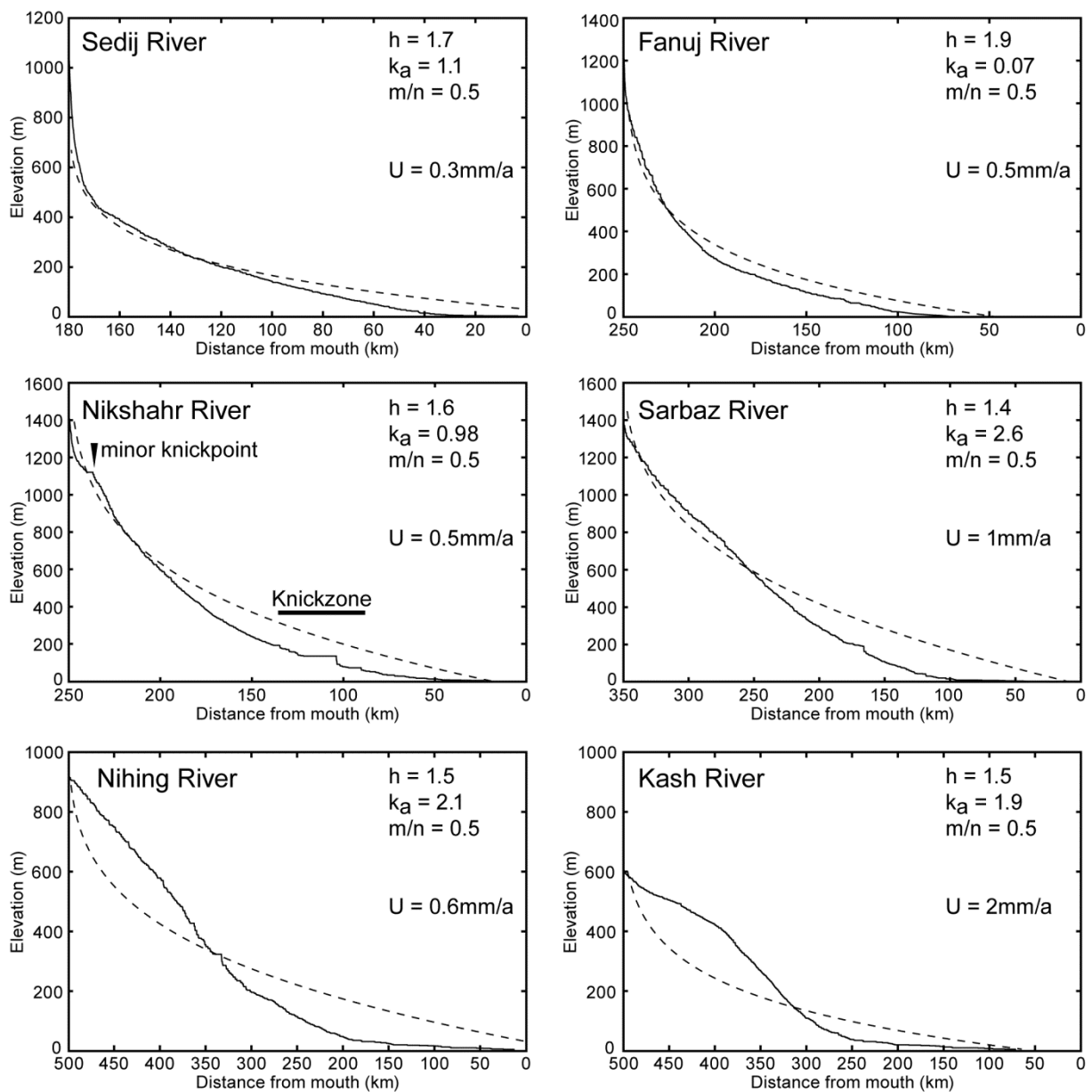


Fig. 8: Modelled steady-state for selected channels. Continuous lines show present-day river profiles; dashed lines correspond to best-fits Hack's law parameters (see text). m and n are area and slope exponents, respectively. k_a and h are the Hack's law coefficient and exponent, respectively (equation 1, paragraph 3.2). U is rock uplift rate.

Fanuj Catchment

The Fanuj catchment drains an area of 8386 km² with 150km diameter (Table 1). We analysed three rivers, from west to east Guredak, Fanuj and Tik Genah, Fig. 9). The three rivers display bedrock and mixed alluvial-bedrock channels (with dominant bedrock exposure) along most of their profiles.

The main channel of Guredak River follows a regular, concave upward longitudinal profile (Fig. 10). The concavity index is $\theta=0.57$ upstream and $\theta=0.65$ downstream, the small difference reflecting an insignificant change in the general shape of the channel profile. Neither the steepness map (Fig. 9) nor the log-log gradient-area plot (Fig. 10) show any remarkable change in K_{Sn} values, whose average is 48-58. These consistent and nearly constant values indicate that the river is in morphological equilibrium on monotonous bedrock that experiences close to constant uplift rate. As validation, modelled and measured profiles largely coincide (Fig. 10).

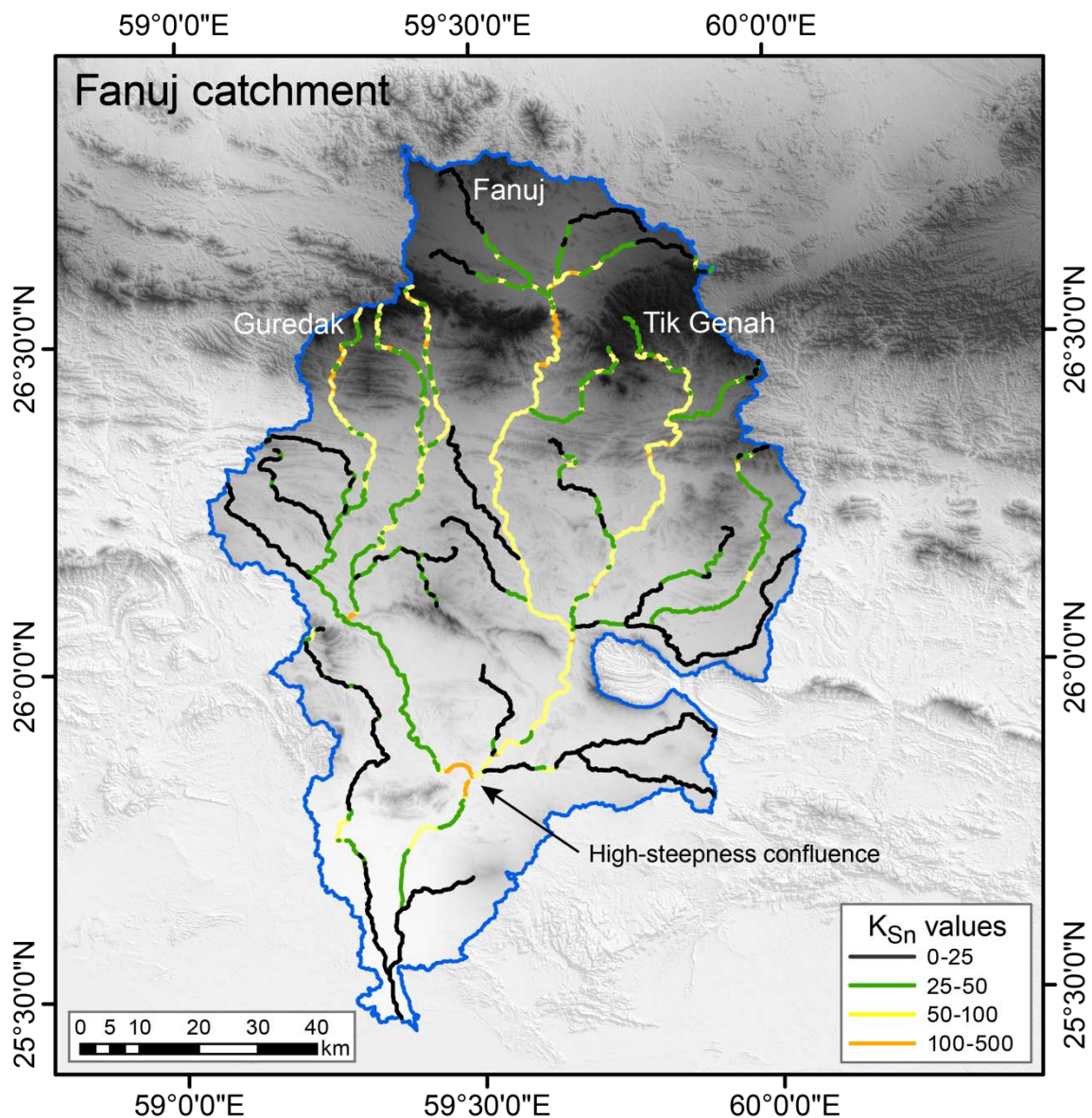


Fig 9: Map of colour-coded steepness indices along the main channels of Fanuj Catchment. Background as in Fig. 5.

Fanuj River is characterized by a relatively low concavity in the upstream part ($\theta = 0.26$), which is due to debris flow channel characteristics down to the knickpoint, about 20km from the divide (Fig. 10). Field investigation indicated a sharp lithological contrast (from volcanic rocks upstream to sediment downstream) and a marked change in the valley width at the 5m high knickpoint.

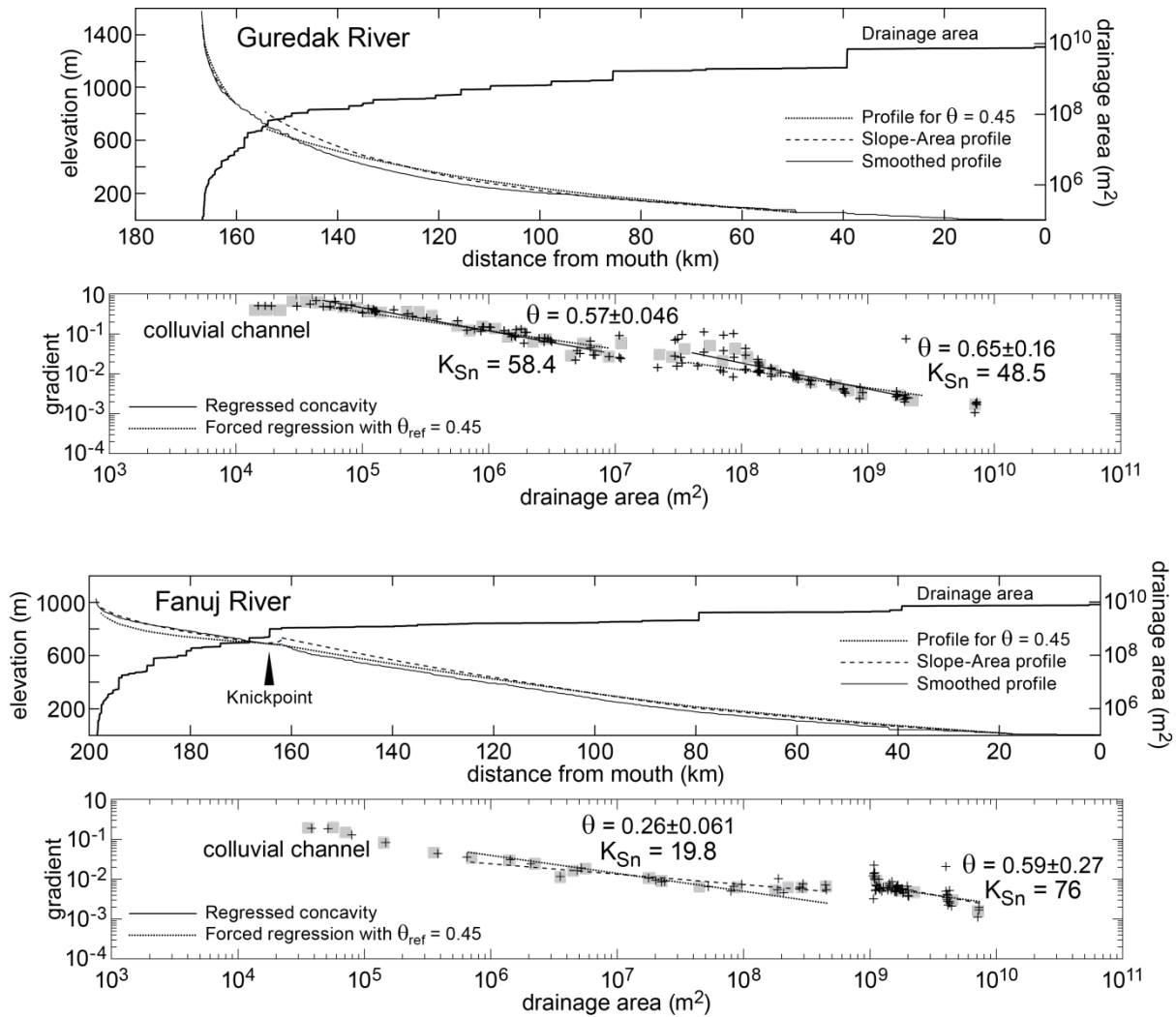


Fig. 10: Longitudinal channel profiles and associated slope–area log–log plots with best-fit regression lines defining concavity and gradient values for studied channels of Fanuj catchment. Same symbols as Fig. 6.

The upstream part of the channel flows into a narrow gorge with big (>1m) boulders that indicate important hillslope contribution to river sediments, yet insufficient to prevent abundant exposure of bedrock. The rather low concavity number is therefore attributed to the lithological signature of the volcanic rocks, arguably stronger than shale-rich turbidite sediments rather than to debris flow or other hillslope processes. Downstream, one other place displays high steepness values (> 100, Fig. 9). It is the confluence to Guredak River; high K_{Sn} is related to physical properties of this junction point. The downstream channel does not show remarkable disturbances and is well equilibrated from there on, out of minor,

lithologically-controlled places. The uplift rate derived from the best fit profile is 0.5mm/a (Fig. 8).

The Tik Genah River has no major knick point. The K_{Sn} map exhibits a homogeneous spatial pattern of channel steepness. The channel profile does not show any significant deviation from equilibrium profile. The best-fit concavity index is 0.46 (Fig. 10). With this value, the measured profile fits to the theoretical profile, which indicates geomorphic equilibrium with constant uplift rate of this channel.

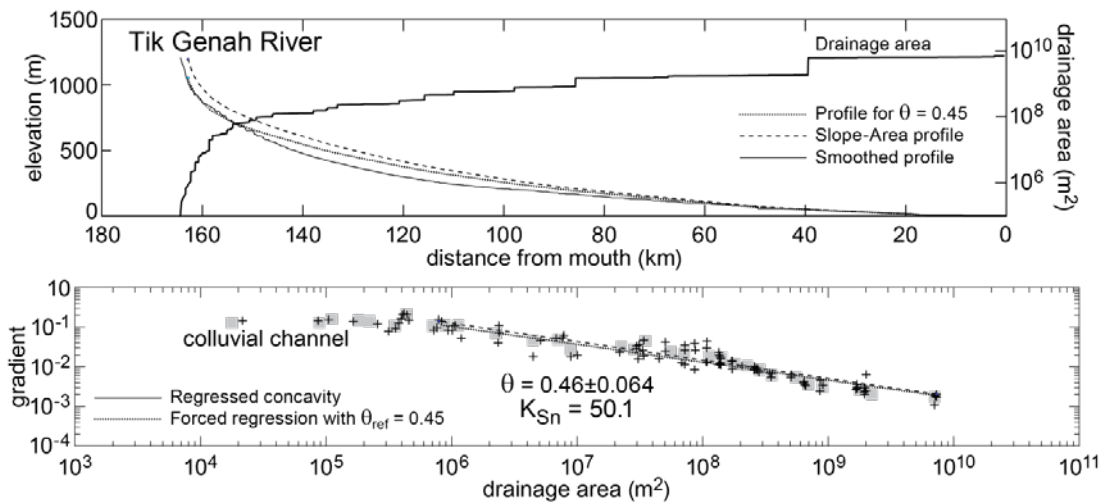


Fig. 10: Longitudinal channel profiles and associated slope–area log–log plots with best-fit regression lines defining concavity and gradient values for studied channels of Fanuj catchment. Same symbols as Fig. 6.

Nikshahr Catchment

The 5399 km² Nikshahr catchment has an elongated shape with a diameter of 144 km (Table 1; Fig. 11). The longitudinal profile of Nikshahr River has a generally concave up shape divided into two segments by a pronounced (but only 3 m high) knickpoint at about 125 km from mouth (Figs. 11 and 12), at the entrance into a knick zone extending down to about 80 km from mouth (Fig. 8). This knickzone overlaps the river segment that cuts through the E-W trending Rahde-Gardz anticline mapped in the underlying Upper Miocene marls and calcareous sandstones (Fig. 11, Dolati, 2010).

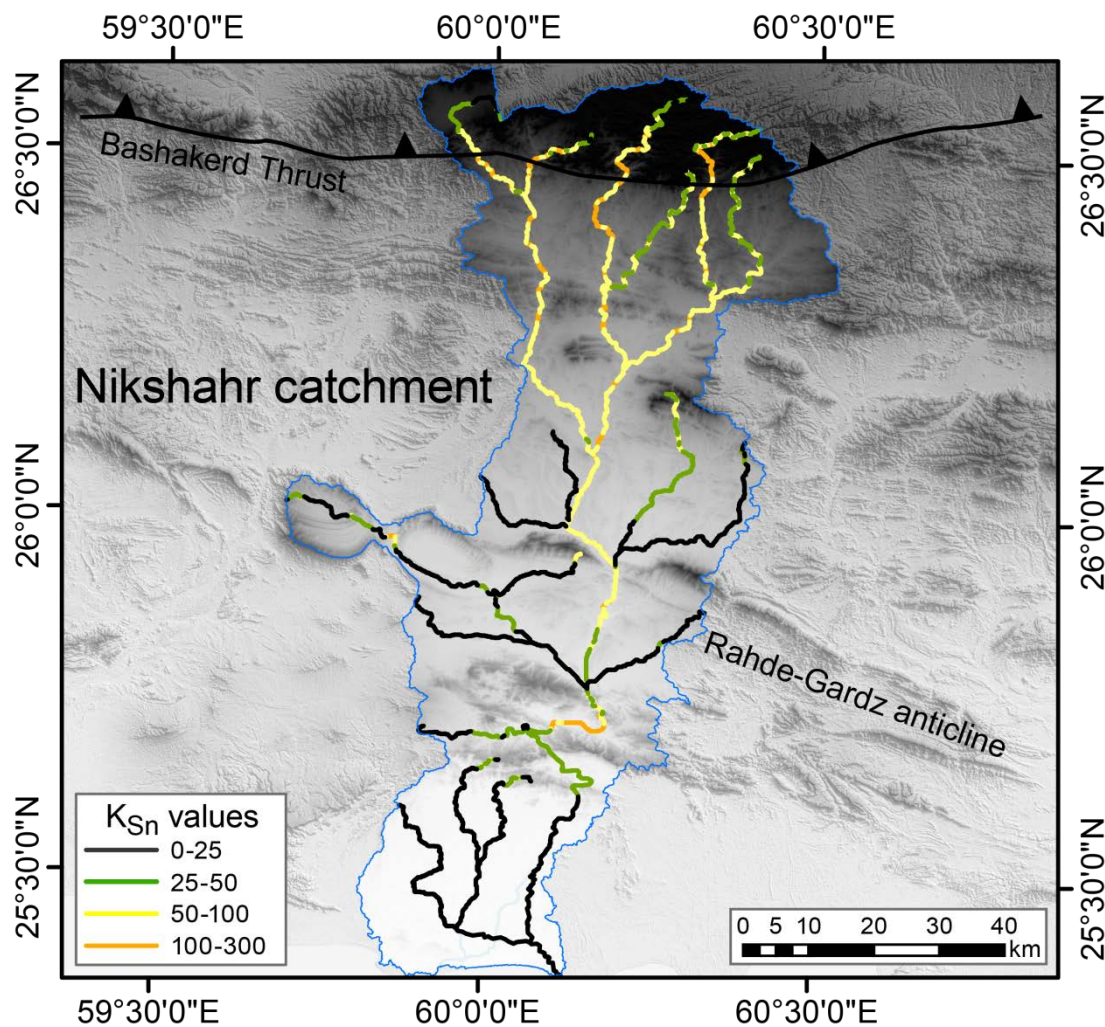


Fig. 11: Map of colour-coded steepness indices along the main channels of Nikshahr Catchment. Trace of thrusts from (Dolati, 2010). Background as in Fig. 5.

Five levels of strath terraces have formed in the knickzone (Fig. 7b). These terraces are increasingly folded with age, tapping recent amplification of the Rahde-Gardz anticline (Haghipour et al., 2012). This growing structure over an ~1.2 km deep décollements is clearly responsible for the significant increase in K_{Sn} value from 94 (upstream the higher knickpoint) to 238 (downstream through the knickzone, Fig. 12). Another smaller knickpoint exist in the upper reach (Figs. 8 and 12) where the river cuts through the so-called Bashakerd Thrust between North and Inner Makran (Fig. 1, Dolati, 2010; Burg et al., 2012). The middle reach is characterized by bedrock floored channel with relatively big (>10cm) boulders (Fig. 7c), which indicates relatively high discharge along this segment whose best-fit concavity index is $\theta = 0.66$. The upstream part of the channel has $\theta = 0.28$ only (Fig. 12), indicating low fluvial erosion. This channel segment was seen in the field to be covered by boulders.

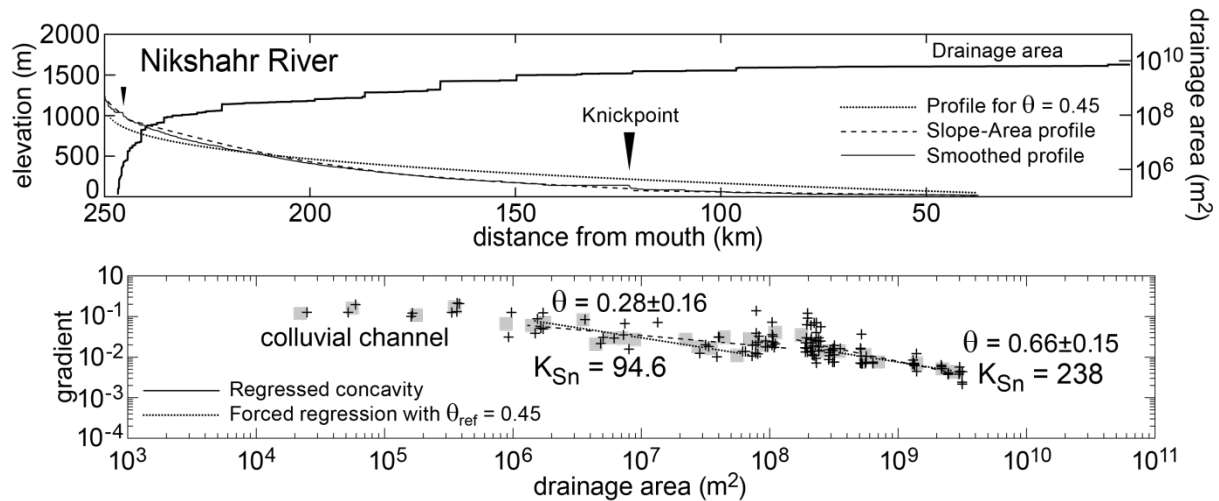


Fig. 12: Longitudinal channel profiles and associated slope–area log–log plots with best-fit regression lines defining concavity and gradient values for Nikshahr River. Explanations and symbols as in Fig. 6.

The downstream channel was excluded from the analysis because it has a thick cover of alluvium. The large difference between measured and modelled channel profiles reflects the tectonic deformation of the channel; the modelled curve of Nikshahr River is obtained for a constant uplift of 0.5 mm/a (Fig.8).

Pishin Catchment

The Pishin catchment is nearly four times larger (20776 km²) and has also a larger diameter (208 km) than the previous ones (Table 1). Its bulk NW-SE orientation differs from the N-S western catchments previously described. The Pishin catchment includes two major rivers, Peer Sohrab to the west and Sarbaz to the east (Fig. 13). Both rivers have similar characteristics, with segments separated by distinct knickpoints in their middle reach (Fig. 14). Both turn course from N-S to E-W flow direction along the northern flank of the high topography ramp anticline in the hanging wall of the Gativan Thrust (Dolati, 2010). In the field, they both display mixed bedrock-alluvial channels for most of their profile (Fig. 7e and f) with the formation of strath terraces.

Peer Sohrab River displays two prominent knick points, one where it cuts the Gativan Thrust (4m difference in elevation, ca 115 km from mouth) and the other (2 m high) where it cuts the Chah-Khan Thrust, between Outer and Coastal Makran, ca 75 km from the mouth (Figs. 13 and 14). At these places, K_{Sn} values reach >300. The upper reach of the river has a best-fit concavity index of $\theta = 0.48$. Good fit between measured and modelled profiles suggests that the uplift rate within this segment is constant. The upper knick point marks a scaling break to low, even negative concavity ($\theta = -0.31$), which designates steepening for the channel segment going down to the lower knickpoint; further downstream the channel has a

high concavity value ($\theta = 1.2$, Fig. 14). The river shows deviation from equilibrium profile along these two segments.

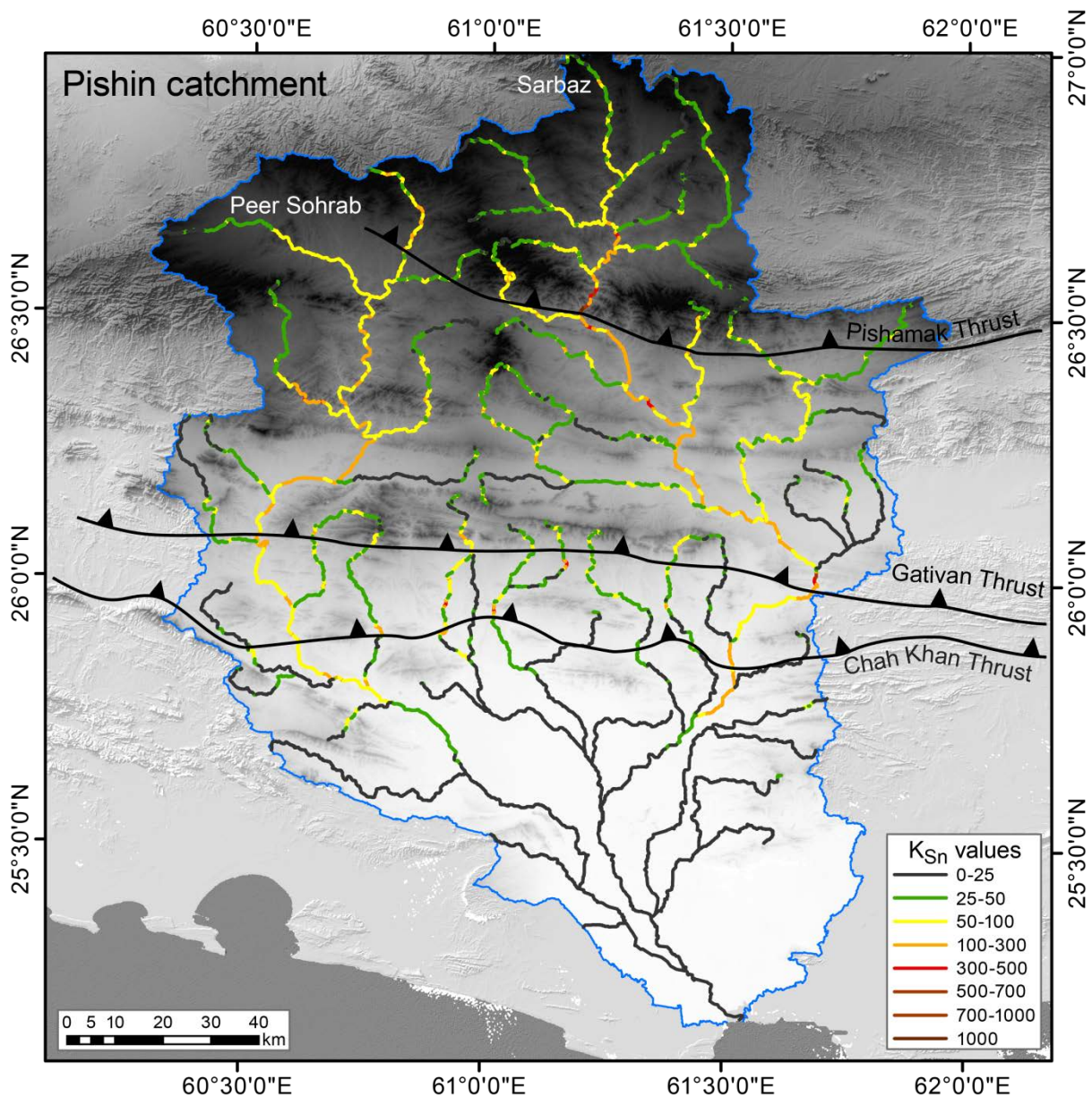


Fig. 13: Map of colour-coded steepness indices along main channels of Pishin Catchment. Trace of thrusts from (Dolati, 2010). Background as in Fig. 5.

Three knickpoints divide the Sarbaz River into four segments (Fig. 14). These knickpoints coincide with the Pishamak (1.7 m difference elevation between Northern and Inner Makran), Gativan and Chah-Khan Thrusts (Figs. 13 and 14). Changes in concavity and K_{Sn} values are most pronounced across the 4 m high knickpoints at the Gativan Thrust (Fig. 14). Upstream this knickpoint, the K_{Sn} values of nearly 50 and the associated low concavity ($\theta \approx 0.22$) indicate either a change in rock resistance to erosion, which was not obvious in the field, or enhanced downstream incision. Downstream, $K_{Sn} \approx 120$ and the concavity index is nearly 1. The spatial distribution of channel steepness index (Fig. 13) readily displays where active faults influence channel profiles. K_{Sn} values are >300 where the channel goes

through the Gativan and Pishamak Thrusts. However, the Pishmak Thrust brings sandstones on mudstones; this lithological change blurs the interpretation of increased channel gradient in terms of tectonic signal. This local complication does not apply to Gativan Thrust where high steepness values clearly reflect differential rock uplift. The loose correlation between modelled and actual profiles (Fig. 8) illustrates the non-equilibrium state of Sarbaz River. The calculated uplift rate from steady state profile fits with a value of 1mm/a.

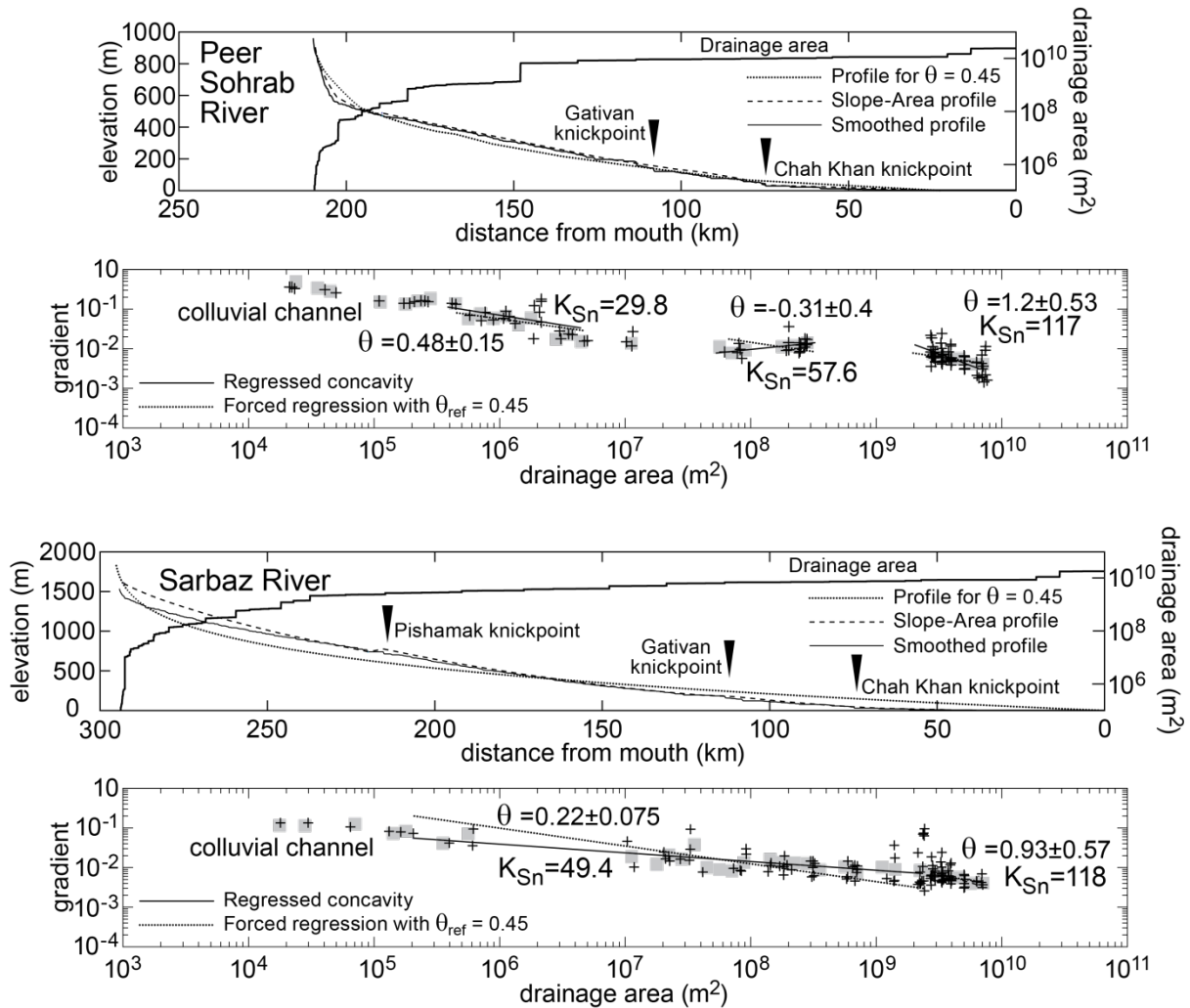


Fig. 14: Longitudinal channel profiles and associated slope–area log–log plots with best-fit regression lines defining concavity and gradient values for studied channels of Pishin catchment. Explanations and symbols as in Fig. 6.

Just downstream the knickpoint on the Gativan Thrust four strath terraces (P-T1-PT4) were initially thought, after satellite and aerial photo-interpretation, to pertain to the Sarbaz catchment, despite their elongated map shape diverging from the Sarbaz channel (Fig. 15). Field mapping revealed that they are 113 (P-T1) to 57m (PT4) higher than the present-day river. Their number and morphology differs from other terraces along Sarbaz River. The four are paired, relatively extensive and covered by less than 2 m gravels. They actually are aligned with, and belong to headwaters of the next, adjacent Torbat catchment largely

developed in Pakistan. The divide between the two drainage basins is virtually the steep east-bank of Sarbaz River. We attribute the specificity of site O to the locally efficient migration of the divide, at the expenses of the topographically higher Torbat system. The lower reach of Sarbaz River has captured the higher reaches of the river that was important enough to deposit the four terrace levels and going down to the Torbat main trunk. The captured, old channel abandoned at higher elevation than the current Sarbaz river is now reduced to small streams, short of water. Capture is apparently younger than the T4 level. We collected samples from the highest (P-T1) and lowest levels (P-T4) (Q-Mak-09-62, and Q-Mak-09-23, respectively).

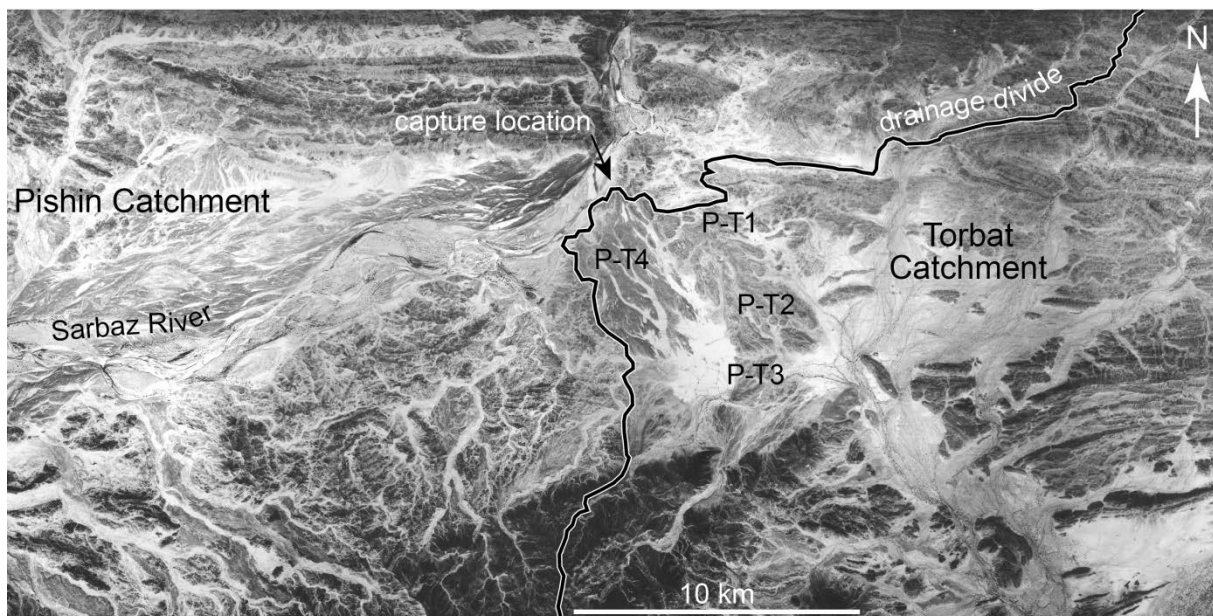


Fig. 15: Aerial photo (original scale = 1/50000, National Geographic Organization, Iran) showing the capture site of Torbat channels by Sarbaz River. GPS of capture point: 25°59'10.77"N, 061°40'35.90"E).

Torbat Catchment

Torbat Catchment is by far the largest (29498km²), comparably having the largest diameter (349km, Table 1). This catchment includes two major trunks, Nihing to the west and Kash to the east (Fig. 16). They merge about halfway their course to form the Dasht River, which reaches the sea few kilometres to the east of the mouth of Pishin catchment, in the Pasabandar-Jiwani Bay. Owing to the large area this catchment covers, we additionally studied the Kulbar River, one of the main tributaries of Nihing, and the Rakhshan River, one of the long streams that come from the eastern extremity of the catchment to join and flow into Kash River, (Fig. 16).

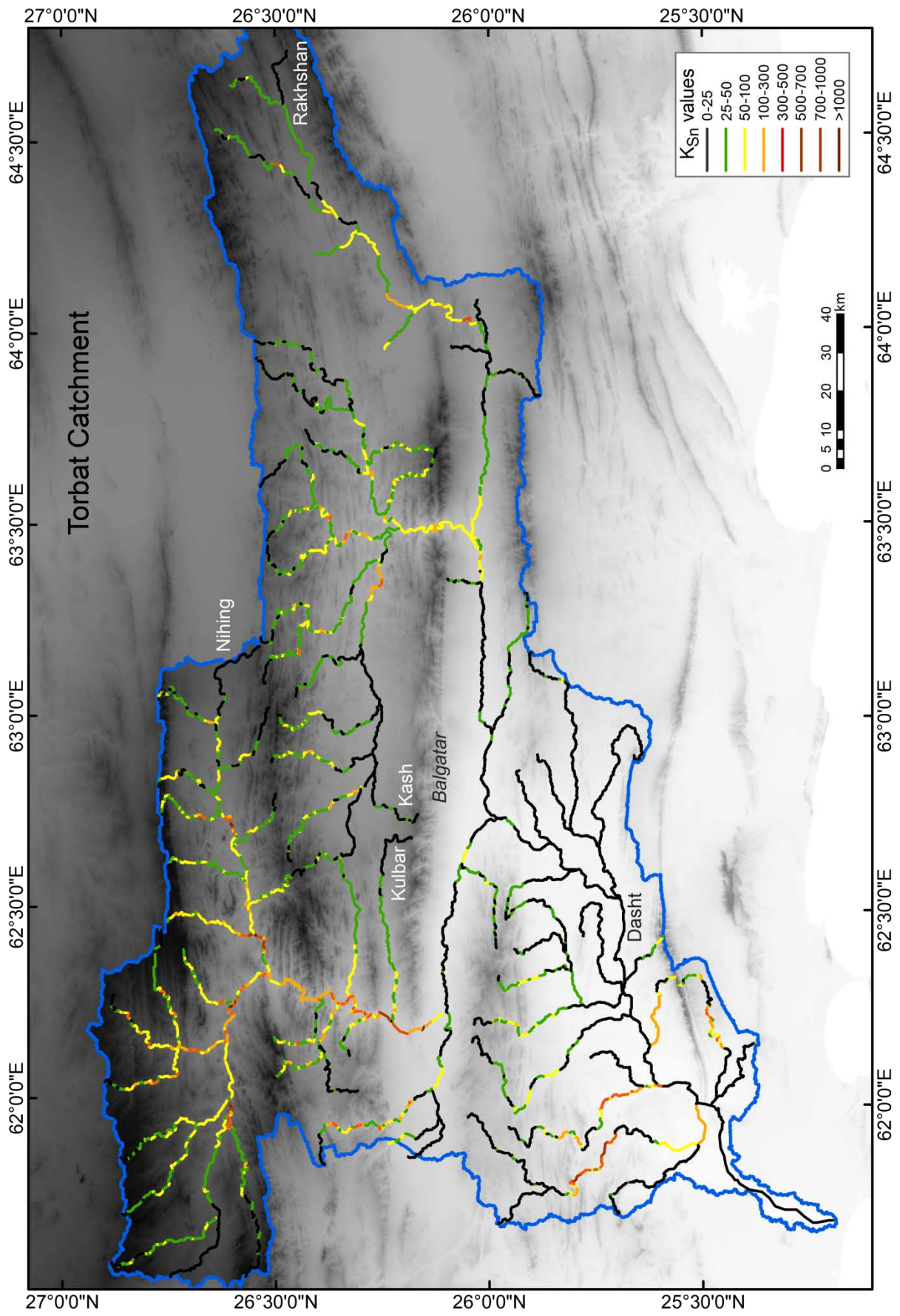


Fig. 16: Map of colour-coded steepness indices along main channels of Torbat Catchment. Background as in Fig. 5.

The Nihing and Kash rivers have similar drainage areas (ca 38000 km²) lengths (nearly 500km) and complex courses deflected from fold and fault parallel, long E-W segments to across structures, short N-S segments (Fig. 16). The resulting, trellis-like pattern suggests antecedence and young tectonic activity. Both channel profiles feature a similar convex part in their middle reach, where the two rivers pass through the prominent, E-W Balgatar ridge (Fig. 16), erected by the so-called Kechband imbricate, anticlinal fold train in Oligocene-Miocene turbidites. This convexity is expressed in negative concavity (-0.34,-0.42) and high steepness ($K_{Sn} \geq 50$, Figs. 16, 17 and 18). K_{Sn} values decrease and the channels tend to a steady-state profile $0.45 < \theta < 0.50$ downstream and upstream the convex middle reaches (Fig 17).

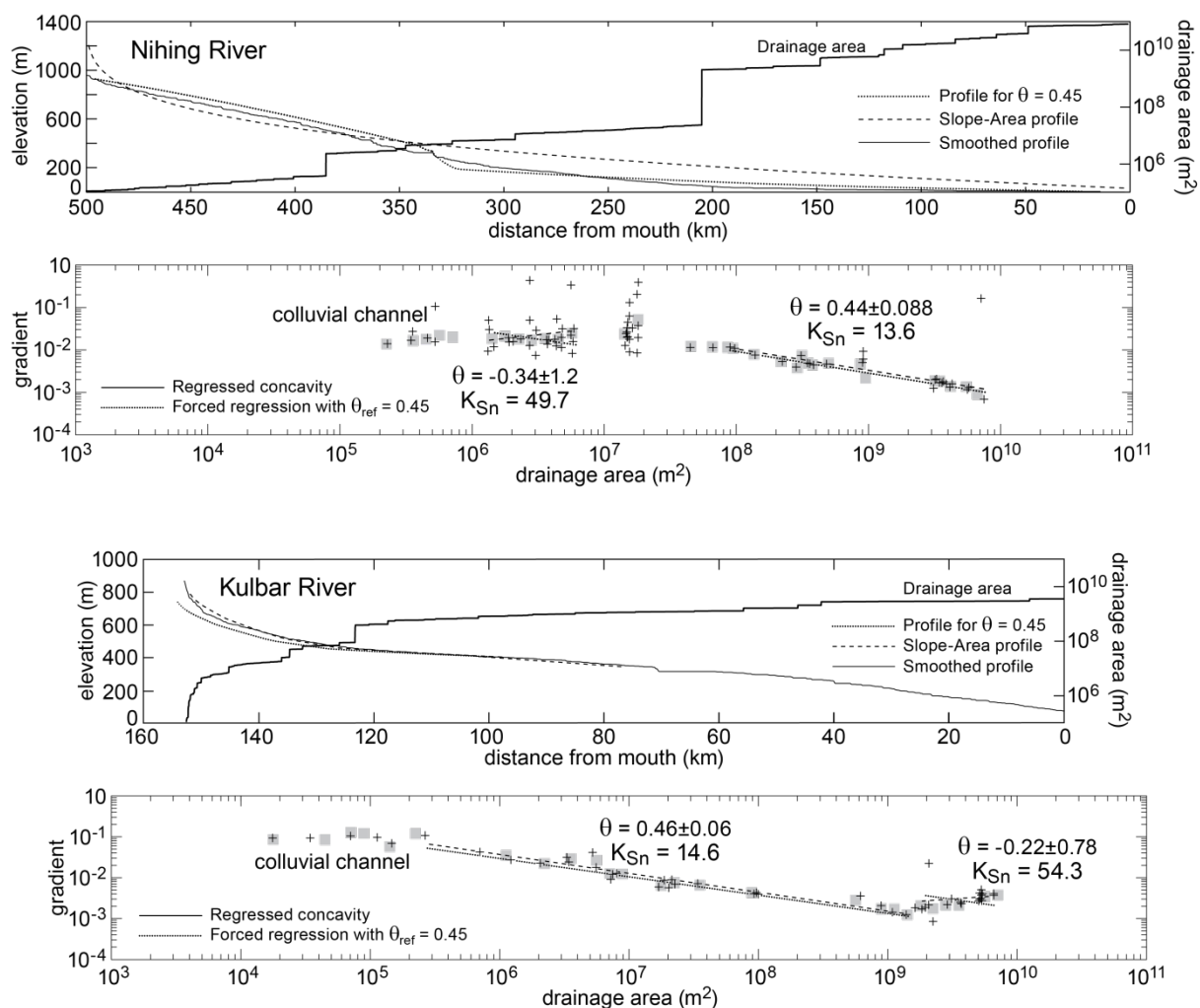


Fig 17: Longitudinal channel profiles and associated slope–area log–log plots with best-fit regression lines defining concavity and gradient values for the main rivers draining the west part of Torbat catchment. Explanations and symbols as in Fig. 6.

Kulbar River, Nihing’s tributary, also displays a three-segment longitudinal profile (Fig. 17). The upper segment is that part of the river that flows E-W, in a long valley parallel to the

main structures (Fig. 16). This channel segment has a concavity index ($\theta \approx 0.46$) that fits very well the reference concavity. The upstream segment finishes at the confluence with Nihing River. Consistently then, the Kulbar middle segment also has negative concavity ($\theta = -0.22$) and higher steepness ($K_{Sn} \geq 50$), pointing out active incision driven primarily by tectonic rock uplift across the Balgatar anticlinal ridge. The lowest segment is shared with Nihing. The concavity value is almost perfectly that expected for equilibrium, at 0.44 instead of 0.45 (Fig. 17).

The Rakhshan River, Kash River's tributary, comes from the far-distant, eastern reaches of Torbat catchment (Fig. 16). Rakhshan upstream flows mostly parallel to regional structures and topography (Fig. 16) with a concavity index $\theta \approx 0.5$ close to equilibrium conditions and a low steepness index $K_{Sn} \sim 15$ (Fig. 18). A rapid change in concavity and steepness ($\theta = -0.97$, $K_{Sn} \sim 40$, Fig. 18) occurs where this tributaries crosses the eastern continuation of the Balgatar ridge, where the channel follows a distinctly convex shape (Fig. 16).

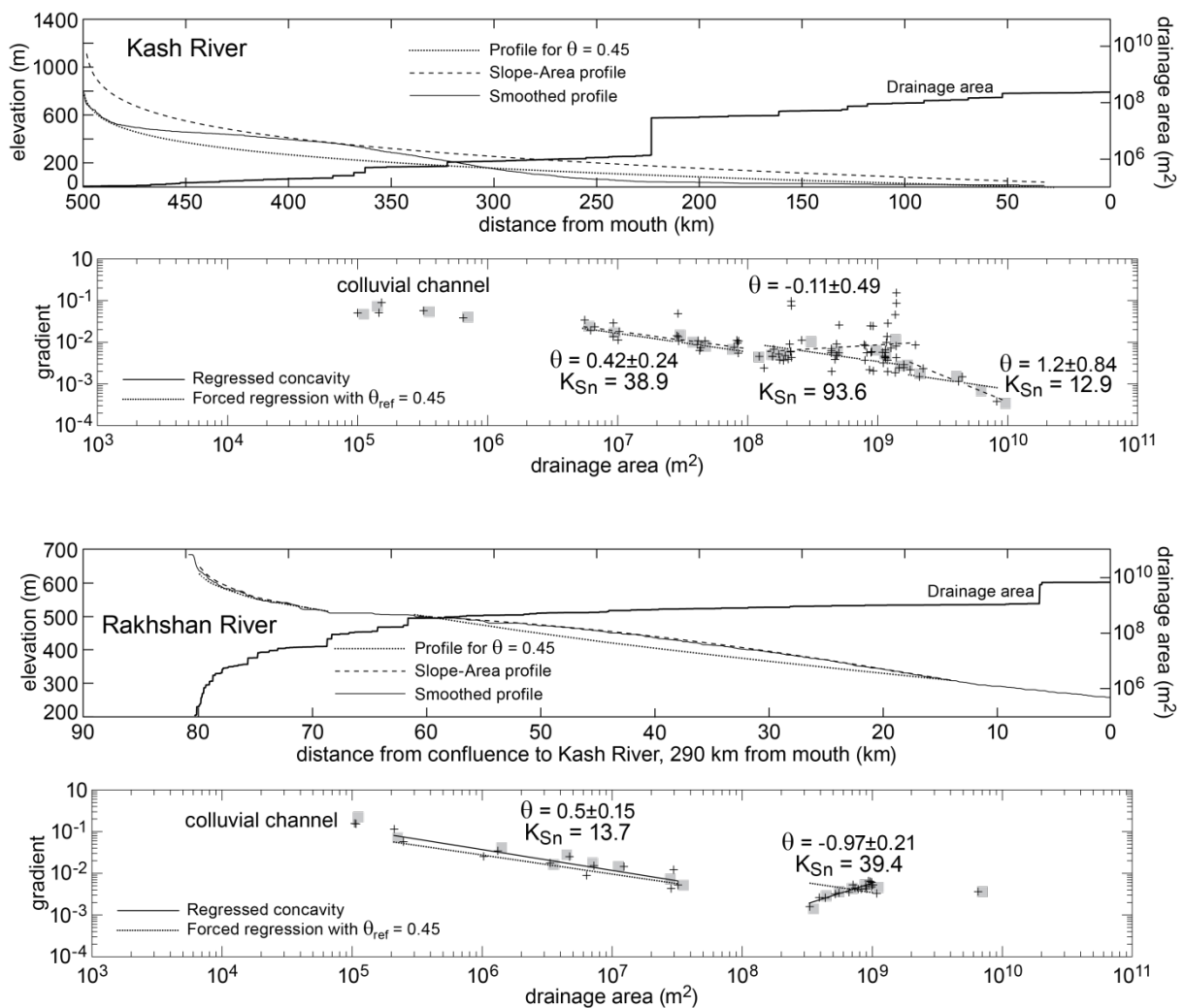


Fig 18: Longitudinal channel profiles and associated slope–area log–log plots with best-fit regression lines defining concavity and gradient values for the main rivers draining the east part of Torbat catchment. Explanations and symbols as in Fig. 6.

The large difference between observed and modelled channel profiles indicates that the Nihing and Kash rivers are, along with their main tributaries, out of geomorphic equilibrium (Fig. 8). They all are adjusting to highly variable uplift rates and/or a change in local base level associated with the regional Balgatar-Kechband fold train. The discrepancy between measured and ideal profiles renders difficult the application of equilibrium models with constant uplift rate all along the channel. This is quantitatively emphasized by comparing the estimated uplift rates (assuming steady-state) from modelled profiles of Nihing and Kash; they would be 0.6 and 2 mm/a, respectively (Fig 8). Both figures are in the range of dynamic amplification / vertical uplift rates known in other actively growing folds (between ca 1 and 20 mm/a, e.g. Rockwell et al., 1988; Burbank and Beck, 1991; Burg et al., 1997; Lavé and Avouac, 2000; Chen et al., 2007).

4-3- Synthesis of results

In summary, the longitudinal profiles of the main stream channels denotes that western and eastern catchments followed different evolutionary trends. The Sedij and Fanuj rivers, which drain the western part of the studied Makran area, have concave up longitudinal profiles without straight segments and prominent knickpoints or knickzones. The value of K_{Sn} plotted as colour-coded maps (Figs. 6, 9, 11, 13 and 16) ranges between 25 and 500 and the concavity index obtained for detachment-limited sectors of main channels range from 0.32 to 0.61 (Table1). These morphometric values are in the range of channels incising a homogeneous substrate that experiences uniform and moderate rock uplift rates (e.g. Kirby and Whipple, 2001). Comparing the present-day with modelled steady state channel profiles, assuming constant uplift and erodibility, classifies the western rivers as graded streams in morphological equilibrium along most of their channel (Figs. 7 and 10). In contrast, the eastern rivers (Nikshahr, Pishin and Torbat) are irregular, with noticeable concave-convex segments and knickpoints/knickzones (Figs. 12, 14 and 17). K_{Sn} values are high (>500) and show a generally increasing trend eastward. In addition, the highest fluvial terraces in the eastern catchments are perched as high as 100m above modern channels whereas the highest differential elevation is 40 m in the western catchments (Haghipour et al., 2012). Negative concavity denotes tectonic disturbance.

5- Discussion and interpretation

5-1- Knickpoints and causes of transient incision

Knickpoints were found at various altitudes and not in all tributaries of adjacent watersheds. The lack of correlation with any narrow elevation range throughout the river system suggests that knickpoints and zones, i.e. transient incision, did not migrate upstream after a eustatic drop of sea level. In support to this assertion, several studies (e.g. Howard 1994; Whipple and Tucker, 1999) have shown that, if transient river profiles respond to a change in sea level, the regressive incision wave causes a slope increase below the distinct knickpoints (Snyder et al., 2000; Van Heijst and Postma, 2001; Jansen et al., 2011). This is not seen in the studied river profiles. The drainage systems where knickpoints are present have stream

discharge under comparable bedrocks and climatic conditions. We could not identify clear scaling between along-stream location of knickpoints and drainage area, as commonly found in fluvial systems (e.g. Bishop et al., 2005; Jansen et al., 2011). It is therefore unlikely that unapparent differences in stream discharge control the differences in distance from mouth and vertical distribution of the knickpoints. In fact, field inspection authenticated the coincidence of major knickpoints with increased numbers of fluvial terraces and local folds and/or folds rather than rock type changes. These observations, conforming to locally high K_{Sn} values, suggest that disturbance of river profiles in eastern Makran is the surface expression of tectonic activity. However, uplifted marine terraces along the coast do indicate surface uplift, hence at least tectonic-driven base level change (in the absence of eustatic adjustment). A time lag between sea-level changes and fluvial response may explain the lack of corresponding signal in knickpoint distribution (e.g. Van Heijst and Postma, 2001; Whipple, 2001). This allegation would be valid if coastal uplift is younger and faster than the response time of the fluvial system. In support to this objection, the raised marine terraces dated using ^{14}C are only 5 and 18ka old (Vita-Finzi, 1987). Yet, ^{10}Be ages of strath terraces date transient incision at knickpoints along the Nikshahr and Sarbaz Rivers between 135 and 185 ka (Haghipour et al., 2012, and work in progress). We take this age bracket as explanation for the lack of transient features along the western rivers where all strath terraces are younger than 100 ka (Haghipour et al., 2012, and work in progress). Following this argumentation, and we confidently interpret transient river profiles in terms of recent differential rock uplift across active faults (principally the major thrusts between Inner and Outer Makran and between Outer and Coastal Makran, Fig. 1) and folds.

5-2- Quaternary uplift

The lack of information and evidence makes it difficult to link fluvial perturbations to base level changes in the Oman Sea. However, some studies argued that the eustatic sea level falls may affect the fluvial system and causes transient erosion if the offshore slopes (above 100-200 isobaths) is steeper than the sub-aerial slope, above the present-day sea level (Snyder et al., 2002; VanLaningham et al., 2006). In Makran the rare information on base level changes concerns Holocene times (Gharibreza and Motamed, 2006). Therefore, if there was a change in sea level, it should be very young, so that the response time of the fluvial systems is not yet attained and the present day river profiles do not show any the evidence.

5-3- Regional variation in topographic growth and tectonic activity

Our morphometric analysis complementing fieldwork revealed obvious variations in channel concavity and steepness from the western to the eastern parts of the studied MAW. The eastern part has relatively higher relief, mean elevation and higher channel steepness. Accordingly, eastern Makran manifests more tectonic activity than the relatively stable western areas, for the recent times.

Generally smooth profiles and rather uniform concavity indexes of $\theta \approx 0.45$ suggest that Western Makran has apparently achieved a morphological equilibrium not reached in

eastern Makran. Installed equilibrium is consistent with the general concept of continuous internal deformation, hence steady surface uplift in response to steady material flux into the convergent wedge (e.g. Davis et al., 1983; Dahlen, 1990; Roe and Brandon, 2011). Disturbance in channel profiles is significantly more pronounced in eastern catchments. Since the basement lithology (rock erodibility) and climate conditions are homogeneous over the study area, the differences in geomorphic indices along the eastern rivers can be linked to differing rates of vertical surface movements along active faults and growing folds. There, surface instability refers to wedge instability at the local scale. Wedge growth processes such as tectonic underplating, blind thrusting and imbrication above active décollement surfaces should strongly control the mean topography. Emergent faults and surface structures impact locally only this topography. Our deduction is consistent with this general interpretation of accretionary wedges.

The swath profiles and modeled long profile are consistent with the active tectonic forcing (Snyder et al., 2000; Kirby and Whipple, 2001). The difference in apparent uplift rate between eastern ($>0.5\text{mm/a}$) and western Makran ($<0.5\text{mm/a}$), as deduced from stream gradients, is consistent with the eastward increasing tectonic activity inferred from instrumentally recorded seismicity and uplifted marine terraces.

5-4- Comparison with other accretionary wedges

Most active orogenic wedges are considered to be in tectonic and erosional steady state, and the western Makran we have studied is another example (e.g. Suppe, 1981; Deffontaines et al., 1994; Bernet et al., 2001; Hodges et al., 2001; Pazzaglia and Brandon, 2001; Willett et al., 2001; Willett and Brandon, 2002; Hilley and Strecker, 2004). The transient state we recognized in eastern Makran comes at variance, albeit shorter time and length scales. There, topographic and geomorphic features provide evidence for a slowly deforming landscape, which remains consistent with the slow tectonic regime (in terms of convergence rate) of the MAW. Simplified models exploring the links between tectonic accretion and bedrock incision have emphasized the role of tectonic rates in controlling the broad shape of active wedges (Hilley and Strecker, 2004). Under constant erosion conditions, steeper and wider wedges are a response to larger fluxes of accreted rocks. Where researchers have invoked climatic variations to interpret changes in shape of orogenic wedges (e.g. the Andes, Horton, 1999 and the Alps, Schlunegger and Simpson, 2002), varying convergence (external) and/or deformation rates (internal rock property) remain a valid parameter. The MAW widens (Fig. 1) and is more actively deforming eastward, which is consistent with increased material accretion eastward. This may have two explanations. One is a larger volume of incoming sediments on the subducting plate, which could be due to the proximity of the Indus River delivering much sedimentary material near its delta. The other is that subduction is faster in the east than in the west, against the fully collided Zagros Mountains.

5-5- Possible drivers of morphometric variations along the Makran Accretionary Wedge

Invoking within-wedge deformation processes to explain the topographic characteristics does not answer the along-strike differences from west to east in terms of driving factors of tectonic activity. Several possibilities may explain the documented pattern of morphometric indices on the MAW. The spatial disparity may reflect changes in subduction rate or in dip angle of the slab, as suggested by (Ellouz-Zimmermann et al., 2007). There is not conclusive and independent evidence for this interpretation. Source parameters of instrumentally recorded earthquakes demonstrate a different depth distribution of focal mechanisms in western and eastern Makran, which has also been interpreted as segmentation of the subduction zone (Byrne et al., 1992). However, these plots do not impose altering the bulk shape and dip of the top-slab plate boundary (Fig. 19).

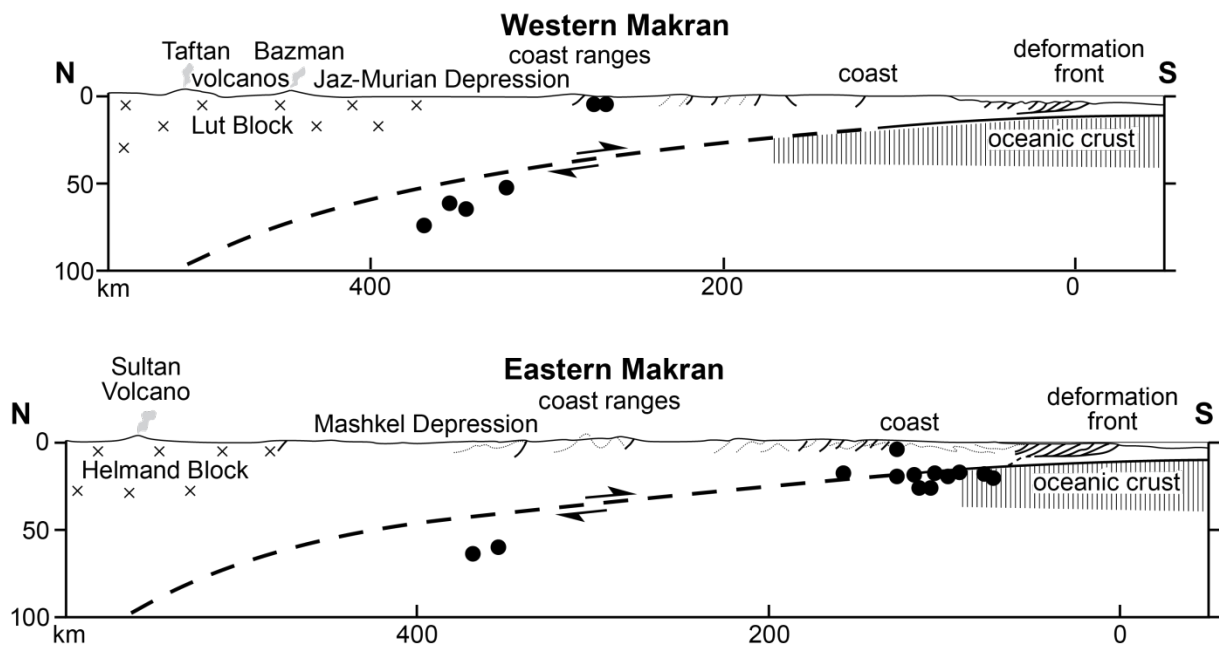


Fig. 19: Cross-sections across western and eastern Makran with main geologic features and projected focal mechanisms, modified after (Byrne et al., 1992).

In the absence of supporting and convincing tomographic and seismic evidence for slab segmentation beneath Makran (Dykstra and Birnie, 1979), changes of slab dip angle are no satisfactory the answer. We prefer to account for the general anticlockwise rotation of the Arabia plate with respect to Eurasia, around a vertical axis located somewhere in Kurdistan, as diagnosed from GPS measurements (Hatzfeld and Molnar, 2010). Such a rotation corroborates the increasing amount of plate convergence from 35.5-36.5 mm/a in the west to 40-42 mm/ in the east (DeMets et al., 2010; DeMets et al., 1990). This difference, albeit small, should be sufficient to introduce more material in the accreting wedge, and hence makes its eastern surface more unstable than the western one, as recorded in this geomorphological study. Faster convergence may increase coupling between the plates, but then remains the main cause of the tectonic difference.

5-6- Coupled erosion and deformation model

We applied the coupled erosion-deformation model developed by (Hilley & Strecker 2004) to interpret the along-strike variation of topography and structural geometry of the inland MAW. This model combines the mechanical properties of the wedge (defined by friction and pore-pressure ratios within the bulk wedge and along the bottom décollement) with erosional efficiency (incorporating basin hydrologic and erosional parameters) and the flux of incoming material. Assuming steady state, erosion on a Coulomb wedge close to its failure limit removes the same amount of material as that tectonically added to the wedge. This balance maintains in a self-similar manner the triangular cross-section of the wedge, and this time independence is expressed by:

$$\frac{vT}{K} = \frac{k_a^{hm} D^{hm+1} \cot^{hm+1} \beta \tan^n \alpha}{hm + 1}$$

(equation 7 of Hilley et al. 2004), where vT is the flux of accreted material, K the regional constant that expresses rock erodibility and climate (equation 3, Howard et al. 1994); k_a and h are the hydrologic constants of Hack's law (equation 1), m and n are two erosion exponents condensed in the concavity index θ of equation (2) (Whipple 2001); D (the depth to sole-out), α (surface slope) and β (dip of the wedge basal décollement) define the wedge geometry (e.g. Davis et al. 1983, Dahlen 1990).

We implemented the k_a and h values obtained from our geomorphic analysis to compare the western and eastern Makran wedge. Values of h do not change much. Therefore we counted it as a fixed parameter (~ 1.6) and were left with k_a as variable between 0.7 and 3.3. We choose lowest values of incision exponents ($m=1/3$ and $n=2/3$, Hilley & Strecker 2004) appropriate for arid regions.

The mechanical properties of the Makran wedge are not defined as justly as in other wedges such as Taiwan (e.g. Davis et al. 1983). We used friction coefficients of 1.1 in the wedge, and 0.85 along the basal décollement, in accordance with Byerlee law under low confining pressure (Davis et al. 1983, Dahlen 1990). We used $\alpha=4.5^\circ$; $\beta=1^\circ$ for western and $\alpha=3^\circ$; $\beta=2^\circ$ for eastern Makran, according to the measured surface slope and inferred critical taper of ca 5° . To take into account large uncertainties depth to the base D derived from cross sections based on field data and seismic profiles projected and extended from offshore information place, we varied this parameter from 20 km (Burg et al. 2012) to 5 km to account for possibly very flat subduction (a dip angle of 2° for White, 1982). This allowed testing how much this geometric parameter affects results.

Calculations yield similar vT/K ratios for western and eastern Makran, with values close to 8 for $D=20$ km and close to 7 for $D=5$ km (Fig. 20). Since K should be the constant reflecting the same climatic conditions over the whole MAW and there is no evidence for a change in thickness of incoming sediments (T of about 7km, Grando and McClay, 2007, we interpret the plot in two ways. Either the plot is significant, and the pore pressure ratio is higher in eastern Makran (ca 0.9) than in western Makran (ca 0.8, Fig. 20), or the difference reflects different m and n values, which would reflect differences in the hydrologic characteristics of

the catchments. Existing information does not permit discrimination of these two possibilities.

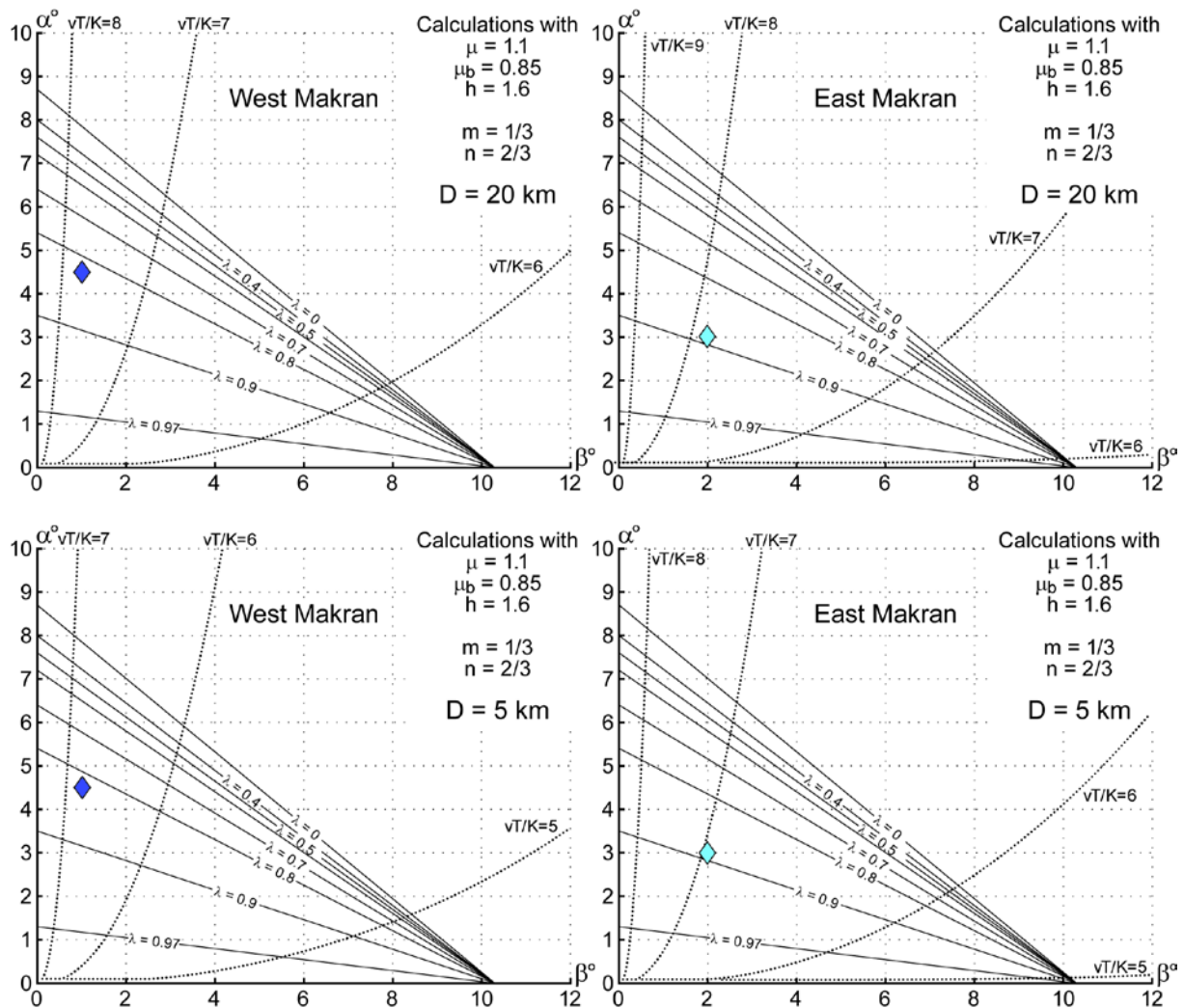


Fig. 20: Calculated relationships between mechanical properties and erosional parameters for the onshore western and eastern Makran accretionary wedge, assuming that erosion removes by from the wedge the same amount of material than tectonically accreted (equations from Hilley and Strecker, 2004). Solid black lines show mechanical stability limits corresponding to the critical taper under the given friction coefficients μ and μ_b and pore pressure ratios λ . Dotted curves: contour base 10 logarithm of vT/K to produce a wedge on which there erosionally removed material balances tectonically accreted material.

6-Conclusion

We carried out the first systematic assessment of the landscape response to the present-day deformation of the onshore Makran accretionary wedge installed in the Oman subduction zone. The morphologic study of the five main catchments draining this wedge, away from the bounding transform fault systems, reveals E-W variations in topographic relief, channel concavity, steepness and incision. Relief in the swath profiles shows fluvial dissection of an uplifted topography and therefore indicates general rock uplift. The comparison of measured channel profiles with modelled equilibrium profiles assuming constant uplift rate

and erodibility shows that the major rivers in the western studied Makran conform to the expectation of a smoothly concave profile, which is taken as symptomatic for morphological equilibrium along most of their course (Sedij, Fanuj). In contrast, the longitudinal profiles of the rivers draining the eastern catchments (Nikshahr, Pishin, Torbat) significantly deviate from a smooth, concave form; they are characterised by out of equilibrium channel segments along which surface uplift rates are locally more rapid than the constant, regional rate of 0.3 mm/a assumed for channel modelling.

These large-scale, spatial changes, extracted over a lithologically homogeneous terrain with insignificant climatic gradient, are interpreted as lateral and rather progressive changes in surface uplift rates. Rivers in western Makran achieved steady-state equilibrium while the landscape and rivers in eastern Makran are still adjusting to a transient stage. Maps of channel slope show that highest values correspond to knickpoints and knickzones on active faults and folds. The onshore MAW is a good example where river profiling in itself is a proxy for identifying spatial patterns of rock uplift.

We emphasize that we did not include to this study rivers on the western and eastern extremities of Makran, where deformation due to the adjacent Minab-Zendan and Ornach-Nal transcurrent faults interferes with deformation of the accretionary wedge. Thus, our results concern active tectonic motions related to the subduction-related accretionary wedge. The regional variation we have documented concurs with seismicity data, which also distinguish western from eastern Makran as seismically quiet and seismically active zones, respectively. Since the MAW is everywhere under similar climatic conditions and everywhere exposes similar lithologies, we contend that the difference in surface uplift expresses slightly different rates of plate convergence. This is consistent also with the critical wedge theory, which predicts wider, lower taper wedges for higher convergence rates.

Acknowledgements

This work was supported by the ETH project No. 0-20481-08 and the Swiss National Fond project No. 2-77644-09. Administrative and logistical support by the Geological Survey of Iran is sincerely acknowledged. We thank Mohamad Faridi for efficient help in the field.

Chapter III

Correlation of fluvial terraces and temporal steady-state incision on the onshore Makran accretionary wedge in SE Iran: Insight from channel profiles and ^{10}Be exposure dating of strath terraces

Key words: ^{10}Be dating, fluvial terraces, Pleistocene, surface uplift, Makran

Abstract

We describe and summarize the geomorphology of fluvial terraces along the four major rivers draining the central, onshore Makran accretionary wedge, in Iran, and describe uplifted marine terraces on the coast of this region. Thirty five strath terraces have been dated using *in situ* produced cosmogenic ^{10}Be concentrations from surfaces and depth profiles. These new measurements reveal abandonment ages between ~ 13 and 379 ka. The age distribution allows determining the chronology of terrace levels and establishing regional correlations between deposits of the four studied rivers. They also provide evidence for time and spatial variations in incision rate and help elucidating tectonic versus climatic controls on their formation. The comparison of incision rates in the adjacent catchments enables distinguishing between a relatively moderate regional, “background” incision rate of $\text{ca } 0.3 \pm 0.04 \text{ mm/a}$ and higher, local incision/uplift ($0.8\text{-}1 \pm 0.1 \text{ mm/a}$) rates. The pattern of incision rates portrays spatial changes where field observation recognizes localized tectonic activity. We also dated, using ^{14}C in shells, four uplifted marine terraces on the coast of the study area. Comparing incision rates derived from strath terraces (0.3 mm/a) with published and new uplift estimates from marine terraces (0.2 mm/a) reveals that fluvial rivers responded to a regional, long-term incision and surface uplift pattern. The homogeneity of the background rate reflects regular wedge growth likely due to tectonic underplating. Locally high incision rates delineate active faults and folds.

1. Introduction

The spatial and temporal distribution of deformation is a central issue to characterize the bulk, natural rheology of major tectonic units. This information is in turn requested to refine our numerical models of geodynamic processes. In this endeavour, tectonic geomorphology has proven to be a very efficient approach, revealing the direct response of surface processes to active tectonic processes (e.g. Burbank & Anderson 2001, Bull 2009). Many applications in active mountain regions have established the relevance of such studies (e.g. Hartshorn et al. 2002, Montgomery & Brandon 2002, Friend et al. 2009). In this work, we extend the techniques of tectonic geomorphology to refine our understanding of the large-scale dynamics of the active accretionary wedge of Makran, in southern Iran and, by extension, of other active and ancient accretionary wedges.

Several studies have shown that incision and aggradation in fluvial networks are dictated by three main factors: (1) base level change (Blum & Törnqvist 2000, Blum et al. 2001), (2) climate oscillations (Molnar et al. 1994) and (3) tectonic activity (e.g. Seeber & Gornitz 1983, Burbank et al. 1994). However, since these factors generally interplay in a complex manner, it remains difficult to decipher their respective roles on identified alterations of river networks. Several sets of fluvial terraces are preserved along all the main valleys of Makran rivers. They offer opportunity to build regional correlations and long-term incision/uplift investigations. This study reports and compares new geochronological data obtained from four adjacent catchments that drain a wide area of the onshore Makran accretionary wedge. Results permit to identify regional patterns of landscape response to tectonic and/or climate changes. We employed ^{10}Be cosmogenic nuclide techniques because the investigated sites did not offer suitable samples for Optically Stimulated Luminescence dating and other datable material such as ash layers and organic material could not be found. The analytical work complementing field observations allows regional correlations and more robust interpretation of the various factors involved in the formation of the studied terraces. We also used dated strath terraces as geomorphic reference markers (Lavé & Avouac 2001, Pazzaglia & Brandon 2001) in combination with river longitudinal profiles to extract and determine local surface uplift/incision (Snyder et al. 2000, Whipple et al. 2000, Kirby & Whipple 2001, Whipple, 2004). The record allows documenting time-averaged uplift/incision rates through different glacial–interglacial cycles during Quaternary times.

2. Setting

2.1. Geological setting

The Makran accretionary wedge was installed in the subduction zone between the Arabian plate, to the south, and the Eurasian plate, to the north. This north-dipping subduction is thought to have initiated in the Late Cretaceous (e.g. Farhoudi 1977, McCall, 1997). The wedge is the largest exposed on Earth, extending more than 1000 km from the Minab Fault Zone to the west, in Iran, to the Chaman Fault Zone to the east, in Pakistan (Fig. 1). The high incoming sediment thickness (~ 7 km) and a low taper angle of $\sim 3^\circ$ (Davis et al. 1983) are

exceptional characteristics of Makran wedge. Accepting the classical Coulomb wedge theory (Davis et al. 1983), the small taper suggests either a weak basal décollement or a high internal strength. In any case, the wedge should grow in a self-similar manner, combining frontal accretion, tectonic underplating and normal faulting, so that its long-term, bulk topography raises uniformly and steadily (Dahlen 1990).

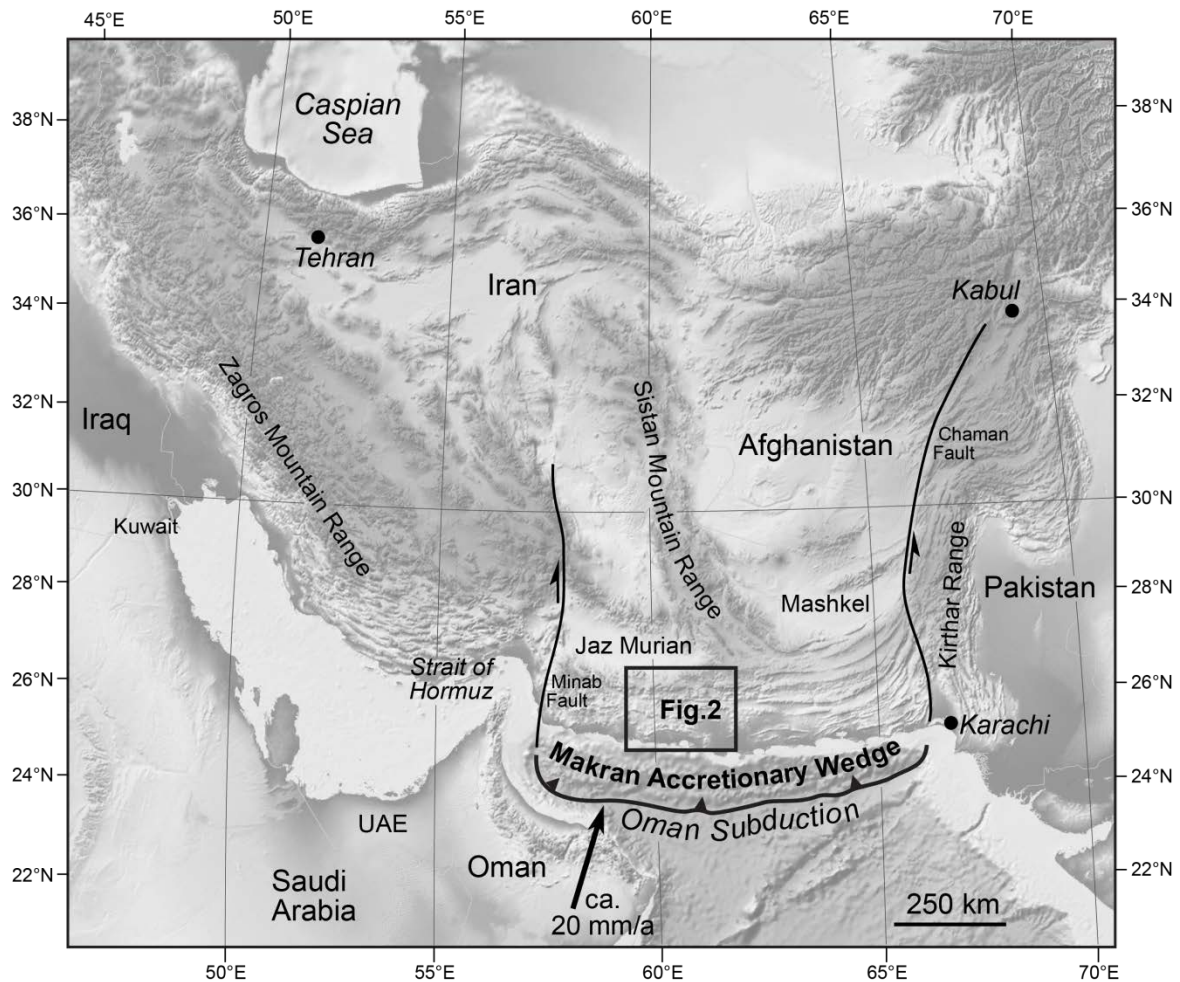


Fig. 1: Tectonic setting of the Makran subduction zone. Background: shaded relief map ETOPO1, <http://www.ngdc.noaa.gov/mgg/global/relief/ETOPO1>. The convergence arrow is the GPS convergence rate between Arabia and stable Eurasia after Vernant et al. (2004).

The studied part of Makran covers an about 150 km across and 250 km trench-parallel area of the exposed accretionary wedge, in SE Iran, away from the lateral, Minab and Chaman transform boundaries. Four tectono-stratigraphic units separated by major thrust faults have been distinguished in the bedrock of the study area (Fig. 2). From the north to the south, i.e. from the structural top to bottom, these units are: North Makran, Inner Makran, Outer Makran and Coastal Makran (Dolati 2010, Burg et al. 2012). The main fault system is comprised of flat-and-ramp thrusts, which reflect a thin-skinned fold-and-thrust belt over blind décollement surfaces (Burg et al. 2012). The Bashakerd Thrust is the tectonic boundary between North Makran, which exposes ophiolite-bearing “coloured mélanges” and deep-sea sediments and volcanics (McCall 2002, Dolati 2010), and the turbidite-dominated Inner

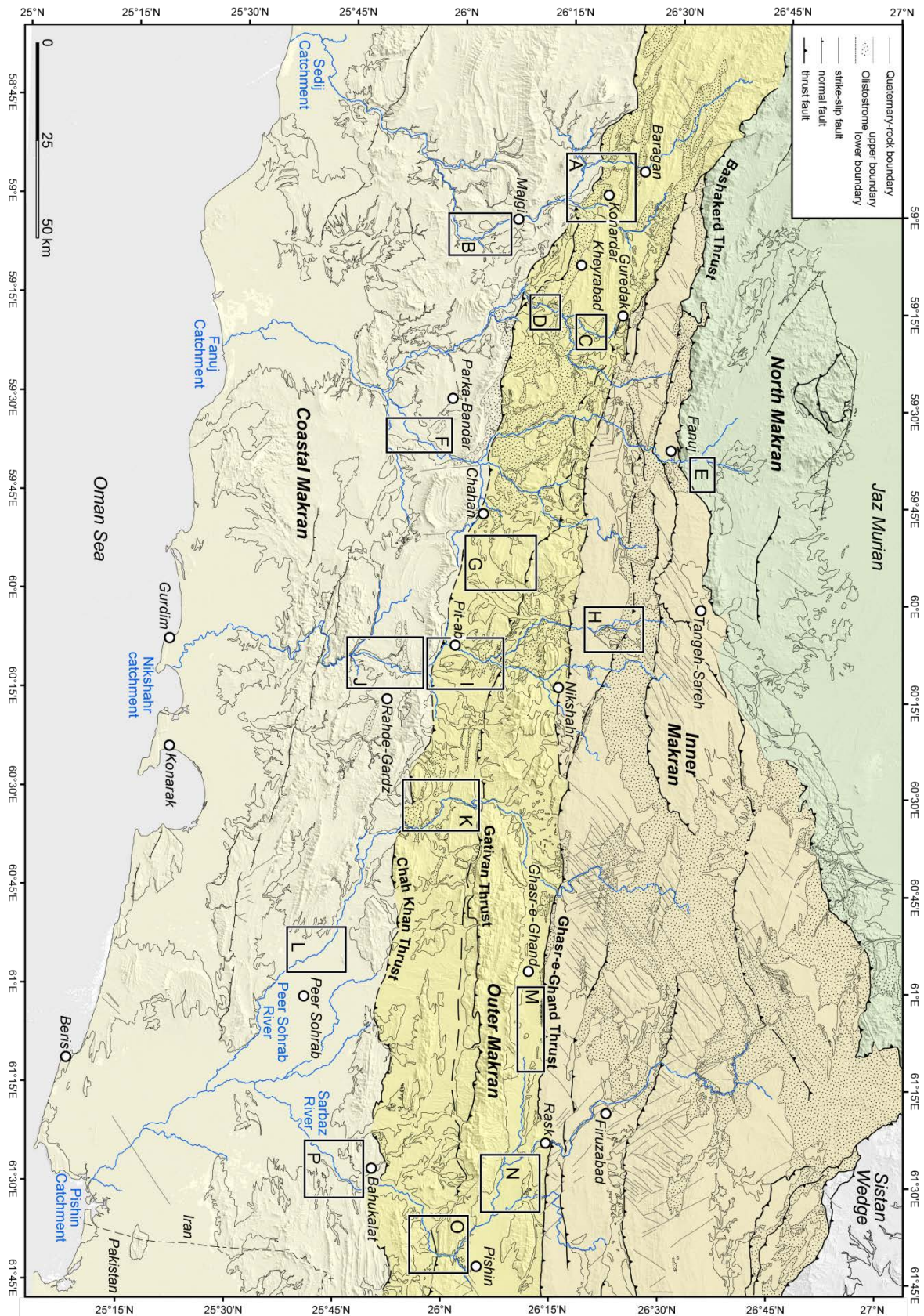


Fig. 2: Simplified geological map of the central Makran fold-and-thrust belt in Iran (extended from Burg et al. 2012). The four litho-tectonic units are: Green, North Makran of mostly Cretaceous rocks; Brown Inner Makran of mostly Eocene to Middle Miocene rocks; Yellow Outer Makran of mostly Upper Oligocene to Middle – Miocene rocks; Light-beige Coastal Makran of mostly Upper Miocene and Plio-Pleistocene sediments. Lettered boxes indicate the studied sites described in text. White circles: city and villages cited in text.

Makran. Inner, Outer and Coastal Makran include Eocene to Recent sediments deformed in the fold –and –thrust belt. Folding and thrusting were active before, and reactivated after the emplacement of a Tortonian (ca 10 Ma) olistostrome (Burg et al. 2008). Folding and thrusting caused Middle Miocene to Pliocene growth structures. Most of the deformation has then been shifted to present-day submarine wedge, perhaps as a consequence of the load brought by the olistostrome (Smit et al. 2010). However, deformation did not stop onshore so that some of the studied terraces have been folded in the last 120 ka (Haghipour et al. 2012). We further constrain the Quaternary deformation of the Makran wedge with this study dedicated at surface uplift, as a proxy of the internal deformation of the wedge, and subsequent incision rate. The only uplift rate reported for Makran were derived from marine terraces dated with Uranium series and ^{14}C (Falcon 1975, Vita-Finzi 1975, Page et al. 1979, Snead 1992). Mean uplift of the coast was estimated at 0.2 mm/a in the Pleistocene and 2mm/a in the Holocene.

2.2. Seismicity – Active tectonics

Geodetic data at the longitude of the Gulf of Oman document a roughly N-S convergence rate of ca 2 cm/a (Vernant et al. 2004, Masson et al. 2005). Compared to other convergence zones (e.g. Tonga subduction zone, 16 cm/a, Bevis et al. 1995, Sumatra Subduction Zone, 6.5 cm/a, Gahalaut & Catherine 2006), Makran is a slow subduction zone, often compared to the Cascadia Subduction Zone (3.5 cm/a, Wong 2005). Although the region experienced large earthquake such as the $M_w = 8.1$, 1945 event (Jackson & McKenzie 1984, Byrne et al. 1992), the present day Makran is also, like the Cascadia, seismically quiet. Byrne et al. (1992) suggested that high pore pressure of unconsolidated and water saturated sediments causes this low seismicity. The low taper would reflect these overpressured, low-friction sediments (Smit et al. 2010). Mud volcanoes along the Iranian and Pakistani coasts of Makran substantiate the concept of overpressured shale layers at depths.

2.3. Climate setting

The frequency, direction and timing of Quaternary climate changes in Iran are sparsely documented, compared to the extensive literature on other parts of the world. Evidence of Pleistocene and Holocene climate fluctuations in Iran are based on several sources, such as lake sediment (e.g. van Zeist & Wright 1963, Djamali et al. 2008) glacial moraines (e.g. Kuhle 2008, Kehl 2009) alluvial sediments (Vita - Finzi 1969) and fluvial and marine terraces (Degens & Paluska 1979, Regard et al., 2006). The present climate of Makran is arid to semi-arid with a mean annual precipitation of 113 mm/a. The dryness is caused by north-easterly winds that mainly transport dry air-masses. It is further enhanced by the mountain ranges in the north (Alborz) and SW (Zagros), which prevent north-westerly and westerly depressions from the Caspian and Mediterranean Sea from entering the Iranian Plateau (Kehl 2009) The modern climate around the Arabian Sea is governed by two main sources of monsoon winds: the summer monsoon and the winter monsoon (Fig. 3). The Inter Tropical Convergence Zone (ITCZ) reaches western Makran (Fig. 3) and is beyond the Indian monsoon domain (Gasse 2000, Fleitmann et al. 2007). The main rain season is from December to February.

The present day water discharge in the four studied catchments is mainly derived from heavy and short winter rain falls engendering flash floods and inundating the coastal plain.

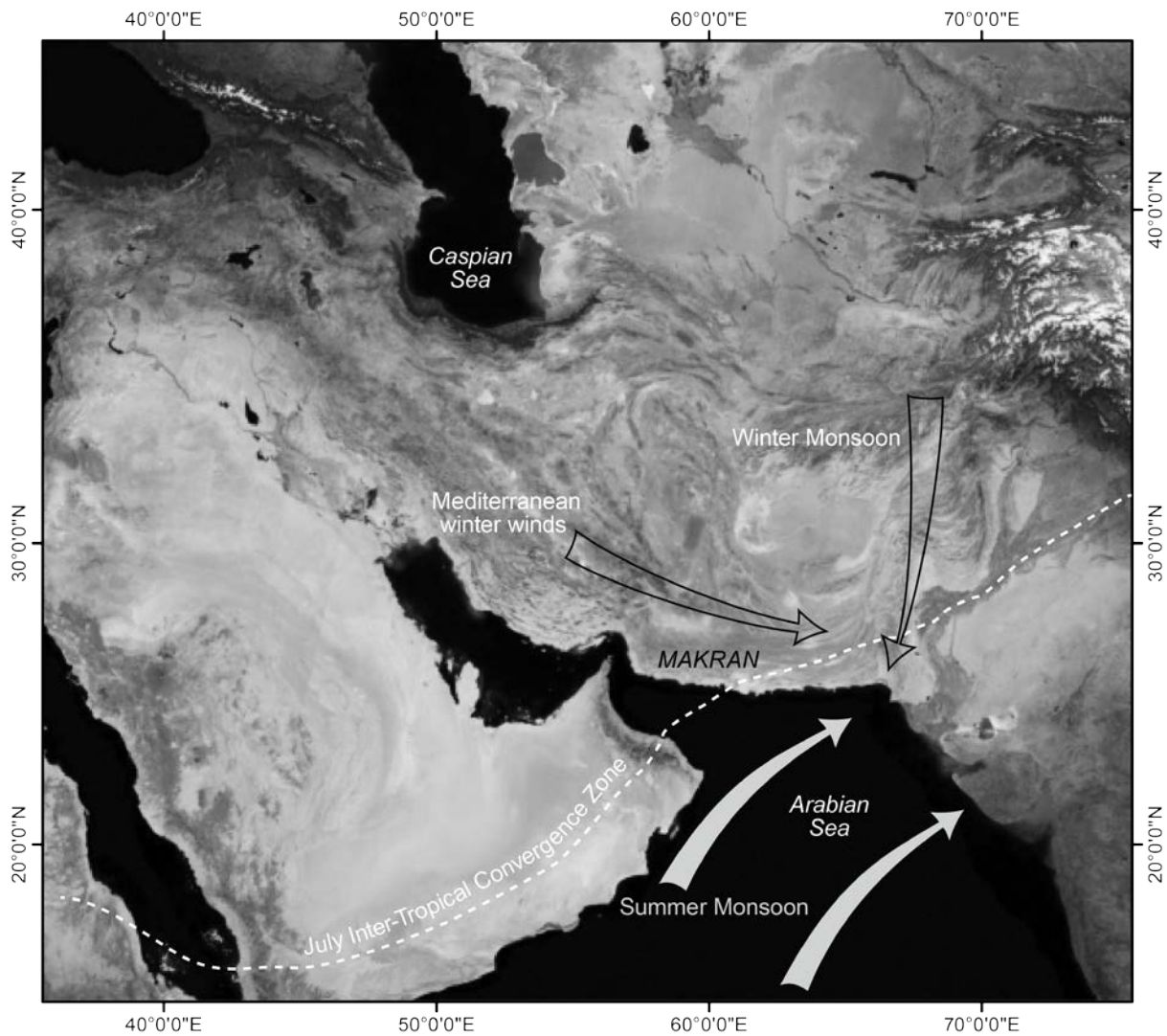


Fig.3: Simplified pattern of the present-day climate in Arabian Sea and adjacent regions. Data compiled from Krishnamurti & Ardanuy (1980) Gasse (2000) Fleitmann et al. (2007) and Kehl (2009).

3. Methods

3.1. Field observation and surveying

Fluvial terraces in Makran had not been studied beyond reconnaissance surveys (Falcon 1975, McCall et al. 1982a). We mapped fluvial terraces in four major and contiguous catchments, all flowing southward, nearly perpendicular to the strike of the major structures (Fig. 2), down to the Oman Sea. Mapping of the terraces developed parallel to the main trunks and important tributaries was based on aerial photographs (scale: 1:50:000) using ERDAS software, satellite images and ASTER Digital Elevation Model (G-DEM) with 1 arcsec (~30 m) resolution. Terraces were mapped and classified in sequence according to their relative elevation with respect to the local stream, in increasing order from T1 the locally

highest level. Field checking was focused on important and critical geomorphologic features identified on remote images. The river segments between these critical points were surveyed in a less detailed manner, unless unexpected features were discovered. A handheld Garmin GPS with barometric altimeter was systematically used to measure the elevation of strath terraces and modern channel beds. We admit a 4m uncertainty for the absolute measured elevations, but claim almost no uncertainty for elevation differences, which were measured within the time needed to walk up, and checked walking down, to elude possible atmospheric pressure variations occurring over longer periods. The thickness of the alluvial cover was measured with a tape. Fieldwork was also aimed at identifying most reliable sampling sites for dating and spatial correlation. Topographic shielding was measured with high precision compass and clinometer (1° error for both measurements). Both aggradational (fill) and degradational (strath) terraces occur along the four river networks. Although strath terraces are dominant, we also dated fill terraces for a complete record of river incision. The description of sampled surface, sample rock types, topographic shielding and GPS positions are given in Table 1.

3.2. Channel steepness indices

The elevation versus distance profile of river courses depends on several variables such as discharge, debris size, hydrologic regime, flow velocity, channel width, bedrock lithology, etc. Over time, the rivers achieve a dynamic equilibrium with their environment, i.e. the amount of sediment they can transport away balances the amount of material their drainage areas deliver. Under some simplifications, which impel constant, equilibrium values to input/output variables, longitudinal profiles of “graded” fluvial channels tend to follow a smooth, concave upward power-law function (Hack 1957, Smith et al. 2000). This empirical approach, based on stream power considerations, professes that the local channel slope (S) is inversely proportional to the upstream drainage area (A) of the river to the power of an exponent θ called the concavity index (Flint 1974). The popularized “Flint’s law” expresses this model relationship:

$$S = K_S A^{-\theta} \quad (1)$$

where the coefficient K_S is the channel steepness index. θ is a critical exponent because it defines the shape of the length profile of detachment-limited channels, those where vertical abrasion and plucking can equal (or overcome) tectonic uplift of the bedrock or base level fall (Hancock et al. 1998, Whipple & Tucker 1999). Long-term equilibrium between erosion rate and rock uplift rate is represented by θ best-fit values ranging between 0.25 and 0.6. The average value of $\theta = 1/2$ is accepted to be pragmatically realistic in modelling fluvial erosion, provided climatic conditions and basement erodibility are uniform over the whole studied drainage system (e.g. Kirby & Whipple 2001, Tucker & Whipple 2002, Wobus et al. 2006). Following the prediction that channel concavity is independent of rock uplift rate for landscapes of uniform lithological content submitted to a uniform climate, the K_S value stands as a convenient and valuable metric index to localize tectonic or lithological

anomalies (e.g. Merritts & Vincent 1989). The steepness index, however, does not quantify uplift rates.

Table 1: Sample information and measured ^{10}Be concentration.

Sample ID	Local Terrace Name	Latitude <i>N</i> (<i>D.D</i>)	Longitude <i>E</i> (<i>D.D</i>)	Elevation (<i>m.a.s.l.</i>)	Depth cm	[Be-10]blank corrected * (10^5 atoms g^{-1})	\pm 10^5 atoms g^{-1}	Topographic shielding	Standard
Sedij Catchment									
Q-Mak-10-36	K-T1	26.3191	58.8900	411	0	4.480	0.20	1	07KNSTD
Q-Mak-10-37	K-T2	26.3161	58.8838	388	0	1.134	0.06	1	07KNSTD
Q-Mak-10-38	B-T2	26.4058	58.8902	471	0	0.998	0.05	1	07KNSTD
Q-Mak-09-41	M-T1	26.0850	59.0622	241	0	4.373	0.19	1	07KNSTD
Q-Mak-09-43	modern channel	26.0908	59.0443	199	0	0.961	0.09	0	07KNSTD
Q-Mak-11-25	modern channel	26.3449	58.8822	380	0	0.746	0.05	0	07KNSTD
Fanuj Catchment									
Q-Mak-09-49	G-T2	26.3188	59.3258	417	0	2.940	0.14	1	07KNSTD
Q-Mak-09-45	G-T5	26.3130	59.3202	373	0	0.636	0.07	1	07KNSTD
Q-Mak-10-40	Kh-T1	26.1966	59.2669	300	0	3.947	0.17	1	07KNSTD
Q-Mak-09-56	F-T1	26.6088	59.7636	941	0	8.550	0.33	1	07KNSTD
Q-Mak-09-57	F-T2	26.6089	59.7615	931	0	1.120	0.06	1	07KNSTD
Q-Mak-09-10	B-T1	25.9817	59.6371	180	0	2.798	0.33	1	07KNSTD
Q-Mak-11-23	Pb-T1	25.8836	59.5755	130	0	3.488	0.11	1	07KNSTD
Q-Mak-10-44	Ch-T1	26.1593	60.0249	464	0	8.644	0.20	1	07KNSTD
Q-Mak-10-45	Ch-T2	26.1114	59.9837	369	0	2.649	0.10	1	07KNSTD
Q-Mak-09-44	modern channel	26.3125	59.3188	370	0	0.541	0.05	0	07KNSTD
Q-Mak-11-24	modern channel	25.8912	59.5748	107	0	0.520	0.05	0	07KNSTD
Nikshahr Catchment									
Q-Mak-10-28	Rz-T1	25.8350	60.1813	240	0	5.801	0.20	1	07KNSTD
Q-Mak-10-31	Rz-T4	25.8413	60.1627	144	0	2.010	0.13	1	07KNSTD
Q-Mak-10-56	Pt-T4	26.0330	60.1366	273	0	0.949	0.04	1	07KNSTD
Q-Mak-10-51	depth-profile	26.0330	60.1366	273	20 \pm 10	0.710	0.03	—	07KNSTD
Q-Mak-10-53	depth-profile	26.0330	60.1366	273	50 \pm 10	0.416	0.03	—	07KNSTD
Q-Mak-10-54	depth-profile	26.0330	60.1366	273	140 \pm 10	0.420	0.05	—	07KNSTD
Q-Mak-10-55	depth-profile	26.0330	60.1366	273	180 \pm 10	0.576	0.06	—	07KNSTD
Q-Mak-11-21	Pt-T1	25.9975	60.1438	281	0	5.858	0.20	1	07KNSTD
Q-Mak-11-15	Pt-T2	26.0425	60.1380	302	0	3.993	0.18	1	07KNSTD
Q-Mak-11-13	Pt-T3	25.9621	60.1624	220	0	1.835	0.07	—	07KNSTD
Q-Mak-11-12	Sh-T1	26.3707	60.1131	759	0	6.966	0.33	1	07KNSTD
Q-Mak-10-50	modern channel	25.8327	60.1657	133	0	0.570	0.04	—	07KNSTD
Q-Mak-11-16	modern channel	26.0320	60.1399	267	0	1.280	0.08	—	07KNSTD
Q-Mak-11-14	modern channel	25.8491	60.1686	144	0	1.949	0.07	0	07KNSTD
Pishin catchment									
Q-Mak-11-01	Bh-T1	25.9336	61.5513	135	0	3.988	0.15	1	07KNSTD
Q-Mak-11-02	Bh-T2	25.9341	61.5477	116	0	1.376	0.07	1	07KNSTD
Q-Mak-09-62	P-T1	25.9824	61.7008	265	0	7.290	0.19	1	07KNSTD
Q-Mak-09-32	P-T3	25.9641	61.6816	209	0	4.033	0.10	1	07KNSTD
Q-Mak-10-22	P-T4	25.9543	61.5543	117	0	1.038	0.09	1	07KNSTD
Q-Mak-10-19	R-T1	26.1393	61.5819	321	0	16.300	0.93	1	07KNSTD
Q-Mak-11-09	R-T2	26.1756	61.4638	391	0	10.245	0.30	1	07KNSTD
Q-Mak-10-14	R-T3	26.1336	61.5569	283	0	6.182	0.30	1	07KNSTD
Q-Mak-10-15	depth-profile	26.1336	61.5569	283	40 \pm 10	3.514	0.14	0	07KNSTD
Q-Mak-10-16	depth-profile	26.1336	61.5569	283	80 \pm 10	2.748	0.11	0	07KNSTD
Q-Mak-10-17	depth-profile	26.1336	61.5569	283	120 \pm 10	1.837	0.10	0	07KNSTD
Q-Mak-10-18	depth-profile	26.1336	61.5569	283	190 \pm 10	1.672	0.07	0	07KNSTD
Q-Mak-10-20	R-T3	26.1348	61.5835	290	0	5.400	0.15	1	07KNSTD
Q-Mak-10-03	F-T1	26.2973	61.3936	558	0	11.801	0.40	1	07KNSTD
Q-Mak-10-23	G-T1	26.1911	61.0767	545	0	7.435	0.28	1	07KNSTD
Q-Mak-10-46	Z-T1	26.0494	60.5197	327	0	2.216	0.08	1	07KNSTD
Q-Mak-10-47	Z-T2	26.0447	60.5247	264	0	1.610	0.06	1	07KNSTD
Q-Mak-11-18	Pr-T1	25.7561	60.7930	117	0	6.759	0.74	1	07KNSTD
Q-Mak-11-19	pr-T2	25.7505	60.8163	84	0	4.801	0.14	1	07KNSTD
Q-Mak-11-11	modern-channel	26.2800	61.4231	444	0	1.540	0.07	0	07KNSTD
Q-Mak-11-06	modern channel	25.9911	61.6806	152	0	0.963	0.05	0	07KNSTD
Q-Mak-11-03	modern-channel	25.9340	61.5470	97	0	0.828	0.07	0	07KNSTD
Q-Mak-11-20	modern-channel	25.7600	60.7889	54	0	1.253	0.05	0	07KNSTD
Q-Mak-10-48	modern channel	26.0458	60.5266	245	0	2.162	0.09	0	07KNSTD
Q-Mak-12-2b	marine terrace	25.351	60.301	77.000	0.000	2.800	0.09	1	07KNSTD

All samples analyzed for $^{10}\text{Be}/^9\text{Be}$ ratio at the ETH Zurich Tandem Accelerator Mass Spectrometry (AMS) facility (Kubik & Christl 2010). Quoted uncertainties are the 1σ internal error. A mean blank $^{10}\text{Be}/^9\text{Be} = 0.004 \times 10^{12}$ was used for correction.

In practice, one extracts a normalized channel steepness index using a reference concavity θ_{ref} to be able comparing relative changes in non-linear profiles of different channels (Sklar & Dietrich 1998, Wobus et al. 2006). Reformulating equation 1, its normalized form is:

$$S = K_{S_n} A^{-\theta_{\text{ref}}} \quad (2)$$

in which the normalized channel steepness index K_{S_n} is a measure of the rock uplift rate in areas with steady state landscape (e.g. Snyder et al. 2000, Kirby & Whipple 2001, Hilley & Arrowsmith 2008). Applying this equation generates ideal long profiles to which actual river profiles can be paralleled. Deviations between ideal, modelled profiles and actual, measured profiles are diagnostic for dynamic disequilibrium between the river and its environment. Field observations in departing river segments provide explanations to decide whether tectonic uplift or subsidence, changes in rock erodibility or base level, climate or other environmental changes are responsible for profile divergence. For this study, we followed the methodology provided by (Wobus et al. 2006) and used the freely available set of Matlab and ArcGIS scripts ([http:// www.geomorphtools.org](http://www.geomorphtools.org)) to calculate K_{S_n} for the studied river networks.

3.3. Cosmogenic nuclide dating and sampling (^{10}Be)

No fluvial terrace in Makran had been directly dated. Their lithological content (essentially mixed pebbles and coarse gravel) and the lack of datable and correlatable material such as sand or silt lenses, ash layers and organic matter restricted dating possibilities to Terrestrial Cosmogenic Nuclides (TCN). The physics fundamentals of this method have been developed in several publications. ^{10}Be and ^{26}Al are produced from the interaction of secondary cosmic rays with Si and O in quartz, at and near the Earth surface (e.g. Lal 1991, Gosse & Phillips 2001). In Makran, the absence of bioturbation (including human occupation), soil development and overbank deposits on top of most terraces makes the surface exposure dating reliable. We selected 35 samples from paved terrace surfaces along six rivers of the four investigated catchments (Fig. 4), and dated them using the amalgamation method (Anderson et al. 1996, Repka et al. 1997). Dating the exposed surface of single clasts is an alternative method, taking the youngest absolute age as the closest estimate of the age of the depositional surface (Frankel et al. 2007, Vassallo et al. 2011). However, ^{10}Be measurements of single clast surfaces may strongly vary from clast to clast, depending on several geologic factors (e.g. Owen et al. 2011). Consequently, the inferred age may be older or younger than the actual time of landform deposition, as much as for the amalgamation approach (Schmidt et al. 2011, Ivy-Ochs et al. 2012). In any case, the small, few centimetres size of clasts in Makran terraces is inappropriate for single clast analysis.

We collected more than 30, equal size (about 5 cm in diameter), resident-quartz-rich clasts (essentially pure crystalline quartz, likely from eroded veins, and chert) on the obviously undisturbed pavement at each sampling site. The gathered clasts were crushed and sieved to a grain size of 0.25-0.7 mm. Purified quartz was physically extracted applying magnetic

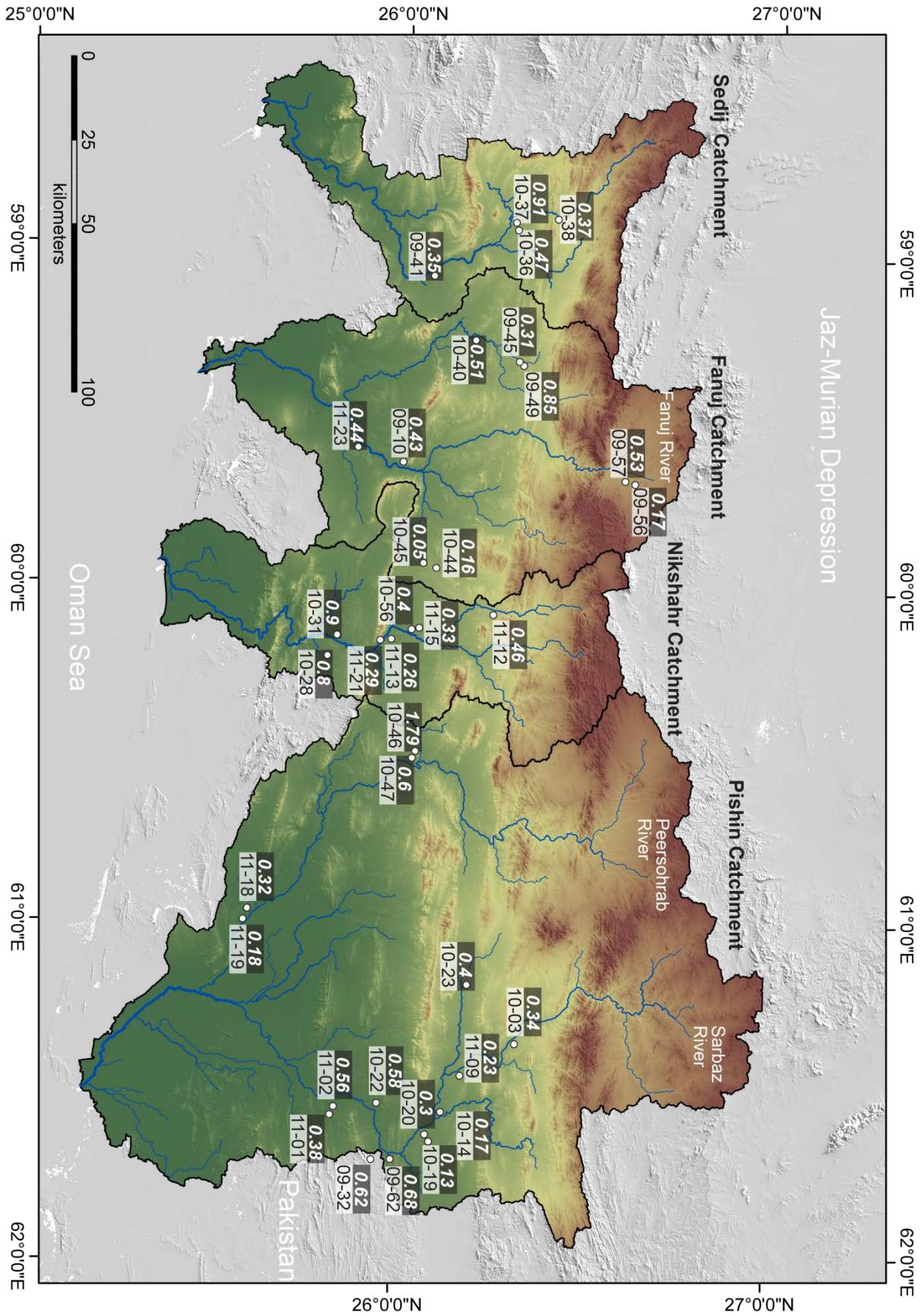


Fig. 4: Shaded relief map (Aster GDEM Version1, NASA) showing the studied catchments in Iran. Dark boxes with italic numbers indicate local incision rates. Light boxes with black numbers are Q-Mak- sample ID reported in Table 2. White dots are sample locations.

and/or heavy liquid separation methods and chemically purified using HF 40 % (e.g. Kohl & Nishiizumi 1992, Bierman & Nichols 2004). A known amount of ^9Be carrier was added to the pure quartz, which was dissolved in concentrated hydrofluoric %40 (HF) and nitric (HNO_3) acids. To extract $\text{Be}(\text{OH})_2$, samples passed through anion and cation exchange columns along with chemical blanks, following the preparation procedure presented by Ochs & Ivy-Ochs (1997).

The samples were analyzed for $^{10}\text{Be}/^9\text{Be}$ ratio at the ETH Zurich Tandem Accelerator Mass Spectrometry (AMS) facility (Kubik & Christi 2010). All $^{10}\text{Be}/^9\text{Be}$ ratios were normalized to the ICN 01-5-1 AMS standard with a nominal value of $^{10}\text{Be}/^9\text{Be} = 28.1 \times 10^{-11}$ (Nishiizumi et al. 2007). The used ^{10}Be half-life is 1.387 ± 0.012 Ma (Chmeleff et al. 2010, Korschinek et al. 2010). Surface exposure ages were calculated using the CRONUS on-line age calculator, Version 2.2 (Balco et al. 2008). Aware of on-going debate and studies regarding geomagnetic corrections (Balco et al. 2009), no correction for the geomagnetic field variations was made. The result for standards, blank and model age calculation are given in the footnote of Tables 1 and 2. The measured shielding was negligible (inclination from sampling site $< 8^\circ$) in all directions, for all sites. Therefore, we did not correct our ages for topographic obstruction. Obviously for a desert like Makran, no vegetation shielding had to be considered either. The ages presented in result, discussion and figures are calculated using scaling schemes from Stone (2000) modified after Lal (1991).

All the ages reported in result section were calculated assuming no erosion / weathering and zero inheritance (Table 2). To overcome inheritance nuclide components, we sampled two depth profiles and twelve modern channels with the same quartz-rich lithologies as in adjacent sampling sites. Estimated values for surface erosion are based on surface condition of sampled terraces, depth profiles and $^{26}\text{Al}/^{10}\text{Be}$ measurements. The model ages corrected for inheritance and differing erosion rates are also given in Table 2.

Sample ID	Local Terrace Name	strath elevation (m.a.s.l)	Thickness m	River bed elevation (m)	Incision (m)	Minimum exposure age (ka)	Incision rate (mm/a)	model exposure age ¹ (ka)	Incision rate (mm/a)	model exposure age ² (ka)	Incision rate (mm/a)	
							erosion rate = 0	erosion rate = 0.5m/Ma		erosion rate = 1 m/Ma		
							inheritance = 0	corrected to inheritance		corrected to inheritance		
Sedji Catchment												
Q-Mak-10-36	K-T1	411	1.5	369	42±2	90 ± 9	0.47	78 ± 8	0.53	80 ± 8	0.52	
Q-Mak-10-37	K-T2	368	0.8	368	20±1	22 ± 2	0.91	7 ± 1	2.80	7 ± 1	2.80	
Q-Mak-10-38	B-T2	471	0.7	462	9±1	19 ± 1	0.47	4± 1	2.25	4 ± 1	2.25	
Q-Mak-09-41	M-T1	241	1	201	40±3	100 ± 10	0.50	80 ± 8	0.50	83 ± 9	0.48	
Fanuj Catchment												
Q-Mak-09-49	G-T2	417	1.5	366	51±1	59 ± 5	0.85	48 ± 5	1.06	49 ± 5	1.04	
Q-Mak-09-45	G-T5	373	3	369	4±0.5	13 ± 1	0.31	1 ± 1	4.00	1 ± 1	4	
Q-Mak-10-40	Kh-T1	300	1.3	256	44±1	86 ± 8	0.51	76 ± 8	0.58	80 ± 8	0.55	
Q-Mak-09-56	F-T1	941	2.7	921	20±3	119 ± 11	0.17	117 ± 12	0.17	124 ± 13	0.16	
Q-Mak-09-57	F-T2	931	3	923	8±3	15 ± 1	0.53	8 ± 1	1.00	8 ± 1	1	
Q-Mak-09-10	B-T1	180	0.9	151	29±0.5	67 ± 9	0.43	55 ± 9	0.53	57 ± 10	0.5	
Q-Mak-11-23	Pb-T1	130	2.5	92	38±1	87 ± 8	0.44	76 ± 7	0.50	78 ± 8	0.48	
Q-Mak-10-44	Ch-T1	464	1-3	438	26±4	174 ± 16	0.16	158 ± 16	0.16	169 ± 18	0.15	
Q-Mak-10-45	Ch-T2	369	2-4	366	3±0.2	55 ± 5	0.05	28 ± 3	0.11	28 ± 3	0.1	
Nikshahr Catchment												
Q-Mak-10-28	Rz-T1	240	1.5	132	106±2	135 ± 12	0.80	128 ± 13	0.84	135 ± 15	0.8	
Q-Mak-10-31	Rz-T4	144	2	99	45±0.8	49 ± 4	0.90	35 ± 3	1.28	36 ± 4	1.25	
Q-Mak-11-21	Pt-T1	281	1.7	242	39±1	132 ± 12	0.29	129 ± 13	0.26	137 ± 15	0.28	
Q-Mak-11-15	Pt-T2	302	2.1	273	29±1	87 ± 8	0.33	81 ± 8	0.36	84 ± 9	0.34	
Q-Mak-11-13	Pt-T3	220	2.3	209	11±0.3	42 ± 4	0.26	33 ± 3	0.33	34 ± 3	0.32	
Q-Mak-10-56	Pt-T4	273	3	265	8±2	20 ± 2	0.40	12 ± 1	0.66	12 ± 1	0.66	
Q-Mak-11-12	Sh-T1	759	1.8	708	51±1	110 ± 11	0.46	93 ± 10	0.55	97 ± 11	0.52	
Pishin catchment												
Q-Mak-11-01	Bh-T1	135	3	97	38±1	99 ± 9	0.38	81 ± 8	0.47	84 ± 9	0.45	
Q-Mak-11-02	Bh-T2	116	2.3	102	14±1	34 ± 3	0.40	13 ± 2	1.07	13 ± 2	1.07	
Q-Mak-09-62	P-T1	265	1	150	115±2	168 ± 15	0.68	154 ± 15	0.75	166 ± 18	0.69	
Q-Mak-09-32	P-T4	209	1.2	150	59±0.5	95 ± 8	0.62	74 ± 7	0.80	77 ± 7	0.76	
Q-Mak-10-22	P-T2	117	2	102	15±0.5	26 ± 3	0.58	5 ± 2	3.00	5 ± 2	3	
Q-Mak-10-19	R-T1	321	>30	254	67±5	379 ± 43	0.18	399 ± 56	0.17	506 ± 99	0.13	
Q-Mak-11-09	R-T2	391	4	341	50±2	217 ± 21	0.23	197 ± 21	0.25	217 ± 26	0.23	
Q-Mak-10-14	R-T3	283	15	260	23±3	139 ± 14	0.17	106 ± 12	0.22	113 ± 13	0.2	
Q-Mak-10-20	R-T5	290	9	254	36±2	120 ± 11	0.30	87 ± 8	0.41	90 ± 9	0.4	
Q-Mak-10-03	Fr-T1	558	5	483	75±2	222 ± 21	0.34	209 ± 23	0.36	231 ± 28	0.32	
Q-Mak-10-23	G-T1	545	7	522	23±4	138 ± 13	0.16	113 ± 12	0.20	119 ± 13	0.19	
Q-Mak-10-46	Z-T1	327	0.5	243	84±4	47 ± 4	1.79	21 ± 2	4.00	21 ± 2	4	
Q-Mak-10-47	Z-T2	264	0.6	243	21±3	35 ± 3	0.60	9 ± 1	2.33	9 ± 1	2.3	
Q-Mak-11-18	Pr-T1	117	3.2	61	56±2	174 ± 15	0.32	151 ± 26	0.37	162 ± 30	0.34	
Q-Mak-11-19	Pr-T2	84	1.8	61	23±2	125 ± 11	0.18	95 ± 9	0.24	99 ± 10	0.23	
Q-Mak-12-02	marine terrace	77	-	-	-	73 ± 6	-	41 ± 4	-	42 ± 4	-	

Table 2: Calculated exposure ages and incision rates for different catchments in Makran. 1 and 2: Model exposure ages corrected for inheritance and erosion rates. Standard atmosphere calculated using the CRONUS-Earth (Balco et al. 2008) Version 2.2. A constant production rate model and scaling scheme for spallation of (Lal 1991) and (Stone 2000). The used reference spallogenic ^{10}Be production rate of 4.49 ± 0.39 atom $\text{g}^{-1} \text{yr}^{-1}$ ($\pm 1\sigma$, SLHL) and muonogenic production after (Heisinger et al. 2002).

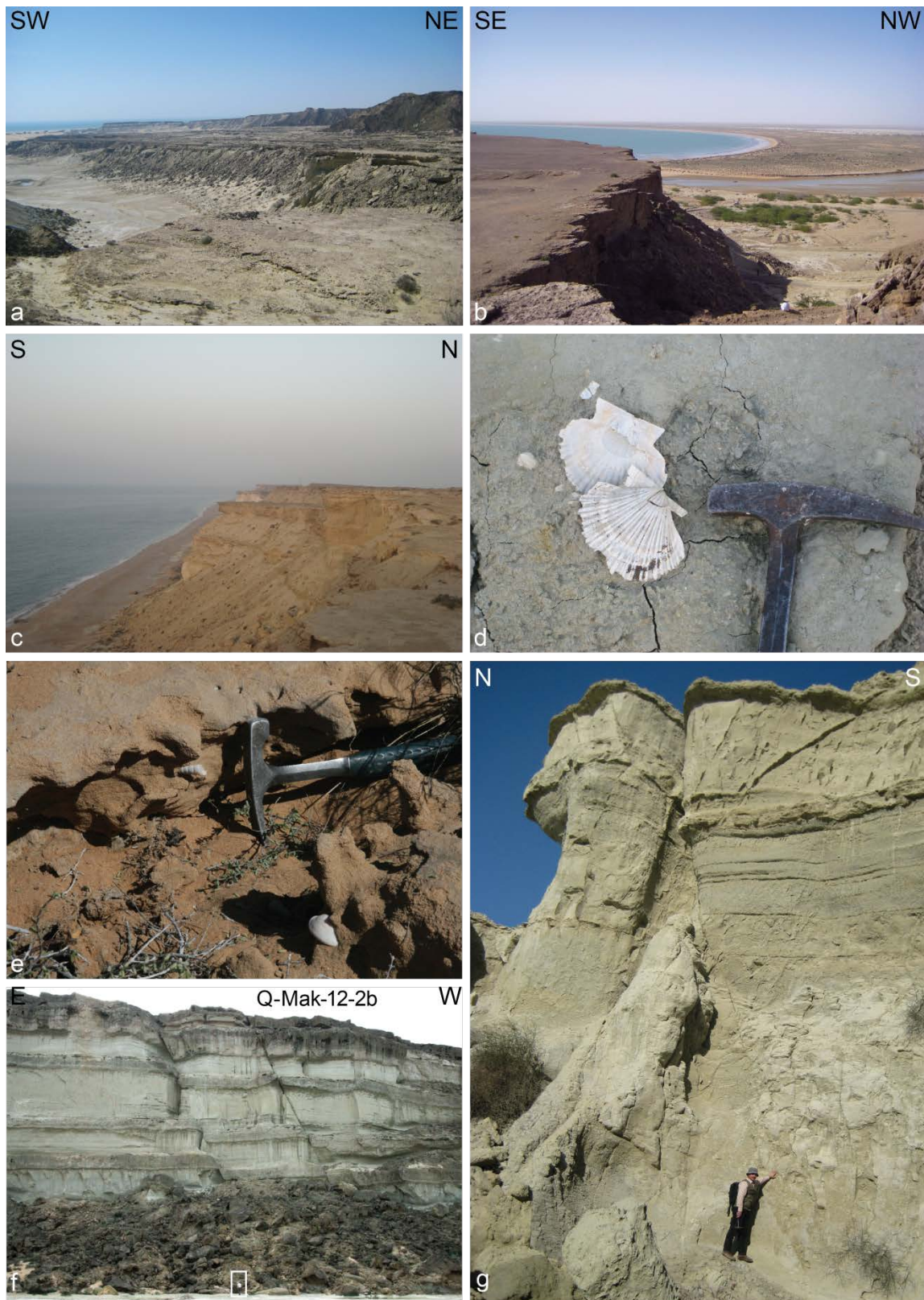


Fig. 5: Photographs of marine terraces along the coast of Makran; nearby cities in Fig. 2, excepted Sedij, just to the west of figure boundary. (a) Near Sedij (GPS: 25°32'59.18"N, 58°50'55.75"E). (b) Near Gurdim (GPS: 25°21'28.57"N, 60° 6'54.64"E). (c) between Chabahar and Beris (GPS: 25°14'10.20"N, 60°53'25.00"E). (d) Shells sampled for ^{14}C dating close to Sedij (GPS: 25°32'51.00"N; 58°50'40.00"E). (e) Shells sampled for ^{14}C dating near Beris (GPS: 25°11'44.90"N, 61° 5'11.50"E) (f) Normal faults cutting marine terraces at Konarak; (GPS: 25°21'10.63"N, 60°18'14.10"E); squared = human scale. (g) Normal fault pointed out by M. Faridi (scale) and cutting marine terraces close to Sedij (GPS: 25°35'26.90"N, 58°48'29.30"E).

3.4. Radiocarbon dating

Four shell samples were collected for ^{14}C dating from four marine terraces along the coast between Konarak and Beris (Table 3, Figs. 2 and 5). ^{14}C has been analyzed at the Laboratory of Ion Beam Physics at the ETH Zurich. After graphitization, the carbon isotopic ratios were measured using accelerator mass spectrometry (Synal et al. 2007). The ^{14}C ages were calibrated using the OxCal v. 4.1 open source program (http://c14.arch.ox.ac.uk/oxcalhelp/hlp_contents.html Bronk Ramsey 2009) and the IntCal09 calibration curve (Reimer et al. 2009). Scanning electron microscopy showed that the aragonite texture is well-preserved in the dated samples (Fig. 6).

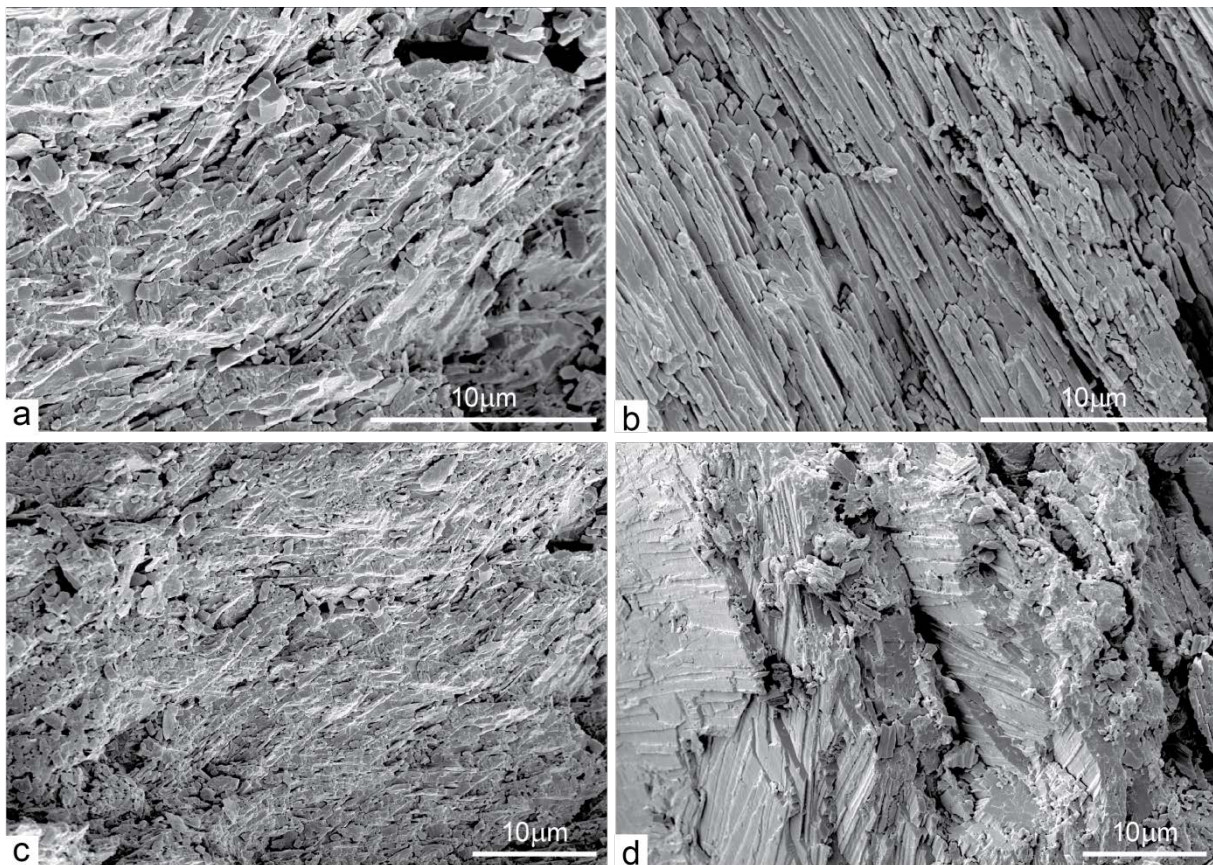


Fig. 6: Scanning electron microscope images showing the well-preserved aragonite texture of dated shells. Elongate to prismatic sections and bladed crystal outlines typify primary, acicular aragonite and/or calcite pseudomorphs after aragonite. a and c: sample F-Mak-12-03; b: sample F-Mak-12-01a; d: sample F-Mak-12-01b

3.5. Calculating incision and uplift rate

To quantify incision rates from in-situ produced cosmogenic nuclides, we paid attention sampling strath surfaces. The studied river terraces are characterized by a very sharp and well-defined basal unconformity and thickness of alluvial cap (Fig. 7, Table 1). The duration of surface occupation, a period of steady discharge and sediment flux (Pazzaglia & Brandon 2001), is difficult to appreciate. We assumed that the river did not spend much more time than measurement uncertainties at a particular surface and that the measured exposure

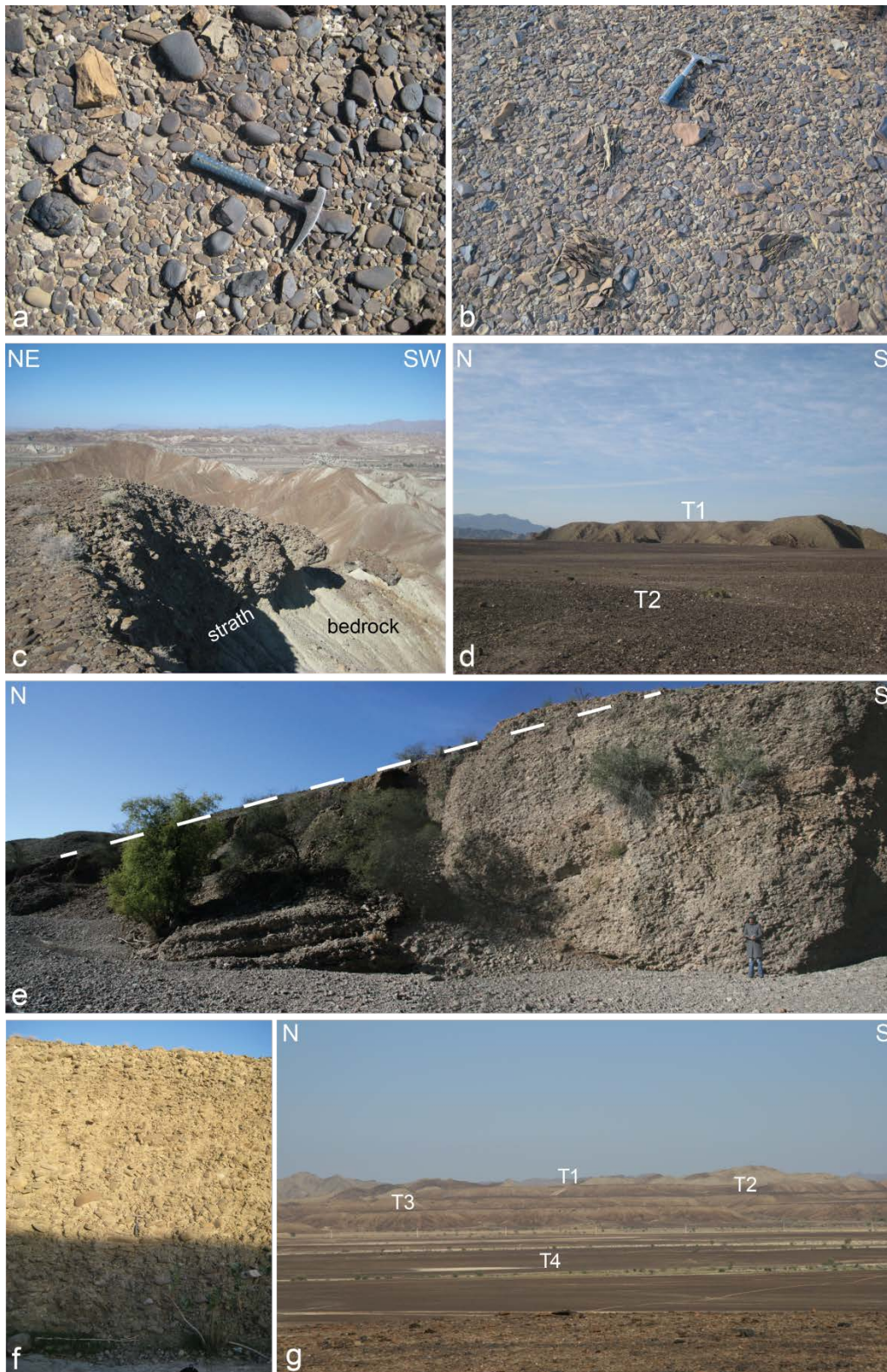


Fig. 7: Photographs of fluvial terraces inland Makran (locations in Fig. 4 and Table 1). (a) Sampled T4 surface Q-MAK- 10-31 for ^{10}Be dating; GPS ($25^{\circ}50'23.07''\text{N}$, $060^{\circ}09'43.50''\text{E}$). (b) Sampled T1 surface Q-MAK- 10-36 for ^{10}Be ; GPS: $26^{\circ}19'19.74''\text{N}$, $058^{\circ}53'37.88''\text{E}$ (c) Profile view showing the sharp strath and the clast supported Rz-T1 fluvial deposits; sample Q-MAK 10-28; GPS: $26^{\circ}19'05.11''\text{N}$, $058^{\circ}53'46.57''\text{E}$. (d) T1 and T2 levels of strath terraces along the Guredak River in Fanuj catchment (GPS: $25^{\circ}50'20.80''\text{N}$, $060^{\circ}11'03.90''\text{E}$). (e) Tilted fill terrace along Sarbaz River (GPS: $26^{\circ}11'48.00''\text{N}$, $059^{\circ}16'01.90''\text{E}$). (f) 10 m thick fluvial fill along Sarbaz River (GPS: $26^{\circ}07'34.61''\text{N}$, $061^{\circ}35'08.86''\text{E}$). (g) T1 to T4 strath terraces along Sarbaz River (GPS: $25^{\circ}58'26.66''\text{N}$, $061^{\circ}40'57.48''\text{E}$).

ages correspond to the abandonment time of the strath at that relative elevation. Hence, we calculated the mean rate of fluvial incision from the ratio of terrace elevation with respect to the present river level versus the abandonment TCN age of the terrace. The uncertainties on incision rates accumulate uncertainties on measured elevations and uncertainties on the timing of strath preservation from exposure ages (Table 2).

This approach is relatively reliable for the western catchments where tectonic influence was visibly limited and where river profiles are consistent with steady-state. Equating incision and uplift rates where local tectonics has clearly affected the terraces is less accurate. In that case, incision of strath terraces roughly records rock uplift and, if there is little erosion of the bedrock, rock uplift will essentially be equivalent to surface uplift (Bishop 2007). We therefore applied the same method for the four studied catchments to uncover the spatial and temporal incision/uplift pattern over a wide area of the wedge (Fig. 8).

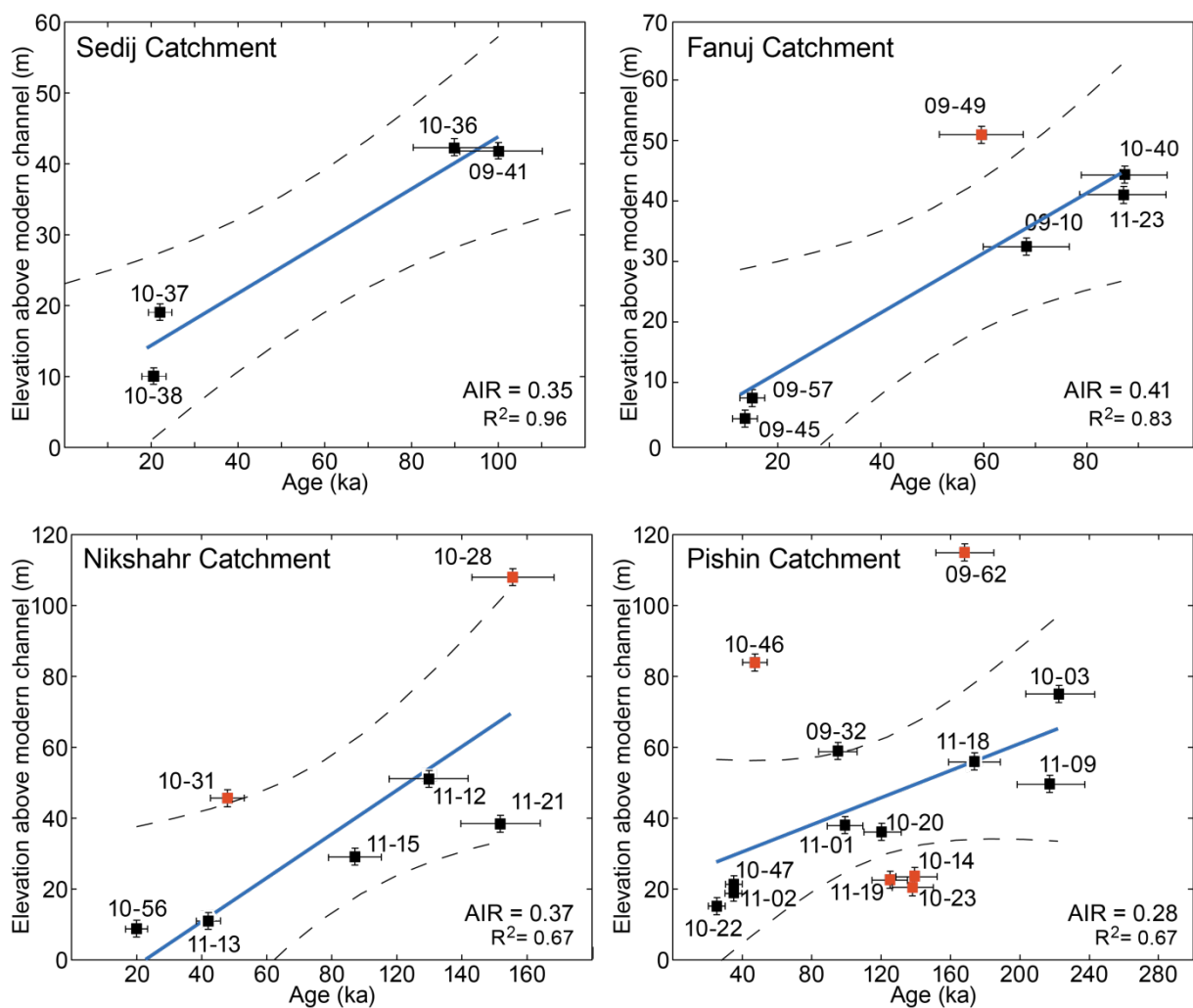


Fig. 8: Incision plots for studied catchments. Solid blue lines are weighted linear regression; dashed lines are envelopes showing 95% confidence limits on the age- incision relationship. AIR= apparent incision rate calculated from weighted linear regression. R² = coefficient of determination. Sample numbers located in Fig. 4 and Table 1. Red samples do not fit the 95% confidence limits. More explanations in text.

4. Site description of dated fluvial terraces

We selected sites where several conditions were met: 1) We mainly targeted paired, well preserved terraces to have wide-scale (regional) signal for tectonic and climate. This precaution was necessary; unpaired, small terraces may result from local tectonic or autocyclic processes that are unrelated to regional tectonic or climate whereas paired surfaces indicate that the river has not shifted laterally for large distances and therefore had a nearly constant geometry since the studied terraces were deposited in the bedrock stream section. 2) We sampled far from human activities or any surface disturbance such as colluviums deposit. 3) We chose wide, planar with little relief terraces whose surface shows the least evidence for erosion (Figs. 7a and b), which could affect TCN ages (e.g. Matmon et al. 2009). 4) We mainly sampled terrace profiles that contain rounded, tiled clasts typifying their fluvial environment. Our field observations did not indicate any stratigraphical development and most of the terraces exhibited homogeneous, clast-supported profiles (Fig. 7c). Lithostratigraphic identities could not be used for correlation since terrace profiles did not offer any remarkable stratigraphy. Therefore, the only criteria used with due caution was initially based on the height above the associated modern channel and, in some cases, the alluvial thickness (Table 1). These two criteria are inadequate where local tectonics has clearly affected the landscape. There, we had to rely on quantitative, age comparisons.

The studied catchments (Fig. 4) are described from west to east. Terraces are described according to their locality, specified as initial letter, and their elevation with respect to the present-day channel. We numbered them from top downward (for instance P-T1 highest to lowest P-T4 near Pishin, Figs. 2 and 7g). The terraces can be tracked along lengthy sections of all studied rivers, aside from their lower ~ 30 km from the coast, where the waterways cut through and meander on the easily eroded Late Miocene marls and Pleistocene continental deposits of the Coastal plain.

4.1. Sedij catchment

The Sedij River drains an area of 4627 km². The longitudinal profile of this river shows an apparent correspondence to a graded condition, reflecting a general landscape rising gently and regularly up valley in accordance with the present stream gradient. Negligible deviation with slightly higher K_{Sn} values than in upstream and downstream reaches are related to lithological resistance of regionally subordinate sandstone layers and channels of the bedrock (Chapter II). Two terrace levels were followed for about 170 km of river–distance, from near Konardar settlement in the north to near Majgi village in the south (Fig. 2). Two 100 km apart sites (A and B, Fig. 2) have been investigated. At both sites the main trunk river is characterized as a bedrock channel. T1 and T2 terrace levels of the two sites are morphologically well correlated thanks to their near-continuity along the Sedij River.

At Site A, close to Konardar (Fig. 2), the two strath terraces K-T1 and K-T2 (both < 2m thick) stand 42m and 20m above the present-day river, respectively (Fig. 9a). Their even thickness over long distances suggests that the area was tectonically stable during the period represented by these degradational terraces, both underlain by Miocene, sand-dominated

turbidites. K-T2 is a paired surface that stretches continuously for several kilometres, whereas K-T1 is more disrupted. K-T1 and K-T2 are samples Q-Mak-10-36 and Q-Mak-10-37, respectively. In addition, we took sample Q-Mak-10-38 from a local T2 level (B-T2), 30 km to the north of site A, to further constrain the age of this regionally extensive, geomorphological level.

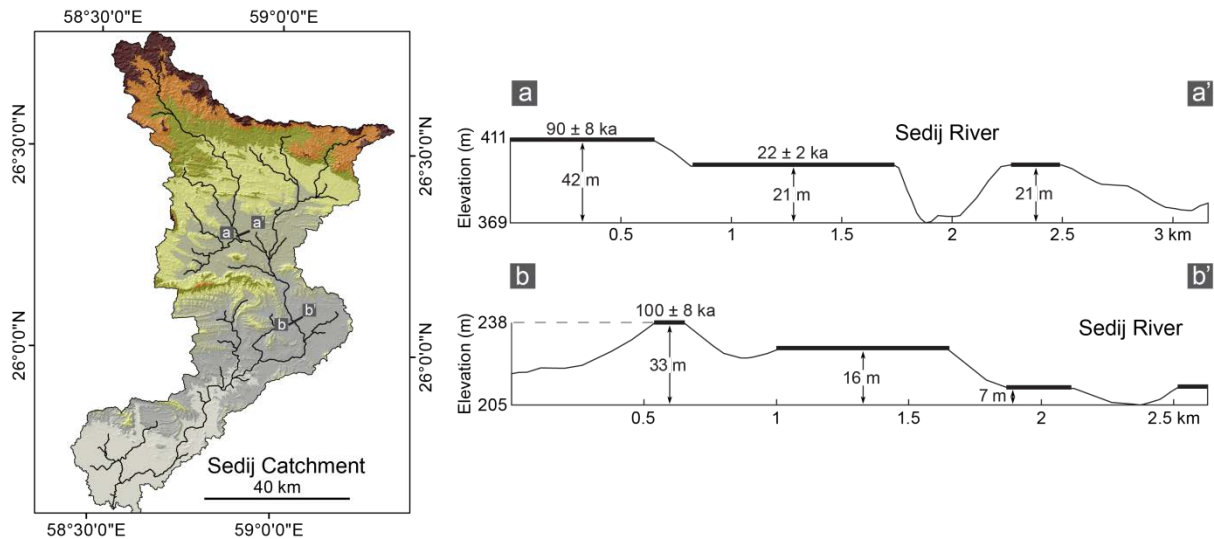


Fig. 9a: Left column: Shaded relief maps (Aster GDEM Version1, NASA) of Sedij catchment with trace of transverse sections (right column) displaying the Quaternary terrace staircases. Bold numbers are abandonment ages obtained from ^{10}Be dating.

At site B, close to Majgi village (Fig. 2), three extended flat strath surfaces (M-T1-M-T3) stand 33, 16, and 7 m above the present-day river (Fig. 9a). The highest, M-T1, has been sampled (Q-Mak-09-41) for temporal correlation with terraces of site A.

Samples made of few centimeters big, 1-2 cm thick pieces chopped off from the surface of quartz-rich cobbles in the modern channel were collected at sites A (Q-Mak-11-25) and B (Q-Mak-09-43) to examine inheritance.

4.2. Fanuj catchment

The Fanuj catchment extends over an area of 11036 km^2 . We surveyed the terraces along the two largest rivers (Guredak to the west and Fanuj to the east), which merge at about 35 km from the mouth. The two rivers display bedrock and mixed alluvial-bedrock channels along most of their course. Miocene sand-dominated turbidites are the main bedrock lithologies.

The main channel of Guredak River follows a regular, concave upward long profile with a concavity index $0.5 < \theta < 0.6$ and nearly constant K_{Sn} values < 60 (Chapter II). Such consistent and nearly constant values normally indicate graded or steady state conditions, in consistency with close correspondence between modeled and measured profile shapes. Fieldwork has revealed that Guredak River abandoned two major levels analogous to those mapped along Sedij River (Fig. 7d). At Site C, south of Guredak village (Figs. 2 and 9b), five terraces are conspicuously preserved. Their number makes level correlation with the

regionally-developed two levels hazardous. The highest and lowest levels are standing 72 and 2m above the contemporary channel, respectively (Fig. 9b). We collected samples from the G-T2 (Q-Mak-09-49) and G-T5 (Q-Mak-09-45) surfaces to determine if there is a significant change in incision rate at that site.

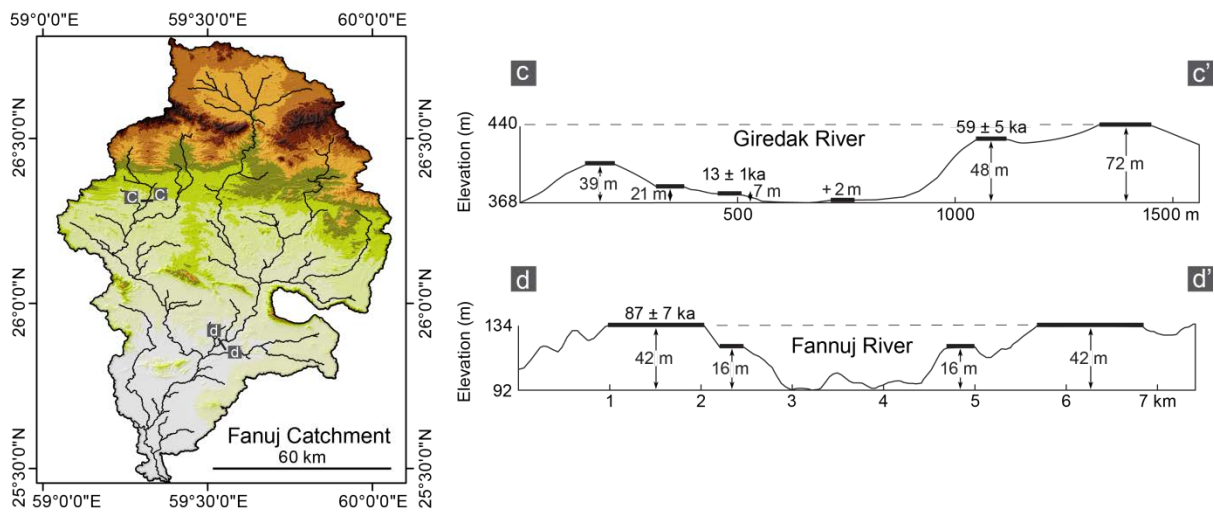


Fig. 9b: Left column: Shaded relief maps (Aster GDEM Version1, NASA) of Fanuj catchment with trace of transverse sections (right column) displaying the Quaternary terrace staircases. Bold numbers are abandonment ages obtained from ^{10}Be dating.

We sampled the two prominent, paired levels, Kh-T1 and Kh-T2 (Q-Mak10-40 the higher and Q-Mak-10-41 the lower) at site closed, close to Kheyrrabad village (Figs. 2 and 7d). The thickness of alluvial cap, composed by thin, clast-supported fluvial pebbles, varies from 0.8 to 3m. Oligo-Miocene turbidites are the main bedrock lithologies.

Fanuj River is generally concave but displays two knickpoints. The upstream knickpoint with a relief of 5 m is lithologically controlled. It is where the stream leaves resistant volcanic rocks of North Makran and enters onto more erodible Eocene-Miocene sediments. The downstream knickpoint is the confluence to Guredak River and is related to physical properties of this junction point (Haghipour 2013).

Two sites (E and F), separated by a meandering channel segment too short to influence the equilibrium profile, have been investigated along Fanuj River (Fig. 2). The meandering part, to the south of Fanuj City, is characterized by an extensive fill terrace. This terrace was not sampled because it is likely related to autocyclic processes.

Two terrace levels, F-T1 and F-T2 have been identified at site E, to the north of Fanuj City (Fig. 2). F-T2 is a large, broad surface 8 m above the modern steam whereas F-T1 consists in small remnant surfaces 12 m higher than F-T2. Q-Mak-09-56 was taken from F-T1 and Q-Mak-09-57 from F-T2. The alluvial parts are 2 m thick for F-T1 and 5m thick for F-T2.

Further south, at site F, close to Parka-Bandar village (Fig. 9b), two <2m thick strath terraces are prominent. We collected samples from these two levels PB-T1 and PB-T2 (Q-Mak-11-23 and Q-Mak-11-24, respectively).

A huge fan system developed close to Chahan village (site G, Fig. 2). We recognized two major, gently tilted levels (Ch-T1 and Ch-T2). We surveyed these surfaces with DGPS for precise record of the tilt (Fig. 10). Based on these measurements and field observation we concluded that this fan system is influenced by the syncline structure against which it abuts (Fig. 10). To put age constraints on the abandonment of this fan system, Q-Mak-10-44 was taken from Ch-T1 and Q-Mak-10-45 from Ch-T2.

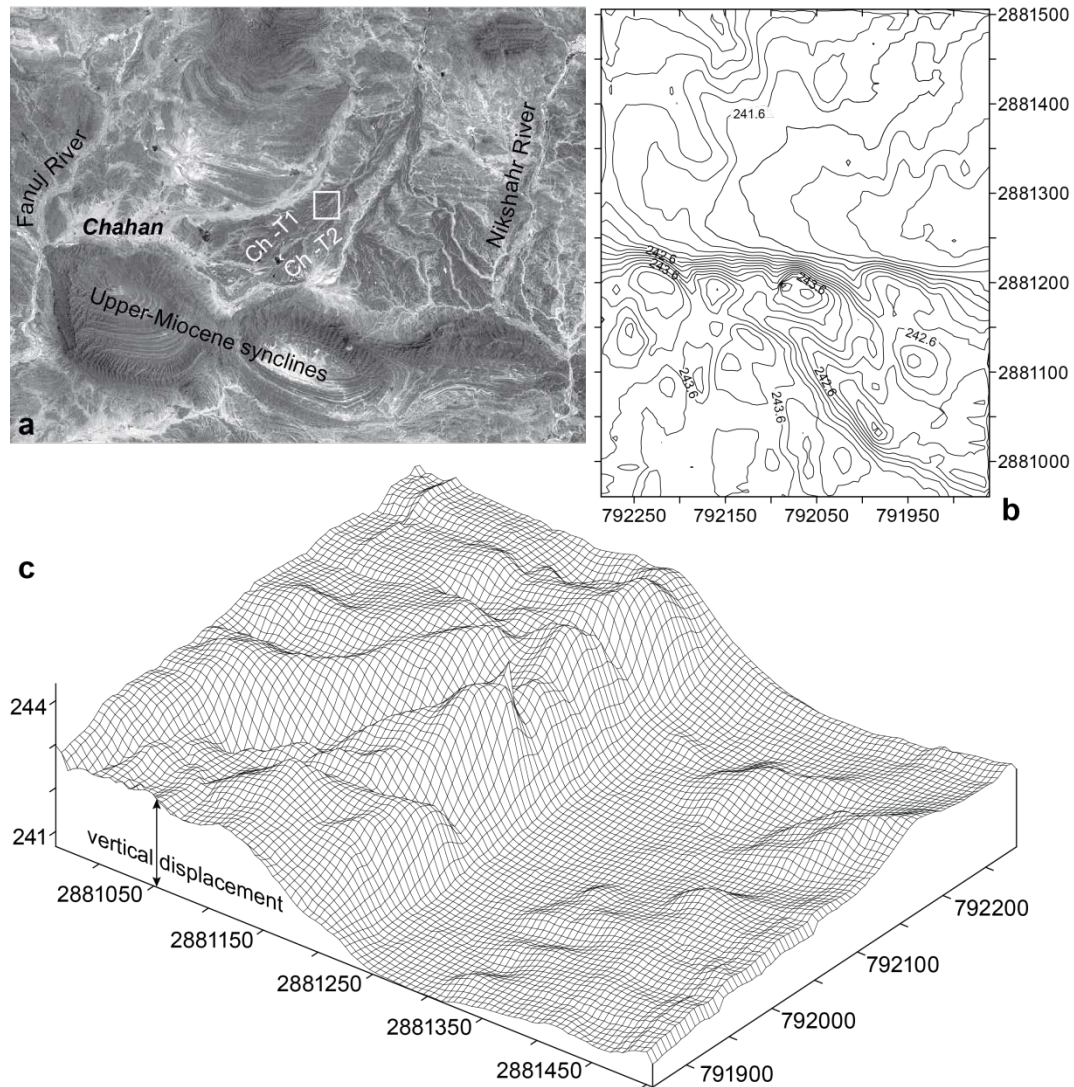


Fig. 10: a) Satellite image of the Chahan fan system blocked by Upper Miocene synclines (Chahan location in Fig. 2). b) Contour map derived from DGPS survey on Ch-T1 (white box in a); the steep linear topographic gradient is interpreted as the scar of an active fault. c) 3D plot of the fault scarp vertically offsetting the Ch-T1 surface by ca 2m.

4.3. Nikshahr catchment

The Nikshahr catchment covers 5399 km² (Fig. 9c). The 250 km long Nikshahr River is concave but displays discontinuities and zonal variations (Chapter II). Strath terraces are present along most of the river, down to about 40 km from the coast, where the river flows on the alluvial coastal plain. The river head is located in Inner Makran. Several alluvial

surfaces line the upstream, bedrock-controlled and mostly bedrock-floored part, where Nikshahr River has carved narrow gorges (North of Tangeh-Sareh, Fig. 2). The matrix-supported profile of these surfaces and their thick (>20 m) colluvial cover of angular clasts (>10 cm big) indicate mass-wasting and hill-slope processes. Therefore we did not consider them for this work. Below this location, Nikshahr River abandoned mainly <3m thick strath terrace deposits of fluvial gravel and pebbles.

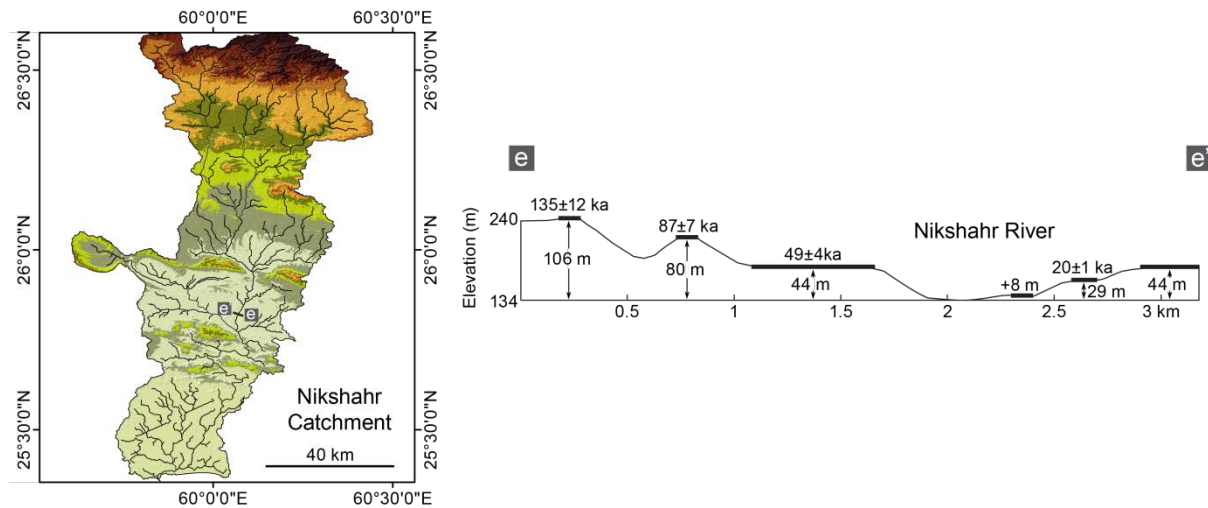


Fig. 9c: Left column: Shaded relief maps (Aster GDEM Version1, NASA) of Nikshahr catchment with trace of the transverse section (right column) displaying the Quaternary terrace staircases. Bold numbers are abandonment ages obtained from ^{10}Be dating.

A knickpoint at about 125 km from the mouth occurs where the river cuts through the so-called Bashakerd Thrust, the tectonic boundary between North and Inner Makran (Fig. 2, Dolati 2010).

The mid-profile has a rather high concavity index ($\theta = 0.66$). The corresponding middle reach is characterized by a bedrock-floored channel with >10 cm big boulders, which indicates relatively high discharge.

At site H, 30 km north of Nikshahr City (Fig. 2), Q-Mak-11-12 was collected for spatial and temporal correlation from the <1m thick Sh-T1, the highest (51 m above the present-day channel) of two stepped strath terraces.

Sites I and J (Fig. 2) represent well-preserved strath terraces that developed large planar surfaces, at both sites in tectonic basins bounded by the Ghasre-Ghand and Chah-Khan thrusts (Fig. 2). At site I, close to Pit-ab village, four paired strath terraces levels (Pt-T1-Pt-T4) are capped with a thin (< 2 m) veneer of gravel (Fig. 11a). They are 35 (Pt-T1) to 16 m (Pt-T4) above the contemporary river bed carved into folded Miocene Turbidites. A sample was collected from each (Table 1). A depth profile was sampled in the Pt-T4 surface.

A convex section within the overall concave profile is associated with a knick zone about 80 km from the mouth, where the river cuts through the so-called Rahde-Gardz anticline. The Nikshahr River has the deepest incision at this location. The bedrock is composed of folded Oligocene-Miocene turbidites in Inner and Outer Makran, and mostly Miocene marls in southern Outer Makran and northern Coastal Makran.

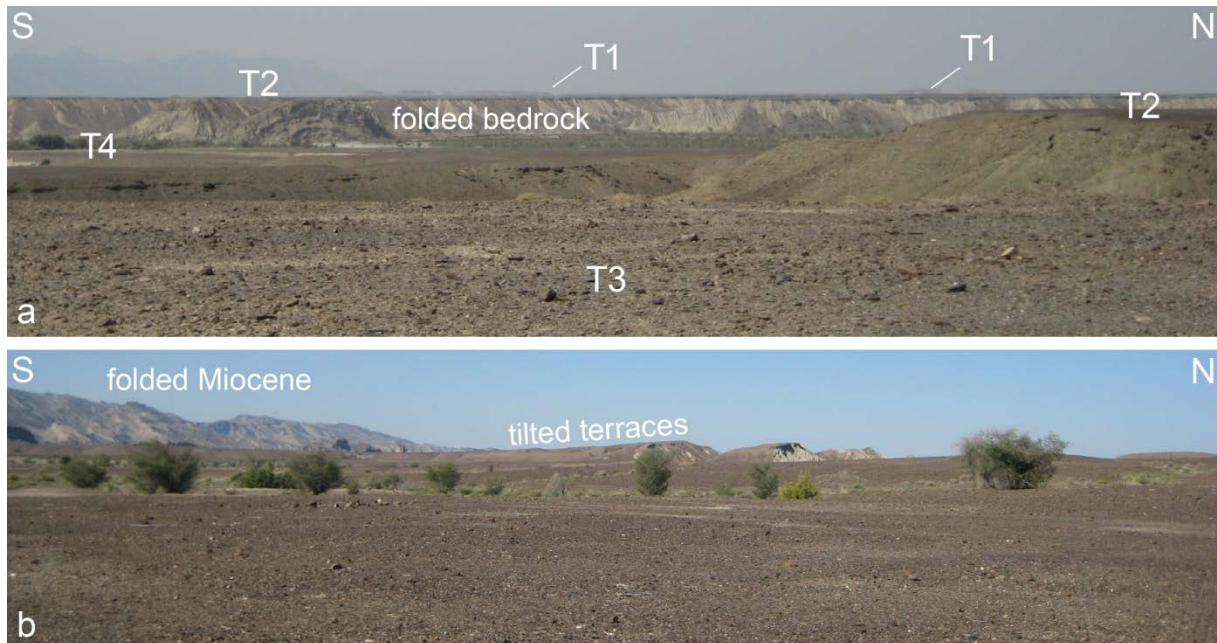


Fig. 11: a) Four levels of strath terraces at site I (Fig. 2) along Nikshahr River, GPS: 26°01'02.84"N, 060°08'41.45"E. b) tilted fluvial terraces at site J (Fig. 2) along Nikshahr River; GPS: 25°49'19.88"N, 060°08'00.24"E.

Site J is close to Rahde-Gardz village (Fig. 2), in the downstream knickzone, where the river has abandoned five levels of variably tilted (Fig. 11b), 1-3 m thick strath terraces (Haghipour et al. 2012, Table1). Rz-T1 stands 106m and Rz-T5 8 m higher than the modern channel. We sampled the flat part of each terrace to avoid relief influence in calculated exposure ages. Sample Q-Mak-10-28 was collected from the highest Rz-T1 and Q-Mak-11-31 from Rz-T4. We link active folding recorded by these terraces to the recent amplification of the Rahde-Gardz anticline mapped in the bedrock (Dolati 2010).

4.4. Pishin catchment

Pishin catchment is twice as big as the other catchments (drainage area $\sim 20711 \text{ km}^2$). It has a NW-SE orientation that makes it different from other catchment, where the main rivers flow nearly N-S. We have surveyed fluvial terraces in two main trunk of Pishin catchment (Peer Sohrab in the west and Sarbaz in the east, Fig. 2), which join together north of Nagur, 60 km from the mouth. Noting that the spacing between the mouths of the Sedij, Fanuj and Nikshahr rivers is regular, and about half that between the Nikshahr and Pishin mouths, we suspect that the Peer Sohrab River has been deviated eastward and joined the Sarbaz River (Fig. 4). The two rivers are deflected from their bulk N-S flow direction along the northern side of the anticline ridge at the front of the hanging wall of Gativan Thrust. The upstream part of Pishin catchment flows over Upper Eocene to Lower Miocene turbidites of Inner Makran. The fluvial terraces along the Peer Sohrab and Sarbaz main trunks were mainly deposited on Outer and Coastal Makran (middle parts of the rivers) in synclines associated with flats of major thrusts. Further south, the lithology is changing to Miocene siltstone and

marl with calcareous sandstone. The relief is strongly influenced by thrust-sheets and associated folds.

Peer Sohrab River displays two prominent knick points, one where it cuts the Gativan Thrust (ca 115 km from mouth) and the other where it cuts the Chah-Khan Thrust, between Outer and Coastal Makran, ca 75 km from the mouth (Fig. 2, and Chapter II). The upper reach of the river has a best-fit concavity index of $\theta = 0.48$ and conforms very well the predicted, smooth concave form, which suggests dynamic equilibrium for this segment. The upper knick point marks a scaling break to low, even negative concavity index ($\theta = -0.31$), which designates an overall non-concave profile accentuated by the high concavity ($\theta = 1.2$) downstream from the lower knickpoint.

Two sites have been investigated along Peer Sohrab River.

Three strath terraces were distinguished at site K, where the river cuts the Gativan Thrust and carved into folded Miocene turbidites. The highest (Z-T1, 79 m above the modern channel) and lowest level (Z-T3, 15 m above the modern channel) were sampled (Q-Mak-10-46, Q-Mak-10-47, respectively). The alluvial caps of both sampled terraces are very thin (<1m).

Site L is located ~ 50 km (straight distance) from the previous site, to the north of Peer Sohrab City (Fig. 2). Two extensive, paired strath terrace levels are 56m (Pr-T1) and 23 m (Pr-T2) above the present river channel. Pr-T1 is folded. Its alluvial part consists of ~3 m consolidated-course conglomerate. Pr-T2 is a planar surface that extends for several kilometres. Two samples were collected, Q-Mak-11-18 from Pr-T1 and Q-Mak-11-19 from Pr-T2.

Three sites have been investigated along Sarbaz River. The longitudinal profile of this river is concave upward with three knick points delimiting four channel segments. These knickpoints coincide with the Pishamak (between Northern and Inner Makran), Gativan (the most prominent), and Chah-Khan Thrusts (Fig. 2 and Chapter II). Related changes in concavity and K_{Sn} values readily display that these emergent faults are active. The loose conformity between modelled and actual profiles illustrates the non-equilibrium state of Sarbaz River.

At site N, close to Rask City (Figs. 2 and 12), three terrace levels (R-T1-R-T3) are characterized by thick (> 30 m), clast-supported alluvial fill representing a massive aggradational stage (Figs. 7e and f). This important volume of alluvium was not observed anywhere else. Based on field observation, we relate these terraces to rapid filling of E-W-trending, flat-syncline basins along which the river course has been deflected behind the ramp and/or fault-propagation anticline formed on the hanging wall of Gativan Thrust (Dolati 2010, Fig. 2). The lack of lake deposits suggests that these intra-mountainous basins were not closed but the growth of the ramp anticline was likely partial obstruction to the river flow. We collected samples from these three paired levels, which sit 67, 43 and 36m above the modern channel. R-T1 is tilted (Fig 7e). We took samples from a depth profile in R-T3.

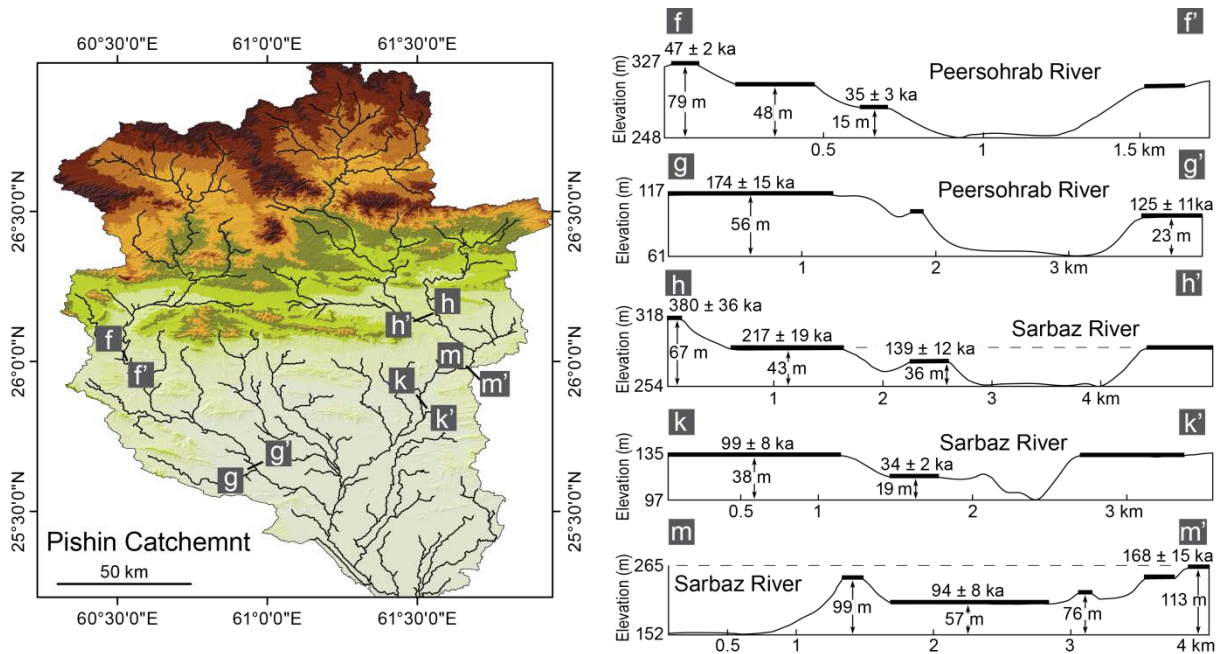


Fig. 12: Shaded relief maps (left, Aster GDEM Version1, NASA) of Pishin Catchment with trace of transverse sections (right column) displaying the Quaternary terrace staircases. Bold numbers are abandonment ages obtained from ^{10}Be dating.

The morphologically equivalent terraces of R-T2 and R-T3 have been sampled in two other places, near Firuzabad (Q-Mak-10-03) and Ghasr-e-Ghand (Q-Mak-10-23) cities (Fig. 2) in order to have better age constraints on the fluvial incision along Sarbaz River. Fr-T1 (Q-Mak-10-03) stands 75 m above the channel with 4m thick fluvial deposits. G-T1 (Q-Mak-10-23) stands 23 m above the present-day river channel with 7 m thick fluvial fill.

Further south, close to Pishin city, just downstream the knickpoint on the Gativan Thrust (Fig. 2, Site O), four strath terraces (P-T1-PT4) stand 113 (P-T1) to 57 m (PT4) higher than the present-day Sarbaz River (Fig. 7g). Their number and morphology differs from Sarbaz terraces and they actually represent an abandoned, now dry stream flowing into the adjacent Torbat catchment, largely developed in Pakistan (Chapter II). The geomorphological characteristics of site O denote capture after deposition of P-T4 of an old, topographically higher Torbat system river by the Sarbaz River (Chapter II). We collected samples from the highest (P-T1) and lowest levels (P-T4) (Q-Mak-09-62, and Q-Mak-09-32, respectively).

At Site P, close to Bahukalat city (Figs. 2 and 12), the two paired levels Bh-T1 and Bh-T2 (samples Q-Mak-11-01 and Q-Mak-11-02, respectively) consist of very thin (1-2 m) alluvial cap (Table. 1). They can be followed for several kilometres and stand 38 and 19 m above the modern channel. Their relative elevations make them comparable to T1 and T2 terraces in sites A,B, and F of Sedij and Fanuj catchments. The modern channels of Pishin catchment were sampled at five sites (Fig. 4 and Table 1).

5. Results

We first present minimum, uncorrected ^{10}Be TCN ages. Modelled ages corrected for inheritance and erosion are given in Table 2.

5.1. ^{10}Be abandonment ages and rates of fluvial incision

Sedij catchment

The abandonment ages of the strath terraces sampled at sites A and B on Sedij River correlate very well numerically and morphologically (Table 1 and Fig. 9a), clustering at about 19 ± 1 ka for the lower level and about 100 ± 8 ka for the higher. All the data in the age-elevation plot fall in the 95% interval bounds, which indicates uniform spatial –temporal incision rate. The calculated mean fluvial incision rate since abandonment is 0.39 mm/a. The exceptionally high incision rate (0.86 mm/a) obtained from the K-T2 surface reveals fast tectonic uplift at the sampling site, which pushed K-T2 10 m higher than its equivalent level (B-T2).

Fanuj catchment

The terraces in Fanuj catchment have more scattered exposure ages, from 13 ± 1 ka to 119 ± 9 ka (Fig. 8). Plotting age versus incision values yields a homogeneous long-term rate of 0.43 mm/a. Two samples did not fit the % 95 interval confidence curve and yield higher (Q-Mak-09-49) or lower (Q-Mak-09-56) incision rates (Fig. 8). Q-Mak-09-49 (59 ± 5 ka) was collected at site C, where the staircase of terraces has six levels instead of the two in other sites of this catchment (Fig. 9b). Therefore, we attributed this high incision rate activity on a mapped splay of the Gativan Thrust). The relatively low incision rate (0.17 mm/a) obtained from Q-Mak-09-56 can result from variations of its alluvial thickness and its fan-terrace characteristic. Field observation indicate that this surface displays sub angular gravels on its profile. Therefore, it is not a perfect fluvial terrace and we excluded this sample from the fluvial incision plot.

Nikshahr catchment

The ^{10}Be exposure ages from strath terraces along Nikshahr vary between 20 and 135 ka (Table 2). The mean incision rate obtained from the age-elevation plot is 0.38 mm/a (Fig. 8). Q-Mak-10-28 and Q-Mak-10-31 do not fit the % 95 interval confidence boundary. We attribute this spatial change in incision rate to the Rahde Gardz anticline, which has also folded the terraces, the youngest least amplified and the oldest most amplified (Haghipour et al. 2012).

Pishin catchment

The ^{10}Be exposure ages obtained from Pishin catchment span from ~ 20 ka to ~ 380 ka (Table 2). The morphological sequence of fluvial terraces differs in age from site to site along both Peer-Sohrab and Sarbaz Rivers. Recent activity of the thrusts mapped in the geological basement is responsible for this bias and dislinkage of fluvial sequences. The age-elevation plot does not show a good fit for all samples of this catchment. The mean incision rate

derived from all samples of Pishin catchment is 0.3 mm/a. Samples 10-46, 09-62 and 09-32 do not fall in the 95% interval confidence boundary of age-elevation plots that yield incision rates higher than the 0.3 mm/a average value (Table 1). This deviation is partly due to recent activity of the Gativan Thrust and also reflects the described river capture where both samples Q- Mak -09-62 and 09-32 were taken (Fig. 8). Conversely, samples 10-14, 10-23 and 11-19 yield low incision rates, <0.2 mm/a. These samples represent fill terraces with relatively thick (> 30m) alluvial cap. The exposure ages for terraces R-T3 (Q-Mak-10-14) and G-T1 (Q-Mak-10-23) are around 140 ka. The local presence of such thick sediments and their deep incision can be explained, in the absence of glacial evidence, by a change in local base level due to tectonic activity on the Gativan Thrust, which also caused a local increase in discharge. Field checking confirmed this interpretation, these surfaces being tilted and folded (Fig. 7e). Ages and terrace morphology at Site P, close to Bahukalat city (Fig. 2), match results on sites of other catchments. At site P, two levels of paired strath terraces (Bh-T1 and Bh-T2) yield exposure ages of 99 ka and 34, respectively. These ages are analogue to the ages obtained at sites A, B, F and H. This geographically widespread correspondence of two terrace levels suggests that their genesis is associated with a regional, climatic-driven force.

5.2. ^{14}C dating result and coastal uplift

The ^{14}C ages obtained from our samples cluster in two groups: Holocene (F-Mak-12-01A at 3663 ± 25 a and F-Mak-12-01B at 4005 ± 25 a) and Pleistocene (F-Mak-12-02 at 45381 ± 1057 a and F-Mak-12-03 at 45381 ± 997 a, Table 3, Fig. 13). Uplift rates calculated from these ages are ~ 3 mm/a for the Holocene and 0.9 to 3mm/a for the Pleistocene (Table 3). These rates are higher than previously reported (Page et al. 1979). However, our new Pleistocene ages are very close to the limit of ^{14}C dating; therefore, they must be considered as minimum ages and caution should be taken for interpretation.

Table 3: Summary of dating on marine terraces, including new ages from this study.

Location (West to East)	Sample name	Longitude	Latitude	Sample elevation (m)	Age (ka)			Reference
					¹⁴ C a BP	Cal/ ¹⁴ C a BP	²³⁰ Th/ ²³⁴ U	
Jask	J-1	-	-	6	-	34310±3000	133±13	Page et al., 1979
	J-2	-	-	6	-	28010±1660	-	Page et al., 1979
	J-3	-	-	6	-	32680±2550	-	Page et al., 1979
	J-4	-	-	6	-	26025±1050	136±14	Page et al., 1979
	HAR-1115	-	-	-	25610±640	-	-	Vita-Finzi (1975)
	HAR-1907	-	-	-	23390±400	-	-	Vita-Finzi (1975)
	JA13	25 38 11	57 45 59	>2	>24000	-	-	Reyss et al., 1998
Konarak	K4	-	-	6	5520±165	5935±165	-	Page et al., 1979
	K6	-	-	-	5880±320	6255±320	-	Page et al., 1979
	K10	-	-	-	5190±120	5595±120	-	Page et al., 1979
	K11	-	-	-	5330±120	5795±120	-	Page et al., 1979
	K8	-	-	-	-	25675±850	138±12	Page et al., 1980
	K9	-	-	-	-	26430±910	-	Page et al., 1981
	K3	-	-	-	-	-	76±12	Page et al., 1982
F-Mak-12-03	60 37 45.3	25 20 21.4	147±3	41567±1068	41486-45571*	-	This study	
Chabahar	CH44	25 19 10	60 37 13	4	3670±50	-	-	Reyss et al., 1998
	F-Mak-12-02	60 37 45.3	25 20 21.4	41±3	41482±1057	45381-41427*	-	This study
Beris	F-Mak-12-01A	60 56 08.07	25 13 38.03	8±1	5165±25	4005-3947*	-	This study
	F-Mak-12-01B	61 05 11.5	25 11 44.9	14±1	4837±25	3663-3629*	-	This study
Gwater (Pakistan)	GW50	25 09 55	61 30 07	3	> 25000	-	-	Reyss et al., 1998
Omara (Pakistan)	-	-	-	6	> 37000	-	-	Page et al., 1981
-	-	-	-	4	2710±135	-	-	Page et al., 1981

New ¹⁴C ages are given with 1σ error. Calibrated ages of this study were produced with the data set IntCal09 (Reimer et al. 2009). * Other probabilities shown in Fig. 13.

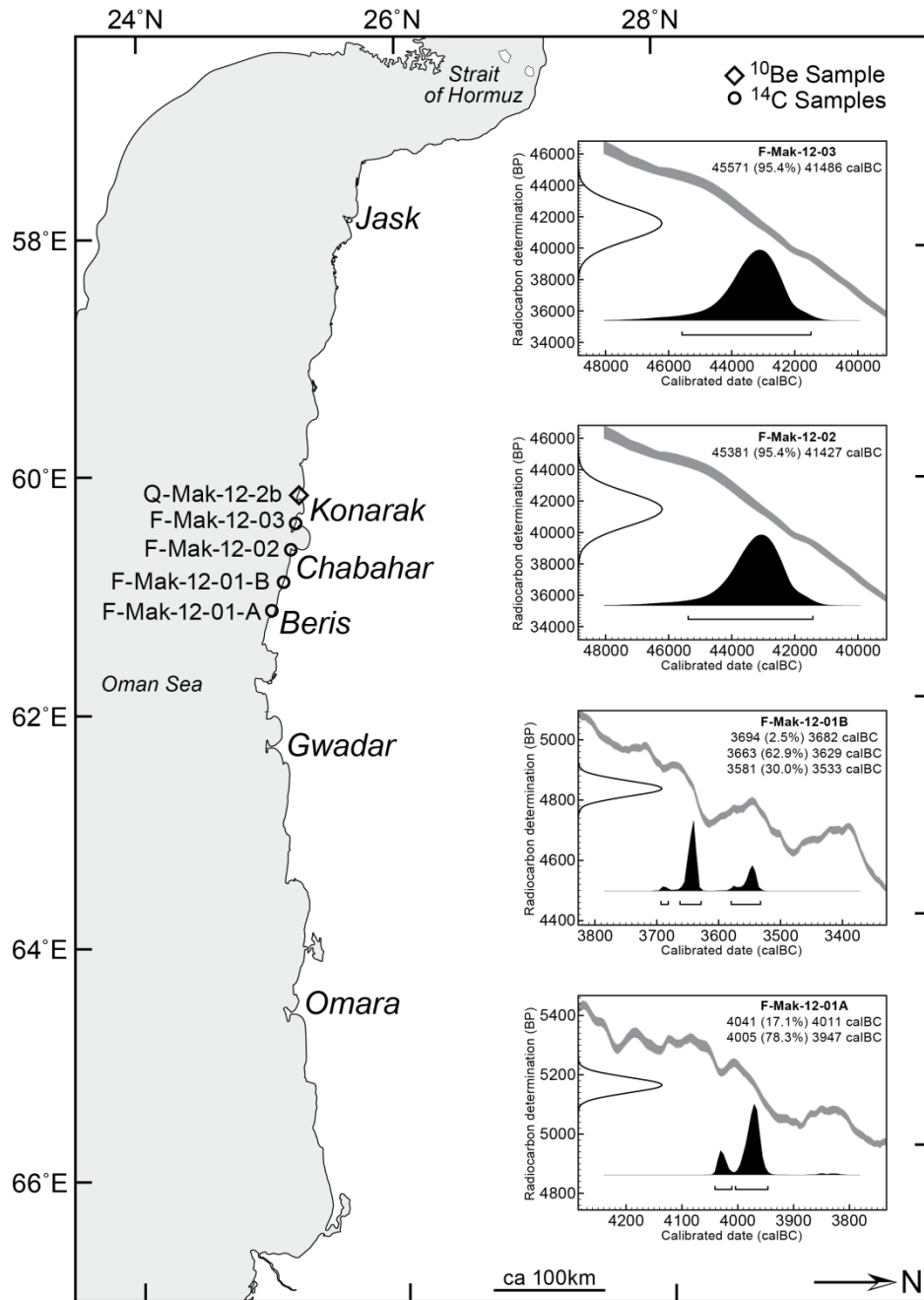


Fig. 13: Location of marine terrace samples dated with ^{14}C and ^{10}Be . Inset plots represent the calculated and calibrated ^{14}C ages using OxCal v.4.1 programme (see text).

5.3. Comparison between incision rate and river gradient

In general, the average K_{Sn} values increase eastward with a positive relationship between channel steepness and incision rate (Fig. 14). The K_{Sn} values and calculated incision rates do not show remarkable changes along Sedij and Fanuj Rivers. Conversely, marked but localized changes in K_{Sn} and incision rates along Nikshahr, Sarbaz and Peersohrab Rivers are clearly associated with faults and or/folds mapped in the bedrocks, the Gativan Thrust being the most prominent, with highest K_{Sn} values and an incision rate of >0.5 mm/a.

Therefore the spatial changes in K_{Sn} and incision rates reflect differential and tectonically-driven rock uplift. Folded and tilted terraces in the vicinity of active structures are additional evidence for current deformation.

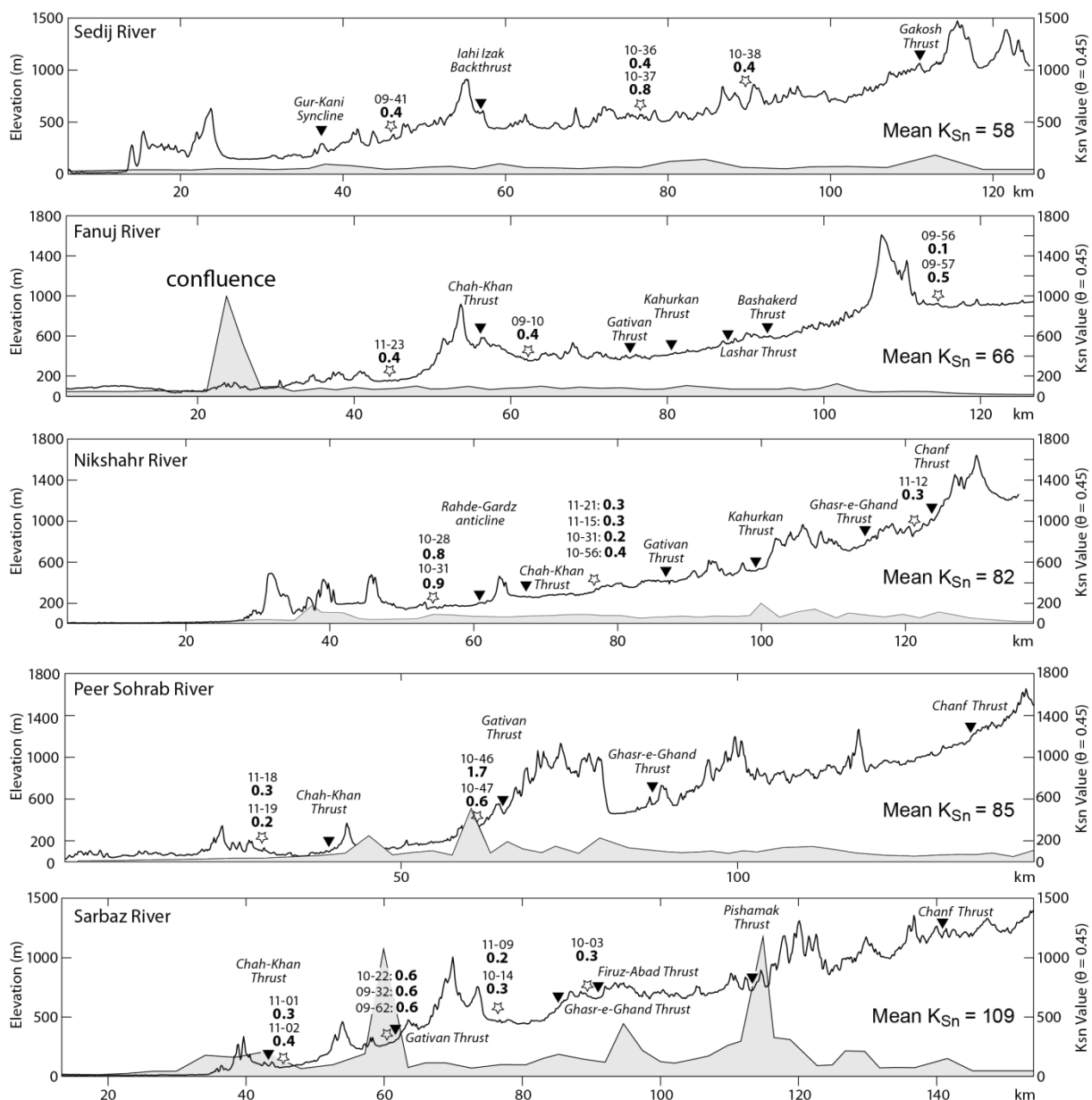


Fig. 14: Stream gradient plots (shaded area) along with topography across studied rivers. Bold numbers give incision rates determined from dated fluvial terraces (Table 2).

6. Discussion

6.1. Age uncertainties and resolution

Although the surface exposure age method provides useful constraints on intermediate time scale (10^3 - 10^5 yr) chronology, the age accuracy suffers from several sources of uncertainties. In particular, TCN ages from surface clasts may be over-estimated if the clasts have acquired

measurable TCN concentrations prior to final deposition (inheritance). Conversely, TCN ages may be underestimated if the clasts have been recently exhumed or weathered. Inheritance uncertainties have far more impact on determining the TCN ages than uncertainties in absolute production rates and scaling factors (e.g. Ivy-Ochs et al. 2012). Total analytical errors on ages including production rates (10%), Accelerator Mass Spectrometry measurements (3-4%) and chemical processing (1-2%) are about 10-15%. The largest analytical uncertainty comes from site estimation of production rate (e.g. Gosse & Phillips 2001). To approach uncertainties related to inheritance and erosion components, we present measurements from depth profiles and samples from modern channel.

Depth profiles

Slightly more than 2m deep depth profiles have been dug and sampled in terraces Pt-T4 (Nikshahr catchment, Fig. 15a) and R-T3 (Pishin catchment, Fig. 15b). The thickness of alluvial cap in the two depth profiles (about 2 m) is the minimum pit required to access the amount of TCN inheritance (Anderson et al. 1996).

We applied the geologically constrained Monte Carlo approach from the best model fit of 100,000 solutions (Hidy et al. 2010) to determine the ^{10}Be model ages of these surfaces, which are 120 ± 10 ka for the older R-T3 and 15 ± 1 ka for the younger Pt-T4. In the older R-T3 terrace, the ^{10}Be concentration plot on an almost perfect curve of exponential decrease with depth. The deepest sample in the Pt-T4 terrace does not fit the theoretically exponential depth versus nuclide concentration profile relationship (e.g. Anderson et al. 1996, Gosse & Phillips 2001). Excluding this sample for simulation, the other measurements fit well the downward exponential decrease in ^{10}Be nuclide concentration. This agreement falls in line with the principle of longevity of desert pavement stability (e.g. Haff & Werner 1996, Matmon et al. 2009). No stratigraphic feature or internal bedding was found in these two depth profiles. Their homogeneity (Fig. 15) strongly suggests that sedimentation of the gravel happened during one event over a short time period. Accordingly, we assumed a constant bulk density ($\sim 2.4 \text{ g.cm}^{-3}$) of sediment through the terrace profiles. The estimated inheritance from best fit in the R-T3 surface is $1.1 \times 10^5 \text{ at/g SiO}_2$ and $0.4 \times 10^5 \text{ at/g SiO}_2$ in Pt-T4. This result indicates that inheritance may alter ages younger than 20 ka but has very small effect on the dating of older terraces. Distributions of ages and inheritance values are displayed in figure 15e (for RT-3) and figure 15f (for Pt-4).

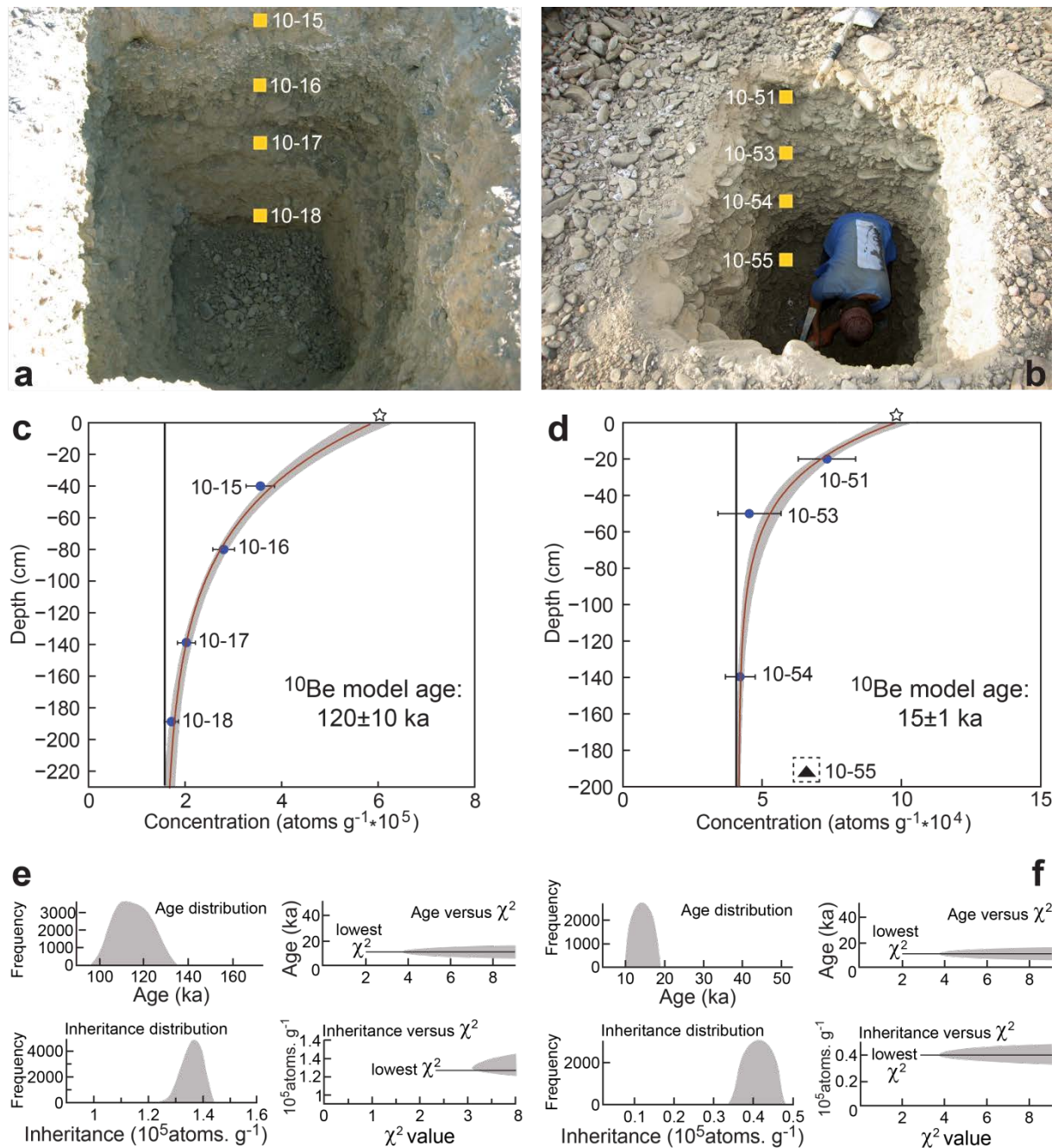


Fig. 15: **a)** Excavated pit in R-T3 (same place as Q-Mak-10-14 Fig. 4, GPS: N26°08'06.04", E061°33'14.50") and **b)** pit in Pt-T4 (same place as Q-Mak-10-56, Fig. 4, GPS: N26°01'58.55", E060°08'12.16"). Both terraces are homogeneous, clast-supported without unconformity and soil. **c)** and **d):** Concentration / depth plots with best fit regression (red lines) from 100 000 Monte Carlo simulations through the samples (blue circles) positioned in **a)** and **b)**. Grey curves cover the solution space. Stars represent the calculated concentrations in amalgamated surface samples. The bottom sample in Pt-T4 profile (black triangle in **d)**) was excluded from simulations because its nuclide concentration does not follow the theoretical depth rule. Analytical results in Table 1. **e)** Results for the 2σ age, inheritance, solution spaces for samples from the R-T3 terrace. **f)** Results for the 3σ age, inheritance, solution spaces for samples from Pt-T4. The chi-square cutoff values are determined from the chi-square probability distribution function introduced in Hidy et al. (2010).

Active channels

Another approach to estimate the inherited nuclide component is to analyze samples from the active channel (Repka et al. 1997, Hancock et al. 1999) assuming that erosion and discharge did not change from the deposition time till present day. However, the assumption behind this approach is not systematic and may lead to misinterpretation of the true ages (e.g. Schaller et al. 2004). We collected eleven amalgamated samples from the active main trunks to determine present-day cosmogenic inheritance (Table 1).

The ^{10}Be concentration from modern channel samples varies between 0.5×10^5 and 2.1×10^5 atoms g^{-1} . These values are equivalent to apparent ages of 11 ± 1 ka and 48 ± 4 ka, respectively. The agreement between concentration accumulated in river bed samples and concentration from depth profile samples suggest that the current source of pebbles has not significantly changed over the last few thousand years (Table 1). The similarity of concentration in modern channels (e.g. Q-Mak-09-44, Q-Mak-10-48) and lowest terrace surfaces in some locations (e.g. Q-Mak-09-45, Q-Mak-10-47, Table 1) suggests that modern samples are reworked by older terraces. Yet, the ^{10}Be concentrations in the two depth profiles are lower. Therefore, concentration values from modern channel samples cannot be used as amount of inheritance component everywhere. To evaluate the significance of the potential average prior-exposure values for each site we subtracted the ^{10}Be concentration obtained from each sample from the ^{10}Be concentration measured in depth profiles and modern channel samples (Table 2). We conclude that samples older than 30 ka are not affected by inheritance. Another argument for small inheritance is that we did not observe any relationship between amount of nuclide concentration and river length (longer travelling time causes more inheritance and therefore older ages). The good consistency between obtained ages and the morphostratigraphy of the terraces is further evidence for minor inheritance effect.

Surface erosion

The surface condition and pavement of sampled terraces record very little erosion out of small, lowest order, narrow and dry, ephemeral thalwegs and bear no anthropogenic disturbance (Fig. 7 a and b). However, the preservation of terraces as old as ca 379 ka suggests that the erosion rate is ≤ 1 cm/ka. The erosion rates reported by other studies of quartz-rich river sediments in tectonically quiescent landscapes under similar climate regimes are few centimeters per thousand years (e.g. Clapp et al. 2002, Matmon et al. 2009). Since there is no independent estimate of erosion rate in Makran and adjacent areas, we modelled for a constant maximum denudation rate of 1 cm/a while allowing for net erosion to vary between 0 and 30 cm using (Hidy et al. 2010) approach (Table 2). The estimated erosion rate from space solution plot for the old R-T3 surface is 0.07 cm/ka and 0.05 cm/ka for the younger Pt-T4 surface. These results, based on minimum age values, confirm that the mean erosion rate is very low.

6.2 Age distribution and modeled ages

An important question was whether the river dynamics were sensitive to climate variability or influenced by the tectonic evolution of the wedge. The distribution of exposure ages obtained in this work help answering that, in Makran, both tectonic and climatic forces controlled river incision with obvious intervention of tectonic forcing in the eastern part of the study area.

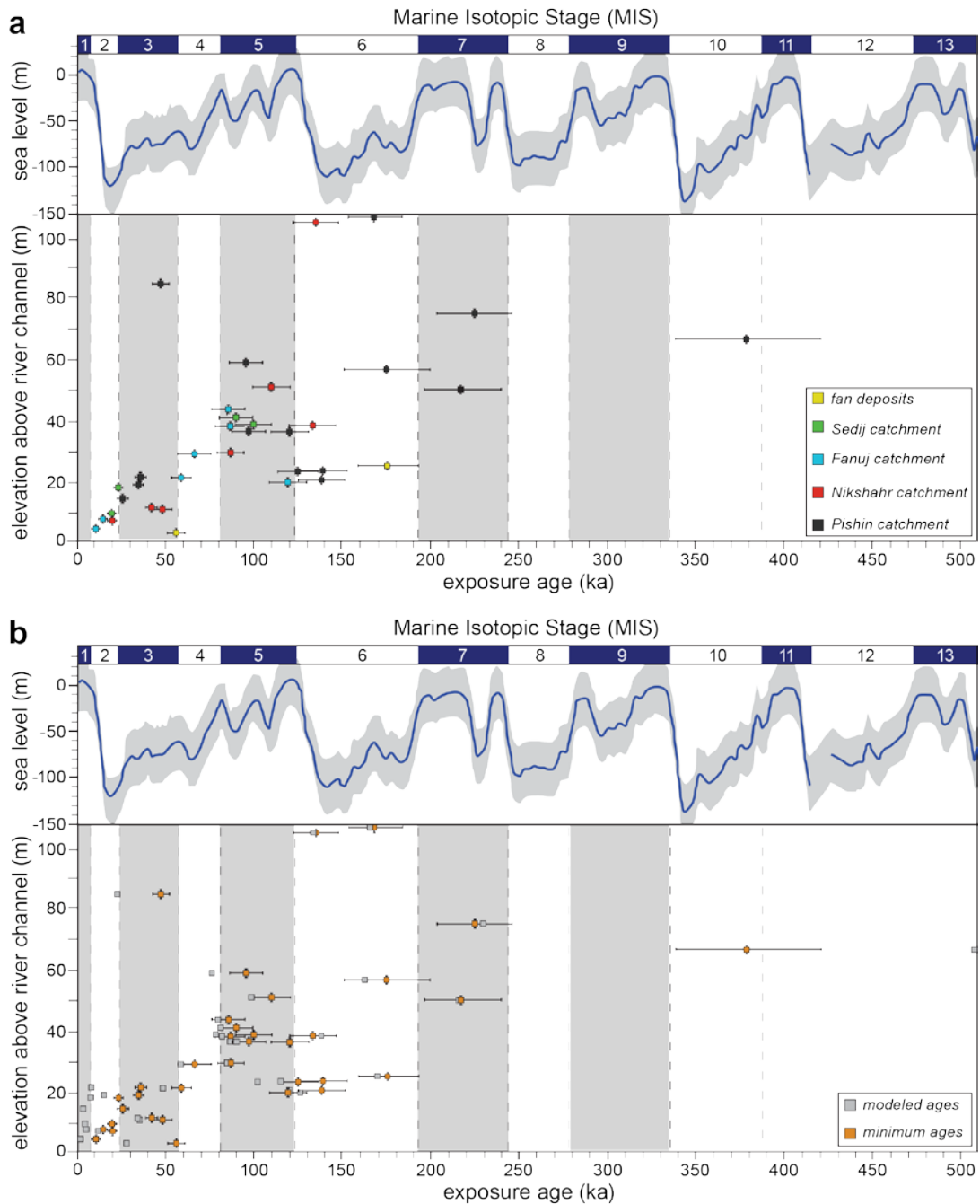


Fig. 16: Terrace correlation based on ^{10}Be surface exposure dating plotted with the eustatic curve for the last 400 ka (Chappell et al. 1996). ^{10}Be ages are represented with their error bars (1σ). Numbers in top bar are Marine Isotopic Stages (MIS) corresponding to glacial (even numbers) and interglacial (odd numbers) periods. a) Uncorrected ^{10}Be ages. b) Comparison between corrected and uncorrected ages. We used the inheritance from each site (Table 1) and a maximum erosion rate of 0.07 cm/ka for age correction (Table 2).

Tectonic forcing is expressed by scattered ages in the Nikshahr and Pishin catchments. The lack of age correlation in accordance to relative terrace levels and the tilting/folding of some terraces demonstrate that they are disconnected surfaces. Disconnection occurs where active growth of folds and thrusts is responsible for localised landscape evolution. This is further supported by coincidence of ensuing high incision rates and field observation of structures with typical geomorphological traits of active tectonics. Therefore, mismatched exposure ages in these catchments cannot be attributed to nuclide inheritance only.

Climatic forcing is recognized in the widespread consistency between the 100ka and 20ka T1 and T2 terrace levels over the four catchments. Such a consistency in age and morphological classification over such a wide area can only be attributed to external, regional processes like climate, since we argued that the basement erodibility cannot be invoked.

One may dispute the reliability and resolution of exposure ages and thus the interpretation we make from their distribution if both inheritance and erosion corrections are not introduced.

For age correction, we applied to each dated site the consistent inheritance obtained from depth profiles and modern channels to correct ages obtained (Table. 2). We also applied a minimum (0.05 cm/ka) and maximum (1 cm/ka) erosion rates to generate modelled ages.

Ages between 20 and 270 ka suffer very small (within error) shifts from uncorrected to modelled values. Accordingly, these ages have a good resolution. Conversely, ages younger than 20 and older than 270 ka shift dramatically with correction and therefore lose their robustness (Fig. 16, Table 2). Therefore the usefulness of quantitative estimates on incision rates is bracketed between these two ages.

6.3. Correlation with Marine Isotopic Stages

The cohabitation of several levels of fluvial terraces generally results from alternating incision and aggradation events linked to rhythmic variations of climate or/ and base level. The last 800 ka changes show intervals of 100 ka in the Milankovitch cycle (Maddy et al. 2005, Bridgland & Westaway 2008). The 20-379 ka record of fluvial terraces in Makran offers a chance to clarify whether these climatic cycles are responsible for regular 100 ka intervals in fluvial deposition. Fluvial terraces in coastal areas were reported to register sea level fluctuations (Blum & Törnqvist 2000) whereas terraces in higher reaches would rather document river discharge and sedimentation due to climate forces (e.g. Tebbens et al. 2000). In fact, uncertainties and resolution inherent to TCN dating often hamper precise correlation with climatic or tectonic events. Our regional scale sampling circumvents misinterpretation relying on single site characteristics and makes correlation to extrinsic events more meaningful and reliable. Yet, the resolution of our TCN ages does not allow straightforward interpretation for terrace formation. Combining information from morphostratigraphy, geomorphology, geochronology and tectonics to strengthen our interpretation, two main sources appear to be responsible for terrace formation in Makran. The ^{10}Be ages obtained from fluvial terraces span from 18 ± 1 to 379 ± 50 ka. Tight age clusters from terraces on a wide region like Makran are received as one average age population that can be confronted to global sea level curves (Chappell et al. 1996, Fig. 16). Seven age populations are identified.

Four are coincidental with large-scale climate changes. The youngest ($\sim 19 \pm 1$ ka) occurs within the Last Glacial Maximum and the other three ($\sim 102 \pm 1$, 207 ± 12 and 379 ± 50 ka) are related to the MIS5, MIS7 and MIS13 interglacial (wet) stages, favourable for aggradation. These four clusters have a 100ka periodicity which supports their interpretation as climatic signals, although the 300+ ka cluster was not found. This interpretation may be disputable for the 379 ± 50 ka terraces because there is the age gap between MIS7 and MIS10. Lacking other sort of evidence and noting that they match a glacial – interglacial transition, it is easier and most plausible to relate abandonment of these oldest surfaces to a climate-induced event.

We associate the abandonments of the $\sim 41 \pm 3$, 135 ± 3 and 176 ± 12 ka terraces to tectonic events for two reasons. They all formed only in the eastern catchments where high incision rates, K_{Sn} values and field observation confirmed more tectonic activity than in the western catchments. Therefore, these abandonment ages are too local to represent a regional, climatic event. Second, the corresponding MIS4 and MIS6 stages are glacial periods. We did not observe any glacial deposit in the studied Makran and there is none reported for this part of Iran. Therefore, a tectonic driven source is the most sensible interpretation.

6.4. Uplift rates

Incision can be used as a proxy for tectonic uplift if incision kept pace with regional uplift (e.g. Burbank & Anderson 2001, Pazzaglia & Brandon 2001) and the river were not adjusting to isostatic or/and eustatic changes. Some studies argued that a river never reaches a state of equilibrium, so that its terraces cannot be used to infer vertical tectonic movement (Kiden & Tornqvist 1998). We did not observe any sign of reoccupation of the strath by a younger channel and we excluded fill terraces for incision/uplift rate calculation. The results show that the mean rates of fluvial incision in Pleistocene times (regionally ~ 0.3 mm/a) are similar to uplift rates previously inferred from marine terraces of the Iranian Makran coast (0.1-0.4 mm/a, Page et al. 1979). This similarity suggests that the same tectonic regime caused uplift of both the fluvial terraces and the marine terraces together. Coastal uplift was apparently faster in Holocene times (2mm/a after Page et al. 1979, 3mm/a in this study); the corresponding difference in uplift rate does not appear in our uncorrected data for fluvial terraces. However, the 13 to 20 ka ages corrected to inheritance and erosion are shifted to <10ka, which then yields also higher incision /uplift rate during the Holocene.

Conclusion

We produced the first absolute ages of the fluvial terraces over a large part of the onshore Makran accretionary wedge. The ^{10}Be exposure ages range between 13 and 320 ka. Cosmogenic radionuclide dates indicate that incision began at least 320 ka ago. The rivers draining central Makran have, since then, undergone several cycles of incision and aggradation.

Two major, regional levels are correlatable over the four adjacent catchments mapped in Central Makran. Our results indicate that terraces were formed at the transition between glacial and interglacial periods. The older one probably dates from the MIS-10; The younger one correlates with MIS 2.

Our results highlight the problems one may face for dating surfaces assuming no erosion and negligible inheritance for very old (>300 ka) or very young (<20 ka) terraces in regions like Makran, with semi-arid climate and moderate tectonic activity.

Obtained ages show that long-term incision occurs at a mean rate of 0.3-0.4 mm/a. The comparison of incision rates in different, adjacent catchments enables distinguishing between this relatively moderate regional, “background” incision rate and higher local incision/uplift (0.8-1 mm/a) rates. The similarity between regional fluvial incision rates (0.3-0.4 mm/a) and Pleistocene coastal uplift rates constrained by the uplifted marine terraces (0.2 mm/a) supports the inference that fluvial rivers responded to a regional, long-term interplay between climatically-driven incision and tectonically-driven surface uplift. The latter reflects the uniform wedge growth due to tectonic underplating during Quaternary times. The obtained uniform incision rate of 0.3 mm/a indicates steady state stage of the wedge on a regional scale. However, perfect steady-state is unlikely on short-length scales. Local instabilities depict localized deformation.

Acknowledgements

This work was supported by the ETH project No. 0-20481-08 and the Swiss National Fond project No. 2-77644-09. Administrative and logistical support by the Geological Survey of Iran is sincerely acknowledged.

Chapter IV

Rate of crustal shortening and non-Coulomb behaviour of an active accretionary wedge: The folded fluvial terraces in Makran (SE, Iran)

N. Haghypour, J.-P. Burg, F. Kober, G. Zeilinger, S. Ivy-Ochs, P.W. Kubik, M. Faridi

This chapter has been published in 2012:

Earth and Planetary Science Letters, **355-356**, 187-198

<http://dx.doi.org/10.1016/j.epsl.2012.09.001>

It has been reformatted for this thesis.

Keywords: Fluvial terraces; ^{10}Be dating; Accretionary wedge; Shortening rate

Abstract:

We surveyed fluvial terraces to decipher the Quaternary increment of crustal shortening and shortening rate in the on-shore Makran Accretionary Wedge. We focused on three major catchment basins and associated fold systems. Terrace profiles reconstructed from differential GPS measurements combined with DEM revealed two regional dominant wavelengths, about 5 km in the northern part of the study area and about 15 km to the south. These two wavelengths suggest the existence of two active décollement layers at two rooting depths. The average shortening rate due to folding is estimated at 0.8-1.2 mm/a over the last 130 ka. This accounts for 10-15% of the shortening rate ($\sim 8\text{mm/a}$) given by kinematic GPS measurements between Chabahar and Bazman and 3% of the convergence between Arabia and Eurasia, across the Makran subduction zone. Despite active deformation and a relatively high shortening rate, the geophysical record shows nearly absent seismic activity in Makran. We propose that strain accumulated in folds over intermediate décollement levels within a thick, incompletely lithified sedimentary cover explain the essentially aseismic, recent tectonics in this region. The importance of folds points to imperfect Coulomb behaviour of the wedge.

Introduction

Although the Makran is one of the largest exposed accretionary wedges, the present day seismicity is amazingly low compared to adjacent areas such as the Zagros collision zone and other subduction zones (e.g. Talebian and Jackson, 2004; Engdahl et al., 2006; Gholamzadeh et al., 2009; Musson, 2009). This peculiarity raises the question as to whether deformation lets apart the Makran region of the Arabia/Eurasia convergence zone or, instead, is imperceptibly seismogenic. This peculiarity also addresses the more general question concerning the seismic and deformation behaviour of subduction zones, which are known as devastatingly active. Tsunamis that have reached the coasts of Pakistan and Iran in the past (Page et al., 1979; Ambraseys and Melville, 1982; Byrne et al., 1992; Heidarzadeh et al., 2008) demonstrate that the offshore Makran Subduction is no exception. Why is onshore Makran so silent? Deformed geomorphic surfaces such as fluvial-alluvial terraces can be used to constrain recent rates of horizontal shortening in active fold-and-thrust belts (Rockwell et al., 1988; Molnar et al., 1994; Burbank et al., 1999; Lavé and Avouac, 2000; Scharer et al., 2006). Therefore, we surveyed the well-preserved fluvial terraces across the exposed Makran Accretionary Wedge (SE Iran) to gain new insight on recent folding, tectonic uplift, shortening rates and their relationships with active décollement layers and wedge growth. Few studies have addressed Quaternary deformation and marine terrace uplift along coastal Makran (Reyss et al., 1999; Hosseini-Barzi and Talbot, 2003), but inland fluvial terraces had not been studied beyond reconnaissance surveys (Falcon, 1975). We first mapped and correlated terraces on Digital Elevation Models (DEM) corroborated by ground assessment of classical geomorphological features. We use ^{10}Be exposure dating (Gosse and Phillips, 2001) to better constrain regional correlations and quantify deformation rates of the structures.

Subsequently, we focused on the three sites where the major rivers cut through folded terraces. Dating and structural measurements allow calculating the crustal shortening rate over the last ca 130 ka. Results indicate that active folding absorbs ~ 15 % of the active shortening recorded by GPS measurements, which may partly explain the missing seismicity of onshore Makran. Creeping more than rupturing weak, blind thrust faults and décollements beneath the folded terraces may participate in this apparent silence, over the short time scale the instrumental record contains.

1- Setting

1-1 Tectonic setting

The Makran accretionary wedge is due to the ongoing subduction of the Arabian Plate beneath the Eurasian plate (Farhoudi and Karig, 1977; McCall, 1997). To the west, Makran is separated from the Zagros continental collision by the dextral Minab strike slip fault. To the East, It is bounded by the sinistral Chaman Fault, in Pakistan (Fig.1). Tectonic reconstructions consider that subduction initiated in the Late Cretaceous (e.g. Arthurton et al., 1982; Berberian et al., 1982). Seismic profiles indicate that the Makran slab dips 2 to 8° to the

north (Kopp et al., 2000; Schlüter et al., 2002). About 7km thick sediments on the incoming oceanic crust are partly underplated below an active décollement (Kopp et al., 2000). The sedimentary hanging wall of the main décollement is folded and imbricated in the modern accretionary prism (e.g. White, 1982; Ellouz-Zimmermann et al., 2007; Grando and McClay, 2007). There is no subsurface data available for onshore Makran. The published maps by the Geological Survey of Iran (1/1'250'000 scale) and associated reports (McCall and Kidd, 1982; McCall, 1983; 1997; 2002) were the only documents for geological background in terms of general structure and stratigraphy for this onshore Makran, in Iran. In this study, our interpretations are mainly based on recent mapping and structural analysis of Central Makran (Dolati, 2010; Burg et al., 2012).

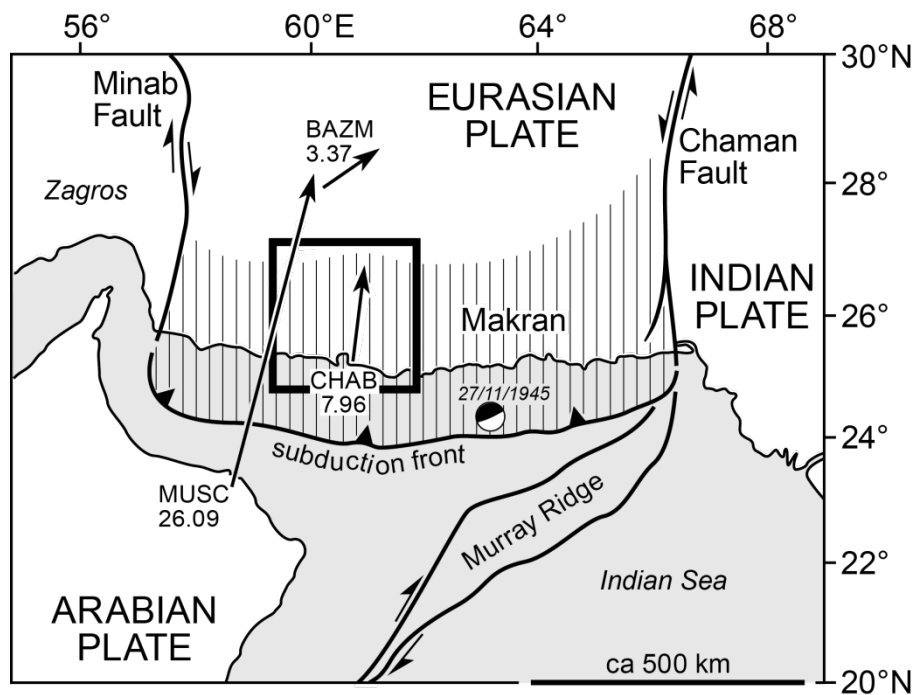


Fig. 1: Tectonic setting of the Makran accretionary wedge (hatched area) including linear velocities (arrows with numbers = N-S movement component in mm/a) of the Arabian plate (MUSC= Muscat), the Makran coast (CHAB = Chabahar) and Central Iran (BAZM = Bazman) with respect to stable Eurasia after Vernant et al. (Vernant et al., 2004). Framed: studied area. Focal mechanism of the 8.1 magnitude earthquake of November 27, 1945 after Byrne et al. (Byrne et al., 1992).

1-2 Seismicity and geodesy background

The present day seismicity level in onshore Makran is low. The largest recorded earthquake is the 27th November 1945 event (8.1 Mw, Page et al., 1979; Ambraseys, 1982) in southeastern Makran, offshore Pakistan (Fig.1). Western Makran is reported as aseismic subduction zone with even less seismic activity than Eastern Makran. However, Ambraseys and Melville (Ambraseys and Melville, 1982) and Byrne et al. (Byrne et al., 1992) argued that a big earthquake occurred in western Makran on 18 February 1483. Byrne et al. (Byrne et al., 1992) suggested that the low apparent friction and high pore pressure of unconsolidated and water-saturated sediments causes the low seismicity. Mud volcanoes along coastal Makran support the concept of overpressured layers in the wedge (Schlüter et al., 2002).

Reassessment of the 1945 to 1980 earthquakes suggests that their sources are < 30km deep (Jackson and McKenzie, 1984; Byrne et al., 1992). Elevated marine terraces along the Makran coast indicate Quaternary surface uplift (Falcon, 1975; Vita-Finzi, 1975; Page et al., 1979). To the south of Konarak (Fig. 1S, supplementary), they reach an altitude of 246 m a.s.l. The uplift rate derived from Uranium series on shells and from ^{14}C chronology, which yields minimum ages, has been estimated at 0.2 mm/a (Page et al., 1979; Reyss et al., 1999). These rates have been ascribed to coseismic uplift.

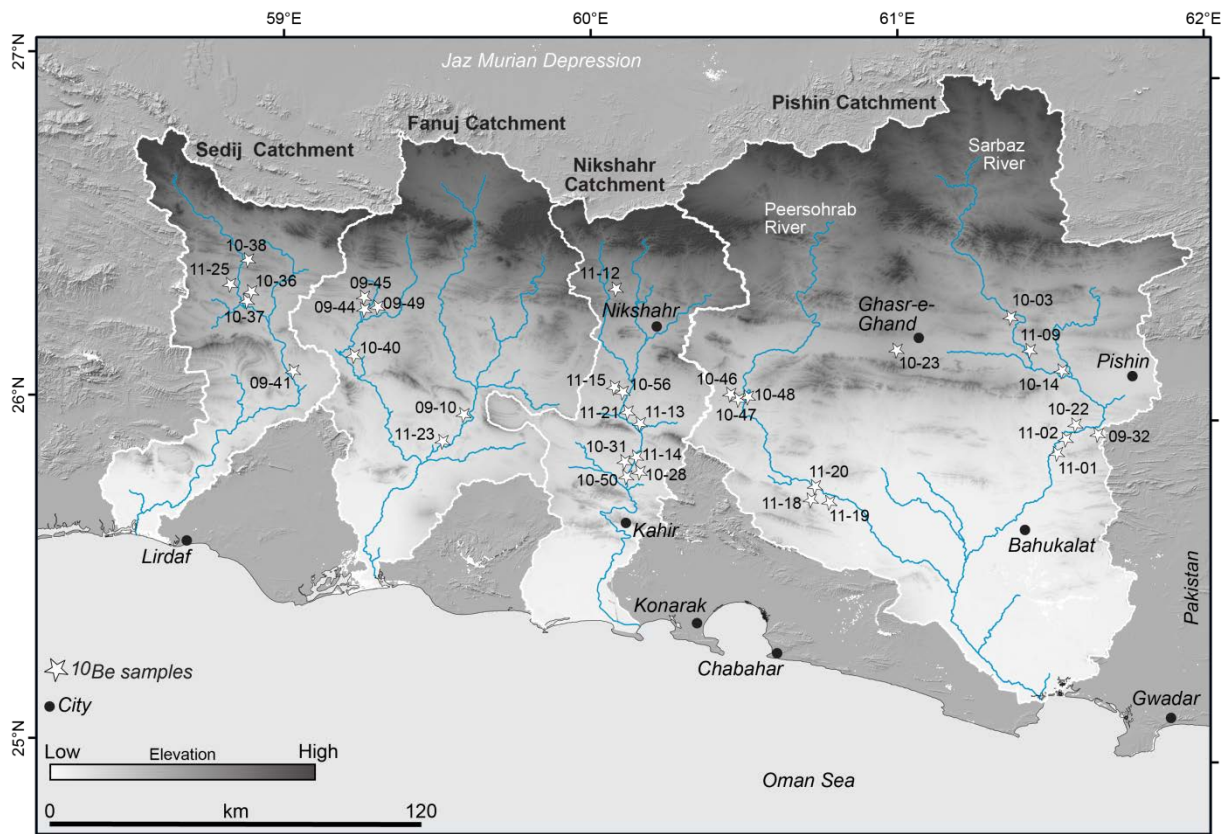


Fig. 1S: Simplified map of the studied catchments in Makran, with Q-Mak sample locations for ^{10}Be exposure dating (measurements, Table 1S). Background = Aster Digital Elevation Model (G-DEM).

Geodetic data document a roughly N-S convergence rate of 26 mm/a between the Arabian and Eurasian plates at the longitude of the Gulf of Oman (Masson et al., 2005). Most of this convergence is absorbed in the Makran subduction. However, a convergence rate of $ca\ 8 \pm 0.1$ mm/a is measured between Chabahar, on the Makran coast, and Bazman in Central Iran (Fig. 1, Vernant et al., 2004; Masson et al., 2005). Therefore, there is shortening within the onshore Makran wedge.

1-3 Structural background of onshore, Central Makran

Changes in lithostratigraphic content and structural pattern outline four tectono-statigraphic units separated by major thrust faults (Figs. 2a and b). From the north to the south, i.e. from the structural top to bottom, these units are: North Makran, Inner Makran, Outer Makran and Coastal Makran (Dolati, 2010; Burg et al., 2012).

North Makran mainly consists of Cretaceous igneous rocks and associated deep marine sediments bounded, to the south, by the Bashakerd Thrust (Fig. 2a). Detailed cross sections and structural measurements indicate generally open, large wavelength (>200m), E-W trending folds (Dolati, 2010). Headwaters of the studied rivers did not leave workable terraces on this unit.

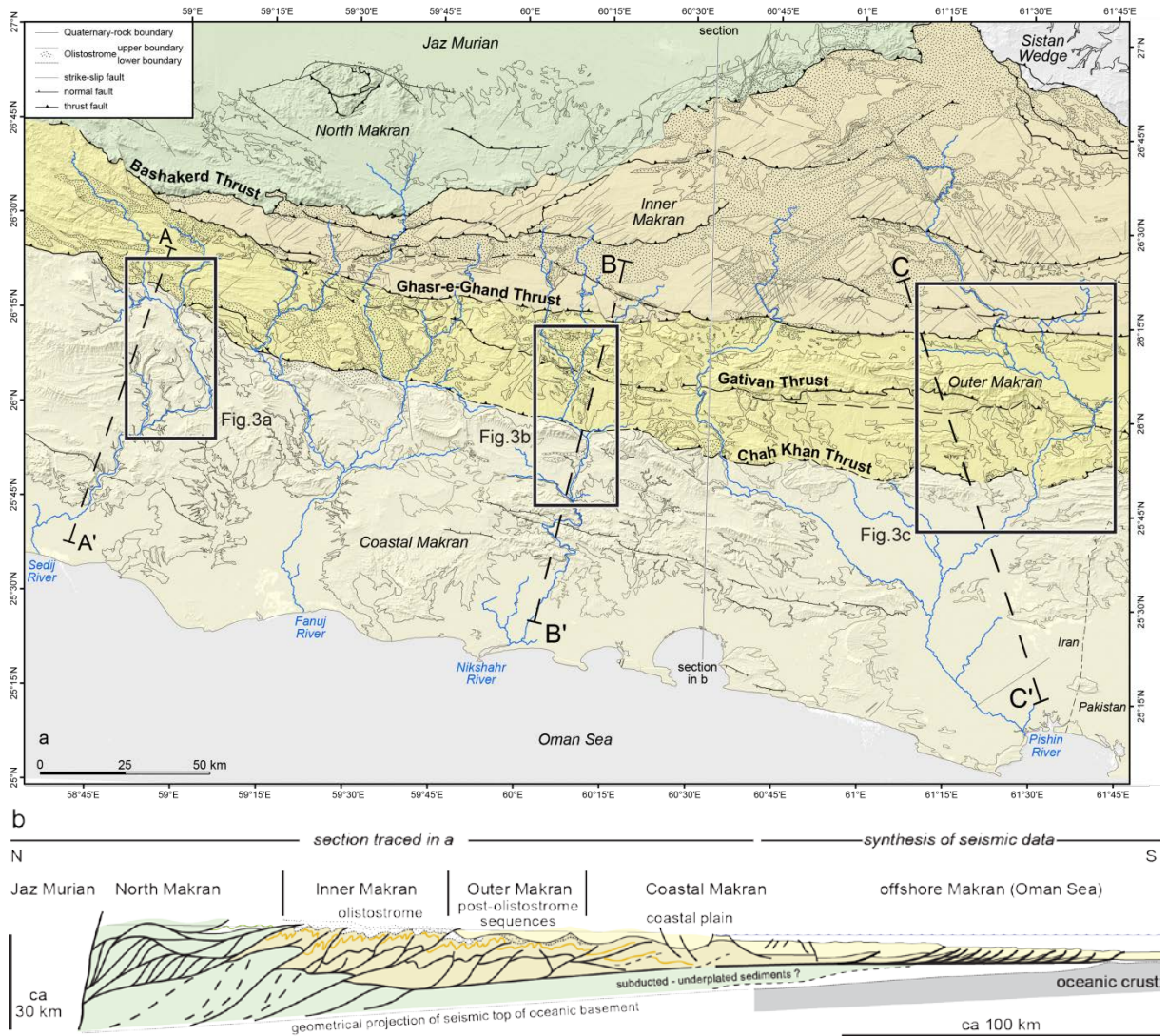


Fig. 2: a) Simplified geological map of Central Makran, in Iran after the geological maps published by the Geological Survey of Iran, (Dolati, 2010) and unpublished work. Tectono-stratigraphic units (coloured) explained in the text. Frames are figure 3. A-A', B-B' and C-C' dashed lines = topographic sections of Fig 5. Background = Aster Digital Elevation Model (G-DEM). b) Cross-section delineated in figure 2a (after Burg et al., 2012).

Inner Makran exposes mostly Upper Eocene to Lower Miocene turbidites. A flat-and-ramp thrust system responsible for strata-parallel gliding surfaces and hanging wall flat-footwall ramp and hanging wall ramp-footwall flat relationships (e.g. McClay, 1992) dominates the structural style. Related folds are close to tight, commonly associated with axial-plane cleavage, which demonstrates significant internal strain besides faulting. All structures and kinematic indicators are consistent with nearly N-S compression (Burg et al., 2012). This unit

is subdivided into six thrust sheets. The bottom Ghasr-e-Ghand Thrust (Fig.2a) displays evidence for recent tectonic activity and is most relevant to this study.

Outer Makran mostly comprises Lower to Middle Miocene siltstones and marls with calcareous sandstones. Nearly E-W trending folds are generally more open and rounded with larger wavelength than in Inner Makran (Dolati, 2010; Burg et al., 2012). The Chah Khan Thrust is the basal boundary of this unit subdivided in upper and lower thrust sheets by the Gativan Thrust. Particularly intense shear structures along the Gativan Thrust suggest that the deformed Middle Miocene shales contain a décollement horizon (Burg et al., 2012). Most studied terraces straddle Outer Makran.

A widespread Tortonian (7-11 Ma) olistostrome (Burg et al., 2008) covered the three previous units. It is a valuable marker to identify old thrust contacts, which it sealed, and those that cut it while being reactivated as out-of sequence faults, in younger times (Burg et al., 2012). The unconformity indicates that most of the onshore Makran fold-and-thrust belt was deforming during the Early to Middle Miocene.

Coastal Makran exposes mostly Late Miocene slope marls grading into Pleistocene coastal to continental deposits. Nearly E-W, cylindrical folds are very open to gentle, with very large (several kilometres) wavelength. Normal faults, which are not seen in other units, cut lithologies younger than Late Miocene (Dolati, 2010).

The general cross-section (Fig. 2b) combining surface, geological observation and offshore, seismic data places the active subduction interface at about 20 km depth below Inner Makran. The mapped flat-and-ramp thrust system that includes post-Tortonian, out-of-sequence thrusts and the morphologically recent/active Ghasr-e-Ghand Thrust should logically splay from this wedge/footwall contact and deform older décollement horizons such as in the Middle Miocene (Gativan Thrust) and Upper Oligocene shales (Burg et al., 2012).

2- Methods

2-1 Mapping and surveying

We have surveyed the fluvial terraces of four adjacent catchments in the east-central Makran, in Iran (Figs. 2a and 1S) with the aim to evaluate the spatio-temporal variation of incision rate as proxy of surface uplift and coeval Quaternary deformation. In this study, exposure ages obtained in Fanuj Catchment were used only for regional correlation. We excluded this catchment for profile construction and shortening calculation because its fluvial terraces are not continuous enough and sufficiently preserved to provide reliable results. Field mapping complemented the analysis of aerial photographs and satellite images to produce detailed maps (Fig. 3). Details of this analysis are beyond the scope of the present work whose main objective is to constrain the rates of shortening and highlight the crustal-scale deformation responsible for surface structures of the onshore wedge.

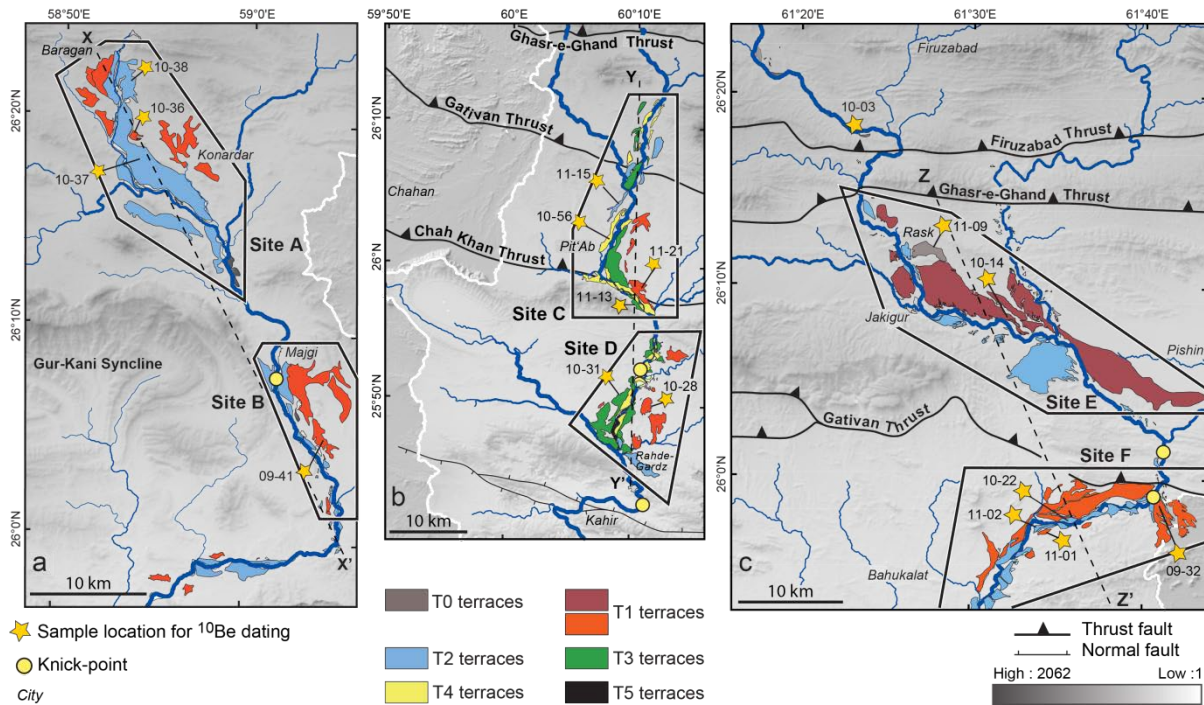


Fig. 3: Morphotectonic maps of fluvial terraces along (a) Sedij River. (b) Nikshahr River and (c) Sarbaz River. X-X', Y-Y' and Z-Z' dashed lines = projected profiles in Fig. 7. Background and thrust traces as in Fig. 2a.

We characterized the deformation pattern from field observations. Tilted and warped terraces (Fig. 4a-b) reflect recent to active folding. We measured the topography of these terraces to calculate recent shortening rates across major folds axes.

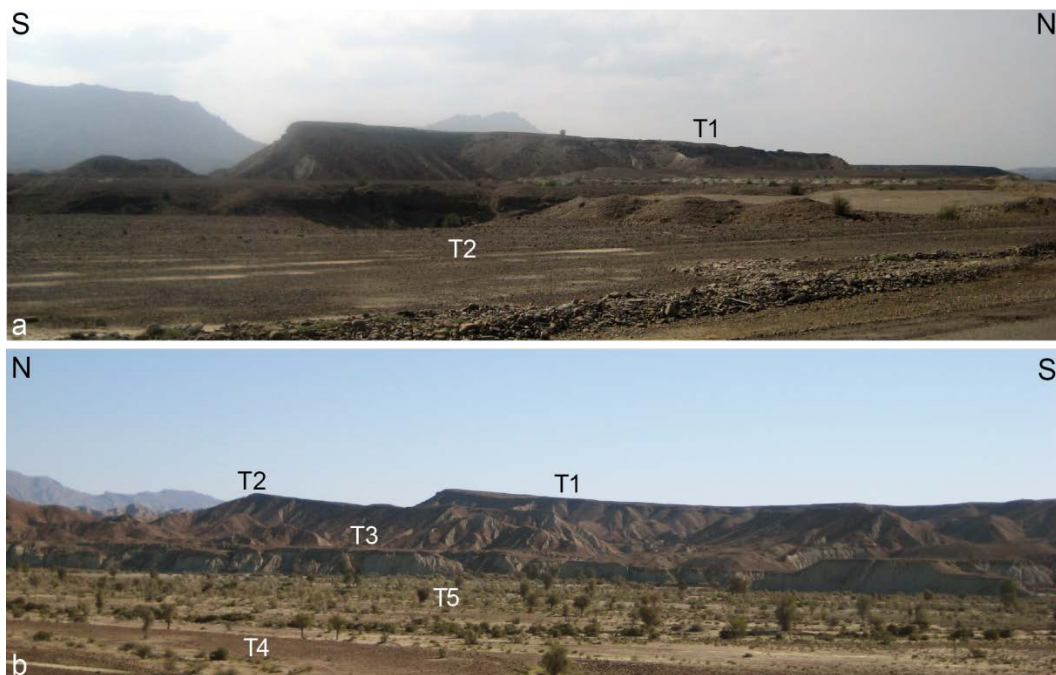


Fig. 4: Field photographs of studied fluvial terraces: (a) Tilted T1 terrace of Pishin catchment (SW of Bahukalat, Fig. 1S, view from GPS: N25°46'49.57", E061°28'42.30"); (b) Folded terraces at site D near Rahde-Gardz (Fig. 3b, view from GPS: N25°50'18.95", E060°09'31.07");

For precise construction of the terrace surfaces we used Trimble Real Time kinematic (RTK), Differential Global Positioning System DGPS combined with ASTER Digital Elevation Model (G-DEM) with 1 arcsec (~ 30 m) resolution for places difficult to access. We treated three adjacent major rivers and intentionally focused on sites with a) strath terraces to avoid over/under-estimating incision/uplift rates and to construct precisely the terrace geometry; b) terraces with good surface preservation and continuity to make reconstructions and correlations more reliable and c) large spatial distribution to cover large structures. We constructed profiles by projecting the terrace surfaces on lines sub-perpendicular to the local structural trends of basement rocks (Fig. 3). The elevations measured by DGPS and handheld GPS were corrected for the thickness of the alluvium cover. We assign an arbitrary uncertainty of 5m for sample elevation measured by handheld GPS. The uncertainties for the point measured by the RTK DGPS are 4cm +1 ppm of the signal RMS in the vertical direction. Topographic- and cross-sections give insights on the control of relief distribution by regional structures. The large anticlines are interpreted as detachment buckle folds and ramp-anticlines separated by flat-synclines that form intermontane basins (Fig. 5, Burg et al., 2012). The fluvial terraces are nested mainly in these flat-synclines.

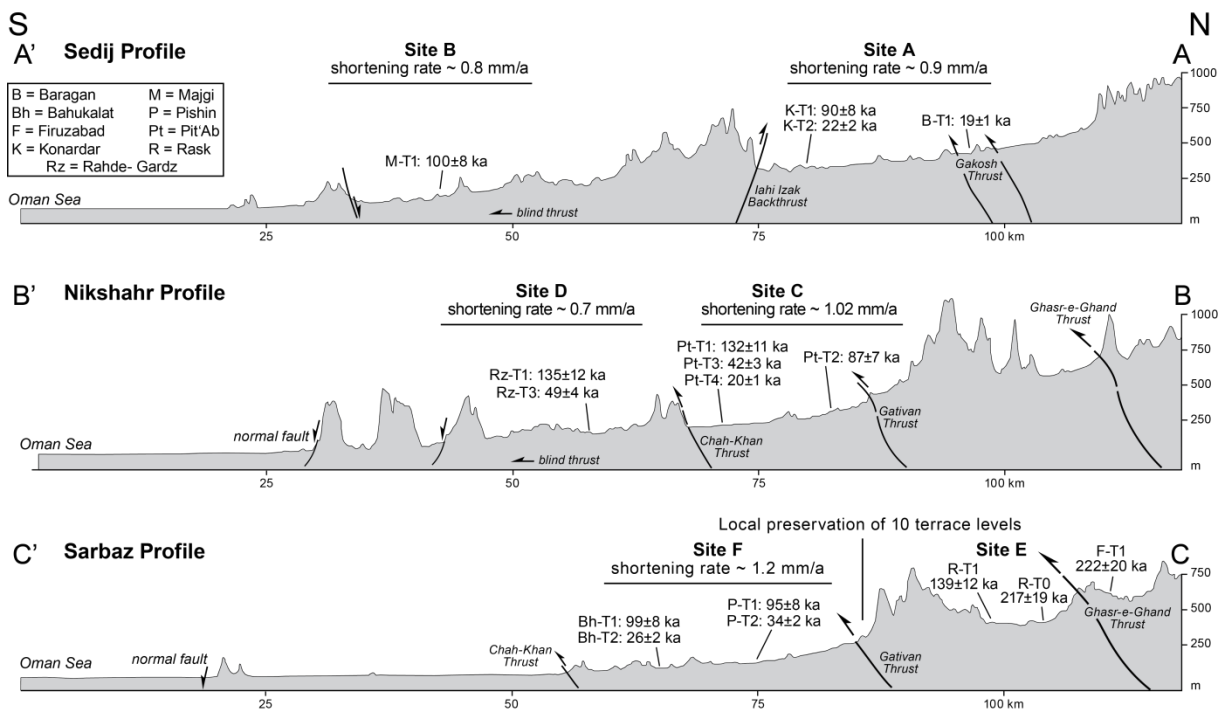


Fig. 5: Topographic sections (A-A', B-B' and C-C' dashed lines traced in Fig. 2a). The investigated terraces are nested in topographic flats on basement synforms (not represented here, see (Dolati, 2010)). Terraces labelled after their location name (abbreviations in inset) and from highest (T1) to lowest (T4).

2-2 Sampling - Terrace description

The arid to semi-arid climate in Makran (precipitation: <113 mm/a) favoured extensive preservation of fluvial terraces. On the surfaces, the terraces are characterized by a desert-packed varnished pavement and pebble-sized (3 to 20 cm) clasts of mainly calcareous sandstone, quartzite, chert, and radiolarite. There are no signs of bioturbation (Fig. 4c).



Fig. 4c: Pavement of the T1 terrace at site E. GPS point: N26°09'14.96", E061°30'14.47"

In profile, the terraces display clast-supported, rounded pebbles typifying their fluvial environment (supplementary, Fig 2Sa). Our field work did not indicate any stratigraphical or soil development so that we consider one depositional event for terrace formation. Therefore, the investigated terraces can be good estimate of river abandonment. The lack of loess deposits (overbank) on the Makran terraces makes the surface exposure dating more reliable (Fig. 6a-b). The location and geomorphic setting of samples are recorded in Table 1S. More detailed description of terraces at each site used in this work is given in the result section.

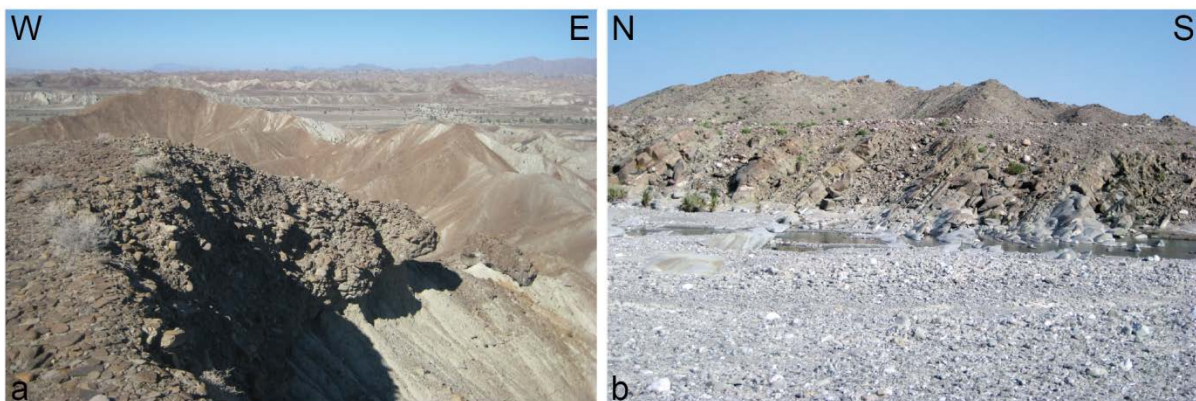


Figure 2S: Field photographs of studied fluvial terraces: **(a)** Profile view of Rz-T1 at Site D (Fig. 3b, view from GPS: N25°50'39.26", E060°10'06.51"); **(b)** Bedrock incision and strath terrace along Sedij River (Fig. 3a; GPS: N26°07'35.01", E059°01'34.70")

2-3 ^{10}Be terrestrial cosmogenic nuclide surface exposure dating

The fluvial terraces in Makran have lack of cobbles. Consequently we applied the amalgamation method (Anderson et al., 1996; Repka et al., 1997; Hancock et al., 1999) to constrain the abandonment ages. All samples were taken from flat and planar surfaces far from topographic highs and human disturbance. For each sample we took a large number ($n > 30$) of quartz and quartz-rich pebbles of comparable size which are the most resistant lithologies in our sites.

With the aim of determining the inherited nuclide component, 9 amalgamated samples have been taken from two depth profiles that were excavated to a depth of ~ 2 m in two different catchments (Fig. 6), one from an old surface (~ 139 ka) and the other from a very young surface (~ 20 ka). This was to determine the possible influence of inheritance for both young and old fluvial deposits in Makran.

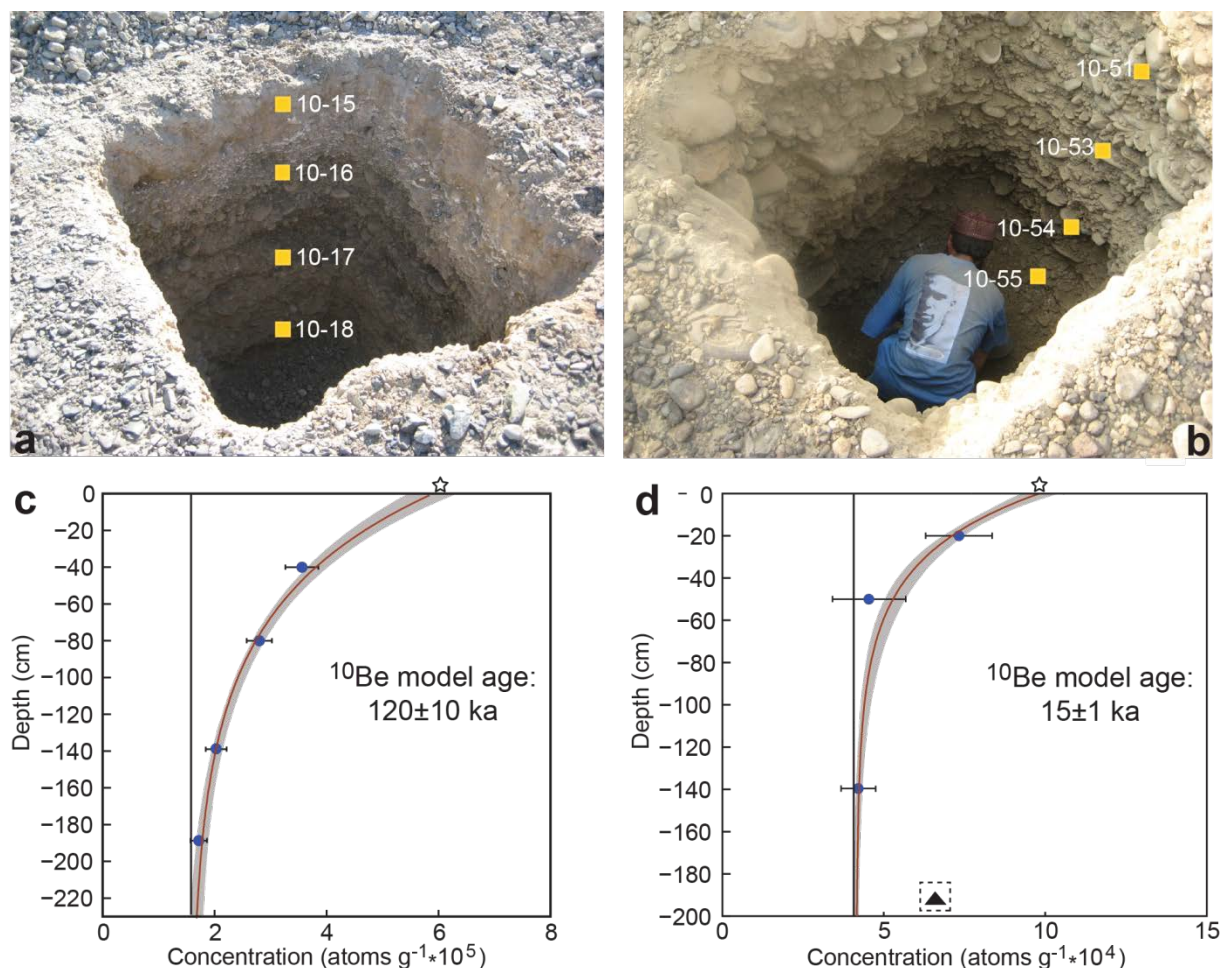


Fig. 6: **a)** Excavated pit in R-T1 (same place as Q-Mak-10-14 Fig. 3c, GPS: N26°08'06.04", E061°33'14.50") and **b)** pit in Pt-T4 (same place as Q-Mak-10-56 Fig. 3b, GPS: N26°01'58.55", E060°08'12.16"). The dug terraces are homogeneous and clast-supported without unconformity and soil. Concentration versus depth plots **c** and **d** illustrate the best fit regression (red lines) from 100 000 Monte Carlo simulations through the depth samples (blue circles) from pits in **a** and **b**, respectively. Grey curves cover the solution space. Stars represent the calculated concentrations in amalgamated surface samples. The lower sample in Pt-T4 profile (black Triangle in **a**) was excluded from simulations because its nuclide concentration with depth does not follow the theoretical rule. See Table 1S for analytical results and text for further discussion.

Sample Name	Surface	Latitude N (D,D)	Longitude E (D,D)	Elevation (m.a.s.l.)	Depth Cm	[Be-10]blank corrected ^a (10 ⁵ atoms g ⁻¹)	± (10 ⁵ atoms g ⁻¹)	Standard	Minimum exposure age (ka)	erosion rate = 0	erosion rate = 0.7 m/Ma	Topographic Shielding
Seojj Catchment												
Q-Mak-10-36	K-T1	26.3191	58.8900	411	0	4.489	0.20	07KNSTD	90 ± 8		96 ± 9	1
Q-Mak-10-37	K-T2	26.3161	58.8838	388	0	1.134	0.06	07KNSTD	22 ± 2		23 ± 2	1
Q-Mak-10-38	B-T2	26.4058	58.8902	471	0	0.998	0.05	07KNSTD	19 ± 1		19 ± 1	1
Q-Mak-09-41	M-T1	26.0850	59.0622	241	0	4.373	0.10	07KNSTD	100 ± 8		107 ± 10	1
Q-Mak-11-25	modern channel	26.3449	58.8822	380	0	0.755	0.05	07KNSTD	[15 ± 1]		[15 ± 1]	0
Fanj Catchment												
Q-Mak-09-49*		26.3188	59.3258	417	0	2.960	0.10	07KNSTD	59 ± 5		61 ± 5	1
Q-Mak-09-44*	modern channel	26.3125	59.3188	370	0	0.563	0.05	07KNSTD	[11 ± 1]		[11 ± 1]	0
Q-Mak-09-45*		26.3130	59.3202	373	0	0.656	0.07	07KNSTD	13 ± 1		13 ± 1	1
Q-Mak-10-40*		26.1966	59.2669	300	0	3.957	0.10	07KNSTD	86 ± 7		91 ± 8	1
Q-Mak-09-10*		25.9817	59.6371	180	0	2.807	0.30	07KNSTD	67 ± 5		69 ± 4	1
Q-Mak-11-23*		25.8836	59.5755	130	0	3.488	0.10	07KNSTD	87 ± 7		91 ± 8	1
Nikshahr Catchment												
Q-Mak-10-28	Rz-T1	25.8350	60.1813	240	0	5.801	0.20	07KNSTD	135 ± 12		147 ± 14	1
Q-Mak-10-31	Rz-T3	25.8413	60.1627	144	0	2.016	0.10	07KNSTD	49 ± 4		50 ± 4	1
Q-Mak-10-56	Pt-T4	26.0330	60.1366	273	0	0.949	0.04	07KNSTD	20 ± 1		21 ± 1	1
Q-Mak-10-51	depth-profile	26.0330	60.1366	273	20 ± 10	0.710	0.03	07KNSTD				
Q-Mak-10-53	depth-profile	26.0330	60.1366	273	50 ± 10	0.416	0.03	07KNSTD				
Q-Mak-10-54	depth-profile	26.0330	60.1366	273	140 ± 10	0.430	0.05	07KNSTD				
Q-Mak-10-55	depth-profile	26.0330	60.1366	273	180 ± 10	0.576	0.06	07KNSTD				
Q-Mak-11-13	Pt-T3	25.9621	60.1624	220	0	1.835	0.07	07KNSTD	42 ± 3		43 ± 3	1
Q-Mak-11-15	Pt-T2	26.0425	60.1380	302	0	3.993	0.10	07KNSTD	87 ± 7		92 ± 8	1
Q-Mak-11-21	Pt-T1	25.9975	60.1438	281	0	5.858	0.20	07KNSTD	132 ± 11		143 ± 14	1
Q-Mak-11-14	modern channel	25.8491	60.1686	144	0	1.949	0.07	07KNSTD	[47 ± 4]		[49 ± 4]	0
Q-Mak-11-12		26.3707	60.1131	759	0	6.966	0.70	07KNSTD	110 ± 9		118 ± 11	1
Q-Mak-10-50	modern channel	25.8327	60.1657	133	0	0.590	0.04	07KNSTD	[14 ± 1]		[14 ± 1]	0
Pishin catchment												
Q-Mak-11-01	Bh-T1	25.9336	61.5513	135	0	3.988	0.15	07KNSTD	99 ± 8		105 ± 10	1
Q-Mak-10-22	Bh-T2	25.9543	61.5543	117	0	1.059	0.09	07KNSTD	26 ± 2		26 ± 2	1
Q-Mak-09-32	P-T1	25.9641	61.6816	209	0	4.033	0.10	07KNSTD	95 ± 8		100 ± 9	1
Q-Mak-11-02	P-T2	25.9341	61.5477	116	0	1.376	0.07	07KNSTD	34 ± 2		34 ± 3	1
Q-Mak-11-09	R-T0	26.1756	61.4638	391	0	10.245	0.30	07KNSTD	217 ± 19		251 ± 27	1
Q-Mak-10-14	R-T1	26.1336	61.5569	283	0	6.190	0.30	07KNSTD	139 ± 12		152 ± 15	1
Q-Mak-10-15	depth-profile	26.1336	61.5569	283	40 ± 10	3.514	0.10	07KNSTD				
Q-Mak-10-16	depth-profile	26.1336	61.5569	283	80 ± 10	2.748	0.10	07KNSTD				
Q-Mak-10-17	depth-profile	26.1336	61.5569	283	140 ± 10	1.837	0.10	07KNSTD				
Q-Mak-10-18	depth-profile	26.1336	61.5569	283	190 ± 10	1.672	0.07	07KNSTD				
Q-Mak-10-03	F-T1	26.2973	61.3936	558	0	11.810	0.40	07KNSTD	222 ± 20		258 ± 28	1
Q-Mak-10-23*	G-T1	26.1911	61.0767	545	0	7.435	0.28	07KNSTD	138 ± 12		151 ± 14	1
Q-Mak-10-46*		26.0494	60.5197	327	0	2.216	0.08	07KNSTD	47 ± 2		48 ± 4	1
Q-Mak-10-47*		26.0447	60.5247	264	0	1.610	0.06	07KNSTD	35 ± 3		36 ± 3	1
Q-Mak-11-18*		25.7561	60.7930	117	0	6.759	0.07	07KNSTD	174 ± 15		195 ± 20	1
Q-Mak-11-19*		25.7505	60.8163	84	0	4.801	0.10	07KNSTD	125 ± 11		135 ± 13	1
Q-Mak-11-20	modern-channel	25.7600	60.7889	54	0	1.253	0.05	07KNSTD	[32 ± 2]		[33 ± 2]	0
Q-Mak-10-48	modern channel	26.0458	60.5266	245	0	2.162	0.09	07KNSTD	[48 ± 4]		[50 ± 4]	0

Table 1S: Sample and analytical data for age calculations

* = ages used for temporal correlation only.

^a Calculated using 07KNSTD standard and calibration.

^b Model exposure ages assuming no inheritance, zero erosion. Standard atmosphere calculated using the CRONUS-Earth (Balco et al., 2008) Version 2.2. A constant production rate model and scaling scheme for spallation of (Lal, 1991) / (Stone, 2000). The used reference spallogenic ¹⁰Be production rate of $4.49 \pm 0.39 \text{ atom g}^{-1} \text{ yr}^{-1}$ ($\pm 1\sigma$, SLHL) and muonogenic production after (Heisinger et al., 2002). The quoted uncertainties are the 1σ internal error. A mean blank ¹⁰Be/⁹Be = 0.004×10^{12} was used for correction.

We employed the Monte Carlo approach of (Hidy et al., 2010) to determine the ¹⁰Be model ages of these two depth profiles. Six amalgamated samples were also taken from modern channels in four catchments (Table 1S) with the assumption that the erosion and discharge rates of these clasts are similar to those that formed the dated abandonment. The collected clasts were crushed; the chemical treatment is based on standard methods (e.g. Kohl and Nishiizumi, 1992; Bierman and Nichols, 2004).

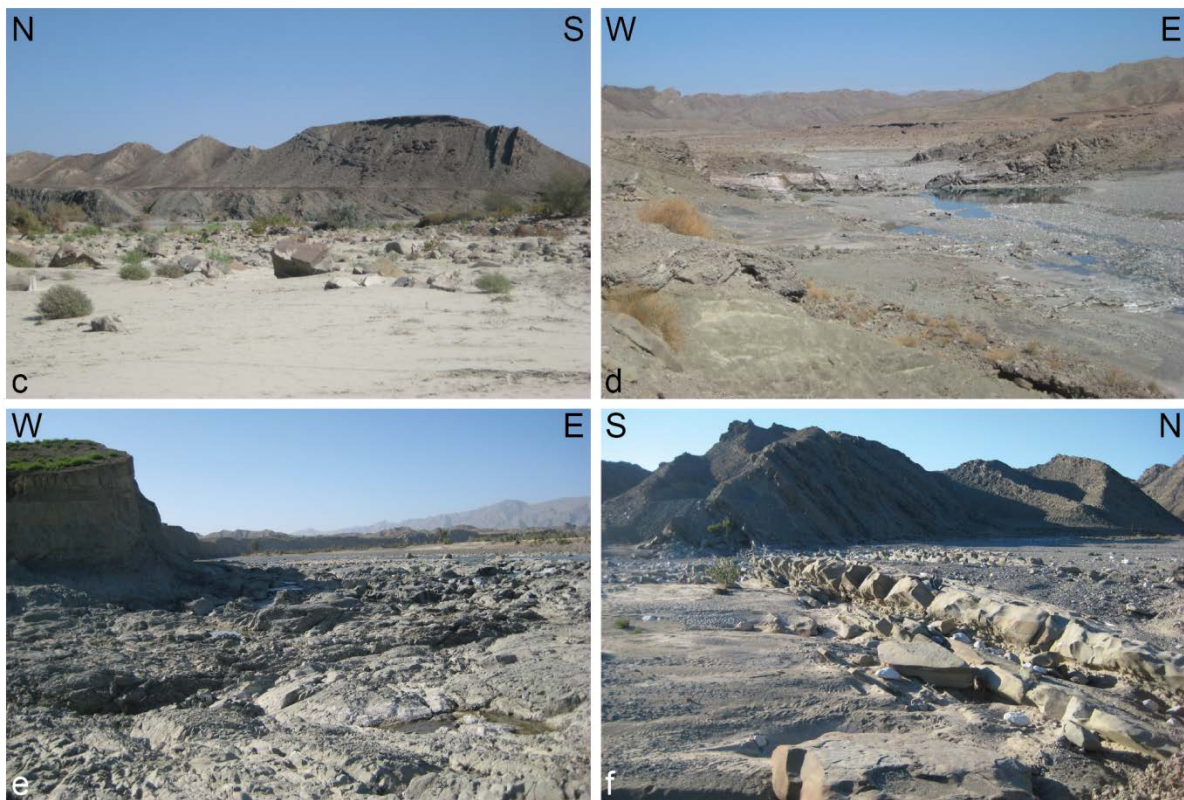


Figure 2S: Field photographs of studied fluvial terraces: **(c)** Bedrock incision and two strath levels along Peersohrab River (Fig. 1S; GPS: N26°02'53.92", E060°31'51.29"); **(d)** Bedrock incision at Site E (Fig. 3a, GPS: N26°19'38.30", E058°52'41.89"); **(e)** Bedrock incision at Site D along Nikshahr River (Fig. 3b, GPS: N25°50'00.43", E060°10'54.64"); **(f)** Bedrock incision along Fanuj River (Fig. 1S, GPS: N26°18'59.18", E059°31'42.57").

The samples were analyzed for ¹⁰Be/⁹Be ratio at the ETH Zurich Tandem Accelerator Mass Spectrometry (AMS) facility (Kubik and Christi, 2010). All ¹⁰Be/⁹Be ratios were normalized to the ICN 01-5-1 AMS standard with a nominal value of ¹⁰Be/⁹Be = 28.1×10^{-11} (Nishiizumi et

al., 2007). The used ^{10}Be half-life is 1.387 ± 0.012 Ma (Chmeleff et al., 2010; Korschinek et al., 2010). Surface exposure ages were calculated using the CROUNUS on-line age calculator, Version 2.2 (Balco et al., 2008). All calculated ^{10}Be ages are model exposure ages, with and without correction for erosion. Therefore the given ages for zero erosion model (Table 1S) should be considered as minimum ages.

Ages corrected to erosion are calculated using erosion rate of 0.7 m/Ma which is reported in the areas with similar climatic condition to Makran (Matmon et al., 2009; Placzek et al., 2010) and is consistent with the results from depth profile. The presented ages in result and discussion sections are neither corrected for inheritance nor erosion because the results from depth profiles concerning age and erosion show negligible influence on our determined surface ages (see discussion 4.1).

2-4 Uplift and shortening estimation

We used the profiles of folded fluvial terraces (strain markers) and applied the classical area-conservation method to measure the amount of shortening due to folding (Rockwell et al., 1988; Suppe and Medwedeff, 1990; Mitra, Shankar, 2003; Daëron et al., 2007). Being aware that the continuous preservation of geomorphic markers is essential to apply this method (Lavé and Avouac, 2000), we choose sites where well-preserved strath terraces could be traced all along across the basement structures (Fig. 2a and 3).

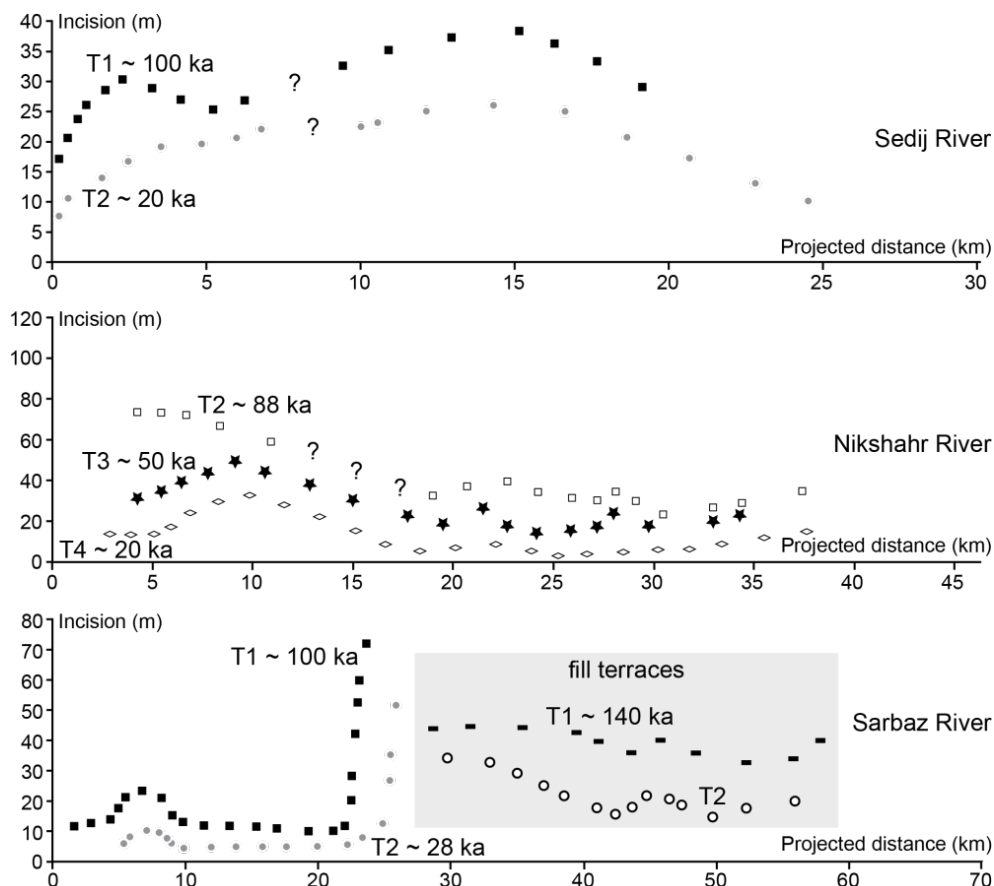


Figure 3S: Incision profiles deduced from dated fluvial terraces along Sarbaz River, Nikshahr River and Sedij River. The profiles from different terrace levels show similar patterns along each river.

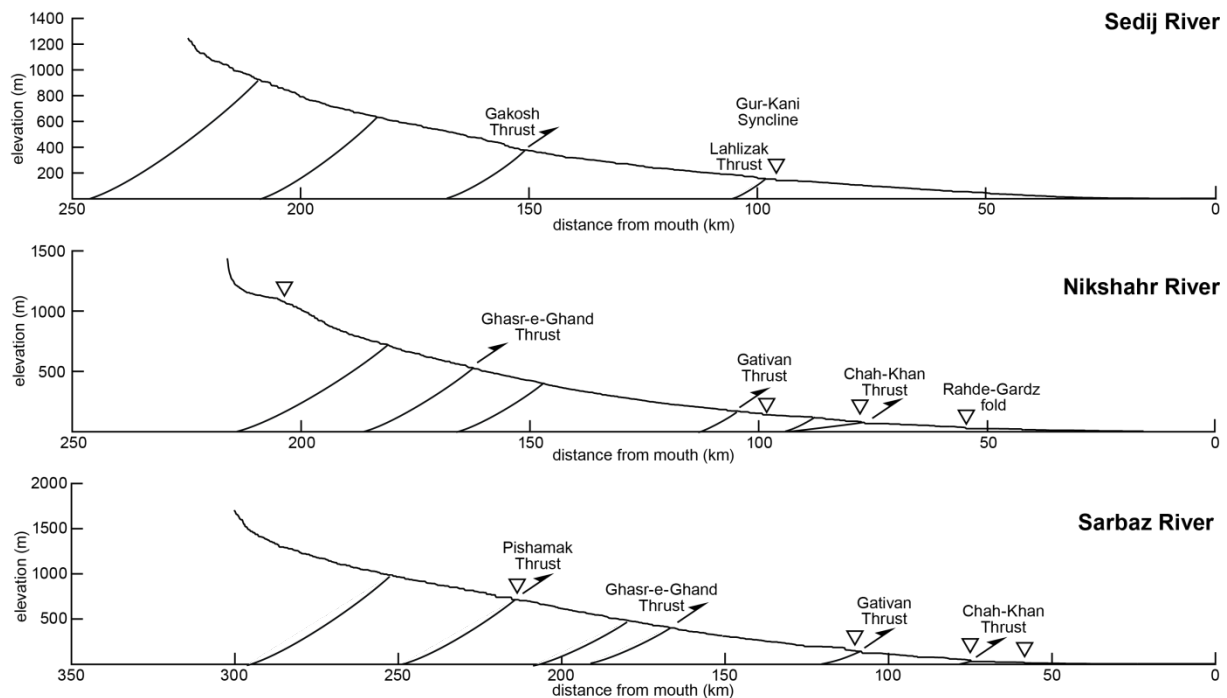


Figure 4S: Longitudinal profiles of the Sarbaz, Nikshahr and Sedij rivers. Smoothing window = 250 m; Triangles = knick points. Curved lines below profiles are thrust faults on the published geological maps.

Accepting thin-skinned tectonics inferred in published seismic and structural profiles on both offshore (Grando and McClay, 2007) and onshore (Burg et al., 2012) Makran, and assuming that very low amplitude and large wavelength folds are incipient shapes, we applied the wavelength and amplitude of the studied folded terraces to estimate the depth of potential décollement layers and measure shortening accommodated by these folds. We will expand this topic in the discussion section.

3- Results

The investigated sites on the three studied major rivers are located in figure 3 a- c. Terraces are labelled and classified according to their locality identity and their respective elevation (e.g. highest P-T1 to lowest P-T5 at location P). Equivalence between geomorphologic definition and sample numbers is given in Table 1S.

3-1 Sites A and B: Sedij River

The Sedij River drains an area of 4627 km² in the western part of the study area. The underlying rocks are predominantly Miocene, sand-dominated turbidites. The river flows roughly in a N-S direction but it displays a bend in the mid-stream, around the Gur-Kani Syncline (Figs. 3a). The studied sites A and B are to the north and to the south of Gur-Kani Syncline, respectively, and concern nearly 30 km of the main trunk of the Sedij River between the Baragan and Majgi cities (Fig. 3a). At Site A, characterized by bedrock incision, the well-developed K-T1 (ca 1 m thick) and K-T2 (ca 0.6 m thick) strath terraces consist of thick gravel standing 35m and 20m above the modern channel, respectively. The K-T1

surface is less continuous than K-T2, which extends over several kilometres. The obtained ages are K-T1 = 90 ± 8 ka and K-T2 = 22 ± 2 ka (Fig. 7). Another T2 sample (B-T2), taken 6 km away from Konardar upstream and close to Baragan village (Fig. 3a) and 7 m above the modern channel, yielded 19 ± 1 ka. Three terrace levels were identified at site B, close to Majgi village, but only M-T1 and T2 were considered in this work because the lowest T3 level is a poorly developed flood plain. A sample collected from the surface of M-T1 yielded an exposure age of 100 ± 8 ka; the estimated incision rate is 0.3 mm/ka.

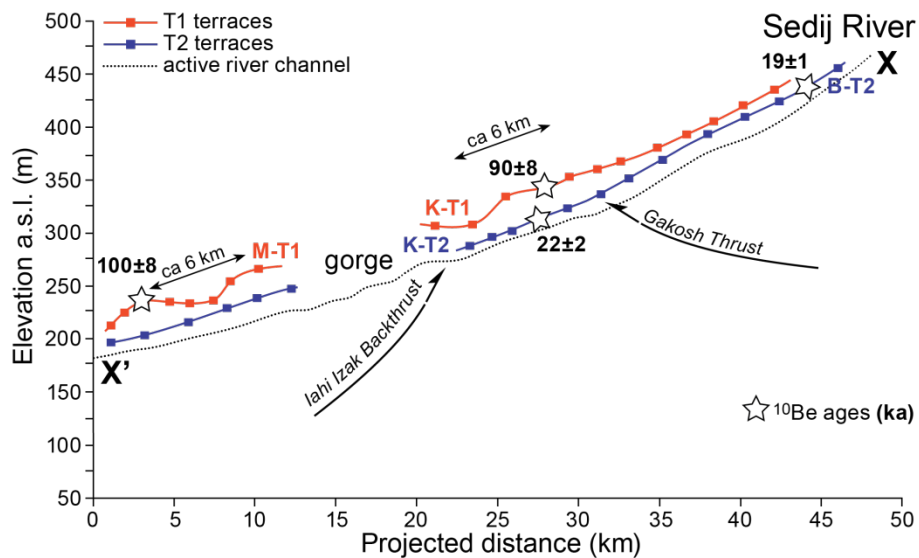


Fig. 7: Profiles of folded fluvial terraces projected onto dashed lines X-X', Y-Y' and Z-Z' in figures 3a, b, c respectively. Note the different wavelengths discussed in text.

The obtained ages allow correlating K-T1 with M-T1 and B-T2 with K-T2. The integrated profile of the T1 surfaces shows that it is folded with a wavelength of ca 6 km in both sites A and B whereas T2 does not display any perceptible fold (Fig. 7). The calculated mean incision rate is 0.3–0.4 mm/a excluding the exceptionally (0.9 mm/a) high rate obtained from K-T2.

3-2 Sites C and D: Nikshahr River

The Nikshahr River flows through the central part of the study area. It drains a catchment of 5399 km². The fluvial terraces can be followed all along the Nikshahr River and its tributaries, except in the narrow gorges south of Pit'Ab, north of Kahir (Figs. 3b) and further north. We particularly investigated the terraces in two localities (sites C and D) on about 60 km of the river between the cities of Nikshahr in the north and Kahir in the south (Fig. 3b). Site C, south of Nikshahr city, is comprised of four terrace levels nested in flat synclines between the Gativan and Chah Khan Thrusts (Fig. 3b). The four strath terraces are covered by thin (0.8 to 2 m) veneer of gravels, and cut into the folded Miocene turbidites and marl layers. They stand 56, 41, 22 and 9 meters above the modern channel, respectively. We collected four samples near Pit'Ab village from the surface of Pt-T1, Pt-T2, Pt-T3 and Pt-T4 (Figs. 3b and 7). They yielded ¹⁰Be exposure ages of 132 ± 11 , 87 ± 7 , 42 ± 3 and 20 ± 1 ka, respectively. Pt-T1, the highest and least-preserved terrace, displays tilting to the north and to the south. Pt-T2, Pt-T3 and Pt-T4 are paired, laterally extensive and have a smaller slope than Pt-T1. The

estimated incision rate is 0.3-0.4 mm/a. The constructed surface profile displays two fold wavelengths of about 5 km in the hanging wall and about 15 km in the footwall of the Chah-Khan Thrust (Fig. 7). This structural change is attributed to thrusting activity on this fault.

Site D is located downstream, further south, in the core of the regional Rahde-Gardz anticline (Fig. 3b). Five <2m thick strath terraces (Rz-T1 - Rz-T5, Fig. 4b) range in elevation from 104 to 5m above the modern channel. Terraces Rz-T1 and Rz-T3 yielded exposure ages of 122 ± 10 and 50 ± 4 ka, respectively. These folded terraces display higher fold amplitude with increasing age (Fig. 4b and 7). Rz-T1 is unpaired and its age constrains an average incision rate of 0.8 ± 0.04 mm/a. The incision rate obtained from Rz-T3 is about 0.2 mm/a.

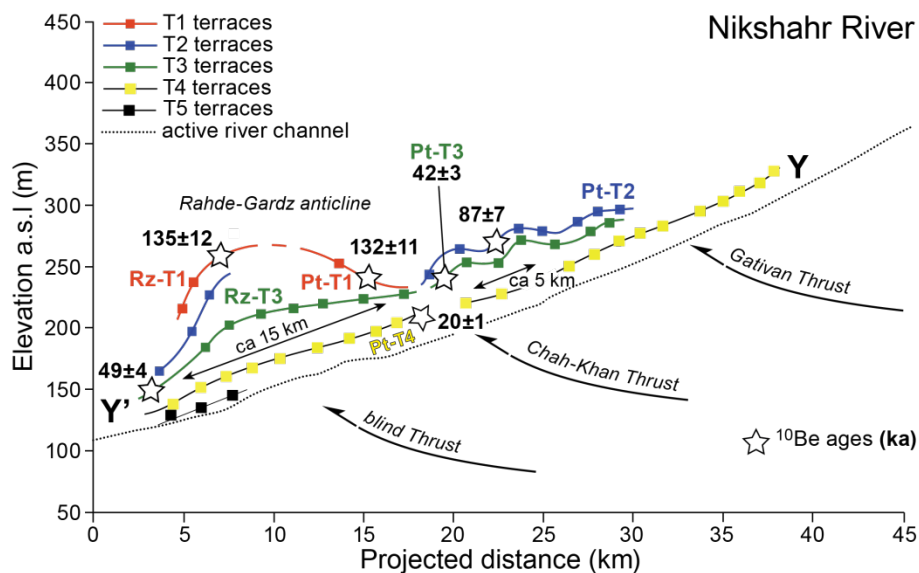


Fig. 7: Profiles of folded fluvial terraces projected onto dashed lines X-X', Y-Y' and Z-Z' in figures 3a, b, c respectively. Note the different wavelengths discussed in text.

The age control obtained in sites C and D allows correlating Pt-T1 with Rz-T1. This correlation can be extended to Rz-T3-Pt-T3 and Rz-T4-Pt-T4 (Fig. 7). The ca 60 m elevation difference between T1 with respect to the modern channels in sites C and D suggests a higher incision / surface uplift rate and tectonic activity in the Rahde-Gardz anticline than on the hanging wall of the Gativan Thrust. The reconstructed terrace profile display Quaternary folded terraces with 15 km wavelength. No emerging thrust fault could be delineated close to the Rahde-Gardz fold, which was accordingly considered to be a detachment or fault-propagation fold (Dolati, 2010). The surface of Rz-T2 is insufficiently continuous to trace it in an anticline, but the good preservation of the other levels allows inferring that it is folded as well. On the basis of increasing tilt with terrace age, and the absence of fault emergence, we suggest active detachment folding with limb rotation as the main process responsible for observed tilted terraces across the Rahde-Gardz anticline (Fig. 7).

3-3 Sites E and F: Sarbaz River – Pishin catchment

The Sarbaz River is the longest river of Iranian Makran flowing from north to south through the Pishin catchment and reaching the Oman Sea in Gwadar Bay (Fig. 1S). The river drains an

area of 20711 km². The underlying rocks are mainly Oligocene and Miocene turbidites down to close to the coast, where Neogene - Quaternary marl and clastic shelf sediments are dominant. Terraces are deposited in the main trunks and in tributaries of the Pishin catchment. We have surveyed all terrace remnants along Sarbaz River from the river mouth up to the north of the Firuzabad Thrust (Fig. 3c), beyond which terraces were not preserved or never deposited. We concentrated this study on two sites (E and F) representing ca 50 km of the river between the Ghasr-e-Ghand Thrust in the north and the Chah-Khan Thrust in the south (Fig. 2a). These two sites are separated by a sharp anticlinal ridge in the hanging wall of the Gativan Thrust, which is marked by a knick point. The anticlinal ridge deflects the middle courses of the two major trunks of Pishin catchment (eastward for the eastern, Sarbaz River, westward for the western Peersohrab river) from their bulk N-S flow directions (Fig. 2a). These morphological features suggest that Gativan Thrust is active. Field observations and topography led us to divide the Sarbaz River into three flat-syncline basins separated by ridges on ramp anticlines (Fig. 5), which were defined by Dolati (Dolati, 2010).

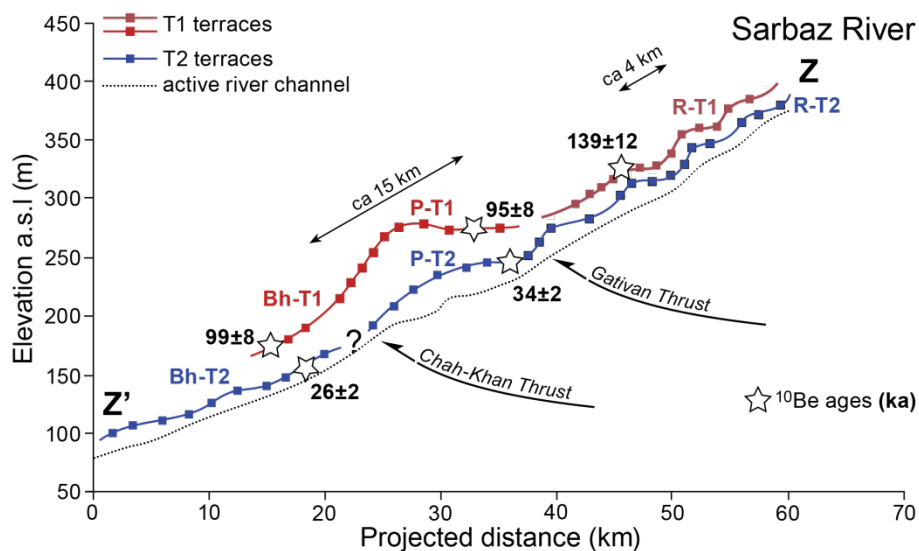


Fig. 7: Profiles of folded fluvial terraces projected onto dashed lines X-X', Y-Y' and Z-Z' in figures 3a, b, c respectively. Note the different wavelengths discussed in text.

Site E, is bounded by the Ghasr-e-Ghand Thrust in the north and the Gativan Thrust in the south (Fig. 3c). There, up to ca- 30 m thick fill deposits brought and left by the river are deeply incised. Two main levels, R-T1 and R-T2, are present in the footwall of Ghasr-e-Ghand Thrust, south of Rask city (Fig. 3c). They are both thick (R-T1 = 15m and R-T2 = 10m) and coarse, clast-supported conglomerates without stratigraphic units, which indicates one aggradation event. We collected samples from a higher terrace (R-T0) whose small remnant does not let any geomorphological approach. Its 217 ± 13 ka exposure age is the oldest we obtained from Makran fluvial deposits. In the same flat syncline we sampled terrace Gh-T1 close to Ghasr-e-Ghand city (Fig. 1S), from a tributary of Sarbaz River, for temporal correlation. We did not observe similar deposits in other flat synclines, so that we link them to a local, tectonic origin rather than any regional, climatic event. The ages of R-T1 (139 ± 12 ka) and Gh-T1 (138 ± 12 ka) support this interpretation since we did not measure terraces as

old as 140 ka in any other flat-syncline. We did not sample R-T2 because its surface is disturbed. The constructed profile of R-T1 and R-T2 terraces displays folds with a wavelength of about 5 km (Fig. 7a). We did not calculate incision and shortening rates from these samples since they represent fill-terraces and a depositional stage of the river.

Site F, downstream from site E, represents a flat-syncline between the Gativan Thrust in the north and the Chah Khan Thrust in the south. Between the ca 30 km apart Pishin and Bahukalat cities (Fig. 3c), two strath terrace levels (in contrast to the fill terraces of site E), T1 and T2, made of less than 3 m gravel deposits are nearly continuous and laterally extensive on the footwall of Gativan Thrust. We sampled these two levels near Pishin and near Bahukalat (Fig. 3c). Close to Pishin, P-T1 and P-T2 yield exposure ages of 95 ± 8 and 34 ± 2 ka, respectively. Their treads lie 60m and 14m above the modern channel, respectively. Downstream, close to Bahukalat City, Bh-T1 and Bh-T2 are 99 ± 8 and 26 ± 2 ka, respectively. Their treads lie 33 m and 10 m above the modern channel. Considering the morphology, altitude, and age control data, we are confident that Bh-T1 and P-T1 terraces belong to the same abandonment surface; this conclusion is valid for Bh-T2 and P-T2 also. We noticed that levels P-T1 and P-T2 are higher near Pishin than Bh-T1 and Bh-T2 with respect to the modern channel. This difference is attributed to deformation since the constructed profile of these terraces depicts folds with a wavelength of about 15 km (Fig. 7a).

The incision rates derived from the dated terraces of Pishin Catchment have mean values of about 0.2 mm/a. The only place of high incision rate (0.8 mm/a) is where the river cuts the Gativan Thrust (Fig. 3c). A knickpoint on the longitudinal profile of the modern river (Fig. 4S) and the local preservation of ten strath terrace levels (Fig. 4d) supports the interpretation of protracted river response to local tectonic activity of this thrust.

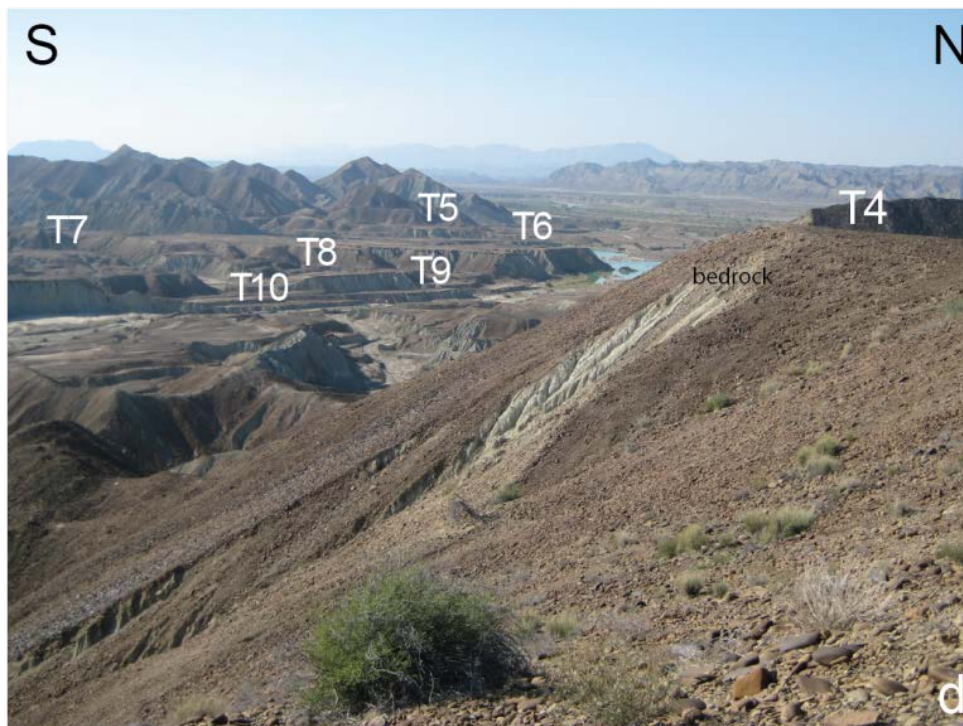


Fig. 4 (d): Local Preservation of ten levels of strath terraces (GPS point: $N25^{\circ}58'53.30''$, $E061^{\circ}40'24.36''$).

4- Discussion

4-1 ^{10}Be age uncertainties

The two main sources of exposure dating uncertainties are erosion and inheritance. The two depth profiles demonstrate an exponential decrease in Terrestrial Cosmogenic Nuclides (TCN) concentration with depth without any sign of bioturbation (Fig. 6a-b). The measured ^{10}Be concentration in surface samples is consistent with the modelled concentration for depth profiles, which supports the longevity of desert pavement stability. The TCN age of the R-T1 surface (Site A), calculated from the best model fit of 100000 Monte Carlo solutions for four depth profile samples, is 120 ± 10 ka (Fig. 6c and d). This is, within uncertainty, very close to the 139 ± 12 ka determined from the amalgamated surface pebbles. The model of the 19 ± 1 ka Pt-T4 surface consistently yields an exposure age of 15 ± 1 ka and inheritance of 0.4×10^{-5} atoms g^{-1} . The deepest sample in this second depth profile was excluded from calculation because it does not obey the theoretical relationship of depth versus ^{10}Be concentration (Fig.6b and d; Table1S). These two depth profile ages show that inheritance has insignificant effects on ages presented as results. The good consistency we have obtained between independent morphological and age correlations reflects also the negligible effect of inheritance on the actual age. Inheritance affects more the younger Pt-T4 surface (< 20 ka) than the older R-T1. This differential influence is in agreement with other studies (Anderson et al., 1996; Vassallo et al., 2011). Since the youngest age population we have measured within the different catchments is ~ 19 ka, inheritance can be discarded and our results should be taken as smaller apparent and conservative ages. All the surfaces we used for shortening calculation are older than 20 ka, hence inconsequentially affected by inheritance. Therefore, any inheritance effect cannot significantly alter our structural conclusions. The ^{10}Be concentration from modern channel samples varies between 0.5×10^5 and 2.1×10^5 ; these values are equivalent to apparent ages of 11 ± 1 ka and 48 ± 4 ka, respectively. The similarity of concentration in modern channels (e.g. Q-Mak-09-44, Q-Mak-10-48) and lowest terrace surfaces in some locations (e.g. Q-Mak-09-45, Q-Mak-10-47, Table 1S) raises the possibility that modern samples reworked older terraces. Yet, the ^{10}Be concentrations in the two depth profiles are lower. Therefore, inheritance values from modern channel samples are not everywhere representative and we did not use them to correct exposure ages. Field observations and the climatic conditions in Makran suggest small erosion rates. Since there is no independent estimate of erosion rate in Makran and adjacent areas, we modelled for a constant maximum denudation rate of 0.5 cm/a while allowing for net erosion to vary between 0 and 30cm (Table 1S). The estimated erosion rate from space solution plot for the old surface is 0.07cm/ka and 0.05 cm/ka for the younger surface. These results, based on minimum age values, confirm that the erosion rate is very low. We report the ages with and without erosion (Table 1S). Therefore the ages should be considered as minimum values.

4-2 Quaternary folding: Insight from fluvial terraces

The terrace profiles along the three studied rivers indicate folding over the past ca. 140 ka (Fig.7). The lack of fault emergence next to most of these folds suggests detachment folding rather than fault-propagation folding, although the latter might play a role for the specific folds adjacent to mapped thrusts (Fig. 3b). We emphasize that detachment folding and fault-propagation folding are kinematic descriptions that do obey the mechanical description of layer buckling (Schmalholz et al., 2002) since detachment folding / buckling may precede fault emergence across the frontal limb of fault-propagation folds (e.g. Suppe and Medwedeff, 1990). Altogether, the very low amplitude, large wavelength folded terraces delineate a symmetric and sinusoidal shape of fold trains. Compared to basement folds and faults (Fig. 8), the folded terraces are nearly “flat” and obviously represent the latest, very small increment of regional shortening. Therefore, the dominant folding process can be safely approached with incipient buckling. In support to this interpretation, the decreasing amplitude from T1 to younger terraces, in particular from T1 to T5 in Nikshahr River (Fig. 7), indicates that the folded terraces record the progressive, active amplification of a surface layer on a viscous substratum.

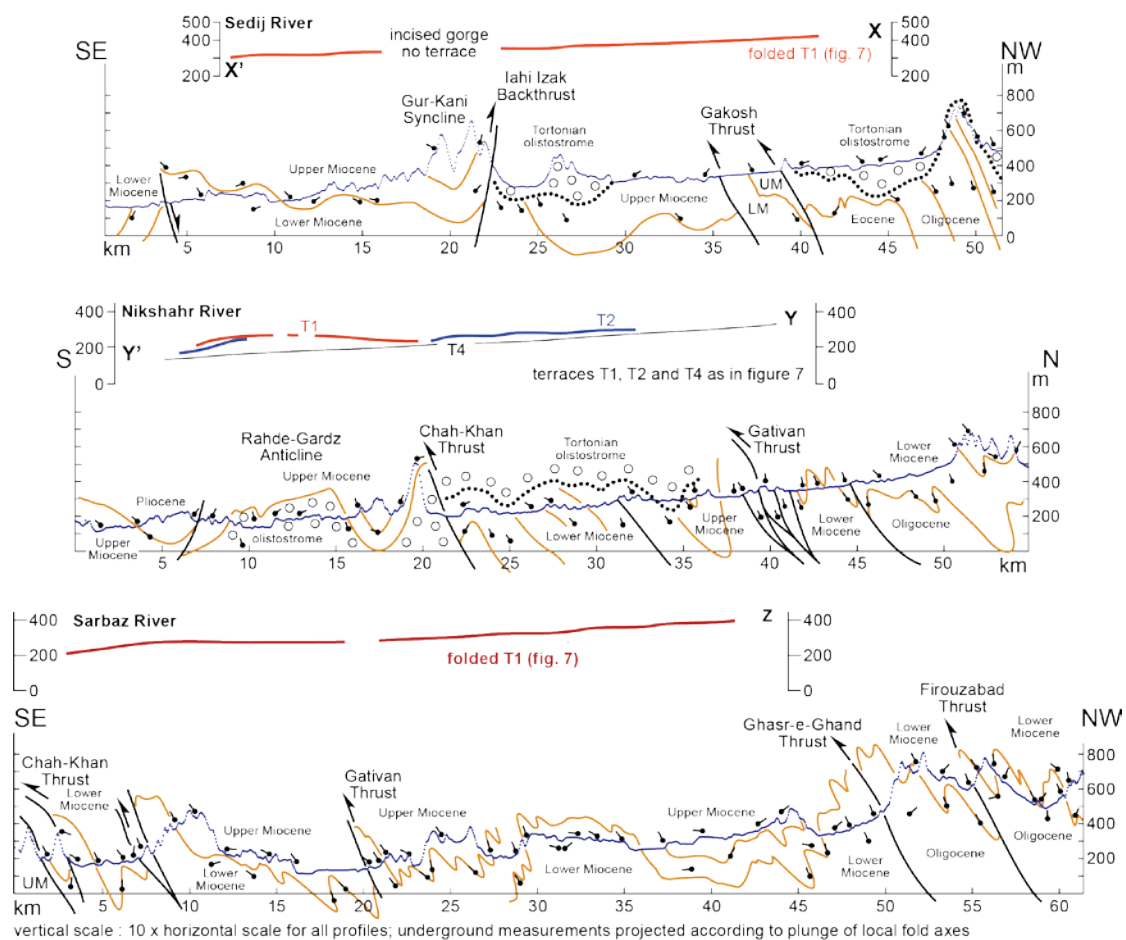


Fig. 8: Cross-sections displaying the highest-amplitude folded fluvial terraces of figure 7 above profiles of underlying basement structures and stratigraphy. Terraces and substratum are at the same scales to visualize the structural context of the quaternary folds. Lines on dots: bedding measurements. Blue line: Topography. Dot line: basal unconformity of Tortonian olistostrome (empty circles). Orange lines: layer boundaries. Stratigraphy reported in profiles. UM and LM: Upper and Lower Miocene, respectively.

Along the Sarbaz and Nikshahr rivers, the folded terraces of same age display two dominant wavelengths: ca 5 km in the hanging wall and ca 15 km in the footwall of the Gativan Thrust (Fig. 7). Along Sedij River, the folded terraces display only a ca 6 km wavelength. The rheological contrast between unconsolidated terraces and underlying, poorly lithified shales is arguably negligible. Such rocks have a complex, non-linear behaviour, even for small strains (Weijermars and Schmeling, 1986). In that case, “resonant folding” is the suitable approximation (e.g. Price and Cosgrove, 1990); material properties play little role and the fold equation (Fig. 9a) predicts a dominant wavelength 3.46 times the thickness of the folded layer. Accordingly, the two measured wavelengths suggest two thicknesses of folded layer, approximately 1.4 and 4.3 km, which for incipient, very low amplitude folds equate depths of underlying décollements surfaces. We suggest that the Gativan Thrust is a ramp that roots in the ca 1.4 km deep décollement, over which the 5-6 km wavelength folds developed. The deeper décollement, in the footwall of the Gativan Thrust, is likely the level in which thrusts known further to the south (e.g. the Chah-Khan Thrust, Figs. 2a and 3b) root, still above the current subduction surface inferred from seismic profiles (Kopp et al., 2000).

4-3 Bulk horizontal shortening and shortening rate deduced from mass conservation

Deducing horizontal shortening from vertical deformation depends on fold kinematics and geometry of passive markers (Fig. 9b). We argued that the fold trains deforming the fluvial terraces are detachment buckle folds. In order to convert the calculated incision rates to tectonic uplift across these folds, we need to know the initial geometry of the terraces at the time of their abandonment. This is possible since we have shown that the rivers have maintained their longitudinal profiles during the age-bracketed deformation.

We applied the area conservation method (Mitra, S., 2002) for well-defined folds thanks to the continuous preservation of terrace tread. We delimited the fold relief required for calculation as the area between the actual T1 terrace profile and the modern channel (fig. 7), considering that shortening responsible for the local river gradient is negligible compared to that responsible for folds. For this reason, the amount of shortening derived from this exercise is slightly underestimated and can be taken as conservative value. We applied this method on seven strath, well developed and older than 50 ka surfaces along the three studied rivers. The results show a homogeneous distribution of shortening across the wedge with an average shortening rate of 1 mm/a (Fig. 5 and supplementary Table 2S). Integrated over the width of the Makran wedge, this would be equivalent to an average strain rate of about 10^{-13} s^{-1} .

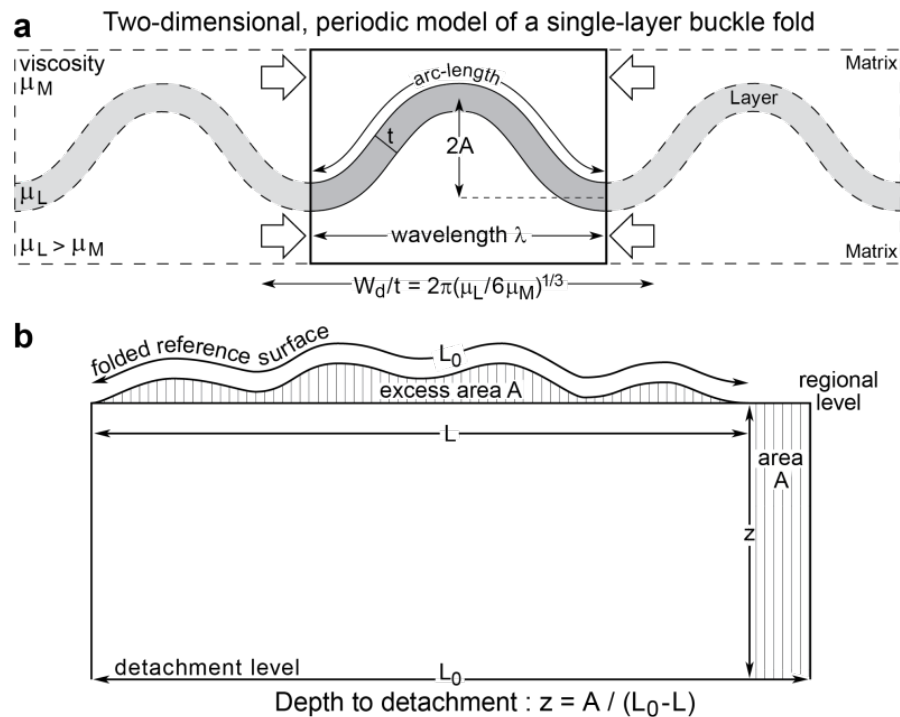


Fig. 9: Folding – shortening relationships: a) for buckling, the dominant wavelength λ_d is $\lambda_d/t = 2\pi(\mu_L/6\mu_M)^{1/3}$ where t is thickness of folded layer and μ_L and μ_M are viscosity of layer and matrix, respectively (e.g. Price & Cosgrove 1990); note that if μ_L approaches μ_M , λ_d approaches a value of $3.46t$ b) Mass conservation method to estimate horizontal shortening (width of area A) and depth to detachment (z) from folded geomorphic markers (e.g. fluvial terrace).

All estimates for incision, uplift and shortening rates are based on minimum ages. We consider 10% uncertainty for the estimated shortening rate, which is essentially due to the uncertainty on the décollement depth.

River	Sample	Area (km ²)	depth to décollement (km)	Shortening (m)	Age (ka)	Shortening rate (mm/a)
Sedij						
K-T1	Q-mak-10-36	0.14	1.4	82	91	0.90
M-T1	Q-mak-09-41	0.12	1.4	87	101	0.86
Nikshahr						
Pt-T2	Q-mak-11-15	0.12	1.4	87	88	0.99
Pt-T3	Q-mak-11-13	0.9	1.4	56	44	1.20
Rz-T3	Q-mak-10-31	0.064	4.3	15	50	0.30
Rz-T1	Q-mak-10-28	0.6	4.3	137	122	1.12
Sarbaz						
P-T1	Q-mak-09-32	0.44	4.3	104	95	1.09
P-T2	Q-mak-11-02	0.21	4.3	50	34	1.47

Table 2S: Terrace data used for shortening rates along the three studied rivers. Area A as in figure 9b

4-4 Seismotectonic Implications

To obtain the long term average shortening rate across the studied part of Makran, we sum for three transects (Fig. 2a) the inferred amounts of shortening recorded by terraces folded during Pleistocene times across the investigated and related river segments. This shortening strain is easily converted into mean shortening rate using the obtained terrace ages. We compare our results with current shortening rates deduced from the rare GPS measurements available in the literature. The convergence rate between Arabia and Eurasia is 25 ± 2 mm/a in western Makran and 26 ± 2 mm/a in eastern Makran (Vernant et al., 2004). From the velocity catalogue published by the latter authors, we extracted a shortening rate of 7.96 mm/a across the onshore Makran between the Chabahar and Bazman stations, i.e. across the studied area (Fig. 1). In the absence of denser GPS information, we must accept this perhaps slim, but meaningful information. The folds used in this study are nearly perpendicular to the convergence direction, so that we neglect the very small obliqueness correction. The shortening rate calculated from the folded fluvial terraces of the Pishin Catchment is 1.2 mm/a. It is 1.1 mm/a for folded terraces of the Nikshahr River and 0.85mm/a along the Sedij River (Table 1S). These figures, obtained for 20-25 km long river segments (Fig. 5), demonstrate very little variation in strain and strain rate distribution over a nearly 200*150 km area of the exposed accretionary wedge and account for much of the overall 7.96 mm/a shortening rate across the 150 km wide exposed Makran. The GPS-defined rate of shortening applies to a period without recorded earthquake in the concerned area. The distributed deformation causing the smooth, folded surface uplift concomitant with river incision is apparently absorbing much of the wedge shortening under stresses smaller than the critical stresses ruling seismogenic, frictional rheology. We conjecture that thrust movement along the detachments underlying the growing Quaternary folds we have described is essentially creeping (or unrecorded slow slip events) along low friction and water-overpressured levels, as those collected in the coastal, active mud-volcanoes. Concomitant folding may be a structural softening process that can prevent stress build-up in competent layers (Leroy et al., 2002; Schmalholz et al., 2005), hence explain the recorded seismic deficit. This is evidence for considering more complex rheology (visco-elasto-plastic) than the classical Mohr-Coulomb (brittle, elasto-plastic) theory to model and understand in more details the topographic and deformation evolutions, in particular the rupturing mode of accretionary wedges.

Conclusion

The detailed geomorphological analysis combined with new ^{10}Be exposure ages of fluvial terraces in three adjacent drainage systems of the onshore Makran accretionary wedge demonstrates active folding of the surface since at least 130 ka. Therefore, the Quaternary deformation and surface uplift are not limited to the coastal and offshore Makran wedge.

Folding and associated shortening rate are homogeneously distributed over a wide area of the wedge, suggesting a rather steady structural development and response of the deforming wedge. The morphotectonic analysis of the deformed strath terraces shows that

recent folding apparently absorbs much of the current shortening rate. Folding is a sufficient structural softening process to explain a large part of the missing seismicity in the area. Creeping on associated, blind décollements and thrust faults may absorb much of the remaining amount of convergence. The importance of folding depicted in this work shows that the classical interpretation of accretionary wedges as “Coulomb” (i.e. brittle) wedges is an excellent, long-term approximation that now requires refinements in terms of bulk rheology. The scenario and the previous sentence do not exclude the potential for seismogenic rupture, even if the instrumental record is scarce.

Acknowledgements

This work is supported by the ETH project (No.0-20481-08) and the Swiss National Fond project (No. 2-77644-09). Administrative and logistic support by the Geological Survey of Iran is strongly acknowledged. We thank J-D. Champagnac for his friendly and pertinent comments on an early version of this work. Three anonymous reviewers provided very useful comments and suggestions to improve presentation of our results.

Chapter V

Conclusion

Discussion and conclusion

The Makran Subduction System offers one of the best-exposed sedimentary wedges on Earth. It is a direct consequence of the Arabia – Eurasia convergence. Despite evidence for recent surface uplift of the coast of the Oman Sea and the importance of active movements for seismic hazard, no quantitative morphotectonic study had attempted to integrate diverse markers of convergence processes over the wide and semi-desertic Makran region. In this thesis, we carried out a detailed morphotectonic study combining (1) the geomorphological analysis of the drainage system based on GIS referenced field control of DEM and aerial remote information (2) age constraints on fluvial terraces using ^{10}Be cosmogenic nuclides and (3) utilisation of the dated terraces as strain markers to determine the Holocene shortening rate and to define the spatial – temporal distribution of Quaternary deformation in the exposed accretionary wedge.

5-1 Along strike variation of tectonic activity inferred from the river morphology

We explored the Makran landscape at different scales to discriminate the role of crustal deformation in the topographic growth of the wedge. Classical geomorphic indices (relief, concavity, steepness) were extracted automatically using open-access algorithms.

Results show a neat difference of longitudinal profiles between the western and eastern catchments, although the channels erode rocks of uniform erodibility. The western rivers, without any pronounced knickpoint, are in or close to morphological, dynamic equilibrium whereas the eastern rivers exhibit profiles with prominent convexities and knickpoints, thus notably diverging from the equilibrium logarithmic and concave up shapes. Coincidence of most knickpoints and convex channel segments with faults and folds reported on existing geological maps indicates that the eastern rivers are deformed by tectonically-driven, upward surface uplift due to active fold growth and thrusting since at least the middle Pleistocene. This tectonic activity has also impacted the general topography, the river pattern and the size and shape of drainage basins, which are much larger in the eastern part smaller and simpler in the west. In short, crustal tectonics dominated the fluvial network and even induced river capture on the inland Makran accretionary wedge.

All the studied catchments share the same base level (the Oman Sea), flow on similar lithologies and developed under uniform climate conditions. Therefore, we could interpret the morphometric differences in terms of differential tectonic forcing and subsequent rock uplift rates. This interpretation is consistent with both uplift rates estimated from marine terraces along the Makran coast and the recorded seismicity. Invoking within-wedge deformation to explain the identified topographic characteristic does not tell why the surface of eastern Makran is uplifted faster than the surface of western Makran. Several possibilities may explain this spatial disparity in surface dynamics. It may reflect changes in subduction rate or in dip angle of the slab. The geodetic data and plate tectonic

reconstructions reveal an eastward increase in convergence rate which may explain this morphological variation along Makran. They are possibly independent evidence supporting our interpretation.

5-2 Surface exposure dating

This study provided the first strath terrace abandonment ages using ^{10}Be exposure dating.

Climatic influence

The ^{10}Be exposure ages (with zero erosion and negligible inheritance) range between 13 and 320 ka. They correspond to both glacial and interglacial episodes. We concluded that both climate and tectonic forces are responsible drivers for the formation of these terraces. They can be interpreted as follow: (1) Clustering of the terrace abandonment ages between 30 and 120ka corresponds to interglacial Marine Isotopes Stages 3, 5 and 7. The obtained exposure ages and their regional distribution indicate that climate fluctuations played a role in terrace development. (2) In contrast, ages between 130 - 180ka correspond to the glacial Marine Isotope Stage 6. Their local preservation and field evidence indicates that they are likely responses to tectonic forces. (3) Terraces younger than 20ka and older than 270 ka are difficult to interpret since surface erosion and nuclide inheritance may have disturbed the actual ages.

Comparing uncorrected and corrected ages suggests that ages between 20 and 250 ka have good resolution; taking into account the possible corrections, these ages still fall within the same Marine Isotope stages (3-5-7 and 6). The correction for exposure ages <20ka and >270ka lead to a large shifts across MIS stages. For example, ages equivalent to MIS2 move to MIS1 and ages corresponding to MIS 10 shift to MIS 13.

Tectonic implication

The new chronologic measurements describe well how erosion and river incision proceeded in parallel with deformation and highlights transient landscapes. The average incision rates derived from strath terraces do not reveal any changes through time but they do show spatial changes. The comparison of incision rates in different, adjacent catchments enables distinguishing between a relatively moderate regional, "background" incision rate (0.3mm/a) and higher local incision/uplift (0.8-1 mm/a) rates. The similarity between regional fluvial incision rates (0.3-0.4 mm/a) and Pleistocene coastal uplift rates constrained by the uplifted marine terraces (0.2 mm/a) supports the inference that fluvial rivers responded to a regional, long-term interplay between climatically-driven incision and tectonically-driven surface uplift- The latter reflects the uniform wedge growth due to tectonic underplating during Quaternary times. The obtained uniform incision rate of 0.4 mm/a indicates steady state stage of the wedge on a regional scale. However, perfect steady-state is unlikely on short-length scales. Local instabilities depict localised deformation.

5-3 Rate of crustal shortening

Rates and patterns of active deformation are vital information for understanding the dynamics of deforming lithospheres. Well-preserved fluvial terraces have been surveyed to decipher the Quaternary increment of crustal shortening and shortening rate in the on-shore Makran Accretionary Wedge. Reconstruction of the terraces profiles revealed two regional dominant fold wavelengths, about 5km in the northern part of the study area and about 15 km to the south. These two wavelengths suggest the existence of two active décollement layers at about 1.5 and 4.5 km depth. We suggest that the Gativan Thrust is a ramp that roots in the shallower of these two décollements levels. The deeper décollement, in the footwall of the Gativan Thrust is likely the level in which thrust known further to the south root, still above the current subduction surface inferred from seismic profiles. The results show a homogeneous, average shortening rate of 1mm/a across the wedge. Integrated over the width of the Makran wedge, this would be equivalent to an average strain rate of about 10^{-13} s^{-1} . The distributed deformation causing the smooth, folded surface uplift concomitant with river incision is apparently absorbing much of the wedge shortening under stresses smaller than the critical stresses ruling seismogenic, frictional rheology. We suggest that thrust movement along the detachments underlying the growing Quaternary folds is essentially creeping (or unrecorded slow slip events) along low friction and water-over pressured levels, as those collected in the coastal, active mud volcanoes. Concomitant folding may be a structural softening process that can prevent stress build-up in competent layers, hence explain the recorded seismic deficit. The importance of folding depicted in this work shows that the highly accepted classical interpretation of accretionary wedges as “Coulomb” wedges is an excellent, long-term approximation that now requires refinements in terms of bulk rheology. The scenario and the previous sentence do not exclude the potential for seismogenic rupture, even if the instrumental record is scarce.

5-4 Outlook

Dating results highlight the problems one may face for dating surfaces assuming no erosion and negligible inheritance for very old (>300ka) or very young (<20 ka) terraces in regions like Makran, with semi-arid climate and moderate tectonic activity. To avoid over/underestimating of the actual depositional age, and not just an abandonment time, it is necessary to apply another independent, crosschecking method. OSL dating on suitable material is a good candidate.

The first step to gain better understanding of the landscape evolution in Makran is to determine the catchment-wide denudation rates using TCN method and see if they are in accord with incision rates.

To complete this work more geodetic data is required, especially across key structures to quantify their individual contribution in absorbing bulk shortening.

Bibliography

- Ahmed, S. S. 1969. Tertiary Geology of Part of South Makran, Baluchistan, West Pakistan. *AAPG Bulletin* **53**(7), 1480-1499.
- Ambraseys, N. N., Jackson, J. A. & Melville, C. P. 2002. Historical seismicity and tectonics: The case of the Eastern Mediterranean and the Middle East. *In: International handbook of earthquake and engineering seismology* (edited by Lee, W. H. K., Kanamori, H., Jennings, P. C. & Kisslinger, C.). *International Geophysics* **81**, part **A**, Academic Press, Amsterdam, 747-763.
- Ambraseys, N. N. & Melville, C. P. 1982. *A history of Persian earthquakes*. Cambridge University Press, London, 219 p.
- Anderson, R. S. & Anderson, S. P. 2010. *Geomorphology : the mechanics and chemistry of landscapes*. Cambridge University Press, Cambridge, 637 p.
- Anderson, R. S., Repka, J. L. & Dick, G. S. 1996. Explicit treatment of inheritance in dating depositional surfaces using in situ ^{10}Be and ^{26}Al . *Geology* **24**(1), 47-51.
- Arthurton, R. S., Farah, A. & Ahmed, W. 1982. The Late Cretaceous-Cenozoic history of western Baluchistan Pakistan - the northern margin of the Makran subduction complex. *In: Trench-Forearc geology: Sedimentation and tectonics of modern and ancient plate margins* (edited by Leggett, J. K.). *Special Publication* **10**, Geological Society, London, 373-385.
- Ashi, J. & Taira, A. 1992. Structure of the Nankai accretionary prism as revealed from IZANAGI sidescan imagery and multichannel seismic reflection profiling. *Island Arc* **1**(1), 104-115.
- Azor, A., Keller, E. A. & Yeats, R. S. 2002. Geomorphic indicators of active fold growth: South Mountain-Oak Ridge anticline, Ventura basin, southern California. *Geological Society of America Bulletin* **114**, 745-753.
- Balco, G. 2009. ^{26}Al - ^{10}Be exposure age/erosion rate calculators: update from v. 2.1 to v. 2.2. http://hess.ess.washington.edu/math/docs/al_be_v22/al_be_docs.html.
- Balco, G., Briner, J., Finkel, R. C., Rayburn, J. A., Ridge, J. C. & Schaefer, J. M. 2009. Regional beryllium-10 production rate calibration for late-glacial northeastern North America. *Quaternary Geochronology* **4**(2), 93-107.
- Balco, G. & Shuster, D. L. 2009. ^{26}Al - ^{10}Be - ^{21}Ne burial dating. *Earth and Planetary Science Letters* **286**(3-4), 570-575.
- Balco, G., Stone, J. O., Lifton, N. A. & Dunai, T. J. 2008. A complete and easily accessible means of calculating surface exposure ages or erosion rates from ^{10}Be and ^{26}Al measurements. *Quaternary Geochronology* **3**(3), 174-195.
- Bayer, R., Chery, J., Tatar, M., Vernant, P., Abbassi, M., Masson, F., Nilforoushan, F., Doerflinger, E., Regard, V. & Bellier, O. 2006. Active deformation in Zagros-Makran transition zone inferred from GPS measurements. *Geophysical Journal International* **165**(1), 373-381.
- Bender, F. K. & Raza, H. A. 1995. *Geology of Pakistan*. Gebrüder Borntraeger, Berlin, 414 p.
- Berberian, F., Muir, I. D., Pankhurst, R. J. & Berberian, M. 1982. Late Cretaceous and early Miocene Andean-type plutonic activity in northern Makran and Central Iran. *Journal of the Geological Society of London* **139**(5), 605-614.

- Bernet, M., Zattin, M., Garver, J. I., Brandon, M. T. & Vance, J. A. 2001. Steady-state exhumation of the European Alps. *Geology* **29**(1), 35-38.
- Bevis, M., Taylor, F. W., Schutz, B. E., Recy, J., Isacks, B. L., Helu, S., Singh, R., Kendrick, E., Stowell, J., Taylor, B. & Calmant, S. 1995. Geodetic observations of very rapid convergence and back-arc extension at the Tonga Arc. *Nature* **374**(6519), 249-251.
- Bierman, P. & Nichols, K. K. 2004. Rock to sediment - slope to sea with ^{10}Be -rates of landscape change. *Annual Review of Earth and Planetary Sciences* **32**, 215-225.
- Bierman, P. R., Marsella, K. A., Patterson, C., Davis, P. T. & Caffee, M. 1999. Mid-Pleistocene cosmogenic minimum-age limits for pre-Wisconsinan glacial surfaces in southwestern Minnesota and southern Baffin Island: a multiple nuclide approach. *Geomorphology* **27**(1-2), 25-39.
- Biju-Duval, B., Le Quellec, P., Mascle, A., Renard, V. & Valery, P. 1982. Multibeam bathymetric survey and high resolution seismic investigations on the Barbados Ridge complex (Eastern Caribbean): A key to the knowledge and interpretation of an accretionary wedge. *Tectonophysics* **86**(1-3), 275-304.
- Bijwaard, H., Spakman, W. & Engdahl, E. R. 1998. Closing the gap between regional and global travel time tomography. *Journal of Geophysical Research* **103**(B12), 30,055-30,078.
- Bishop, P. 2007. Long-term landscape evolution: linking tectonics and surface processes. *Earth Surface Processes and Landforms* **32**(3), 329-365.
- Bishop, P., Hoey, T. B., Jansen, J. D. & Artza, I. L. 2005. Knickpoint recession rate and catchment area: the case of uplifted rivers in Eastern Scotland. *Earth Surface Processes and Landforms* **30**(6), 767-778.
- Blum, M. D., Misner, T. J., Collins, E. S., Scott, D. B., Morton, R. A. & Aslan, A. 2001. Middle Holocene Sea-Level Rise and Highstand at +2 M, Central Texas Coast. *Journal of Sedimentary Research* **71**(4), 581-588.
- Blum, M. D. & Törnqvist, T. E. 2000. Fluvial responses to climate and sea-level change: a review and look forward. *Sedimentology* **47**, 2-48.
- Borja, R. I. & Dreiss, S. J. 1989. Numerical modeling of accretionary wedge mechanics: Application to the Barbados Subduction problem. *Journal of Geophysical Research* **94**(B7), 9323-9339.
- Bridge, J. S. & Demicco, R. V. 2008. *Earth surface processes, landforms and sediment deposits*. Cambridge University Press, New York, 815 p.
- Bridgland, D. & Westaway, R. 2008. Climatically controlled river terrace staircases: A worldwide Quaternary phenomenon. *Geomorphology* **98**(3-4), 285-315.
- Brocard, G. Y. 2003. Long-term fluvial incision rates and postglacial river relaxation time in the French Western Alps from ^{10}Be dating of alluvial terraces with assessment of inheritance, soil development and wind ablation effects. *Earth and Planetary Science Letters* **209**, 197-214.

- Brocard, G. Y. & van der Beek, P. A. 2006. Influence of incision rate, rock strength, and bedload supply on bedrock river gradients and valley-flat widths: Field-based evidence and calibrations from western Alpine rivers (southeast France). *In: Tectonics, climate, and landscape evolution* (edited by Willett, S. D., Hovius, N., Brandon, M. T. & Fisher, D. M.). *Penrose Conference Series* **398**, Geological Society of America, Special Papers, Boulder, 101-126.
- Bronk Ramsey, C. 2009. Bayesian analysis of radiocarbon dates. *Radiocarbon* **51**(1), 337-360.
- Brown, E. T., Trull, T. W., Jean-Baptiste, P., Raisbeck, G., Bouchès, D., Yiou, F. & Marty, B. 2000. Determination of cosmogenic production rates of ^{10}Be , ^3He and ^3H in water. *Nuclear Instruments and Methods in Physics Research Section B: Beam Interactions with Materials and Atoms* **172**(1-4), 873-883.
- Buiter, S. J. H., Babeyko, A. Y., Ellis, S., Gerya, T. V., Kaus, B. J. P., Kellner, A., Schreurs, G. & Yamada, Y. 2006. The numerical sandbox: comparison of model results for a shortening and an extension experiment. *Geological Society, London, Special Publications* **253**(1), 29-64.
- Bull, W. B. 1979. Threshold of critical power in streams. *Geological Society of America Bulletin* **90**(5), 453-464.
- Bull, W. B. 2007. *Tectonic geomorphology of mountains. A new approach to paleoseismology*. Blackwell Publishing Ltd, Oxford, 316 p.
- Bull, W. B. 2009. *Tectonically active landscapes* Wiley-Blackwell, Chichester, 326 p.
- Burbank, McLean, Bullen, Abdrakhmatov & Miller. 1999. Partitioning of intermontane basins by thrust-related folding, Tien Shan, Kyrgyzstan. *Basin Research* **11**(1), 75-92.
- Burbank, D., Meigs, A. & Brozović, N. 1996. Interactions of growing folds and coeval depositional systems. *Basin Research* **8**(3), 199-223.
- Burbank, D. W. & Anderson, R. S. 2001. *Tectonic Geomorphology*. Blackwell Science, Malden, 273 p.
- Burbank, D. W. & Beck, R. A. 1991. Rapid, long-term rates of denudation. *Geology* **19**(12), 1169-1172.
- Burbank, D. W., Beck, R. A. & Mulder, T. J. 1994. The Himalayan foreland basin. *In: Tectonic evolution of Asia* (edited by Yin, A. & Harrison, T. M.), Cambridge University Press, Cambridge, United Kingdom, 149-188.
- Burg, J.-P., Bernoulli, D., Smit, J., Dolati, A. & Bahroudi, A. 2008. A giant catastrophic mud-and-debris flow in the Miocene Makran. *Terra Nova* **20**(3), 188-193.
- Burg, J.-P., Davy, P., Nievergelt, P., Oberli, F., Seward, D., Diao, Z. & Meier, M. 1997. Exhumation during crustal folding in the Namche-Barwa syntaxis. *Terra Nova* **9**(2), 53-56.
- Burg, J.-P., Dolati, A., Bernoulli, D. & Smit, J. 2012. Structural style of the Makran Tertiary accretionary complex in SE-Iran. *In: Lithosphere dynamics and sedimentary basins: The Arabian Plate and analogues* (edited by Al Hosani, K., Roure, F., Ellison, R. & Lokier, S.), Springer Verlag, Heidelberg, 239-259.

- Byrne, D. E., Sykes, L. R. & Davis, D. M. 1992. Great Thrust Earthquakes and Aseismic Slip Along the Plate Boundary of the Makran Subduction Zone. *Journal of Geophysical Research* **97**(B1), 449-478.
- Chappell, J., Omura, A., Esat, T., McCulloch, M., Pandolfi, J., Ota, Y. & Pillans, B. 1996. Reconciliation of late Quaternary sea levels derived from coral terraces at Huon Peninsula with deep sea oxygen isotope records. *Earth and Planetary Science Letters* **141**(1-4), 227-236.
- Chapple, W. M. 1978. Mechanics of thin-skinned fold-and-thrust belts. *Geological Society of America Bulletin* **89**(8), 1189-1198.
- Chaumillon, E. & Mascle, J. 1997. From foreland to forearc domains: New multichannel seismic reflection survey of the Mediterranean ridge accretionary complex (Eastern Mediterranean). *Marine Geology* **138**(3-4), 237-259.
- Chen, J., Burbank, D. W., Scharer, K. M., Sobel, E., Yin, J., Rubin, C. & Zhao, R. 2002. Magnetochronology of the Upper Cenozoic strata in the Southwestern Chinese Tian Shan: rates of Pleistocene folding and thrusting. *Earth and Planetary Science Letters* **195**(1-2), 113-130.
- Chen, J., Heermance, R., Burbank, D. W., Scharer, K. M., Miao, J. & Wang, C. 2007. Quantification of growth and lateral propagation of the Kashi anticline, southwest Chinese Tian Shan. *Journal of Geophysical Research* **112**(B3), B03S16.
- Chmeleff, J., von Blanckenburg, F., Kossert, K. & Jakob, D. 2010. Determination of the ^{10}Be half-life by multicollector ICP-MS and liquid scintillation counting. *Nuclear Instruments and Methods in Physics Research Section B: Beam Interactions with Materials and Atoms* **268**(2), 192-199.
- Clapp, E. M., Bierman, P. R. & Caffee, M. 2002. Using ^{10}Be and ^{26}Al to determine sediment generation rates and identify sediment source areas in an arid region drainage basin. *Geomorphology* **45**(1-2), 89-104.
- Clemens, S. C. & Prell, W. L. 2003. A 350,000 year summer-monsoon multi-proxy stack from the Owen Ridge, Northern Arabian Sea. *Marine Geology* **201**(1-3), 35-51.
- Cockburn, H. A. P. & Summerfield, M. A. 2004. Geomorphological applications of cosmogenic isotope analysis. *Progress in Physical Geography* **28**(1), 1-42.
- Daëron, M., Avouac, J.-P. & Charreau, J. 2007. Modeling the shortening history of a fault tip fold using structural and geomorphic records of deformation. *Journal of Geophysical Research* **112**(B3), B03S13.
- Dahlen, F. A. 1990. Critical taper model of fold-and-thrust belts and accretionary wedges. *Annual Reviews of Earth and Planetary Sciences* **18**, 55-99.
- Dahlen, F. A., Suppe, J. & Davis, D. 1984. Mechanics of fold-and-thrust belts and accretionary wedges: Cohesive Coulomb theory. *Journal of Geophysical Research* **89**(B12), 10087-10101.
- Dahlstrom, C. D. A. 1969. Balanced cross sections. *Canadian Journal of Earth Sciences* **6**(4), 743-757.
- Davis, D., Suppe, J. & Dahlen, F. A. 1983. Mechanics of fold-and-thrust belts and accretionary wedges. *Journal of Geophysical Research* **88**(B2), 1153-1172.

- Deffontaines, B., Lee, J.-C., Angelier, J., Carvalho, J. & Rudant, J.-P. 1994. New geomorphic data on the active Taiwan orogen: A multisource approach. *Journal of Geophysical Research* **99**(B10), 20243-20266.
- Degens, E. T. & Paluska, A. 1979. Tectonic and climatic pulses recorded in quaternary sediments of the Caspian-Black Sea region. *Sedimentary Geology* **23**(1-4), 149-163.
- DeMets, C., Gordon, R. G. & Argus, D. F. 2010. Geologically current plate motions. *Geophysical Journal International* **181**(1), 1-80.
- DeMets, C., Gordon, R. G., Argus, D. F. & Stein, S. 1990. Current plate motions. *Geophysical Journal International* **101**(2), 425-478.
- DeMets, C., Gordon, R. G., Argus, D. F. & Stein, S. 1994. Effect of recent revision to the geomagnetic reversal time scale on estimates of current plate motions. *Geophysical Research Letters* **21**(20), 2191-2194.
- DiBiase, R. A., Whipple, K. X., Heimsath, A. M. & Ouimet, W. B. 2010. Landscape form and millennial erosion rates in the San Gabriel Mountains, CA. *Earth and Planetary Science Letters* **289**(1-2), 134-144.
- Djamali, M., de Beaulieu, J.-L., Shah-hosseini, M., Andrieu-Ponel, V., Ponel, P., Amini, A., Akhiani, H., Leroy, S. A. G., Stevens, L., Lahijani, H. & Brewer, S. 2008. A late Pleistocene long pollen record from Lake Urmia, NW Iran. *Quaternary Research* **69**(3), 413-420.
- Dolati, A. 2010. *Stratigraphy, structure geology and low-temperature thermochronology across the Makran accretionary wedge in Iran*. PhD Thesis, ETH Zurich. 309 p.
- Dragert, H., Wang, K. & James, T. S. 2001. A Silent Slip Event on the Deeper Cascadia Subduction Interface. *Science* **292**(5521), 1525-1528.
- Dykstra, J. D. & Birnie, R. W. 1979. Segmentation of the Quaternary subduction zone under the Baluchistan region of Pakistan and Iran. *In: Geodynamics of Pakistan* (edited by Farah, A. & Dejong, K. A.), Geological Survey of Pakistan, Quetta 319-323.
- Ehlers, T. A. 2005. Crustal Thermal Processes and the Interpretation of Thermochronometer Data. *Reviews in Mineralogy and Geochemistry* **58**(1), 315-350.
- Ellouz-Zimmermann, N., Deville, E., Müller, C., Lallemand, S., Subhani, A. B. & Tabreez, A. R. 2007a. Impact of sedimentation on convergent margin tectonics: Example of the Makran Accretionary Prism (Pakistan). *In: Thrust belts and foreland basins: From fold kinematics to hydrocarbon systems* (edited by Lacombe, O., Lavé, J., Roure, F. & Vergés, J.), Springer Verlag, Berlin, 327-350.
- Ellouz-Zimmermann, N., Lallemand, S. J., Castilla, R., Mouchot, N., Leturmy, P., Battani, A., Buret, C., Chérel, L., Desaubliaux, G., Deville, E., Ferrand, J., Lügcke, A., Mahieux, G., Mascle, G., Mühr, P., Pierson-Wickmann, A.-C., Robion, P., Schmitz, J., Danish, M., Hasany, S., Shahzad, A. & Tabreez, A. 2007b. Offshore frontal part of the Makran Accretionary Prism (Pakistan): The Chamak Survey. *In: Thrust belts and foreland basins: From fold kinematics to hydrocarbon systems* (edited by Lacombe, O., Lavé, J., Roure, F. & Vergés, J.), Springer-Verlag, Berlin, 351-366.
- Engdahl, E. R., Jackson, J. A., Myers, S. C., Bergman, E. A. & Priestley, K. 2006. Relocation and assessment of seismicity in the Iran region. *Geophysical Journal International* **167**, 761-778.

- Epard, J. L. & Groshong, R. H. 1995. Kinematic model of detachment folding including limb rotation, fixed hinges and layer-parallel strain. *Tectonophysics* **247**(1-4), 85-103.
- Erslev, E. A. 1991. Trishear fault-propagation folding. *Geology* **19**(6), 617-620.
- Falcon, N. L. 1975. From Musandam to the Iranian Makran. *The Geographical Journal* **141**(1), 55-58.
- Farhoudi, G. & Karig, D. E. 1977. Makran of Iran and Pakistan as an active arc system. *Geology* **5**(11), 664-668.
- Fleitmann, D., Burns, S. J., Mangini, A., Mudelsee, M., Kramers, J., Villa, I., Neff, U., Al-Subbary, A. A., Buettner, A., Hippler, D. & Matter, A. 2007. Holocene ITCZ and Indian monsoon dynamics recorded in stalagmites from Oman and Yemen (Socotra). *Quaternary Science Reviews* **26**(1-2), 170-188.
- Flint, J. J. 1974. Stream gradient as a function of order, magnitude and discharge. *Water Resources Research* **10**, 969-973.
- Frankel, K. L., Brantley, K. S., Dolan, J. F., Finkel, R. C., Klinger, R. E., Knott, J. R., Machette, M. N., Owen, L. A., Phillips, F. M., Slate, J. L. & Wernicke, B. P. 2007. Cosmogenic ¹⁰Be and ³⁶Cl geochronology of offset alluvial fans along the northern Death Valley fault zone: Implications for transient strain in the eastern California shear zone. *Journal of Geophysical Research* **112**(B6), B06407.
- Friend, P. F., Jones, N. E. & Vincent, S. J. 2009. Drainage Evolution in Active Mountain Belts: Extrapolation Backwards from Present-Day Himalayan River Patterns. *In: Fluvial Sedimentology VI*, Blackwell Publishing Ltd., 305-313.
- Frisch, W. 1999. *Tectonic geomorphology* Borntraeger, Berlin, 268 p.
- Fruehn, J., White, R. S. & Minshull, T. A. 1997. Internal deformation and compaction of the Makran accretionary wedge. *Terra Nova* **9**(3), 101-104.
- Gahalaut, V. K. & Catherine, J. K. 2006. Rupture characteristics of 28 March 2005 Sumatra earthquake from GPS measurements and its implication for tsunami generation. *Earth and Planetary Science Letters* **249**(1-2), 39-46.
- Gasse, F. 2000. Hydrological changes in the African tropics since the Last Glacial Maximum. *Quaternary Science Reviews* **19**(1-5), 189-211.
- Gharibreza, M. R. & Motamed, A. 2006. Late Quaternary paleoshorelines and sedimentary sequences in Chabahar Bay (Southeast of Iran). *Journal of Coastal Research* **22**(6), 1499-1504.
- Gholamzadeh, A., Yamini-Fard, F., Hessami, K. & Tatar, M. 2009. The February 28, 2006 Tiab earthquake, Mw 6.0: Implications for tectonics of the transition between the Zagros continental collision and the Makran subduction zone. *Journal of Geodynamics* **47**(5), 280-287.
- Gosse, J. C. 2011. Terrestrial Cosmogenic Nuclide Techniques for Assessing Exposure History of Surfaces and Sediments in Active Tectonic Regions. *In: Tectonics of Sedimentary Basins*, John Wiley & Sons, Ltd, 63-79.
- Gosse, J. C. 2012. Terrestrial cosmogenic nuclide techniques for assessing exposure history of surfaces and sediments in active tectonic regions. *In: Tectonics of Sedimentary Basins: Recent Advances*.

- Gosse, J. C. & Phillips, F. M. 2001. Terrestrial in situ cosmogenic nuclides: theory and application. *Quaternary Science Reviews* **20**(14), 1475-1560.
- Grando, G. & McClay, K. 2007. Morphotectonics domains and structural styles in the Makran accretionary prism, offshore Iran. *Sedimentary Geology* **196**(1-4), 157-179.
- Granger, E. D. & Smith, L. A. 2000. Dating buried sediments using radioactive decay and muogenic production of ²⁶Al and ¹⁰Be. *Nuclear Instruments and Methods in Physics Research Section B: Beam Interactions with Materials and Atoms* **172**(1-4), 822-826.
- Graveleau, F., Malavieille, J. & Dominguez, S. 2012. Experimental modelling of orogenic wedges: A review. *Tectonophysics* **538-540**, 1-66.
- Hack, J. T. 1957. Studies of longitudinal stream profiles in Virginia and Maryland. *United States Geological Survey Professional Paper* **294-B**, 45-97.
- Haff, P. K. & Werner, B. T. 1996. Dynamical processes on desert pavements and the healing of surficial disturbances. *Quaternary Research* **45**(1), 38-46.
- Hafkenscheid, E., Wortel, M. J. R. & Spakman, W. 2006. Subduction history of the Tethyan region derived from seismic tomography and tectonic reconstructions. *Journal of Geophysical Research* **111**(B8), B08401.
- Haghipour, N., Burg, J.-P., Kober, F., Zeilinger, G., Ivy-Ochs, S., Kubik, P. W. & Mohammadi, F. 2012. Rate of crustal shortening and non-Coulomb behaviour of an active accretionary wedge: The folded fluvial terraces in Makran (SE, Iran). *Earth and Planetary Science Letters* **355-356**, 187-198.
- Hall, S. R., Farber, D. L., Audin, L., Finkel, R. C. & Mériaux, A.-S. 2008. Geochronology of the pediment surfaces in southern Peru : Implications for Quaternary deformation of the Andean forearc. *Tectonophysics* **459**(1-4), 186-205.
- Hancock, G. S., Anderson, R. S., Chadwick, O. A. & Finkel, R. C. 1999. Dating fluvial terraces with ¹⁰Be and ²⁶Al profiles: application to the Wind River, Wyoming. *Geomorphology* **27**(1-2), 41-60.
- Hancock, G. S., Anderson, R. S. & Whipple, K. X. 1998. Beyond power: Bedrock river incision process and form. In: *Rivers over rock: Fluvial processes in bedrock channels* (edited by Tinkler, K. & Wohl, E. E.). *Geophysical monograph* **107**, American Geophysical Union, Washington, DC 35-60.
- Harms, J. C., Cappel, H. N. & Francis, D. C. 1984. The Makran coast of Pakistan: its stratigraphy and hydrocarbon potential. In: *Marine Geology and Oceanography of Arabian Sea and Coastal Pakistan* (edited by Haq, B. U. & Milliman, J. D.), Van Nostrand Reinhold Co., New York, United States, 3-27.
- Harms, J. C., Cappel, H. N., Francis, D. C. & Marathon Oil Company, U. S. A. 1982. Geology and Petroleum Potential of the Makran Coast, Pakistan. In: *Offshore South East Asia Show Exploration III*, Geology session. Society of Petroleum Engineers Singapore, 9-12 February 1982, 1-9.
- Harrison, J. V. & Falcon, N. L. 1936. Gravity collapse structures and mountain ranges, as exemplified in south-western Iran. *Quarterly Journal of the Geological Society* **92**(91-102).
- Hartshorn, K., Hovius, N., Dade, W. B. & Slingerland, R. L. 2002. Climate-Driven Bedrock Incision in an Active Mountain Belt. *Science* **297**(5589), 2036-2038.

- Hatzfeld, D. & Molnar, P. 2010. Comparisons of the kinematics and deep structures of the Zagros and Himalaya and of the Iranian and Tibetan plateaus and geodynamic implications. *Reviews of Geophysics* **48**(2), RG2005.
- Heck, N. H. 1947. List of seismic sea waves. *Bulletin of the Seismological Society of America* **37**(4), 269-286.
- Heidarzadeh, M., Pirooz, M. D., Zaker, N. H., Yalciner, A. C., Mokhtari, M. & Esmaeily, A. 2008. Historical tsunami in the Makran Subduction Zone off the southern coasts of Iran and Pakistan and results of numerical modeling. *Ocean Engineering* **35**(8-9), 774-786.
- Heisinger, B., Lal, D., Jull, A. J. T., Kubik, P., Ivy-Ochs, S., Knie, K. & Nolte, E. 2002. Production of selected cosmogenic radionuclides by muons: 2. Capture of negative muons. *Earth and Planetary Science Letters* **200**(3-4), 357-369.
- Hidy, A. J., Gosse, J. C., Pederson, J. L., Mattern, J. P. & Finkel, R. C. 2010. A geologically constrained Monte Carlo approach to modeling exposure ages from profiles of cosmogenic nuclides: An example from Lees Ferry, Arizona. *Geochemistry Geophysics Geosystems* **11**, Q0AA10.
- Hilley, G. E. & Arrowsmith, J. R. 2008. Geomorphic response to uplift along the Dragon's Back pressure ridge, Carrizo Plain, California. *Geology* **36**(5), 367-370.
- Hilley, G. E. & Strecker, M. R. 2004. Steady state erosion of critical Coulomb wedges with applications to Taiwan and the Himalaya. *Journal of Geophysical Research* **109**(B1), B01411.
- Hirose, H., Hirahara, K., Kimata, F., Fujii, N. & Miyazaki, S. i. 1999. A slow thrust slip event following the two 1996 Hyuganada Earthquakes beneath the Bungo Channel, southwest Japan. *Geophysical Research Letters* **26**(21), 3237-3240.
- Hodges, K. V., Hurtado, J. M. & Whipple, K. X. 2001. Southward extrusion of Tibetan crust and its effect on Himalayan tectonics. *Tectonics* **20**(6), 799-809.
- Holbrook, J. & Schumm, S. A. 1999. Geomorphic and sedimentary response of rivers to tectonic deformation: a brief review and critique of a tool for recognizing subtle epeirogenic deformation in modern and ancient settings. *Tectonophysics* **305**(1-3), 287-306.
- Horton, B. K. 1999. Erosional control on the geometry and kinematics of thrust belt development in the central Andes. *Tectonics* **18**(6), 1292-1304.
- Hosseini-Barzi, M. & Talbot, C. J. 2003. A tectonic pulse in the Makran accretionary prism recorded in Iranian coastal sediments. *Journal of the Geological Society of London* **160**(6), 903-910.
- Hovius, N. 2000. Macroscale process systems of mountain belt erosion. In: *Geomorphology and global tectonics* (edited by Summerfield, M. A.), Wiley and Sonspp, Chichester 77-105.
- Howard, A. D. 1994. A detachment-limited model of drainage basin evolution. *Water Resources Research* **30**(7), 2261-2285.
- Howard, A. D., Dietrich, W. E. & Seidl, M. A. 1994. Modeling fluvial erosion on regional to continental scales. *Journal of Geophysical Research* **99**(B7), 13971-13986.

- Hsieh, M. L. & Chyi, S. J. 2010. Late Quaternary mass-wasting records and formation of fan terraces in the Chen-yeo-lan and Lao-nung catchments, central-southern Taiwan. *Quaternary Science Reviews* **29**(11-12), 1399-1418.
- Huber, H. 1952. Geology of the western coastal Makran area. Iranian National Oil Company, Tehran. GR 9IB
- Hunting Survey Corporation, L. 1960. *Reconnaissance geology of part of West Pakistan. A Colombo plan co-operative project*. Maracle Press Limited, Toronto, 550 p.
- Ivy-Ochs, S., Dühnforth, M., Densmore, A. L. & Alifimov, V. 2012. Dating fan deposits with cosmogenic nuclides. *In: Dating torrential processes on fans and cones* (edited by Schneuwly-Bollschweiler, M.). *Advances in Global Change Research* **47**, Springer ScienceCBusiness Media, Dordrecht.
- Ivy-Ochs, S. & Schaller, M. 2010. Examining processes and rates of landscape change with cosmogenic radionuclides. *In: Environmental radionuclides : tracers and timers of terrestrial processes* (edited by Froehlich, K.). *Radioactivity in the environment*, 16. Elsevier, Amsterdam, 231-294.
- Jackson, J. & McKenzie, D. 1984. Active tectonics of the Alpine- Himalayan Belt between western Turkey and Pakistan. *Geophysical Journal - Royal Astronomical Society* **77**(1), 185-264.
- Jacob, K. H. & Quittmeyer, R. C. 1979. The Makran Region of Pakistan and Iran: Trench arc system with active plate subduction. *In: Geodynamics of Pakistan* (edited by Farah, A. & Dejong, K. A.), Geological Survey of Pakistan, Quetta, 305-317.
- Jamison, W. R. 1987. Geometric analysis of fold development in overthrust terranes. *Journal of Structural Geology* **9**(2), 207-219.
- Jansen, J. D., Fabel, D., Bishop, P., Xu, S., Schnabel, C. & Codilean, A. T. 2011. Does decreasing paraglacial sediment supply slow knickpoint retreat? *Geology* **39**(6), 543-546.
- John, C. 2002. Sea level changes forced ice breakouts in the Last Glacial cycle: new results from coral terraces. *Quaternary Science Reviews* **21**(10), 1229-1240.
- Kanamori, H. & Kikuchi, M. 1993. The 1992 Nicaragua Earthquake - a slow tsunami earthquake associated with subducted sediments. *Nature* **361**, 714-716.
- Kehl, M. 2009. Quaternary climate change in Iran - The state of knowledge. *Erdkunde* **63**(1), 1-17.
- Khan, M. A., Raza, H. A. & Alam, S. 1991. Petroleum geology of the Makran region: Implications for hydrocarbon occurrence in cool basins. *Journal of Petroleum Geology* **14**(1), 5-18.
- Kiden, P. & Tornqvist, T. E. 1998. Can river terrace flights be used to quantify Quaternary tectonic uplift rates? *Journal of Quaternary Science* **13**(6), 573-574.
- Kirby, E., Johnson, C., Furlong, K. & Heimsath, A. 2007. Transient channel incision along Bolinas Ridge, California: Evidence for differential rock uplift adjacent to the San Andreas fault. *Journal of Geophysical Research* **112**(F3), F03S07.

- Kirby, E. & Ouimet, W. B. 2011. Tectonic geomorphology along the eastern margin of Tibet: Insights into the pattern and processes of active deformation adjacent to the Sichuan Basin. *In: Growth and collapse of the Tibetan Plateau* (edited by Gloaguen, R. & Ratschbacher, L.) **353**, Geological Society Special Publications, London, 165-188.
- Kirby, E. & Whipple, K. 2001. Quantifying differential rock-uplift rates via stream profile analysis. *Geology* **29**(5), 415-418.
- Kirby, E. & Whipple, K. X. 2012. Expression of active tectonics in erosional landscapes. *Journal of Structural Geology* **44**, 54-75.
- Kirby, E., Whipple, K. X., Tang, W. & Chen, Z. 2003. Distribution of active rock uplift along the eastern margin of the Tibetan Plateau: Inferences from bedrock channel longitudinal profiles. *Journal of Geophysical Research* **108**(B4), 2217.
- Kirchner, J. W., Finkel, R. C., Riebe, C. S., Granger, D. E., Clayton, J. L., King, J. G. & Megahan, W. F. 2001. Mountain erosion over 10 yr, 10 k.y., and 10 m.y. time scales. *Geology* **29**(7), 591-594.
- Kohl, C. P. & Nishiizumi, K. 1992a. Chemical isolation of quartz for measurement of in-situ-produced cosmogenic nuclides. *Geochimica Cosmochimica Acta* **56**(9), 3583-3587.
- Kohl, C. P. & Nishiizumi, K. 1992b. Scientific comment. Chemical isolation of quartz for measurement of in-situ -produced cosmogenic nuclides. *Geochimica Cosmochimica Acta* **56**, 3583-3587.
- Koons, P. O. 1989. The topographic evolution of collisional mountain belts; a numerical look at the Southern Alps, New Zealand. *American Journal of Science* **289**(9), 1041-1069.
- Kopp, C., Fruehn, J., Flueh, E. R., Reichert, C., Kukowski, N., Bialas, J. & Klaeschen, D. 2000. Structure of the Makran subduction zone from wide-angle and reflection seismic data. *Tectonophysics* **329**(1-4), 171-191.
- Korschinek, G., Bergmaier, A., Faestermann, T., Gerstmann, U. C., Knie, K., Rugel, G., Wallner, A., Dillmann, I., Dollinger, G., von Gostomski, C. L., Kossert, K., Maiti, M., Poutivtsev, M. & Remmert, A. 2010. A new value for the half-life of ^{10}Be by Heavy-Ion Elastic Recoil Detection and liquid scintillation counting. *Nuclear Instruments and Methods in Physics Research Section B: Beam Interactions with Materials and Atoms* **268**(2), 187-191.
- Krishnamurti, T. N. & Ardanuy, P. 1980. The 10 to 20-day westward propagating mode and "Breaks in the Monsoons". *Tellus* **32**(1), 15-26.
- Kubik, P. W. & Christi, M. 2010. ^{10}Be and ^{26}Al measurements at the Zurich 6 MV Tandem AMS facility. *Nuclear Instruments and Methods in Physics Research Section B: Beam Interactions with Materials and Atoms* **268**, 880-883.
- Kubik, P. W., Ivy-Ochs, S., Masarik, J., Frank, M. & Schlüchter, C. 1998. ^{10}Be and ^{26}Al production rates deduced from an instantaneous event within the dendro-calibration curve, the landslide of Köfels, Ötz Valley, Austria. *Earth and Planetary Science Letters* **161**(1-4), 231-241.
- Kuhle, M. 2008. The Pleistocene Glaciation (LGP and pre-LGP, pre-LGM) of SE Iranian Mountains Exemplified by the Kuh-i-Jupar, Kuh-i-Lalezar and Kuh-i-Hezar Massifs. *Polarforschung* **77**(2-3), 71-88.

- Kühni, A. & Pfiffner, O. A. 2001. The relief of the Swiss Alps and adjacent areas and its relation to lithology and structure: topographic analysis from a 250-m DEM. *Geomorphology* **41**(4), 285-307.
- Kukowski, N., Schillhorn, T., Flueh, E. R. & Huhn, K. 2000. Newly identified strike-slip plate boundary in the northeastern Arabian Sea. *Geology* **28**(4), 355-358.
- Kukowski, N., Schillhorn, T., Huhn, K., von Rad, U., Husen, S. & Flueh, E. R. 2001. Morphotectonics and mechanics of the central Makran accretionary wedge off Pakistan. *Marine Geology* **173**(1-4), 1-19.
- Lal, D. 1991. Cosmic ray labeling of erosion surfaces: in situ nuclide production rates and erosion models. *Earth and Planetary Science Letters* **104**, 424-439.
- Lal, D. & Peters, B. 1967. Cosmic ray produced radioactivity on the Earth. In: *Handbuch der Physik = Encyclopedia of physics* (edited by Flügge, S.) **46/2**, Springer, Berlin, 551-612.
- Lavé, J. & Avouac, J.-P. 2000. Active folding of fluvial terraces across the Siwaliks Hills, Himalayas of central Nepal. *Journal of Geophysical Research* **105**(B3), 5735-5770.
- Lavé, J. & Avouac, J.-P. 2001. Fluvial incision and tectonic uplift across the Himalayas of central Nepal. *Journal of Geophysical Research* **106**(B11), 26,561-26,591.
- Leggett, J. K. & Platt, J. L. 1984. Structural features of the Makran fore-arc on Landsat imagery. In: *Marine geology and oceanography of Arabian Sea and Coastal Pakistan* (edited by Haq, B. U. & Milliman, J. D.), Nostrand Reinhold, New York, 33-43.
- Leroy, Y. M., Guiton, M. L. E. & Triantafyllidis, N. 2002. Post-buckling of an elastic plate over an inviscid and buoyant fluid. *International Journal of Solids and Structures* **39**(13-14), 3873-3891.
- Litchfield, N., Wilson, K., Berryman, K. & Wallace, L. 2010. Coastal uplift mechanisms at Pakarae River mouth: Constrains from a combined Holocene fluvial and marine terrace dataset. *Marine Geology* **270**, 72-83.
- Lückge, A., Dooze-Rolinski, H., Khan, A. A., Schulz, H. & von Rad, U. 2001. Monsoonal variability in the northeastern Arabian Sea during the past 5000 years: geochemical evidence from laminated sediments. *Palaeogeography, Palaeoclimatology, Palaeoecology* **167**(3-4), 273-286.
- Maddy, D., Long, A. J. & Bridgland, D. R. 2005. Quaternary land-ocean correlation: A tribute to professor David Q. Bowen - Preface. *Quaternary Science Reviews* **24**(14-15), 1543-1546.
- Malavieille, J. 1984. Modélisation expérimentale des chevauchements imbriqués : application aux chaînes de montagnes. *Bulletin de la Société géologique de France* **(7) 26**, 129-138.
- Masarik, J. 2002. Numerical simulation of *in situ* production of cosmogenic nuclides. *Geochimica et Cosmochimica Acta* **66**(Supplement 1), A491.
- Masek, J. G., Isacks, B. L., Gubbels, T. L. & Fielding, E. J. 1994. Erosion and tectonics at the margins of continental plateaus. *Journal of Geophysical Research* **99**(B7), 13941-13956.

- Masson, F., Anvari, M., Djamour, Y., Walpersdorf, A., Tavakoli, F., Daignières, M., Nankali, H. & Van Gorp, S. 2007. Large-scale velocity field and strain tensor in Iran inferred from GPS measurements: new insight for the present-day deformation pattern within NE Iran. *Geophysical Journal International* **170**(1), 436–440.
- Masson, F., Chéry, J., Hatzfeld, D., Martinod, J., Vernant, P., Tavakoli, F. & Ghafory-Ashtiani, M. 2005. Seismic versus aseismic deformation in Iran inferred from earthquakes and geodetic data. *Geophysical Journal International* **160**, 217-226.
- Matmon, A., Bierman, P. R., Larsen, J., Southworth, S., Pavich, M. & Caffee, M. 2003. Temporally and spatially uniform rates of erosion in the southern Appalachian Great Smoky Mountains. *Geology* **31**(2), 155-158.
- Matmon, A., Simhai, O., Amit, R., Haviv, I., Porat, N., McDonald, E., Benedetti, L. & Finkel, R. 2009. Desert pavement-coated surfaces in extreme deserts present the longest-lived landforms on Earth. *Geological Society of America Bulletin* **121**(5-6), 688-697.
- McCall, G. J. H. 1983. Mélanges of the Makran, southeastern Iran. *In: Ophiolitic and related mélanges* (edited by McCall, G. J. H.) Benchmark Papers in Geology / **66**, Hutchinson Ross Publishing Company, Stroudsburg, Pennsylvania, 292–299.
- McCall, G. J. H. 1997. The geotectonic history of the Makran and adjacent areas of southern Iran. *Journal of Asian Earth Sciences* **15**(6), 517-531.
- McCall, G. J. H. 2002. A summary of the geology of the Iranian Makran. *In: The tectonic and climatic evolution of the Arabian Sea Region* (edited by Clift, P. D., Kroon, F. D., Gaedecke, C. & Craig, J.). *Special Publication* **195**, Geological Society, London, 147–204.
- McCall, G. J. H. & Kidd, R. G. W. 1982a. The Makran, Southeastern Iran: the anatomy of a convergent plate margin active from Cretaceous to Present. *In: Trench-fore-arc geology: sedimentation and tectonics of modern and ancient plate margins* (edited by Leggett, J. K.). *Special Publication* **10**, Geological Society, London, 387-397.
- McCall, G. J. H. & Kidd, R. G. W. 1982b. The Makran, Southeastern Iran: the anatomy of a convergent plate margin active from Cretaceous to Present. *Geological Society, London, Special Publications* **10**(1), 387-397.
- McClay, K. R. 1992. *Thrust tectonics*. Chapman & Hall, London, 447 p.
- Merritts, D. & Vincent, K. R. 1989. Geomorphic response of coastal streams to low, intermediate, and high-rates of uplift, Mendocino triple junction region, Northern California. *Geological Society of America Bulletin* **101**(11), 1373-1388.
- Meyer, B., Mouthereau, F., Lacombe, O. & Agard, P. 2006. Evidence of Quaternary activity along the Deshir Fault: implication for the Tertiary tectonics of Central Iran. *Geophysical Journal International* **164**(1), 192-201.
- Mitra, S. 2002. Structural models of faulted detachment folds. *American Association of Petroleum Geologists Bulletin* **86**(9), 1673-1694.
- Mitra, S. 2003. A unified kinematic model for the evolution of detachment folds. *Journal of Structural Geology* **25**(10), 1659-1673.

- Molin, P., Fubelli, G., Nocentini, M., Sperini, S., Ignat, P., Grecu, F. & Dramis, F. 2012. Interaction of mantle dynamics, crustal tectonics, and surface processes in the topography of the Romanian Carpathians: A geomorphological approach. *Global and Planetary Change* **90–91**(0), 58-72.
- Molin, P. & Pazzaglia, F. J. 2004. Geomorphic expression of active tectonics in a rapidly-deforming forearc, silia massif. *American Journal of Science* **304**, 559-589.
- Molnar, P. 1995. Temperatures in zones of steady-state underthrusting of young oceanic lithosphere. *Earth and Planetary Science Letters* **131**(1-2), 57-70.
- Molnar, P., Brown, E. T., Burchfiel, B. C., Qidong, D., Xianyue, F., Jun, L., Raisbeck, G. M., Jianbang, S., Zhangming, W., Yiou, F. & Huichuan, Y. 1994. Quaternary climate-change and the formation of river terraces across growing anticlines on the north flank of the Tien-Shan, China. *Journal of Geology* **102**(5), 583-602.
- Montgomery, D. R. & Brandon, M. T. 2002. Topographic controls on erosion rates in tectonically active mountain ranges. *Earth and Planetary Science Letters* **201**(3–4), 481-489.
- Mouthereau, F., Lacombe, O. & Meyer, B. 2006. The Zagros folded belt (Fars, Iran): constraints from topography and critical wedge modelling. *Geophysical Journal International* **165**(1), 336-356.
- Mouthereau, F., Lacombe, O., Tensi, J., Bellahsen, N., Kargar, S. & Amrouch, K. 2007a. Mechanical Constraints on the Development of the Zagros Folded Belt (Fars)
- Thrust Belts and Foreland Basins (edited by Lacombe, O., Roure, F., Lavé, J. & Vergés, J.). *Frontiers in Earth Sciences*, Springer Berlin Heidelberg, 247-266.
- Mouthereau, F., Tensi, J., Bellahsen, N., Lacombe, O., De Boisgrollier, T. & Kargar, S. 2007b. Tertiary sequence of deformation in a thin-skinned/thick-skinned collision belt: The Zagros Folded Belt (Fars, Iran). *Tectonics* **26**(5), TC5006.
- Musson, R. M. W. 2009. Subduction in the Western Makran: the historian's contribution. *Journal of the Geological Society, London* **166**, 387-391.
- Niedermann, S., Graf, T., Kim, J. S., Kohl, C. P., Marti, K. & Nishiizumi, K. 1994. Cosmic-ray-produced ^{21}Ne in terrestrial quartz: the neon inventory of Sierra Nevada quartz separates. *Earth and Planetary Science Letters* **125**(1–4), 341-355.
- Nilforoushan, F., Masson, F., Vernant, P., Vigny, C., Martinod, J., Abbassi, M., Nankali, H., Hatzfeld, D., Bayer, R., Tavakoli, F., Ashtiani, A., Doerflinger, E., Daignières, M., Collard, P. & Chéry, J. 2003. GPS network monitors the Arabia-Eurasia collision deformation in Iran. *Journal of Geodesy* **77**(7), 411-422.
- Nishiizumi, K., Imamura, M., Caffee, M. W., Southon, J. R., Finkel, R. C. & McAninch, J. 2007. Absolute calibration of ^{10}Be AMS standards. *Nuclear Instruments and Methods in Physics Research Section B: Beam Interactions with Materials and Atoms* **258**(2), 403-413.
- Ochs, M. & Ivy-Ochs, S. 1997. The chemical behavior of Be, Al, Fe, Ca and Mg during AMS target preparation from terrestrial silicates modeled with chemical speciation calculations. *Nuclear Instruments and Methods in Physics Research Section B: Beam Interactions with Materials and Atoms* **123**(1–4), 235-240.

- Owen, L. A., Bright, J., Finkel, R. C., Jaiswal, M. K., Kaufman, D. S., Mahan, S., Radtke, U., Schneider, J. S., Sharp, W., Singhvi, A. K. & Warren, C. N. 2007. Numerical dating of a Late Quaternary spit-shoreline complex at the northern end of Silver Lake playa, Mojave Desert, California: A comparison of the applicability of radiocarbon, luminescence, terrestrial cosmogenic nuclide, electron spin resonance, U-series and amino acid racemization methods. *Quaternary International* **166**(1), 87-110.
- Owen, L. A., Frankel, K. L., Knott, J. R., Reynhout, S., Finkel, R. C., Dolan, J. F. & Lee, J. 2011. Beryllium-10 terrestrial cosmogenic nuclide surface exposure dating of Quaternary landforms in Death Valley. *Geomorphology* **125**(4), 541-557.
- Page, W. D., Alt, J. N., Cluff, L. S. & Plafker, G. 1979. Evidence for the recurrence of large-magnitude earthquakes along the Makran coast of Iran and Pakistan. *Tectonophysics* **52**(1-4), 533-547.
- Pazzaglia, F. J. & Brandon, M. T. 2001. A fluvial record of long-term steady-state uplift and erosion across the Cascadia Forearc High, Western Washington State. *American Journal of Science* **301**(4-5), 385-431.
- Pazzaglia, F. J., Gardner, T. W. & Merritts, D. J. 1998. Bedrock fluvial incision and longitudinal profile development over geologic timescales determined by fluvial terraces. In: *Rivers over rock: Fluvial processes in bedrock channels* (edited by Tinkler, K. & Wohl, E. E.). *Geophysical monograph* **107**, American Geophysical Union, Washington, DC
- Placzek, C. J., Matmon, A., Granger, D. E., Quade, J. & Niedermann, S. 2010. Evidence for active landscape evolution in the hyperarid Atacama from multiple terrestrial cosmogenic nuclides. *Earth and Planetary Science Letters* **295**(1-2), 12-20.
- Platt, J. P. 1986. Dynamics of orogenic wedges and the uplift of high-pressure metamorphic rocks. *Geological Society of America Bulletin* **97**(9), 1037-1053.
- Platt, J. P., Leggett, J. K., Young, J., Raza, H. & Alam, S. 1985. Large-scale sediment underplating in the Makran accretionary prism, southwest Pakistan. *Geology* **13**(7), 507-511.
- Poblet, J., McClay, K., Storti, F. & Muñoz, J. A. 1997. Geometries of syntectonic sediments associated with single-layer detachment folds. *Journal of Structural Geology* **19**(3-4), 369-381.
- Ponza, A., Pazzaglia, F. J. & Picotti, V. 2010. Thrust-fold activity at the mountain front of the Northern Apennines (Italy) from quantitative landscape analysis. *Geomorphology* **123**(3-4), 211-231.
- Price, N. J. & Cosgrove, J. W. 1990. *Analysis of geological structures*. Cambridge University Press, Cambridge, 502 p.
- Quittmeyer, R. C. & Jacob, K. H. 1979. Historical and modern seismicity of Pakistan, Afghanistan, northwestern India and southeastern Iran. *Bulletin of the Seismological Society of America* **69**(3), 773-823.
- Regard, V., Bellier, O., Braucher, R., Gasse, F., Bourlès, D., Mercier, J., Thomas, J. C., Abbassi, M. R., Shabanian, E. & Soleymani, S. 2006. ¹⁰Be dating of alluvial deposits from Southeastern Iran (the Hormoz Strait area). *Palaeogeography, Palaeoclimatology, Palaeoecology* **242**(1-2), 36-53.

- Reimer, P. J., Baillie, M. G. L., Bard, E., Bayliss, A., Beck, J. W., Blackwell, P. G., Bronk Ramsey, C., Buck, C. E., Burr, G. S., Edwards, R. L., Friedrich, M., Grootes, P. M., Guilderson, T. P., Hajdas, I., Heaton, T. J., Hogg, A. G., Hughen, K. A., Kaiser, K. F., Kromer, B., McCormac, F. G., Manning, S. W., Reimer, R. W., Richards, D. A., Southon, J. R., Talamo, S., Turney, C. S. M., van der Plicht, J. & Weyhenmeyer, C. E. 2009. IntCal09 and marine 09 radiocarbon age calibration curves, 0–50,000 years CAL BP. *Radiocarbon* **51**(4), 1111-1150.
- Repka, J. L., Anderson, R. S. & Finkel, R. C. 1997. Cosmogenic dating of fluvial terraces, Fremont River, Utah. *Earth and Planetary Science Letters* **152**(1-4), 59-73.
- Reyss, J. L., Pirazzoli, P. A., Haghypour, A., Hatté, C. & Fontugne, M. 1999. Quaternary marine terraces and tectonic uplift rates on the south coast of Iran. In: *Coastal tectonics* (edited by Stewart, I. S. & Vita-Finzi, C.). *Special Publication* **146**, Geological Society, London, 225-237.
- Ricou, L.-E. 1994. Tethys reconstructed: plates, continental fragments and their boundaries since 260 Ma from Central America to South-eastern Asia. *Geodinamica Acta* **7**(4), 169-218.
- Rigon, R., Rodriguez-Iturbe, I., Maritan, A., Giacometti, A., Tarboton, D. G. & Rinaldo, A. 1996. On Hack's law. *Water Resources Research* **32**(11), 3367–3374.
- Rockwell, T. K., Keller, E. A. & Dembroff, G. R. 1988. Quaternary rate of folding of the Ventura Avenue anticline, western Transverse Ranges, southern California. *Geological Society of America Bulletin* **100**(6), 850-858.
- Roe, G. H. & Brandon, M. T. 2011. Critical form and feedbacks in mountain-belt dynamics: Role of rheology as a tectonic governor. *Journal of Geophysical Research* **116**(B2), B02101.
- Rogers, G. & Dragert, H. 2003. Episodic Tremor and Slip on the Cascadia Subduction Zone: The Chatter of Silent Slip. *Science* **300**(5627), 1942-1943.
- Ruh, J. B., Kaus, B. J. P. & Burg, J.-P. 2012. Numerical investigation of deformation mechanics in fold-and-thrust belts: Influence of rheology of single and multiple décollements. *Tectonics* **31**(3), TC3005.
- Safran, E. B., Bierman, P. R., Aalto, R., Dunne, T., Whipple, K. X. & Caffee, M. 2005. Erosion rates driven by channel network incision in the Bolivian Andes. *Earth Surface Processes and Landforms* **30**(8), 1007-1024.
- Schaller, M., von Blanckenburg, F., Veldkamp, A., Tebbens, L. A., Hovius, N. & Kubik, P. W. 2002. A 30 000 yr record of erosion rates from cosmogenic ^{10}Be in Middle European river terraces. *Earth and Planetary Science Letters* **204**(1–2), 307-320.
- Schaller, M., von Blanckenburg, F., Hovius, N., Veldkamp, A., van den Berg, M. W. & Kubik, P. W. 2004. Paleoerosion rates from cosmogenic ^{10}Be in a 1.3 Ma terrace sequence: Response of the River Meuse to changes in climate and rock uplift. *The Journal of Geology* **112**(2), 127-144.
- Scharer, K. M., Burbank, D. W., Chen, J. & Weldon, R. J., II. 2006. Kinematic models of fluvial terraces over active detachment folds: Constraints on the growth mechanism of the Kashi-Atushi fold system, Chinese Tian Shan. *Geological Society of America Bulletin* **118**(7-8), 1006-1021.

- Schlunegger, F. & Simpson, G. 2002. Possible erosional control on lateral growth of the European Central Alps. *Geology* **30**(10), 907-910.
- Schlüter, H. U., Prexl, A., Gaedicke, C., Roeser, H., Reichert, C., Meyer, H. & von Daniels, C. 2002. The Makran accretionary wedge: sediment thicknesses and ages and the origin of mud volcanoes. *Marine Geology* **185**, 219-232.
- Schmalholz, S. M., Podlachidkov, Y. & Burg, J.-P. 2002. Control of folding by gravity and matrix thickness : Implications for large-scale folding. *Journal of Geophysical Research* **107**(B1), doi: 10.1029/2001JB000355.
- Schmalholz, S. M., Podlachikov, Y. Y. & Jamtveit, B. 2005. Structural softening of the lithosphere. *Terra Nova* **17**(1), 66-72.
- Schmalholz, S. M. & Podladchikov, Y. Y. 2001. Strain and competence contrast estimation from fold shape. *Tectonophysics* **340**(3-4), 195-213.
- Schmidt, S., Hetzel, R., Kuhlmann, J., Mingorance, F. & Ramos, V. A. 2011. A note of caution on the use of boulders for exposure dating of depositional surfaces. *Earth and Planetary Science Letters* **302**(1-2), 60-70.
- Schumm, S., Dumont, J. & Holbrook, J. 2000. *Active tectonics and alluvial rivers*. Cambridge University Press, Cambridge, 292 p.
- Schumm, S. A. 1977. *The fluvial system*. Wiley, New York, 338 p.
- Seeber, L. & Gornitz, V. 1983. River profiles along the Himalayan arc as indicators of active tectonics. *Tectonophysics* **92**(4), 335-367.
- Sella, G. F., Dixon, T. H. & Mao, A. 2002. REVEL: A model for recent plate velocities from space geodesy. *Journal of Geophysical Research* **107**(B4), 2081, 30 pp.
- Sengor, C. A. M. 1991. The role of Accretionary Wedges in the growth of continents : asiatic examples from Argand to plate tectonics. *Eclogae geologicae Helvetiae* **84**(3), 535-597.
- Shaw, J. H. & Suppe, J. 1994. Active faulting and growth folding in the eastern Santa Barbara Channel, California. *Geological Society of America Bulletin* **106**(5), 607-626.
- Siddall, M., Bard, E., Rohling, E. J. & Hemleben, C. 2006. Sea-level reversal during Termination II. *Geology* **34**(10), 817-820.
- Simpson, G. D. H. 2010. Formation of accretionary prisms influenced by sediment subduction and supplied by sediments from adjacent continents. *Geology* **38**(2), 131-134.
- Sirocko, F., Sarnthein, M., Lange, H. & Erlenkeuser, H. 1991. Atmospheric summer circulation and coastal upwelling in the Arabian Sea during the Holocene and the last glaciation. *Quaternary Research* **36**(1), 72-93.
- Sklar, L. S. & Dietrich, W. E. 1998. River longitudinal profiles and bedrock incision models: Stream power and the influence of sediment supply. In: *Rivers over rock: Fluvial processes in bedrock channels* (edited by Tinkler, K. & Wohl, E. E.). *Geophysical monograph* **107**, American Geophysical Union, Washington, DC 237-260.
- Smit, J., Burg, J.-P., Dolati, A. & Sokoutis, D. 2010. Effects of mass waste events on thrust wedges: Analogue experiments and application to the Makran accretionary wedge. *Tectonics* **29**, TC3003.

- Smith, G., McNeill, L., Henstock, T. J. & Bull, J. 2012. The structure and fault activity of the Makran accretionary prism. *Journal of Geophysical Research-Solid Earth* **117**.
- Smith, T. R., Merchant, G. E. & Birnir, B. 2000. Transient attractors: towards a theory of the graded stream for alluvial and bedrock channels. *Computers & Geosciences* **26**(5), 541-580.
- Snead, R. E. 1967. Recent morphological changes along the coast of West Pakistan. *Annals of the Association of American Geographers* **57**(3), 550-565.
- Snead, R. J. 1992. Uplifted marine terraces along the makran Coast of Pakistan and Iran. In: *Himalaya to the sea: geology, geomorphology, and the Quaternary* (edited by Shroder, J. F.), Routledge, London, 327-361.
- Snyder, N. P., Whipple, K. X., Tucker, G. E. & Merritts, D. J. 2000. Landscape response to tectonic forcing: Digital elevation model analysis of stream profiles in the Mendocino triple junction region, northern California. *Geological Society of America Bulletin* **112**, 1250-1263.
- Snyder, N. P., Whipple, K. X., Tucker, G. E. & Merritts, D. J. 2002. Interactions between onshore bedrock-channel incision and nearshore wave-base erosion forced by eustasy and tectonics. *Basin Research* **14**(2), 105-127.
- Stöcklin, J. 1952. Geology of the central coastal Makran area. Iranian National Oil Company, Tehran. GR 91C
- Stockmal, G. S. 1983. Modeling of large-scale accretionary wedge deformation. *Journal of Geophysical Research* **88**(B10), 8271-8287.
- Stoecklin, J. 1968. Structural history and tectonics of Iran; a review. *AAPG Bulletin* **52**(7), 1229-1258.
- Stone, J. O. 2000. Air pressure and cosmogenic isotope production. *Journal of Geophysical Research* **105**(B10), 23753-23759.
- Stone, J. O., Allan, G. L., Fifield, L. K. & Cresswell, R. G. 1996. Cosmogenic chlorine-36 from calcium spallation. *Geochimica et Cosmochimica Acta* **60**(4), 679-692.
- Stüwe, K., White, L. & Brown, R. 1994. The influence of eroding topography on steady-state isotherms. Application to fission track analysis. *Earth and Planetary Science Letters* **124**(1-4), 63-74.
- Suppe, J. 1981. Mechanics of mountain building and metamorphism in Taiwan. *Memoir of the Geological Society of China* **4**, 67-89.
- Suppe, J. & Medwedeff, A. 1990. Geometry and kinematics of fault-propagation folding. *Ecolgae Geologicae Helvetiae* **83**(3), 409-454.
- Synal, H.-A., Stocker, M. & Suter, M. 2007. MICADAS: A new compact radiocarbon AMS system. *Nuclear Instruments and Methods in Physics Research Section B: Beam Interactions with Materials and Atoms* **259**(1), 7-13.
- Talebian, M. & Jackson, J. 2004. A reappraisal of earthquake focal mechanisms and active shortening in the Zagros mountains of Iran. *Geophysical Journal International* **156**, 506-526.

- Tebbens, L. A., Veldkamp, A., Van Dijke, J. J. & Schoorl, J. M. 2000. Modeling longitudinal-profile development in response to Late Quaternary tectonics, climate and sea-level changes: the River Meuse. *Global and Planetary Change* **27**(1-4), 165-186.
- Tirrul, R., Bell, I. R., Griffis, R. J. & Camp, V. E. 1983. The Sistan suture zone of eastern Iran. *Geological Society of America Bulletin* **94**(1), 134-150.
- Tucker, G. E. & Whipple, K. X. 2002. Topographic outcomes predicted by stream erosion models: Sensitivity analysis and intermodel comparison. *Journal of Geophysical Research* **107**(B9), 2179.
- Van Heijst, M. W. I. M. & Postma, G. 2001. Fluvial response to sea-level changes: a quantitative analogue, experimental approach. *Basin Research* **13**(3), 269-292.
- van Zeist, W. & Wright, H. E. 1963. Preliminary Pollen Studies at Lake Zeribar, Zagros Mountains, Southwestern Iran. *Science* **140**(3562), 65-67.
- Vance, D., Bickle, M., Ivy-Ochs, S. & Kubik, P. W. 2003. Erosion and exhumation in the Himalaya from cosmogenic isotope inventories of river sediments. *Earth and Planetary Science Letters* **206**(3-4), 273-288.
- VanLaningham, S., Meigs, A. & Goldfinger, C. 2006. The effects of rock uplift and rock resistance on river morphology in a subduction zone forearc, Oregon, USA. *Earth Surface Processes and Landforms* **31**(10), 1257-1279.
- Vassallo, R., Ritz, J.-F. & Carretier, S. 2011. Control of geomorphic processes on ¹⁰Be concentrations in individual clasts: Complexity of the exposure history in Gobi-Altay range (Mongolia). *Geomorphology* **135**(1-2), 35-47.
- Vernant, P., Nilforoushan, F., Hatzfeld, D., Abbassi, M. R., Vigny, C., Masson, F., Nankali, H., Martinod, J., Ashtiani, A., Bayer, R., Tavakoli, F. & Chéry, J. 2004. Present-day crustal deformation and plate kinematics in the Middle East constrained by GPS measurements in Iran and northern Oman. *Geophysical Journal International* **157**(1), 381-398.
- Vigny, C., Huchon, P., Ruegg, J., Khanbari, K. & Asfaw, L. M. 2006. Confirmation of Arabia plate slow motion by new GPS data in Yemen. *Journal of Geophysical Research* **111**(B02402), doi:10.1029/2004JB003229.
- Vita-Finzi, C. 1975. Quaternary Deposits in the Iranian Makran. *The Geographical Journal* **141**(3), 415-420.
- Vita-Finzi, C. 1987. ¹⁴C deformation chronologies in coastal Iran, Greece and Jordan. *Journal of the Geological Society* **144**(4), 553-560.
- Vita - Finzi, C. 1969. *The mediterranean valleys : geological changes in historical times*. Cambridge University Press, London, p.
- von Blanckenburg, F., Hewawasam, T. & Kubik, P. W. 2004. Cosmogenic nuclide evidence for low weathering and denudation in the wet, tropical highlands of Sri Lanka. *Journal of Geophysical Research* **109**(F3), F03008.
- Weijermars, R. & Schmeling, H. 1986. Scaling of Newtonian and non-Newtonian fluid dynamics without inertia for quantitative modelling of rock flow due to gravity (including the concept of rheological similarity). *Physics of the Earth and Planetary Interiors* **43**(4), 316-330.

- Weyhenmeyer, C. E., Burns, S. J., Waber, H. N., Macumber, P. G. & Matter, A. 2002. Isotope study of moisture sources, recharge areas, and groundwater flow paths within the eastern Batinah coastal plain, Sultanate of Oman. *Water Resources Research* **38**(10), 2-1-2-22.
- Whipple, K. X. 2001. Fluvial Landscape Response Time: How Plausible Is Steady-State Denudation? *American Journal of Science* **301**(4-5), 313-325.
- Whipple, K. X. 2004. Bedrock rivers and the geomorphology of active orogens. *Annual Review of Earth and Planetary Sciences* **32**(1), 151-185.
- Whipple, K. X., Snyder, N. P. & Dollenmayer, K. 2000. Rates and processes of bedrock incision by the Upper Ukak River since the 1912 Novarupta ash flow in the Valley of Ten Thousand Smokes, Alaska. *Geology* **28**(9), 835-838.
- Whipple, K. X. & Tucker, G. E. 1999. Dynamics of the stream-power river incision model: Implications for height limits of mountain ranges, landscape response timescales, and research needs. *Journal of Geophysical Research* **104**(B8), 17661-17674.
- White, R. S. 1982. Deformation of the Makran accretionary sediment prism in the Gulf of Oman (north-west Indian Ocean). *Geological Society, London, Special Publications* **10**(1), 357-372.
- White, R. S. & Loudon, K. E. 1982. The Makran continental margin: structure of a thickly sedimented convergent plate boundary. *In: Studies in continental margin geology* (edited by Watkins, J. S. & Drake, C. L.) **34**, American Association of Petroleum Geologists, Memoir, Tulsa, 499-518.
- Willett, S., Beaumont, C. & Fullsack, P. 1993. Mechanical model for the tectonics of doubly vergent compressional orogens. *Geology* **21**(4), 371-374.
- Willett, S. D. 1992. Dynamic and kinematic growth and change of a Coulomb wedge. *In: Thrust tectonics* (edited by McClay, K. R.), Chapman and Hall, London, 19-31.
- Willett, S. D. 2010. Erosion on a line. *Tectonophysics* **484**(1-4), 168-180.
- Willett, S. D. & Brandon, M. T. 2002. On steady states in mountain belts. *Geology* **30**(2), 175-178.
- Willett, S. D., Fisher, D., Fuller, C., En-Chao, Y. & Chia-Yu, L. 2003. Erosion rates and orogenic-wedge kinematics in Taiwan inferred from fission-track thermochronometry. *Geology* **31**(11), 945-948.
- Willett, S. D., Slingerland, R. & Hovius, N. 2001. Uplift, Shortening, and Steady State Topography in Active Mountain Belts. *American Journal of Science* **301**(4-5), 455-485.
- Wobus, C., Heimsath, A., Whipple, K. & Hodges, K. 2005. Active out-of-sequence thrust faulting in the central Nepalese Himalaya. *Nature* **434**(7036), 1008-1011.
- Wobus, C., Whipple, K. X., Kirby, E., Snyder, N., Johnson, J., Spyropolou, K., Crosby, B. & Sheehan, D. 2006a. Tectonics from topography: Procedures, promise, and pitfalls. *Geological Society of America Special Paper* **398**, 55-74.

- Wobus, C., Whipple, K. X., Kirby, E., Snyder, N., Johnson, J., Spyropolou, K., Crosby, B. & Sheehan, D. 2006b. Tectonics from topography: Procedures, promise, and pitfalls. In: *Tectonics, Climate, and Landscape Evolution* (edited by Willett, S. D., Hovius, N., Brandon, M. T. & Fisher, D. M.). *Geological Society of America Special Papers* **398**, Geological Soc Amer Inc, Boulder, 55-74.
- Wobus, C. W., Hodges, K. V. & Whipple, K. X. 2003. Has focused denudation sustained active thrusting at the Himalayan topographic front? *Geology* **31**(10), 861-864.
- Wong, I. G. 2005. Low potential for large intraslab earthquakes in the central Cascadia subduction zone. *Bulletin of the Seismological Society of America* **95**(5), 1880-1902.
- Ye, S., Bialas, J., Flueh, E. R., Stavenhagen, A., von Huene, R., Leandro, G. & Hinz, K. 1996. Crustal structure of the Middle American Trench off Costa Rica from wide-angle seismic data. *Tectonics* **15**(5), 1006-1021.
- Zahno, C., Akçar, N., Yavuz, V., Kubik, P. W. & Schlüchter, C. 2010. Chronology of Late Pleistocene glacier variations at the Uludağ Mountain, NW Turkey. *Quaternary Science Reviews* **29**(9-10), 1173-1187.
- Zhang, P., Molnar, P. & Downs, W. R. 2001. Increased sedimentation rates and grain sizes since 2–4 Myr ago due to the influence of climate change on erosion rates. *Nature* **410**, 891–897.

Acknowledgments

First of all, I would like to express my gratitude to *Jean-Pierre Burg* for giving me the chance to do this PhD. Thanks for teaching me self confidence and also for your help in difficult last months of the PhD. His broad knowledge in geology and enthusiasm about science have guided me on my learning process. I appreciate your support and motivation, and the liberty you gave me during my work. Special thanks to *Florian Kober* for his guidance and supervision throughout my PhD. Many many thanks to *Susan Ivy-Ochs* for your great support and constant encouragement – and nice discussions and moments we had. I would like to thank *Gerold Zeilinger* for his supports in the field and teaching me remote sensing methods. Thanks to *Sean Willett* and *Mark Brandon* for being the co-referees of my dissertation. I am also very grateful to *Mohammad Faridi* for his special supports during the field work and the great time we had in the field. The useful discussions with *Daniel Bernoulli* are acknowledged.

The successful outcome of this thesis would not have been possible without the great support of the *Ion Beam Physics Group at ETH Höggerberg*. I have greatly enjoyed working with them and special thank goes to: *Peter W. Kubik, Marcus Christl, Irka Hajdas*. I would like to thank Michael Rüttimann and Montana Maureman for their great assistants in the lab.

During my PhD, I have had the opportunity to be a part of the dynamic Structural Geology and Tectonics Group (SGT) which I have benefited from the interesting discussion and seminars. Thanks to all of you.

Geological survey of Iran deserves special thanks for its contribution to this project. Thanks to *Mohammad Reza Ghassemi (GSI)* for his role in setting up the field project with our team, and for providing abundant logistical support throughout the project. For his enthusiasm, support, and his role in getting the project underway. I am glad to have met *Kristina Hippe* and the nice moments we shared in the lab.

It was a pleasure sharing an office with *Daniela, Sarah, Pipo, Claudio and Jonas*. Thanks for the great times we shared together work related and non-work related.

I will not forget the supports of *Regula Schaelchli* from the first day of my arriving in Zurich.

I wish to make a special acknowledgment to my dearest *Leily and Parisa* who, even from Iran were always present during my PhD. Her friendships, care and advices were very valuable and always a source of strength and encouragement to me.

I want to express my deep gratitude to my dear parents, *Molouk and Hamid*, to whom I dedicate my work and all my victories during my PhD. I thank them for their love and for being the source of inspiration for my work.

The final thanks are for *Andreas*, thanks for all your supports and being patient...

Curriculum Vitae

Personal information

Name	Negar Haghipour
Date of Birth	May 17 th , 1977
Place of Birth	Tehran (Iran)
Citizenship	Iranian

Education

2008-2013	PhD in Structural Geology and Tectonics at the ETH-Zurich
1999-2002	MSc degree in Geology (Azad University of Tehran - North Branch, Iran)
1995-1999	BSc in Geology (Azad University of Tehran - North Branch, Iran)

Work experience

2003-2008	Structural Geologist, Geological Survey of Iran (Tehran, Iran)
-----------	--

Language skills

Persian	Native language
English	Fluent in writing and speaking
French	Fluent in speaking
German	Basic